Distribution Agreement

In presenting this thesis or dissertation as a partial fulfillment of the requirements for an advanced degree from Emory University, I hereby grant to Emory University and its agents the non-exclusive license to archive, make accessible, and display my thesis or dissertation in whole or in part in all forms of media, now or hereafter known, including display on the world wide web. I understand that I may select some access restrictions as part of the online submission of this thesis or dissertation. I retain all ownership rights to the copyright of the thesis or dissertation. I also retain the right to use in future works (such as articles or books) all or part of this thesis or dissertation

Signature:

_____ _____

Zhuangqun Huang Date

Charge Transfer Dynamics in Homogeneous and Heterogeneous Artificial Photosynthetic Systems

By

Zhuangqun Huang
Doctor of Philosophy

Chemistry

_____
Dr. Tianquan Lian, Advisor

_____
Dr. Craig L. Hill, Committee Member

_____
Dr. Michael C. Heaven, Committee Member

Accepted:

_____
Lisa A. Tedesco, Ph. D.
Dean of the James T. Laney School of Graduate Studies

_____
Date

Charge Transfer Dynamics in Homogeneous and Heterogeneous Artificial Photosynthetic Systems

By

Zhuangqun Huang

B.S., Nanjing University, China, 2006

Advisor: Tianquan Lian, Ph. D.

An Abstract of
A dissertation submitted to the Faculty of the
James T. Laney School of Graduate Studies of Emory University
in partial fulfillment of the requirements for the degree of
Doctor of Philosophy
in Chemistry
2011

Abstract

Charge Transfer Dynamics in Homogeneous and Heterogeneous Artificial Photosynthetic Systems

By Zhuangqun Huang

The direct, efficient, and sustained sunlight-driven water splitting process as a method to store energy in the simplest but highest energy-dense chemical bond, H_2, remains one of the most desirable targets to achieve energy and environmental sustainability. The three general goals of this thesis are: (1) utilization of polyoxometalate (POM) WOCs for solar-driven water oxidation; (2) preparation of triads and all inorganic dyads while tuning their charge separation dynamics and O_2 evolution properties, and (3) evaluation of the interfacial electron transfer dynamics and O_2 evolution properties of these dyads and triads.

This thesis starts from the evaluation of the all-inorganic polyoxometalate WOCs in a homogeneous system. These WOCs are oxidatively, hydrolytically and thermally stable, can accommodate multiple metals with varying potentials, and therefore are promising for efficient solar fuel production. The spectroscopic studies of the charge separation dynamics in homogeneous systems show that an integrated acceptor-photosensitizer-WOC composite with intact, directly-connected structure is a promising approach to accelerate the water oxidation process and hence improve the selectivity and quantum efficiency of the WOC. Before discussing heterogeneous systems, it is vital to understand the photophysics of the polyoxometalate molecules, where the nature of the metal-to-polyoxometalate charge transfer in a POM chromophore is discussed in detail. This investigation facilitates our understanding of the interfacial change transfer dynamics in composite electrodes, and more importantly the development of all inorganic dyadic photoanodes with POM choromophores as photosensitizers. After that, the efforts to prepare and characterize stable nano-assembles of triads and dyads are presented, where the triadic and dyadic electrodes are extensively investigated by transient spectroscopy. Throughout the whole work, various spectroscopic tools are employed to understand the relevant fundamental photophysics, photochemistry, and photoelectrochemistry in order to improve the performances of the existing systems and to guide the designs of new constructs.

Charge Transfer Dynamics in Homogeneous and Heterogeneous Artificial Photosynthetic Systems

By

Zhuangqun Huang

B.S., Nanjing University, China, 2006

Advisor: Tianquan Lian, Ph. D.

A dissertation submitted to the Faculty of the
James T. Laney School of Graduate Studies of Emory University
in partial fulfillment of the requirements for the degree of
Doctor of Philosophy
in Chemistry
2011

Acknowledgments

Reaching this milestone of my life, too many names come to my mind to be possibly listed here completely.

Without any hesitation, I offer my first heartfelt thanks and gratitude to my advisor, Dr. Tianquan Lian, who has supported me throughout my graduate career. I also never hesitate to express my sincere appreciation to Dr. Craig Hill, who is more like another advisor of mine rather than a committee member. Without the patient guidance from both Dr. Lian and Dr. Hill over the past five years, it would be impossible for me to be a well-trained researcher in my field. Their encouraging challenges in critical thinking, as always, completely re-construct the way that I thought about science, and research, which is the most profound life-long influence to me. This dissertation is a tribute to their continued supports and guidance, without which it might have been left in vain.

I also wish to extend my sincere thanks and appreciation to Dr. Michael Heaven, the third member of my graduate committee, and Dr. Djamaladdin Musaeve, the third principle investigator in my collaborated research projects, for both the valuable time and thoughtful advice that they have contributed to my research progress throughout the years, and particularly for their strong recommendations for my postdoctoral applications.

I would also like to thank Dr. Bryan Dyer for his guidance in understanding spectroscopy and in identifying the central problem of unresolved issues. His spectroscopy class is one of the best that I have attended during my school life.

I also deeply appreciate and extremely enjoyed working with Dr. Yurii Geletii, who is the primary person who guided me into the depth of this research project step by step in my early graduate years. Dr. Geletii is also a person that I can always count on to discuss the tiniest details of a problem.

Before I show my deep appreciation to others, I definitely must thank Ms Ann Dasher Englert, who is our considerate graduate student coordinator. She is always ready to help me out with the many problems (too many to name them) that I have had in the past five years. She is incredibly helpful to my life at Emory.

Dr. David Stockwell, Dr. Jier Huang and Dr. Shengye Jin are other three special colleagues and friends that I must acknowledge. My hands-on experience with the ultrafast spectroscopy system was provided by Dr. Stockwell, who is also the best mentor in American culture that I had. My initial training with colloidal synthesis was done with

Dr. Jier Huang. I need to mention here that this thesis only accounts for approximately half of my graduate works. The other half is focused on quantum dot-based research. I completed that work with Dr. Jier Huang closely, yielding many decent publications. Dr. Jier Huang was also the best neighbor to me especially during my hard times with a severe ankle fracture. In addition, I did my training in time-resolved fluorescence spectroscopy under the supervision of Dr. Shengye Jin's. I have also learned a lot from Dr. Shengye Jin about how to make a complex system simple. I enjoyed the very good old days when these people worked in the group.

Chantelle Anfuso and Dr. Patrick Coppock are another two best American friends, best language instructors, and first American classmates of mine. Without them, my graduate life will be much less wonderful.

I am also very lucky to have David Wu and Qiushi Yin as my other two best friends. They are the most brilliant people in their ages that I have seen and their tremendous helps to both my research work and personal life are really crucial to what I have achieved today.

Dr. Xu Xiang is a very special friend and colleague to me. He joined in this group as a visiting professor in my last graduate year. He is a trememdous help to my last stage of graduate research. Without his participation, most of the works in Chapter 9-11 of this thesis would be greatly delayed.

Working with these valuable friends, Dr. Zhen Luo, Dr. Yu Hou, Dr. William Rodríguez-Córdoba, Dr. Alexey Kaledin, Dr. Allen Ricks, Dr. John Fielden, and Dr. Zheng Liu, greatly improves my laboratory skills and broadens my research scopes in many areas, especially in the polyoxometalate, metal oxide, electrochemistry, plasmonics and laser spectroscopy fields. I really appreciate their great help in my academic life.

There are so many collaborators that I definitely cannot miss their names here. Dr. Kyoung-Shin Choi in Purdue University greatly helped me with not only the hematite sample preparation but also the photoelectrochemistry. Dr. Edwin Constable at University of Basel, Dr. Karl Hagen at Emory, Dr. Duanwei Wang in Boston College and Dr. Seth Marder from Georgia Institute of Technology were other sources of materials. In addition, Dr. Stefan Lutz, Dr. Shuming Nie and Dr. Kurt Warncky at Emory have special spectrometers that are always open to me for use. Furthermore, Dr. Russell Schemel from Tulane University helped me in understanding the MLCT process. I also highly appreciate helps from students and post doctors (also my friends) in these and other

groups: Emma Dunphy, Yongjin Lin, Brandon Greene, Wesley Robertson, Jing Gu, Andrew Smith, Chun Huang and Ximei Qian.

I am also grateful to our lab families from both the Lian and Hill groups: Haiming Zhu, Beibei Ma, Ye Yang, Kaifeng Wu, Nianhui Song, Weimin Liu, Claire Besson, Chongchao Zhao, James Vickers, Guibo Zhu, Jie Song, Kevin O'Halloran, Naifei Zhang, and Hongjin Lv. They are always excellent inspiring colleagues when discussing challenging topics, always helpful in miscellaneous lab works and always supportive whenever I am facing personal difficulty.

I would also like to thank the important help from many staffs in the departments, especially, Dr. Daphne Norton in the general chemistry lab; Dr. Yi Hong, Dr. Elizabeth Wright, and Dr. Jeannette Talyor in the electron microscopy center where I spent a wonderful year and was trained as service instructor; Steve Krebs and Patti Barnet, two patient, friendly and helpful persons from the strockroom.

There are many friends and mentors who accompanied me to get through the difficult times in both personal life and research for the past five years. They are friends at Emory: Weilin Peng, Jin Liu, Xiao Postell, Dr. Chao Chen, Dr. Liang Shang, Dr. Dandan Chen, Yi Xu, Lei Chu, Dr. Rongbiao Tong, Dr. Lin Xu, Dr. William Cassels (mentor in Toasmasters), … and friends outside Emory: Dr. Yi Shi (my undergraduate advisor), Dr. Jianwei Zhao (my undergraduate advisor), Dr. Xinran Wang, Dr. Philip Earis, Dr. Lijia Pan, Dr. Lin Pu, Dr. Han Zhu, Jing Chen, Dr. Xiaohui Peng, Dr. Wenjing Song, Fang Ye, Li Yao, Dr. Yejia Li, Roslyn Lian, Zehui Chen …

I give great thanks to my entire family. To make my mother and father be proud of me has been always an impetus to me for success. My sister Liuzhen, to whom this dissertation is dedicated, is also critical to my graduate life here in USA. My brother Zhuangxiong, the only person with whom I can share both my research and life in depth, has been both supportive and critical throughout my entire scholastic career.

Finally, I thank my loving Zhengying Lou and her family. Doro and her parents could not have been more supportive and understanding since Doro came into my life in 2007. Doro has been encouraging me persistently to pursue this career and helping me to concentrate when I have become distracted. Her love helps me get through the darkness. Her personality unconsciously influences that of mine, which greatly helps to improve my productivity and even my critical thinking when dealing with a dilemma. I am wholeheartedly grateful for her dedication and encouragement.

Table of Contents

Part I: Introduction

Part II: Experimental Methods

Part III: Homogeneous Light-driven Water Oxidation

Part IV: Photophysics of Polyoxometalates

Part VI: Heterogeneous systems: composite dyadic photoanodes

List of Figures

Chapter 1

Chapter 3

Chapter 4

Chapter 5

Chapter 6

Chapter 7

Chapter 8

Chapter 9

Chapter 10

Chapter 11

List of Tables

Part I: Introduction

CHAPTER

1

Fundamentals and Mechanisms in Natural and Artificial Photosynthetic Systems

1.1 Overview

The direct harvest, conversion, and storage of sunlight energy into chemical bonds, such as that which occurs in natural photosynthesis, is highly desired in order to meet the global clean energy demand and to bridge the intrinsic gaps—safety, intermittency and inefficiency—among existing renewable energy technologies.[1-8] In particular, the direct, efficient, and sustained sunlight-driven water splitting process ($H_2O + h\nu \rightarrow H_2 + ½ O_2$) as a method to store energy in the simplest but highest energy-dense chemical bond, H_2, remains one of the most desirable targets to achieve energy and environmental sustainability.[9-30] H_2 can be used either directly as a fuel or as a high energy substrate for producing other chemical fuels; for instance, it may be used for CO_2 reduction to form liquid fuels such as gasoline, diesel or biodiesel.

The splitting of H_2O can be divided into two half reactions: water oxidation to release O_2, eq 1.1, and proton reduction to release H_2, eq 1.2.

$$2\ H_2O \rightarrow O_2 + 4\ H^+ + 4\ e^- \qquad E = 0.82\ \text{V, at pH 7} \qquad (1.1)$$

$$2\ H^+ + 2\ e^- \rightarrow H_2 \qquad E = 0.41\ \text{V, at pH 7} \qquad (1.2)$$

The oxidation potentials for the oxidation and the reduction are 0.82 V and 0.41 V per electron transferred, respectively, with respect to the standard hydrogen electrode (SHE). Both processes involve multiple-proton-coupled multiple electron transfer, where the generation of one O_2 molecule requires the loss of 4 electrons and 4 protons from 2 H_2O molecules, and a thermodynamic minimum energy of 4×0.82 eV = 3.28 eV at pH 7. Because of the higher intrinsic complexity, water oxidation is more difficult than proton reduction, and becomes the thermodynamic uphill in water splitting and other related solar fuel producing processes.

A near infrared photon with a wavelength of 1.5 μm carries a photon energy of ~0.82 eV. Thus, thermodynamically, ~ 90% of the photons from sunlight in terms of the Air Mass 1.5 solar spectra can be used as energy input to drive the reaction to evolve O_2, if an active site exists that allows for the accumulation of 4 holes generated by these photons. This active site is generally a water oxidation catalyst (WOC) that lowers the overall activation energy requirement, and can be oxidized or reduced by several electrons. [16,17,19,20,22,28,31-52] However, in most systems, one absorbed photon only results in a single electron transfer event. Thus, a system that is capable of successive light-absorptions, charge separations and accumulations together is necessary for successful water oxidation and subsequent solar fuel production. Generally, a system with the following attributes is highly desired:

1. the photon receptor can absorb a large portion of the solar spectrum;
2. the charge acceptor can efficiently separate electrons and holes to compete with intrinsic charge recombination and to keep up with the solar flux;
3. the WOC can accumulate holes; and
4. the catalytic turnover of the WOC can keep up with the solar flux.

Practically, the system is also required to be robust, self-sustained with H_2O (and CO_2) as the electron and proton sources (and reaction substrates), and with sufficiently low costs that would allow for large-scale production.

Therefore, an effective, multi-component structure is highly desired that integrates all the functional units including light receptors, charge acceptors and WOCs, and that couples one-photon absorption and single electron transfer events with the multi-electron water splitting process. In addition, this system is also required be capable of

connecting to or combining with other reduction half reactions, such as proton or CO_2 reductions, in order to employ the energetic photogenerated electrons for producing solar fuels.

Since the seminal work by Fujishima and Honda in 1972,[53] four decades of research efforts towards solar fuel production have not yet fulfilled the general goal to have a system simultaneously be efficient, robust, and cheap. To advance this progress, the challenges in solar fuel production must be indentified first. To a large extent, most studies in this field are biomimetic, or based on the reverse engineering of the natural photosynthetic systems in green plants. The next section will give a brief description of the current understanding of the fundamental principles governing the mechanistics in natural photosynthetic systems. Following that, general challenges in artificial photosynthetic systems will be discussed.

1.2 Photosystem II: fundamentals and mechanisms

Nature offers a blueprint—photosynthesis—for converting and storing sunlight energy in chemical bonds. The highly energetic redox reaction of water splitting occurs in the photosystem II (PSII) of oxygenic photosynthetic organisms. Figure 1.1 shows a simplified scheme of a typical natural PSII construct, which illustrates the main energy-kinetic features and shows the structure of the Mn_4CaO_5 catalytic core for water oxidation. [54-56]

Interestingly, the absorption spectrum of the primary electron donor in the reaction center, P680, overlaps poorly with the solar spectrum and is not a good light receptor. To enhance the light harvesting, a variety of pigments serving as light antennas

are organized surrounding the PSII reaction center.[56-58] The antenna system has both spatial and energetic advantages, constructing an energy funneling channel for capturing the solar flux. Energetically, this arrangement allows the excitation energy to flow from pigments that absorb bluer photons to those that absorb lower photonic energy, and, consequently, broadens the overall absorption spectrum of the reaction center. Spatially, by arranging species that absorb higher energy photons further away from the reaction center and placing those that absorb lower photonic energy close to the center, not only can the excitation energy be funneled down to the reaction center, but the light-absorbing space is also expanded. This allows for the harvesting of photons from more relatively diffuse sources of sunlight

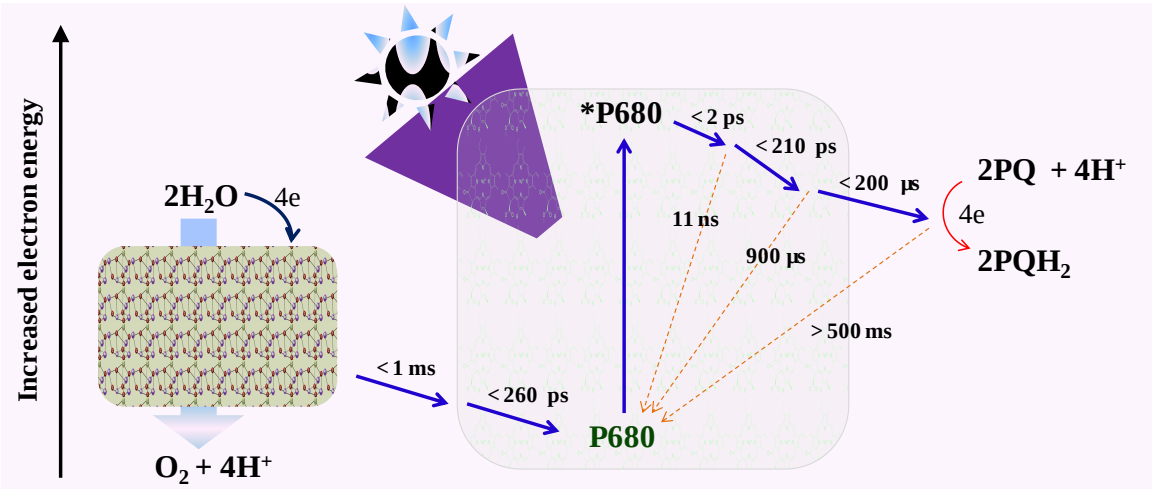

Figure 1.1 A schematic representation of the PSII reaction center and its energy-kinetic diagram for the photochemistry and energy-/electron-transfer processes.[56-62] Intermediates are omitted. Solid blue lines indicate the electron transport train; red dashed lines show the charge recombination pathways.

The underlying photophysics for the light antenna effect is a non-radiative resonance energy transfer process from excited donor (D*) to ground state acceptor (A), as shown in eq 1.3,

$$D^* + A \rightarrow D + A^* \quad (1.3)$$

This well-known process has been detailed in the Förster model.[63] The Förster theory is based on the long-term dipole-dipole approximation,[64] assuming that the donor and acceptor chromophores are weakly coupled and that their separation is large (up to 10 nm) with respect to the pigment dimensions. The Förster resonance energy transfer (FRET) rate (k_{EnT}) depends on the mutual orientation (κ), the intrinsic radiative rate of the donor (k_0), the spectral overlap integral (J) between the donor emission and acceptor absorption, and the donor-acceptor distance, as shown in eq 1.4.

$$k_{EnT} = \alpha \frac{\kappa^2 k_0}{r^6} J \quad (1.4)$$

where α is a constant. Due to the Stokes shift from the absorption to the emission spectrum of a fluorescent molecule, FRET is always accompanied by the loss of photonic energy as waste heat through vibrational relaxation. This provides a certain irreversibility to this process, which facilitates the effective energy transfer from the donor to the acceptor.

As shown in Figure 1.1, excitation of P680 produces a strong reducing species, P680*, and initiates the first ultrafast electron transfer event (< 2 ps), which is followed by further electron movements along the electron-transfer train.[59-62] Following a cascade of electron-transfer events, the photo-induced energetic electron gradually loses part of its energy. However, it is so spatially separated from the resulting $P680^+$ that the probability of charge recombination is reduced by many orders of magnitude. On the other side of

the electron-transfer train, $P680^+$ is the strongest oxidizing cofactor in living organisms with a reduction potential of ~1.25 V (vs SHE). In PSII, $P680^+$ takes electrons from the Mn_4CaO_5 catalyst, by which the ground state P680 is regenerated.

In addition to the increased efficiency of light-harvesting due to the light antenna effect, nature has also established an effective electron transfer scheme in PSII.[65,66] An electron transfer from the donor (D) to the acceptor (A) can be expressed as,

$$D + A \rightarrow D^+ + A^- \tag{1.5}$$

The basic theoretical framework for describing electron transfer between weakly coupled donor and acceptor states was developed in the 1960s and is well-known as the Marcus theory.[67-69] For a non-adiabatic process, the electron transfer rate (k_{ET}) is given by,

$$k_{ET} = \frac{2\pi}{h} \frac{|H|^2}{\sqrt{4\pi\lambda k_B T}} \exp\left[-\frac{(\lambda + \Delta G)^2}{4\lambda k_B T} \right] \tag{1.6}$$

where H is the electronic coupling and is a function of the overlap of donor and acceptor orbitals; λ is the total reorganization energy which describes molecular structural changes from the reactant to product states; ΔG is the Gibbs free-energy change for the reaction, also known as the driving force; and, k_B and T are the Boltzmann constant and the temperature, respectively.

First, the electronic coupling strength H depends on spatial, energetic, geometric, and symmetry factors. The dominant factor is the donor-acceptor distance, where H decreases exponentially as the distance increases. This indicates that electron transfer demands a great deal of spatial overlap between the orbitals involved. Thus, as the electron moves away from the donor molecule, the back electron transfer rate is exponentially diminished partially due to the decreased electronic coupling strength. In

addition, nature has tuned the structural arrangement of different units in PSII to favor efficient energy transfer while preventing destructive electron-transfer processes from energetic antenna pigments to the reaction center.

Additionally, the exponential term in eq 1.6 indicates that electron transfer can occur in three regimes. When $-\Delta G < \lambda$, called the normal region, k_{ET} increases with the driving force; when $-\Delta G = \lambda$, the electron transfer k_{ET} is maximized; and when $-\Delta G > \lambda$, the system is in the inverted region and k_{ET} is reduced with increasing driving force. In PSII, the electron transfer chain is embedded in the thylakoid membrane, and consequently, the reorganization energy is relatively small (~0.2 – 0.7 eV). However, charge recombination processes are generally highly exergonic reactions, so the electron transfer reactions fall into the inverted region.[69] Under these circumstances, the back electron transfer processes are considerably inhibited, facilitating the forward electron transfer reactions.

As mentioned above, $P680^+$ is the most strongly oxidizing redox cofactor known in biology. However, the reduction potential of $P680^+$ (1.25 V vs SHE) is much lower than that required by the water oxidation pathway through the radical formation,

$$H_2O \rightarrow OH^{\bullet} + H^+ \qquad E = 2.33 \text{ V vs SHE, at pH 7} \qquad (1.7)$$

Therefore, the oxogenetic water splitting in PSII must proceed through the minimum energy four-electron pathway with an averaged required energy of 0.82 eV per transferred electron, as shown in eq 1.1. Thus, each photonic excitation of P680 only results in one oxidizing equivalent of $P680^+$. In this regard, a WOC that serves as a capacitor is required to successively store oxidation equivalents through four individual photo-induced charge separation events. In PSII, the catalytic water oxidation is

performed by the Mn_4CaO_5 catalyst at near zero over potential and a modest turnover (50 O_2 molecules per second). This multi-metal catalytic center is capable of capturing and releasing multiple electrons due to the multi-valence transition metals involved. Another greatly attractive feature of this catalytic core is that this naturally occurring WOC consists of only earth abundant elements.

In summary, the compact natural PSII construct integrates multiple spatially-separated functional units that allow for all of the fundamental steps involved in the overall water oxidation process: light absorption, excitation energy transfer, charge separation and accumulation, and catalytic water oxidation. These functional units consist of photosensitizers, electron acceptors, and a WOC. The water oxidation mechanism in PSII can be simplified to a cyclic circle following P680 at different energetic states, which can be further generalized to any WOC mechanism as shown in Figure 1.2. By replacing the appropriate materials of PSII but maintaining the corresponding functions, as well as improving the configuration using PSII as an inspiration, artificial photosynthetic systems can be constructed with much better performance.

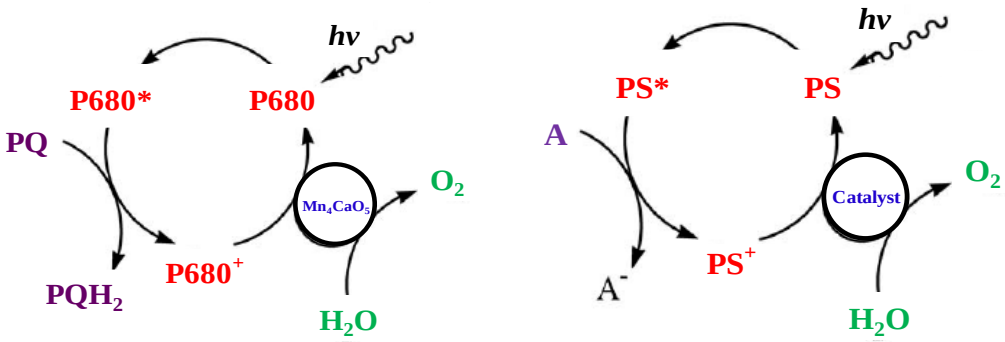

Figure 1.2. Left: a schematic representation of the cyclic reactions among different functional units in PSII. Right: a generalized scheme of the processes involved in PSII. Notation: PS, photosensitizer; A, electron acceptor.

1.3 General challenges in artificial photosynthesis

Figure 1.3 shows a simplified representation of an artificial water splitting system, which can be transformed into a fuel-producing system if one replaces the water reduction catalyst (WRC) with a CO_2 reduction catalyst.

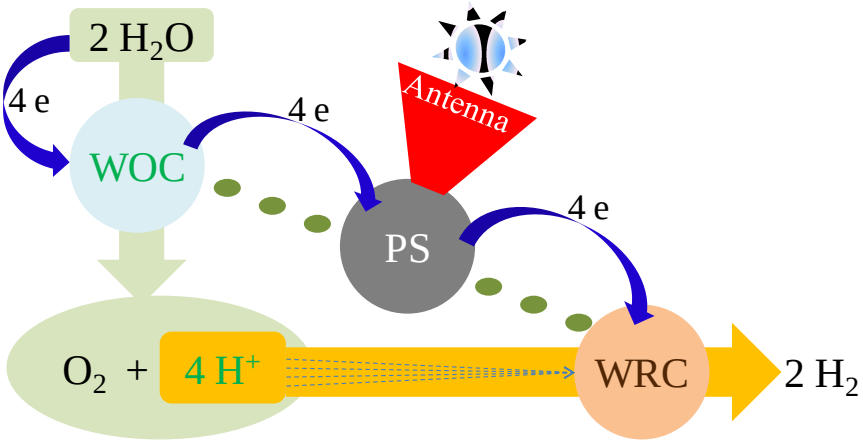

Figure 1.3. General scheme for splitting water into O_2 and H_2. Light is harvested by an antenna structure and transferred to the central photosensitizer (PS). The subsequent electron-transfer events assisted by the bridged moieties (green dots) produce charge separation states with lifetimes long enough for charge accumulations on the water oxidation (WOC) and reduction (WRC) catalysts to split water. Protons released from the WOC are efficiently transferred to the WRC through a specific channel.

To a large extent, this scheme is inspired by the natural photosynthetic construct, from which the main attributes remain: light collection, charge transfer, and catalytic reactions.[70] The general challenges for artificial photosynthesis can be gleaned from Figure 1.1. The central goal is that the rate of energy conversion needs to be fast enough to optimally keep up with the incident radiant power. In this regard, the control of relative

rates in different processes (energy transfer, charge separation, and catalytic turnover) is critical throughout such a system, both in each component and in the overall structure as one single unit.[71-75]

First, light absorbers are required in this system to transform the solar energy into oxidizing and reducing chemical potentials to drive the reactions for splitting water. The capability of a particular photosensitizer to absorb light sets the maximum efficiency for the ultimate energy conversion, which depends on the energy gap (E_g) between the highest-occupied-molecular and lowest-unoccupied-molecular orbitals (HOMO-LUMO) for molecular photosensitizers, or between the bottom of the conduction band and the top of the valence band for semiconductor light absorbers. The photo converter is transparent to photons with energy smaller than E_g, and although it can capture photons with energy larger than E_g, it suffers from energy loss as heat through internal conversion or intraband thermalization. On the basis of these considerations, the ideal bandgap for a single-photosensitizer device is ~1.3 eV (920 nm) with a conversion efficiency limit of ~33%, the well-known Shockley-Queisser limit. [76]

In terms of the known solar spectrum,[77] the number of solar photons with a specific energy quantum or at a particular wavelength, $n(\lambda)$, can be estimated using eq 8a,

$$\begin{cases} n(\lambda)d\lambda = \dfrac{P(\lambda)d\lambda}{hc/\lambda} & \text{(a)} \\ n = \displaystyle\int_0^{\lambda} \frac{P(\lambda')}{hc/\lambda'}d\lambda & \text{(b)} \end{cases} \tag{1.8}$$

where $P(\lambda)$ is the power intensity at a given wavelength λ. Therefore, the number of solar photons with photonic energy higher than a given threshold, n, can be calculated by eq 1.8b, as shown in Figure 1.4.

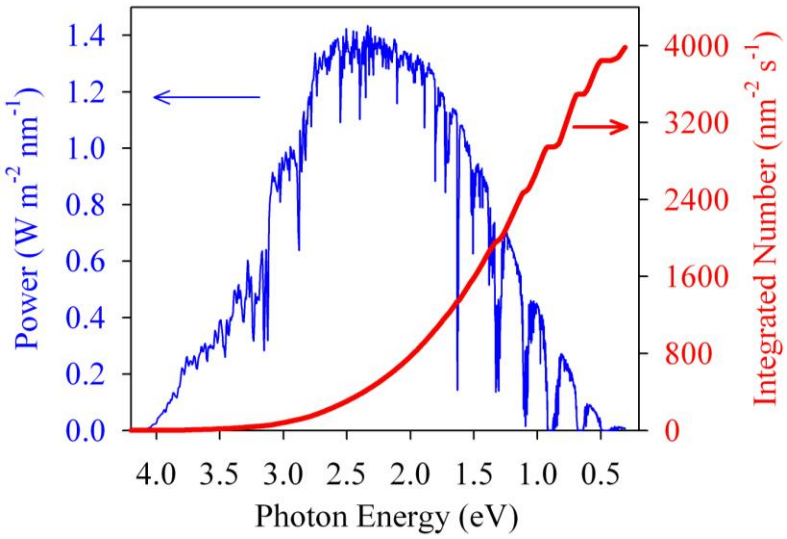

Figure 1.4. Air Mass 1.5 solar spectrum on the earth's surface (blue) and the integrated photon numbers per area (nm^2) per second with integration from high to low photon energy. These curves are based on the American Society for Testing and Materials (ASTM) Terrestrial Reference Spectra.[77]

For example, the number of solar photons with energy higher than 1.3 eV, the threshold for an ideal single-photosensitizer device, is ~3000 per second for an area of 1 nm^2, or ~3 $ms^{-1} \cdot nm^{-2}$. Area is given in units of nm^2 here because most photosensitizers are on the nm scale. As shown in Figure 1.1, the charge separation can occur on the μs or even ps time scale, so the charge separation should be capable of keeping up with the radiant flux. However, much as in PSII, the catalytic water oxidation is actually the rate-limiting step in artificial photosynthetic systems; specifically, the last step in the four-electron reaction occurs in ~1 ms.[55] Since water oxidation is a four-electron process, the estimation above requires a catalytic center with 1 nm^2 surface area to have a turnover frequency of ~750 s^{-1}. Thus the lack of efficient, robust, and low-cost WOCs that meet this requirement is currently the main challenge in artificial photosynthesis.[30,78]

Currently, the most investigated and established approach in artificial photosynthetic systems to realize the two half reactions, eqs 1.1 and 1.2, is shown in Figure 1.5.[30]

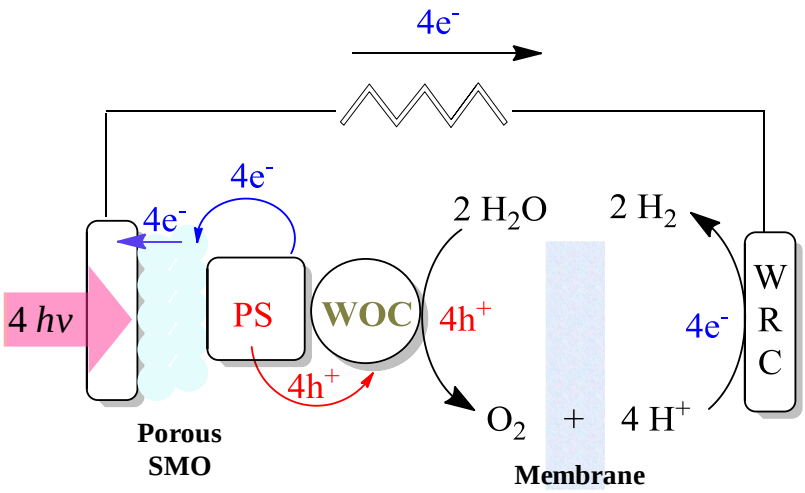

Figure 1.5. General schematic representation for a typical light-driven water splitting photoelectrochemical cell. Notations: SMO, semiconductor metal oxide; PS, photosensitizer; WOC, water oxidation catalyst; WRC, water reduction catalyst.

At the water oxidation anode, upon optical excitation, the electrons of the excited photosensitizer (PS in Figure 1.5) are transferred to the nanoporous semiconductor metal oxide supported on a transparent conducting substrate.[24,25,79-81] Meanwhile, the holes are left behind in the photosensitizer and sequentially oxidize the WOC. The performance of such an anode can be evaluated by connecting the triadic anode to an external circuit, such that the photoinjected electrons are immediately removed from the anode to reduce H_2O to H_2 at the cathode (Figure 1.3), which can be equipped with a water (or CO_2) reduction catalyst (WRC). In some cases, narrow-band semiconductor metal oxides (α-

Fe_2O_3, doped TiO_2, TaON, etc.) are introduced as both the light absorber and the charge (exciton) separation center to construct a dyadic anode. [30,82-86]

To achieve high electron/hole transfer rates and high quantum yields in these photodriven water oxidation systems, optimization of the individual functions is needed. First, the photosensitizer should have the optimal absorption characteristics to capture the maximal amount of terrestrial sunlight, and upon which, to generate a long-lived excited state that allows for the subsequent charge separation and accumulation. Second, the cascade of electron-transfer events must be efficient enough to produce a maximally long-lived charge-separated state in order to increase the probability of capturing the energetic electron before it recombines and produces waste heat. Most importantly, the WOC needs to be selective for water oxidation and have a fast enough turnover rate to keep up minimally with the charge capture and accumulation and maximally with the solar flux as shown above.

In addition, each component of these systems as well as the entire nano-assembly or photoelectrochemical cell as a whole must be hydrolytically and oxidatively stable. Indeed, the hydrolytic and oxidative stability of each component, as well of the intact nano-assembly (triad) is one of the three central challenges (robust, efficient, and low cost) in developing reliable solar-fuel producing devices. In the process of water oxidation, the system generates a large amount of energetic electrons, radicals and intermediates that can damage the whole construct, unless these species can be efficiently consumed for water oxidation and thus quickly regenerate the system. However, the four-electron/four-proton water oxidation process is the rate-limiting step. In this regard, the stability concerns can be greatly mitigated by improving the WOC performance.

Therefore, creating an efficient and robust WOC made from earth-abundant elements is of central importance to economic solar fuel production.

1.4 Polyoxometalate water oxidation catalysts

As shown in eq 1.1, the theoretically required thermodynamic potential minimum for water oxidation is 0.82 V (vs. SHE) at pH 7. However, experimentally, an overpotential requirement of > 0.5 V is very common mainly due to the existence of an activation barrier from high energy intermediates generated during the water oxidation. Significantly lowering the overpotential for water oxidation is critical to achieving efficient solar fuel production; this can be accomplished by the introduction of WOCs. As mentioned above, WOCs can serve as capacitors to store charges for multiple-electron water oxidation in order to bypass the thermodynamically unfavourable one-electron radical-generation step (eq 1.7). Additionally, as shown in Figure 1.6, a WOC can provide an active site for bound water molecules to facilitate concerted multiple-bond re-arrangements between two H_2O through coupling the highly exergonic O-H dissociation with the energy-releasing O-O bond formation.[2] This avoids the generation of energetic, reactive intermediates. Transition metal complexes or oxide clusters are capable of coordinating water and storing charges and thus make suitable active sites. The most famous example must be the catalytic Mn_4CaO_5 core in PSII as shown in Figure 1.1, where its crystal structure at a resolution of 1.9 Å clearly shows the binding of water molecules on both transition metals, Mn and Ca.[56]

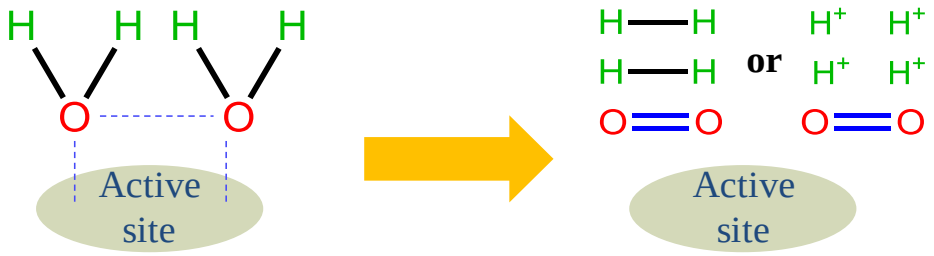

Figure 1.6. Schematic representation of water splitting catalyzed by an active site.

There has been considerable research on the development of WOCs since the first observation of water oxidation catalyzed by various metal oxides in the late 1970s[10,87] and the initial report of a Ru-based molecular WOC in 1982 by T. J. Meyer and co-workers.[11] After three decades of development, to date, there are two broad categories of WOCs. One system is based on heterogeneous (insoluble) transition metal oxide nanoparticles, most of which contain Ru, Ir, Mn, or Co. [4,25,88-92] This type of WOC has been successfully coupled with photoanodes consisting of either narrow-bandgap (doped TiO_2, WO_3 and hematite) or dye-sensitized wide-bandgap semiconductor metal oxides. Mostly inspired by the catalytic center in PSII, the other WOC family is a homogeneous species, including mono-, di- and tri-Ru complexes, Ir derivatives, and mono-, di- or tetra-Mn homogeneous molecules.[93-96] There have been numerous successful applications of these molecular catalysts in homogenous systems, but only a few reports about their immobilization on heterogeneous photoanode surfaces. [32,37,97]

Both homo- and heterogeneous WOCs have their own assets and liabilities. Insoluble WOCs are robust, more easily synthesized, and have lower costs, whereas molecular WOCs demonstrate higher selectivity and higher efficiency per active site metal. Generally, however, molecular WOCs contain organic ligands that are easily

oxidized in competition with water, and thus have relatively low turnover numbers. Unfortunately, such destructive processes when using this type of WOC are inevitable because organic ligands are thermodynamically less stable than the substrate, H_2O. Meanwhile, the product, O_2, creates a highly oxidative environment. In addition, many organic-ligand-stabilized molecular WOCs are notorious for their rapid hydrolytical decomposition in aqueous systems. Therefore, it is desirable to develop WOCs with the positive properties of both heterogeneous and homogeneous catalysts and without the major negative properties of each.[78]

Recently, a new family of molecular WOCs based on early-transition-metal oxygen anion clusters (polyoxometalates, or "POMs") have been reported. [43-52,98] These WOCs are composed of multiple d-electron metal oxide clusters, such as Ru_4O_4 and Co_4O_4, stabilized by POM ligands. These multi-transition metal substituted POM complexes are bridged by oxide ions and self assemble in water, and are therefore oxidatively and hydrolytically stable. In addition, POM complexes are generally amenable to extensive alteration, resulting in highly tunable physiochemical properties (acidity, thermal stability, redox potential, solubility, size, shape, and charge). [99-106] Not surprisingly, there has been a great deal of recent research on the fundamentals and the applications of these WOCs in solar fuel production, which is also the central thrust of this thesis.

1.5 **Goals of this thesis and outline**

The central motivation of this work is to develop solar-driven water oxidation and splitting systems that are lower-cost, more stable and more efficient than existing systems.

The three general goals of this thesis are: (1) utilization of the carbon-free, hydrolytically and oxidatively stable polyoxometalate WOCs for solar-driven water oxidation; (2) preparation of triads (TiO_2-photosensitier-WOCs) and all-inorganic dyads (dyads (hematite-WOCs and SMO-WOCs) while tuning their charge separation dynamics and O_2 evolution properties, and (3) evaluation of the interfacial electron transfer dynamics and O_2 evolution properties of these dyads and triads.

The rest of this work will be organized as follows: experimental details are compiled in Chapter 2. The Part III has three chapters: Chapter 3 focuses on the evaluation of the efficiency and selectivity of different polyoxometalate WOCs in homogeneous systems and the optimization of the overall efficiency of each system. The charge transfer dynamics in homogeneous systems are investigated and shown in Chapter 4. Subsequently, other designs for improved photocatalytic water oxidation are shown in Chapter 5, which outlines our initial attempts to improve the homogeneous system. These attempts eventually led to the development of heterogeneous photoelectrochemical systems. Before discussing heterogeneous systems, Chapter 6 and 7 describe our efforts in understanding the photophysics of the polyoxometalate molecules, where the nature of the metal-to-polyoxometalate charge transfer in a POM chromophore is discussed in details. Finally, the efforts to prepare and characterize stable nano-assembles of triads and dyads are presented in Part V (Chapters 8-11), where the triadic and dyadic electrodes are extensively investigated. Throughout the whole work, various spectroscopic tools (static, time-resolved, ultrafast, absorption, fluorescence, visible, infrared, etc.) are employed to understand the relevant fundamental photophysics, photochemistry, and

photoelectrochemistry in order to improve the performances of the existing systems and to guide the designs of new constructs.

1.6 References

(1) Chow, J.; Kopp, R. J.; Portney, P. R. *Science* **2003**, *302*, 1528.

(2) Lewis, N. S.; Nocera, D. G. *Proc. Nat. Acad. Sci.* **2006**, *103(43)*, 15729.

(3) Balzani, V.; Credi, A.; Venturi, M. *ChemSusChem* **2008**, *1*, 26.

(4) Kanan, M. W.; Nocera, D. G. *Science* **2008**, *321*, 1072.

(5) Flamigni, L.; Collin, J.-P.; Sauvage, J.-P. *Acc. Chem. Res.* **2008**, *41*, 857.

(6) Magnuson, A.; Anderlund, M.; Johansson, O.; Lindblad, P.; Lomoth, R.; Polivka, T.; Ott, S.; Stensjö, K.; Styring, S.; Sundström, V.; Hammarström, L. *Accts. Chem. Res.* **2009**, *42*, 1899.

(7) Gust, D.; Moore, T. A.; Moore, A. L. *Accts. Chem. Res.* **2009**, *42*, 1890.

(8) Dau, H.; Zaharieva, I. *Accts. Chem. Res.* **2009**, *42*, 1861.

(9) Wada, T.; Tsuge, K.; Tanaka, K. *Angew. Chem. Int. Ed.* **2000**, *39*, 1479.

(10) Shafirovich, V. Y.; Khannanov, N. K.; Strelets, V. V. *Nouveau J. de Chimie* **1980**, *4*, 81.

(11) Gersten, S. W.; Samuels, G. J.; Meyer, T. J. *J. Am. Chem. Soc.* **1982**, *104*, 4029.

(12) Harriman, A.; Pickering, I. J.; Thomas, J. M.; Christensen, P. A. *J. Chem. Soc. Faraday Trans. 1*, **1988**, *84*, 2795.

(13) Elizarova, G. L.; Zhidomirov, G. M.; Parmon, V. N. *Catal. Today* **2000**, *58*, 71.

(14) Wada, T.; Tsuge, K.; Tanaka, K. *Angew. Chem. Int. Ed.* **2000**, *39*, 1479.

(15) Limburg, J.; Vrettos, J. S.; Chen, H.; Paula, J. C. d.; Crabtree, R. H.; Brudvig, G. W. *J. Am. Chem. Soc.* **2001**, *123*, 423.

(16) Hurst, J. K. *Coord. Chem. Rev.* **2005**, *249*, 313.

(17) Zong, R.; Thummel, R. *J. Am. Chem. Soc.* **2005**, *127*, 12802.

(18) Hoertz, P. G.; Kim, Y.-I.; Youngblood, W. J.; Mallouk, T. E. *J. Phys. Chem. B* **2007**, *111*, 6845.

(19) Eisenberg, R.; Gray, H. B. *Inorg. Chem.* **2008**, *47*, 1697.

(20) Muckerman, J. T.; Polyansky, D. E.; Wada, T.; Tanaka, K.; Fujita, E. *Inorg. Chem.* **2008**, *47*, 1787.

(21) Kohl, S. W.; Weiner, L.; Schwartsburd, L.; Konstantinovski, L.; Shimon, L. J. W.; Ben-David, Y.; Iron, M. A.; Milstein, D. *Science* **2009**, *324*, 74.

(22) Hull, J. F.; Balcells, D.; Blakemore, J. D.; Incarvito, C. D.; Eisenstein, O.; Brudvig, G. W.; Crabtree, R. H. *J. Am. Chem. Soc.* **2009**, *131*, 8730.

(23) Kunkely, H.; Vogler, A. *Angew. Chem. Int. Ed.* **2009**, *48*, 1685.

(24) Youngblood, W. J.; Lee, S.-H. A.; Kobayashi, Y.; Hernandez-Pagan, E. A.; Hoertz, P. G.; Moore, T. A.; Moore, A. L.; Gust, D.; Mallouk, T. E. *J. Am. Chem. Soc.* **2009**, *131*, 926.

(25) Youngblood, W. J.; Lee, S.-H. A.; Maeda, K.; Mallouk, T. E. *Accts. Chem. Res.* **2009**, *42*, 1966.

(26) Dismukes, G. C.; Brimblecombe, R.; Felton, G. A. N.; Pryadun, R. S.; Sheats, J. E.; Spiccia, L.; Swiegers, G. F. *Accts. Chem. Res.* **2009**, *42*, 1935.

(27) Romain, S.; Vigara, L.; Llobet, A. *Accts. Chem. Res.* **2009**, *42*, 1944.

(28) Concepcion, J. J.; Jurss, J. W.; Brennaman, M. K.; Hoertz, P. G.; Patrocinio, A. O. T.; Iha, N. Y. M.; Templeton, J. L.; Meyer, T. J. *Accts. Chem. Res.* **2009**, *42*, 1954.

(29) Jiao, F.; Frei, H. *Angew. Chem., Int. Ed.* **2009**, *48*, 1841.

(30) Walter, M. G.; Warren, E. L.; McKone, J. R.; Boettcher, S. W.; Mi, Q. X.; Santori, E. A.; Lewis, N. S. *Chem Rev* **2010**, *110*, 6446.

(31) Binstead, R. A.; Chronister, C. W.; Ni, J.; Hartshorn, C. M.; Meyer, T. J. *J. Am. Chem. Soc.* **2000**, *122*, 8464.

(32) Yagi, M.; Kaneko, M. *Chem. Rev.* **2001**, *101*, 21.

(33) McDaniel, N. D.; Coughlin, F. J.; Tinker, L. L.; Bernhard, S. *J. Am. Chem. Soc.* **2008**, *130*, 210.

(34) Brimblecombe, R.; Swiegers, G. F.; Dismukes, G. C.; Spiccia, L. *Angew. Chem. Int. Ed.* **2008**, *47*, 7335.

(35) Hurst, J. K.; Cape, J. L.; Clark, A. E.; Das, S.; Qin, C. *Inorg. Chem.* **2008**, *47*, 1753.

(36) Betley, T. A.; Surendranath, Y.; Childress, M. V.; Alliger, G. E.; Fu, R.; Cummins, C. C.; Nocera, D. G. *Phil. Trans. R. Soc. B* **2008**, *363*, 1293.

(37) Sala, X.; Romero, I.; ǵuez, M. R.; Escriche, L. í; Llobet, A. *Angew. Chem. Int. Ed.* **2009**, *48*, 2842.

(38) Cao, R.; Ma, H.; Geletii, Y. V.; Hardcastle, K. I.; Hill, C. L. *Inorg. Chem.* **2009**, *48*, 5596.

(39) Jiao, F.; Frei, H. *Angew. Chem. Int. Ed.* **2009**, *48*, 1841.

(40) Kuznetsov, A. E.; Geletii, Y. V.; Hill, C. L.; Morokuma, K.; Musaev, D. G. *J. Am. Chem. Soc.* **2009**, *131*, 6844.

(41) Duan, L.; Xu, Y.; Gorlov, M.; Tong, L.; Andersson, S.; Sun, L. *Chem. Eur. J.* **2010**, *16*, 4659.

(42) Masaoka, S.; Sakai, K. *Chem. Lett.* **2009**, *38*, 182.

(43) Geletii, Y. V.; Botar, B.; Kögerler, P.; Hillesheim, D. A.; Musaev, D. G.; Hill, C. L. *Angew. Chem. Int. Ed.* **2008**, *47*, 3896.

(44) Sartorel, A.; Carraro, M.; Scorrano, G.; Zorzi, R. D.; Geremia, S.; McDaniel, N. D.; Bernhard, S.; Bonchio, M. *J. Am. Chem. Soc* **2008**, *130*, 5006.

(45) Geletii, Y. V.; Huang, Z.; Hou, Y.; Musaev, D. G.; Lian, T.; Hill, C. L. *J. Am. Chem. Soc.* **2009**, *131*, 7522.

(46) Geletii, Y. V.; Besson, C.; Hou, Y.; Yin, Q.; Musaev, D. G.; Quinonero, D.; Cao, R.; Hardcastle, K. I.; Proust, A.; Kögerler, P.; Hill, C. L. *J. Am. Chem. Soc.* **2009**, *131*, 17360.

(47) Sartorel, A.; Miro, P.; Salvadori, E.; Romain, S.; Carraro, M.; Scorrano, G.; Valentin, M. D.; Llobet, A.; Bo, C.; Bonchio, M. *J. Am. Chem. Soc.* **2009**, *131*, 16051.

(48) Puntoriero, F.; Ganga, G. L.; Sartorel, A.; Carraro, M.; Scorrano, G.; Bonchio, M.; Campagna, S. *Chem. Commun.* **2010**, *46*, 4725.

(49) Besson, C.; Huang, Z.; Geletii, Y. V.; Lense, S.; Hardcastle, K. I.; Musaev, D. G.; Lian, T.; Proust, A.; Hill, C. L. *Chem. Commun.* **2010**, 2784.

(50) Orlandi, M.; Argazzi, R.; Sartorel, A.; Carraro, M.; Scorrano, G.; Bonchio, M.; Scandola, F. *Chem. Commun.* **2010**, *46*, 3152.

(51) Toma, F. M.; Sartorel, A.; Iurlo, M.; Carraro, M.; Parisse, P.; Maccato, C.; Rapino, S.; Gonzalez, B. R.; Amenitsch, H.; Ros, T. D.; Casalis, L.; Goldoni, A.; Marcaccio, M.; Scorrano, G.; Scoles, G.; Paolucci, F.; Prato, M.; Bonchio, M. *Nat. Chem.* **2010**, *2*, 826.

(52) Yin, Q.; Tan, J. M.; Besson, C.; Geletii, Y. V.; Musaev, D. G.; Kuznetsov, A. E.; Luo, Z.; Hardcastle, K. I.; Hill, C. L. *Science* **2010**, *328*, 342.

(53) Fujishima, A.; Honda, K. *Nature* **1972**, *238*, 37.

(54) Bolton, J. R.; Hall, D. O. *Annu Rev Energy* **1979**, *4*, 353.

(55) Moore, G. F.; Brudvig, G. W. *Annu Rev Conden Ma P* **2011**, *2*, 303.

(56) Umena, Y.; Kawakami, K.; Shen, J. R.; Kamiya, N. *Nature* **2011**, *473*, 55.

(57) Pearlstein, R. M. *Photosynth Res* **1996**, *48*, 75.

(58) Trissl, H. W.; Bernhardt, K. *Bba-Bioenergetics* **1999**, *1409*, 125.

(59) Ort, D.; Yocum, C. *Oxygenic Photosynthesis: The Light Reactions*; Dordrecht: Kluwer Acad, 1996.

(60) de Wijn, R.; van Gorkom, H. J. *Bba-Bioenergetics* **2002**, *1553*, 302.

(61) Babcock, G. T.; Barry, B. A.; Debus, R. J.; Hoganson, C. W.; Atamian, M.; Mcintosh, L.; Sithole, I.; Yocum, C. F. *Biochemistry-Us* **1989**, *28*, 9557.

(62) Rappaport, F.; Guergova-Kuras, M.; Nixon, P. J.; Diner, B. A.; Lavergne, J. *Biochemistry-Us* **2002**, *41*, 8518.

(63) Forster, T. *Discussions of the Faraday Society* **1959**, 7.

(64) Forster, T. *Ann Phys-Berlin* **1948**, *2*, 55.

(65) Moser, C. C.; Keske, J. M.; Warncke, K.; Farid, R. S.; Dutton, P. L. *Nature* **1992**, *355*, 796.

(66) Gray, H. B.; Winkler, J. R. *Annu Rev Biochem* **1996**, *65*, 537.

(67) Marcus, R. A. *Annu Rev Phys Chem* **1964**, *15*, 155.

(68) Marcus, R. A. *Angew Chem Int Edit* **1993**, *32*, 1111.

(69) Marcus, R. A.; Sutin, N. *Biochim Biophys Acta* **1985**, *811*, 265.

(70) Hambourger, M.; Moore, G. F.; Kramer, D. M.; Gust, D.; Moore, A. L.; Moore, T. A. *Chem Soc Rev* **2009**, *38*, 25.

(71) Meyer, T. J. *Accounts Chem Res* **1989**, *22*, 163.

(72) Gust, D.; Moore, T. A.; Moore, A. L. *Accounts Chem Res* **2009**, *42*, 1890.

(73) Gust, D.; Moore, T. A.; Moore, A. L. *Accounts Chem Res* **2001**, *34*, 40.

(74) Gust, D.; Moore, T. A.; Moore, A. L. *Accounts Chem Res* **1993**, *26*, 198.

(75) Sun, L. C.; Hammarstrom, L.; Akermark, B.; Styring, S. *Chem Soc Rev* **2001**, *30*, 36.

(76) Shockley, W.; Queisser, H. J. *J Appl Phys* **1961**, *32*, 510.

(77) ASTM; http://rredc.nrel.gov/solar/spectra/am1.5/ American Society for Testing and Materials (ASTM) Terrestrial Reference Spectra for Photovoltaic Performance Evaluation: 2004.

(78) Geletii, Y. V.; Yin, Q. S.; Hou, Y.; Huang, Z. Q.; Ma, H. Y.; Song, J.; Besson, C.; Luo, Z.; Cao, R.; O'Halloran, K. P.; Zhu, G. B.; Zhao, C. C.; Vickers, J. W.; Ding, Y.; Mohebbi, S.; Kuznetsov, A. E.; Musaev, D. G.; Lian, T. Q.; Hill, C. L. *Israel J Chem* **2011**, *51*, 238.

(79) Spiccia, L.; Brimblecombe, R.; Koo, A.; Dismukes, G. C.; Swiegers, G. F. *J Am Chem Soc* **2010**, *132*, 2892.

(80) Spiccia, L.; Brimblecombe, R.; Koo, A.; Dismukes, G. C.; Swiegers, G. F. *ChemSusChem* **2010**, *3*, 1146.

(81) Xu, Y. H.; Duan, L. L.; Tong, L. P.; Akermark, B.; Sun, L. C. *Chem Commun* **2010**, *46*, 6506.

(82) Sivula, K.; Le Formal, F.; Gratzel, M. *ChemSusChem* **2011**, *4*, 432.

(83) Sun, J. W.; Zhong, D. K.; Gamelin, D. R. *Energ Environ Sci* **2010**, *3*, 1252.

(84) Kay, A.; Cesar, I.; GrÃ¤tzel, M. *Journal of the American Chemical Society* **2006**, *128*, 15714.

(85) Hagfeldt, A.; Gratzel, M. *Chem. Rev.* **1995**, *95*, 49.

(86) Maeda, K.; Domen, K. *The Journal of Physical Chemistry C* **2007**, *111*, 7851.

(87) Shafirovich, V. Y.; Shilov, A. E. *Kinet Catal* **1979**, *20*, 950.

(88) Harriman, A.; Pickering, I. J.; Thomas, J. M.; Christensen, P. A. *J Chem Soc Farad T 1* **1988**, *84*, 2795.

(89) Mills, A. *Chem Soc Rev* **1989**, *18*, 285.

(90) Greenblatt, M.; Robinson, D. M.; Go, Y. B.; Dismukes, G. C. *J Am Chem Soc* **2010**, *132*, 11467.

(91) Jaramillo, T. F.; Gorlin, Y. *J Am Chem Soc* **2010**, *132*, 13612.

(92) Frei, H.; Han, H. X. *J Phys Chem C* **2008**, *112*, 16156.

(93) Concepcion, J. J.; Jurss, J. W.; Brennaman, M. K.; Hoertz, P. G.; Patrocinio, A. O. T.; Iha, N. Y. M.; Templeton, J. L.; Meyer, T. J. *Accounts Chem Res* **2009**, *42*, 1954.

(94) Ruttinger, W.; Dismukes, G. C. *Chem Rev* **1997**, *97*, 1.

(95) Sala, X.; Romero, I.; Rodriguez, M.; Escriche, L.; Llobet, A. *Angew Chem Int Edit* **2009**, *48*, 2842.

(96) Yagi, M.; Kaneko, M. *Chem Rev* **2001**, *101*, 21.

(97) Spiccia, L.; Brimblecombe, R.; Dismukes, G. C.; Swiegers, G. F. *Dalton T* **2009**, 9374.

(98) Huang, Z. Q.; Luo, Z.; Geletii, Y. V.; Vickers, J. W.; Yin, Q. S.; Wu, D.; Hou, Y.; Ding, Y.; Song, J.; Musaev, D. G.; Hill, C. L.; Lian, T. Q. *J Am Chem Soc* **2011**, *133*, 2068.

(99) Pope, M. T.; Müller, A. *Angew. Chem.* **1991**, *103*, 56.

(100) Hill, C. L.; Prosser-McCartha, C. M. *Coord. Chem. Rev.* **1995**, *143*, 407.

(101) Neumann, R. *Prog. Inorg. Chem.* **1998**, *47*, 317.

(102) *Polyoxometalate Chemistry From Topology via Self-Assembly to Applications*; Pope, M. T.; Müller, A., Eds.; Kluwer Academic Publishers: Dordrecht, 2001.

(103) Moffat, J. B. *Metal-Oxygen Clusters: The Surface and Catalytic Properties of Heteropoly Oxometalates.*; Kluwer Academic/Plenum Publishers: New York, 2001; Vol. 9.

(104) Kozhevnikov, I. V. *Catalysis by Polyoxometalates*; Wiley: Chichester, England, 2002; Vol. 2.

(105) Borrás-Almenar, J. J.; Coronado, E.; Müller, A.; Pope, M. T. *Polyoxometalate Molecular Science*; Kluwer Academic Publishers: Dordrecht, 2003; Vol. 98.

(106) Hill, C. L. In *Comprehensive Coordination Chemistry-II: From Biology to Nanotechnology*; Wedd, A. G., Ed.; Elsevier Ltd.: Oxford, UK, 2004; Vol. 4, p 679.

Part II: Experimental Methods

CHAPTER

2

Experimental Methods

2.1 Materials

All common laboratory chemicals were reagent grade, purchased from commercial sources and, unless otherwise noted, used without further purification.

Tris(2,2'-bipyridyl)dichlororuthenium(II) hexahydrate ($[Ru(bipy)_3]^{2+}$), and sodium persulfate (98+%) were purchased from Aldrich.

2.2 Synthesis

Preparation and characterization of Bis{4'-(4-methylpyridinio)-2,2':6,2''-terpyridine} ruthenium (IV),[1] α-Fe_2O_3 nanoparticles and nanoporous films,[2,3] RuP2, RuC2,[4] $[\{Ru_4O_4(OH)_2(H_2O)_4\}(\gamma\text{-}SiW_{10}O_{36})_2]^{10-}$ (Ru_4POM),[5] $[\{Ru_4O_4(OH)_2(H_2O)_4\}(\gamma\text{-}SiW_{10}O_{36})_2]^{10-}$ (Ru_4-(P)-POM)[6] and $[Co_4(H_2O)_2(PW_9O_{34})_2]^{10-}$($Co_4POM$)[7] were reported elsewhere.

TiO_2 colloids and nanoporous films: TiO_2 nanocrystalline thin films were synthesized according to previously published procedures.[8,9] Briefly, 250 mL of water and 80 mL of acetic acid (> 99.7%, Aldrich) were mixed in an ice bath. 10 mL of anhydrous isopropanol (99.5%, Aldrich) and 37 mL of titanium (IV) isopropoxide (97%, Aldrich) were mixed and purged by nitrogen, then added drop-wise to the acetic acid solution under vigorous stirring. After vigorous stirring for 8 hours, the transparent colloid solution was slowly evaporated at 80°C for 3-4 h. The resulting gel was autoclaved at 230°C for 12 h and slowly cooled down to room temperature.[9] About 10 ml of the resulting gel phase was then stirred with 20 drops of TritonX-100 (Aldrich) for several days to disperse the aggregated particles. Films were prepared by doctor blading the TiO_2 gel onto clean sapphire windows, followed by baking at 400°C in an oven for 1.5 h.

Water soluble TiO_2 nanoparticles: The TiO_2 nanoparticle (~5 nm) solution was prepared by controlled hydrolysis of titanium(IV) tetra-isopropoxide ($Ti[OCH(CH_3)_2]_4$, Aldrich, 97%).[10] A 100 mL solution of $Ti[OCH(CH_3)_2]_4$ in 2-propanol (5:95) was added drop-wise to 900 mL of water in an ice bath at pH 1.5 (adjusted with HNO_3). The solution was then stirred overnight until a transparent colloidal solution was formed. The resulting solution was concentrated by a rotary evaporator and then dried with a N_2 flow. The resulting white powder was re-dissolved in water for further application. TiO_2 colloidal solution synthesized by this approach has been used extensively in our lab to prepare different TiO_2/molecule nanocomposites for spectroscopic studies.[11-13]

γ-Fe_2O_3 nanoparticles: γ-Fe_2O_3 nanoparticle capped with oleic acid was synthesized according to established procedures.[14] Briefly, γ-Fe2O3 nanoparticles were synthesized under a nitrogen flow as follows. $Fe(CO)_5$ was injected into a mixture containing 20 mL of octyl ether (Aldrich, 99%) and oleic acid (Aldrich, 90%) at 100 ℃. The resulting mixture was slowly heated and refluxed (~300 ℃) for 2 h. During reflux, the yellow orange mixture changed to colorless and then to dark. This solution was cooled to room temperature (intermediate iron oxide), or aerated for 14 h at 80 ℃, and then refluxed (~300 ℃) for 2 h (aerated iron oxide). The solution was treated with excess iso-propanol and separated by centrifugation. The particle sizes can be controlled by varying molar ratios of $Fe(CO)_5$ to oleic acid.

Synthesis of the tetra-*n*-heptylammonium salt of $[Co_4(H_2O)_2(PW_9O_{34})_2]^{10-}$ (THA salt of Co_4POM) The tetra-*n*-heptylammonium POM salt was prepared as follows: 0.5 g of $Na_{10}[Co_4(H_2O)_2(PW_9O_{34})_2]\cdot 27H_2O$ (FW: 5447.12 g/mol) was dissolved in 10 mL of H_2O. The solution was mixed with 720 mg of $THANO_3$ (FW: 490.70 g/mol) in 10 mL of

toluene with vigorous stirring for 30 minutes. After the solution was allowed to sit overnight for layer separation, the organic (toluene) layer was collected and dried using a rotary evaporator. The resulting product was re-dissolved in toluene and again dried using a rotary evaporator affording 860 mg for use. TGA analysis shows 70% weigh loss at 600 °C which indicates that excess $THANO_3$ exists in the final THAPOM product, $THA_{10}[Co_4(H_2O)_2(PW_9O_{34})_2]\cdot 14THANO_3$.

A modified preparation results in THAPOM without excess $THANO_3$ and fewer THA cations in the final product. This procedure is as follows: to 20 mL of distilled water was added 30 mg of Co_4POM. The solution was then mixed with 180 mg of $THANO_3$ in 30 mL of CH_2Cl_2. The mixture was vigorously stirred with the addition of 0.2 mL of 1 M HCl. After standing for 30 minutes the resulting mixture separated into two layers and the aqueous layer became colorless. The organic phase was collected by a separating funnel and concentrated using a rotary evaporator. TGA shows 40% weigh loss at 600 ℃, which gives the formula: $THA_{7.6}H_{2.4}[Co_4(H_2O)_2(PW_9O_{34})_2]$

Estimation of the number of THA cations required to protect the Co_4POM. A reasonable approach is to have sufficient THA cations to effectively cover the surface of the Co_4POM. The geometry of the Co_4POM can be taken as a cuboid with length × width × height = 15 × 10 × 10 Å (based on the crystal structure[2]). The average length of the four seven-carbon chains of the THA cation is about 8.0 Å (from the N center to the terminus carbon), therefore the maximum covering area of the THA will be no larger than $(8.0 \times 2)^2 / 2 = 128$ Å^2 (set the THA as a square with diagonal = 8.0 × 2 Å). We set the average THA-to-POM distance as 4 Å, then the effective surface area of the Co_4POM will be $(10 + 8) \times (10 + 8) \times 2 + (10 + 8) \times (15 + 8) \times 4 = 2304$ Å^2. Therefore, 2304/128

≈ 18 is the minimum number of THA cations required for covering and protecting the Co_4POM cuboidal surface.

2.3 Sensitization of TiO_2

TiO_2/Ru470 homogenous solution: The solution was prepared by mixing Ru470 powder with the TiO_2 solution. The presence of the TiO_2 nanoparticles in the solution dramatically increases the solubility of Ru470 at the same pH, indicating the attachment of Ru470 onto the TiO_2 colloidal surface.

TiO_2-Ru470 films: TiO_2 films were sensitized in ethanol solutions of Ru470 [tris(2,2'-bipyridyl-4,4'-dicarboxylic acid) ruthenium(II) dichloride] (Solaronix). The electrode was then prepared by soaking the dye-sensitized films in an acidic solution (pH = 1) of Ru_4POM (prepared according to established literature approaches[5]). Optical densities of the sensitized films were controlled by varying the solution concentrations and soaking times.

TiO_2-RuP2 and TiO_2-RuC2 films: TiO_2 films coated on Sapphire or FTO (Hardford, TEC8) substrate were sensitized in RuP2 (or RuC2) solution (3mg in 0.1 M $HClO_4$) for 24 hours. The freshly sensitized electrodes were soaked in neutral water for 24~32 more hours to completely remove the free dyes on the electrode.

2.4 Sensitization of γ-Fe_2O_3 nanoparticles

γ-Fe_2O_3/RhB assemblies were prepared by adding RhB to γ-Fe_2O_3 solution in heptane followed by sonication and filtration to remove undissolved RhB molecules. Our previous fluorescence anisotropy measurements [15] have shown RhB molecules bind to

QD particles, and since RhB was insoluble in heptane, all dissolved dyes were believed to be bound to γ-Fe_2O_3 nanoparticles. A control sample without QDs showed no measurable absorbance peaks in the UV-vis spectral region. The concentration of RhB in γ-Fe_2O_3 solution was controlled by varying the amount of added RhB.

2.5 Coating of surface catalysts

TiO_2/Ru470/Ru_4POM electrode: The electrode was prepared by soaking the dye-sensitized films in an acidic solution (pH = 1) of Ru_4POM. Optical densities of the sensitized films were controlled by varying the solution concentrations and soaking times.

TiO_2/RuP2(or RuC2)/Ru_4POM electrode: The electrode was prepared by soaking the dye-sensitized films in an acidic solution (pH = 3.2) of Ru_4POM. Optical densities of the sensitized films were controlled by varying the solution concentrations and soaking times.

Hematite/THA-Co_4POM: The hydrophobic POM modified eletrodes were prepared as follows: two drops of a 0.1 μM toluene solution of $THA_{10}[Co_4(H_2O)_2(PW_9O_{34})_2]\cdot 14THANO_3$ was cast on the hematite electrode surface. The solution was dried under air for at least 20 minutes and a $THA_{10}[Co_4(H_2O)_2(PW_9O_{34})_2]\cdot 14THANO_3$ layer formed on the surface. The coating layer was washed with a large amount of 1 M NaOH followed by rinsing with a large amount of water prior to assessment of the PEC properties.

2.6 General instrumentations

Static UV-Vis: An Agilent 8453 spectrophotometer equipped with a diode-array detector.

Static fluorescence: A steady state emission measurement was studied using a SPEX® FluoroLog®-3 self-contained and fully automated spectrofluorometer.

Homogeneous light-driven systems: Analysis of dioxygen in the reaction headspace was performed using Agilent 7890a gas-chromatography system equipped with a thermo-conductivity detector and a HP-MOLESIEVE capillary column (30m x 0.535 mm x 25.00 μm) with Argon as a carrier gas. A Hamamatsu Xe-lamp (model C2577) was used as a light source and the desired wavelength range was created with a 420-470 nm band pass filter. A magnetically-coupled stirring system (SYS 114, SPECTROCELL) was used for reaction solutions. The stirring rate in revolutions per minute (RPM) was determined by a home-built set-up consisting of a helium-neon laser (IMATTRONIC), a magnetic stick (VP 736-1, V&P scientific), a photo-diode detector (PDA 55, ThorLabs), and an oscilloscope (LT262, LeCroy). Light induced water oxidation was performed in a cylindrical cuvette (NSG, 32G10).

2.7 Time-resolved fluorescence measurements

Time-resolved fluorescence measurements were performed in the time-correlated single photon counting (TCSPC) mode under right-angle sample geometry. A femtosecond laser pulse (100 fs) with a repetition rate of 80 MHz was generated from a mode-locked Ti:Sapphire laser (Tsunami oscillator pumped by 10 W Millennia Pro, Spectra-Physics). The output centered at 800 nm was doubled through a BBO crystal to generate 400 nm

light that was used to excite the sample. The emission was detected by a Micro-channel-plate-photomultiplier tube (Hamamatsu R3809U-51), whose output was amplified and analyzed by a TCSPC board (Becker&Hickel SPC 600).

2.8 Transient absorption measurement

Ultrafast visible transient absorption measurements for the homogeneous water oxidation system and the TiO_2-Ru470-Ru_4POM triadic system. Transient absorption measurements were based on a regeneratively amplified Ti:Sapphire laser system (Coherent Legend, 800 nm, 150 fs, 2.5 mJ/pulse, 1KHz repetition rate). The 400 nm pump pulses were produced through second harmonic generation of the fundamental 800 nm beam in a BBO crystal. Pump powers were controlled using a series of neutral density filters. The visible probe was generated by attenuating and focusing ~10 μJ of the 800 nm pulse into a 2 mm thick sapphire window, producing a white light continuum from 420 to 750 nm. The pump and probe pulses were combined at the sample and the delay time between them was controlled through a manual delay stage. The transmitted portion of the probe was focused into a fiber-coupled spectrometer (Ocean Optics USB2000, 2048 pixel CCD, ~.25 nm/pixel readout) and detected at a frequency of 10 Hz. The pump pulses were chopped by a synchronized chopper to the same frequency. The absorbance change was calculated from the intensities of sequential probe pulses with and without the pump. During the data collection, samples were constantly translated at a speed of 5 mm/min to avoid photo-degradation.

Nanosecond transient absorption measurements. Measurements of the homogeneous system were carried out in an EOS spectrometer (Ultrafast Systems LLC). The pump

pulses at 400 nm were generated from the same laser system described above. The probe pulse, a 0.5-ns white-light source operating at 20 kHz, was synchronized with the femtosecond amplifier, and the delay time was controlled by a digital delay generator. The probe light was detected in a fiber-optic-coupled multichannel spectrometer with a complementary metal−oxide−semiconductor (CMOS) sensor. The absorbance change was calculated from the intensities of sequential probe pulses with and without the pump. A flow cell was used to guarantee fresh sample during the measurement.

Ultrafast Visible Transient Absorption Measurements. Our femtosecond transient absorption spectrometer is based on a regeneratively amplified Ti:sapphire laser system (coherent Legend, 800 nm, 150 fs, 3 mJ/pulse and 1 kHz repetition rate) and the Helios spectrometer (Ultrafast Systems LLC). The excitation pulse at 400 nm was generated by doubling the frequency of the fundamental 800 nm pulse in a β-barium borate (BBO) type I crystal. The energy of the 400 nm pump pulse was controlled (typically, 50 ~250 nJ/pulse) with neutral density filters. The pump beam diameter at the sample was ~400 μm. A white light continuum (450~720 nm), used as a probe, was generated by attenuating and focusing 10 μJ of the fundamental 800 nm pulse into a sapphire window. This WLC was split in two parts used as a probe and reference beams. The probe beam was focused with an aluminum parabolic reflector into the sample with a beam diameter of ~150 μm. The reference and probe beams were focused into a fiber-coupled multichannel spectrometer with CMOS sensors and detected at a frequency of 1 kHz. To minimize low-frequency laser fluctuations every other pump pulse was blocked with a synchronized chopper (New Focus Model 3501) at 500 Hz, and the absorbance change was calculated with two adjacent probe pulses (pump-blocked and pump-unblocked). The

delay between the pump and probe pulses was controlled by a motorized translational stage. Samples were kept in a 1 mm quartz cuvette (NSG Precision Cells) and constantly stirred by a magnetically-coupled stirring system (SYS 114, SPECTROCELL). In all transient absorption spectra, the chirp and time zero correction were performed with Surface Explorer software (v.1.1.5, Ultrafast Systems LCC) using a dispersion correction curve obtained by fitting the representative kinetics of the transient absorption experiments of the solvent. The typical instrument response of our spectrometer is well represented by a Gaussian function with a full width at half-maximum (FWHM) of 180 ± 10 fs.

Ultrafast Visible Pump/IR Probe and IR Pump/IR Probe Transient Absorption Measurements. Our tunable femtosecond infrared spectrometer is based on a Clark IR optical parametric amplifier (OPA) which generated two tunable near-IR pulses in the 1.1 to 2.5 μm spectral range (signal and idler, respectively). The broad mid-IR pulses centered at 2000, 1900 and 1870 cm^{-1} were generated by difference frequency generation (DFG) combining the corresponding signal and idler in a 1-mm-thick type II $AgGaS_2$ crystal. The frequency tuning of the mid-IR pulses was achieved changing the signal and idler frequencies at the OPA and optimizing the timing between the pulses and the phase matching angles of the BBO (OPA crystal) and the $AgGaS_2$ crystal. After the difference frequency generation, the mid-IR pulse was collimated and split in two parts with a 90% beamsplitter. The 90% reflected part was used as a pump in the IR Pump-IR Probe experiments, while the 10% transmitted part was used as a probe in both the Visible-IR and IR-IR transient absorption measurements**.** To prevent cumulative heating in the sample and to avoid the saturation of the detector, the intensity of the probe mid-IR pulse

was attenuated using neutral density filters to approximately 40 μJ, before it was focused into a 0.4 μm CaF_2 path length cell containing the sample. At the focal point, the probe was spatially overlapped with the temporally delayed 400 nm or mid-IR excitation pulse with pump energy of about 2 or 0.7 μJ/pulse, respectively. To avoid rotational diffusion effects, the polarization angle of the excitation beams were controlled with a half-wave plate and set to the magic angle (54.7 °) relative to the probe beam. The diameter of the pump and probe beams were 400 and 200 μm, respectively.

In both experimental setups, the mid-infrared probe pulse was spectrally dispersed with an imaging spectrograph (CVI, Digikrom 240) and imaged onto a 32-element infrared HgCdTe (MCT) array detector. The difference absorption spectra were calculated subtracting the absorption spectrum of the excited sample minus the absorption spectrum of the sample in the ground state by blocking every other pump pulse with a phase-locked optical chopper (New Focus) at 500 Hz. The instrument response function of our spectrometer was well represented by a Gaussian function with a 230 ± 10 and 270 ± 10 fs full width at half-maximum (FWHM) for the VIS-IR and the IR-IR setup, respectively.

2.9 General procedures

Homogeneous water oxidation:[6,16,17] The vessel was filled with solution with the desired concentrations of reactants and buffer. The reaction vessel was then sealed with a rubber septum, carefully deairated and filled with Ar. All procedures were performed with a minimum exposure to ambient light. The reaction was initiated by unblocking the light from a Xe-lamp. The reaction vessel was then vigorously shaken to equilibrate

dioxygen concentrations in liquid and gas phases, and the headspace was analyzed for O_2 content. For O_2 content analysis, 0.1 mL of the gas in the headspace gas of the reaction vessel was withdrawn through a septum using a deairated gas-tight syringe and injected into gas chromatograph. Contamination of the head-space by air was corrected by quantification of N_2 present in the head-space (from the N_2 peak in the GC traces). The total amount of unreacted persulfate in reaction solution was determined after turning off the light. The quantification of persulfate is documented elsewhere.

Conditions: Xe-lamp, 420-470 nm, 16.8 mW light beam with a diameter of ~0.75 cm focused on the reaction solution, 1.0 mM $[Ru(bpy)_3]^{2+}$, 5.0 mM $Na_2S_2O_8$, 80 mM sodium borate buffer (initial pH 8.0), total reaction volume 2 mL, vigorous stirring ($5x10^3$ RPM).

Photoquenching studies ($Ru(bpy)_3^{2+}$ and $S_2O_8^{2-}$):[18] The solutions of $Ru(bpy)_3^{2+}$, $S_2O_8^{2-}$, and their mixtures were prepared and stored under darkroom conditions to avoid photoreaction. All solutions were purged with Ar before measurements. A 10x1 mm dual-path-length quartz cuvette and 1.8-nm excitation and emission slits were used in all steady-state luminescence measurements. Samples were excited at 450 nm, and emission intensity data were collected at 20 ℃ at 617-620 nm. Integration time was set at 0.05 s. To minimize light induced reactions during the measurements, the acquisition time was kept to less than 1 s. Repetitive measurements showed that the emission intensity decreased by less than 2% during this acquisition time.

Photoquenching studies ($[Ru(mptpy)_2]^{4+}$ and $S_2O_8^{2-}$):[1] Solutions of $[Ru(mptpy)_2]^{4+}$, $[S_2O_8]^{2-}$, and their mixtures were prepared and stored in the dark to avoid photoreactions. We used 5 μM $[Ru(mptpy)_2]^{4+}$ and less than 10 mM $[S_2O_8]^{2-}$ for all measurements due to the low solubility of the $[Ru(mptpy)_2]^{4+}/[S_2O_8]^{2-}$ mixture in the applied solvents. All

solutions were degassed with N_2 before measurements. Samples were excited at 500 nm, and emission intensity data were collected at 640-720 nm at 20 ℃ under vigorous stirring.

Photoelectrochemical test: A Hamamatsu Xe-lamp (model C2577) was used as a light source and the desired wavelength range was created with a 320-720 nm KG-3 (ThorLabs) band pass filter combined with other necessary narrow-band filters. The electrochemical work station is a BAS CV-50W voltammetric analyzer (BASi)

2.10 References

(1) Kaledin, A. L.; Huang, Z. Q.; Yin, Q. S.; Dunphy, E. L.; Constable, E. C.; Housecroft, C. E.; Geletii, Y. V.; Lian, T. Q.; Hill, C. L.; Musaev, D. G. *J Phys Chem A* **2010**, *114*, 6284.

(2) Spray, R. L.; Choi, K. S. *Chem Mater* **2009**, *21*, 3701.

(3) Spray, R. L.; McDonald, K. J.; Choi, K. S. *J Phys Chem C* **2011**, *115*, 3497.

(4) Rice, C. R.; Guerrero, A.; Bell, Z. R.; Paul, R. L.; Motson, G. R.; Jeffery, J. C.; Ward, M. D. *New J Chem* **2001**, *25*, 185.

(5) Geletii, Y. V.; Botar, B.; Koegerler, P.; Hillesheim, D. A.; Musaev, D. G.; Hill, C. L. *Angew Chem Int Edit* **2008**, *47*, 3896.

(6) Besson, C.; Huang, Z. Q.; Geletii, Y. V.; Lense, S.; Hardcastle, K. I.; Musaev, D. G.; Lian, T. Q.; Proust, A.; Hill, C. L. *Chem Commun* **2010**, *46*, 2784.

(7) Yin, Q. S.; Tan, J. M.; Besson, C.; Geletii, Y. V.; Musaev, D. G.; Kuznetsov, A. E.; Luo, Z.; Hardcastle, K. I.; Hill, C. L. *Science* **2010**, *328*, 342.

(8) Kalyanasundaram, K.; Gratzel, M. *Coordin Chem Rev* **1998**, *177*, 347.

(9) Zaban, A.; Ferrere, S.; Sprague, J.; Gregg, B. A. *J Phys Chem B* **1997**, *101*, 55.

(10) Bahnemann, D.; Henglein, A.; Lilie, J.; Spanhel, L. *J Phys Chem-Us* **1984**, *88*, 709.

(11) Ghosh, H. N.; Asbury, J. B.; Weng, Y. X.; Lian, T. Q. *J Phys Chem B* **1998**, *102*, 10208.

(12) Wang, Y. H.; Hang, K.; Anderson, N. A.; Lian, T. Q. *J Phys Chem B* **2003**, *107*, 9434.

(13) Weng, Y. X.; Wang, Y. Q.; Asbury, J. B.; Ghosh, H. N.; Lian, T. Q. *J Phys Chem B* **2000**, *104*, 93.

(14) Woo, K.; Hong, J.; Choi, S.; Lee, H. W.; Ahn, J. P.; Kim, C. S.; Lee, S. W. *Chem Mater* **2004**, *16*, 2814.

(15) A. Boulesbaa, A. I., D. Stockwell, Z. Huang, J. Huang, J. Guo, and T. Lian *Journal of the American Chemical Society* **2007**, *129*, 15132

(16) Huang, Z. Q.; Luo, Z.; Geletii, Y. V.; Vickers, J. W.; Yin, Q. S.; Wu, D.; Hou, Y.; Ding, Y.; Song, J.; Musaev, D. G.; Lian, T. Q.; Hill, C. L. *Journal of the American Chemical Society* **2011**, *133*, 2068.

(17) Geletii, Y. V.; Huang, Z. Q.; Hou, Y.; Musaev, D. G.; Hill, C. L.; Lian, T. Q. *Journal of the American Chemical Society* **2009**, *131*, 7522.

(18) Kaledin, A. L.; Huang, Z. Q.; Geletii, Y. V.; Lian, T. Q.; Hill, C. L.; Musaev, D. G. *J Phys Chem A* **2010**, *114*, 73.

Part III: Homogeneous Light-driven Water Oxidation

CHAPTER

3

Homogeneous Light-driven Water Oxidation

Partially in articles:

1. Zhu, G.; Lv, H.; Vickers, J. W.; Geletii, Y.V.; Luo, Z.; Song, J.; **Huang, Z.**; Musaev, D.G.; Hill, C.L.; "*Structural and mechanistic studies of tunable, stable, fast multi-cobalt water oxidation catalysts*", ***Proc. SPIE*, 2011**, *8109*, 81090A
2. Geletii, Y. V.; Yin, Q.; Hou, Y.; **Huang, Z.**; Ma, H.; Song, J.; Besson, C.; Luo, Z.; Cao, R.; O'Hallora, K.; Zhao, C.; Vickers, J. W.; Ding, Y.; Mohebbi, S.; Kuznetsov, A. E.; Musaev, D. G,; Lian, T.; Hill. C. L.; "*Polyoxometalates in the Design of Effective and Tunable Water Oxidation Catalysts" **Isr. J. Chem.***, **2011**, *51*, 238
3. **Huang, Z.;** Luo, Z.; Geletii, Y. V.; Vikers, J. W.; Yin, Q.; Wu, D.; Hou, Y.; Ding, Y.; Song, J.; Musaev, D. G,; Hill. C. L.; Lian, T.; "*Efficient Light-Driven Carbon-Free Cobalt-Based Molecular Catalyst for Water Oxidation*", ***J. Am. Chem. Soc.*, 2011**, *133*, 2068
   The main part of this chapter is "Reproduced with permission from [***J. Am. Chem. Soc.*, 2011**, *133*, 2068] Copyright [2011] American Chemical Society." Electronic link: http://pubs.acs.org/doi/abs/10.1021/ja109681d
4. Besson, C.; **Huang, Z.**; Geletii, Y. V.; Lense, S.; Hardcastle, K. I.; Musaev, D. G.; Lian, T.; Prousta, A.; Hill, C. L.; *"$Cs_9[(\gamma\text{-}PW_{10}O_{36})_2Ru_4O_5(OH)(H_2O)_4]$, a new all-inorganic, soluble catalyst for the efficient visible-light-driven oxidation of water", **Chem. Commun.* 2010**, *46*, 2784
5. Geletii, Y. V.; **Huang, Z.**; Hou, Y.; Musaev D. G.; Lian, T.; Hill, C.L., "*Homogeneous Light-Driven Water Oxidation Catalyzed by a Tetraruthenium Complex with All Inorganic Ligands*", ***J. Am. Chem. Soc.*, 2009**, *131*, 7522

Abstract: This chapter describes a totally homogeneous (molecular) system for the visible-light driven catalytic water oxidation. It uses three organic-structure-free, hence oxidatively stable molecular water oxidation catalysts (WOCs): $[\{Ru_4O_4(OH)_2(H_2O)_4\}(\gamma\text{-}SiW_{10}O_{36})_2]^{10-}$ (Ru_4POM), $[\{Ru_4O_4(OH)_2(H_2O)_4\}(\gamma\text{-}SiW_{10}O_{36})_2]^{10-}$ (Ru_4-(P)-POM) and $[Co_4(H_2O)_2(PW_9O_{34})_2]^{10-}$($Co_4POM$). Co_4POM consists of only earth-abundant metals. This system catalyzed by these polyoxometalate WOCs produces O_2 rapidly and in high quantum yields: (24% and 30% for Ru_4POM and Co_4POM, respectively). Many efforts for system optimizations were conducted.

3.1 Introduction

Development of H_2O oxidation catalysts (WOCs) in artifical photosynthetic constructs, comprising coupled visible light photosensitizers, water reduction catalysts and WOCs, is one of the grand challenges in the sustained production of solar fuels. [1-3] The development of efficient water oxidation catalysts (WOCs) remains a major scientific challenge despite considerable progress in recent years.[4-21] Polyoxometalate molecular WOCs, exhibiting the positive properties of both heterogenous and homogeneous catalysts and without the major negative properties of each, have been demonstrated to be efficient WOCs both in homogeneous chemical water oxidation systems and in a heterogeneous electrochemical system in the dark. [22-31]

In 2009, the first polyoxometalate molecular WOC $[\{Ru_4O_4(OH)_2(H_2O)_4\}(\gamma\text{-}SiW_{10}O_{36})_2]^{10-}$ (henceforth noted as Ru_4POM) was reported simultaneously by the Hill[25] and Bonchio groups.[26] The Hill group demonstrated that Ru_4POM catalyzes the homogeneous water oxidation $[Ru(bpy)_3]^{3+}$ (eq 3.1) in a phosphate buffer at pH 7.2, [25]

$$4[Ru(bpy)_3]^{3+} + 2\ H_2O \rightarrow 4\ [Ru(bpy)_3]^{2+} + O_2 + 4H^+ \quad (3.1)$$

while the Bonchio group reported that this complex could catalyze the oxidation of water by Ce(IV) in strong acid.[26] In addition, in 2010, the Bonchio group, in collaboration with others, demonstrated that Ru_4POM immobilized on electrodes modified by multi-walled carbon nanotubes is a highly efficient electrocatalyst for water oxidation at low overpotentials.[30] Meanwhile, the isotructural phosphorus analogue of this catalyst, $[\{Ru_4O_4(OH)_2(H_2O)_4\}(\gamma\text{-}SiW_{10}O_{36})_2]^{10-}$ (henceforth noted as Ru_4-(P)-POM), was successfully prepared and thoroughly characterized by the Hill's group.[28] The latter complex contains two P(V) centers in place of the two Si(IV) centers in the initial Ru_4POM complex.

Ru is a precious metal, and thus, its use will be inevitably questionable for many large-scale economic green energy applications. Therefore, the development of POMs containing earth-abundant metals only, as potential WOCs is desirable. The breakthrough has been achieved by the Hill group in 2010 when they reported a tetra-cobalt sandwich-type POM, $[Co_4(H_2O)_2(PW_9O_{34})_2]^{10-}$ (henceforth "Co_4POM").[31] Using $[Ru(bpy)_3]^{3+}$ as the oxidant (eq 3.1), Co_4POM catalyzes water oxidation at a rate > $5s^{-1}$ in aqueous buffer at pH 8.[31]

Recently, we have demonstrated that all these three catalysts: Ru_4POM, Ru_4-(P)-POM and Co_4POM, can be utilized as WOCs in a totally homogeneous visible-light driven artificial photosynthetic scheme similar to that in PSII (Figure 1.2) using $[Ru(bpy)_3]^{2+}$ as a photonsensitier and $[S_2O_8]^{2-}$ as a sacrificial electron acceptor. [24,28,32] This system is displayed in Figure 3.1, which is a generic example of biomimetic case based on PSII.

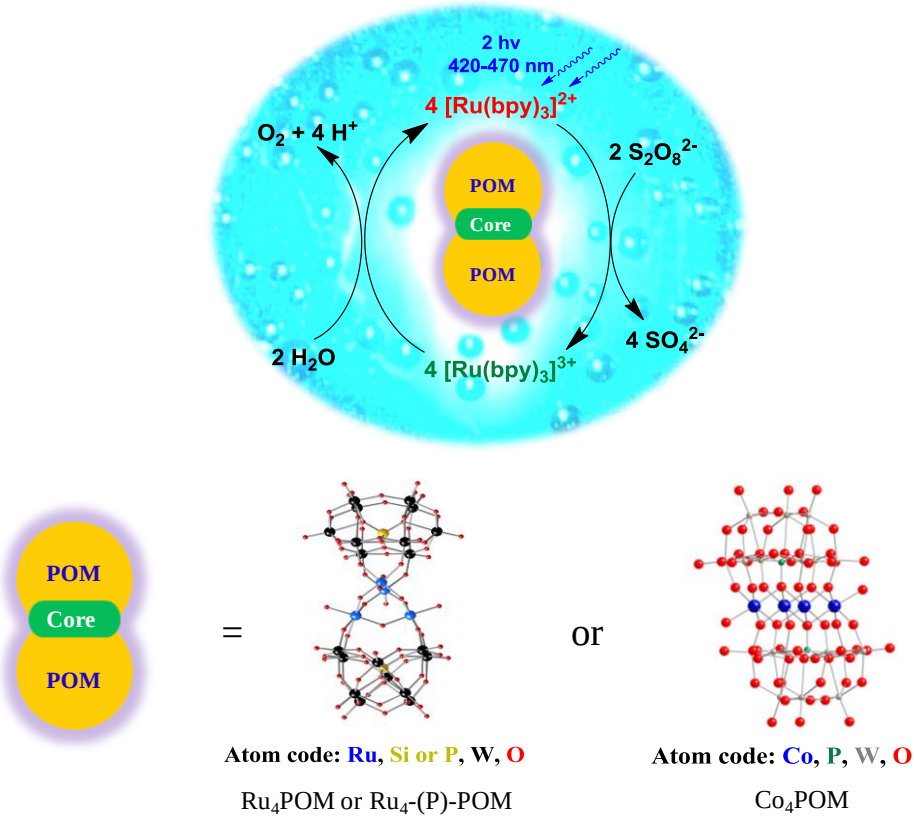

Figure 3.1. Scheme of homogeneous light-driven water oxidation systems.

This artificial photocatalytic system is driven by the absorption of photons and the consumption of a sacrificial electron acceptor (persulfate):

$$2[S_2O_8]^{2-} + 2H_2O + 2h\nu \rightarrow 4SO_4^{2-} + O_2 + 4H^+ \qquad (3.\ 2)$$

This system was initially tested with our Ru_4POM catalyst.[24] Using 5 μM [Ru_4POM], 5 mM $Na_2S_2O_8$ and the sodium phosphate buffer (20 mM, pH 7.2), this system was first reported to have a quantum efficiency of 9%, which was later improved to 27% after using an optimized apparatus. Our preliminary studies have revealed that the rate of O_2 formation (k_{O_2}) depends on the incident light intensity (I_0), $[S_2O_8]^{2-}$, $[Ru(bpy)_3]^{2+}$ and [Ru_4POM], given by eq 3.2

$$k_{O_2} \propto I_0[S_2O_8^{2-}][Ru(bpy)_3^{2+}]^{1.4}[Ru_4POM]^x, \quad x > 1 \tag{3.3}$$

Other factors are non-trivial as well to the water oxidation efficient, such as mass transport (stirring rate), light intensity, shape and volume of the reaction vessel, etc.

We further sought to assess the effects of changing ground state reduction potential and other properties of Ru_4POM. We initially make a subtle change in the POM ligand, while keeping the tretra-Ru core intact. As mentioned above, the isostructural phosphorus analogue, Ru_4-(P)-POM were prepared.[28] This synthesis changes the charge on the WOC polyanion, which in turn changes the redox potentials of the complex. The rates for catalytic photodriven water oxidation by Ru_4POM and Ru_4-(P)-POM in the photodriven system noted above were compared. Due to the similarity between the redox potentials of Ru_4POM and Ru_4-(P)-POM, a comparable catalytic activity is expected and observed. However, Ru_4-(P)-POM has an overall catalytic performance due to this change in the redox potential.

In the dark chemical water oxidation (eq 3.1), Co_4POM, based on earth-abundant Co, exhibits a turnover frequency (TOF) at pH 8 ~20 times higher than that of Ru_4POM at pH 7.2 (5 vs. 0.25 s^{-1}).[22,31] In the light-driven system (Figure 3.2) Co_4POM does the same as that of Ru_4POM and Ru_4-(P)-POM but exhibits substantially higher rates and O_2 evolution quantum yields (ca. 30%) than Ru_4POM and all other POM-based WOCs. Significantly, Co_4POM and Ru_4POM have different selectivity features indicating that the reactivities of one POM WOC aren't necessarily operable for others.[22-31] In this chapter, the optimization details and mechanism of the light-driven system (Figure 3.1) catalyzed by Co_4POM will be revealed.

3.2 Results and discussion

3.2.1 System optimization.

In this work, we used a cylindrical cuvette for the water oxidation reactions. With the maximum stable stirring rate (5 x 10^3 RPM), this cell produced a ~three-fold increase in initial quantum yields (Φ_{QY}, 2 $(\Delta[O_2]/\Delta(h\nu))_0$) (9.0% vs 27%) with similar final turnover numbers (TON, $[O_2]_f$/[catalyst]) (180 vs 200) compared to our system catalyzed by Ru_4POM in a round flask under a moderate agitation. [24,28]

In addition, for reasons yet to be understood, the nature of buffer also affects the efficiency of O_2, formation (Figure 2.5). In this work, 80 mM borate buffer was found to maintain the pH well with only a 0.1-0.3 pH unit drop by the end of the reaction.

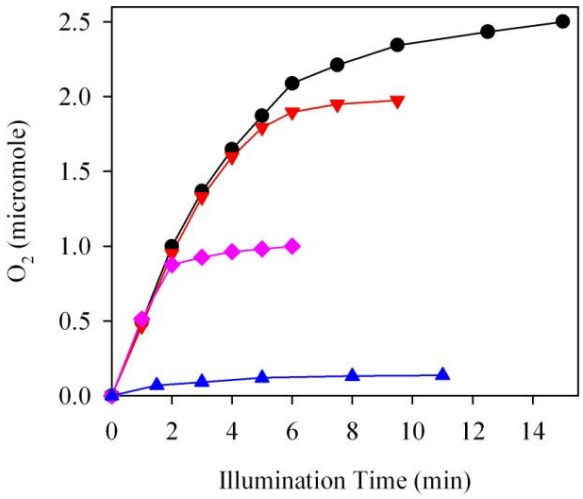

Figure 3.2. Kinetics of O_2 formation with pH 8 buffers: 20 mM sodium phosphate (NaPi; blue triangles, final pH 6.5), 20 mM sodium borate (NaB: pink diamonds, final pH 2.0), 40 mM NaB (red inverted triangles, final pH 5.3) and 80 mM NaB (black circles, final pH 7.9). Conditions: 1.0 mM $[Ru(bpy)_3]^{2+}$, 5.0 mM $Na_2S_2O_8$, 5.0 μM Co_4POM, total reaction volume 2 mL. Illumination: 16.8 mW, 420-470 nm. RPM: 5 x 10^3

3.2.2 Oxygen evolution

This photocatalytic system was evaluated under the optimized experimental conditions described. As shown in Figure 3.3, dioxygen was formed quickly under visible-light illumination (420-470 nm) catalyzed by even 0.5 mM of Co_4POM. A series of control experiments confirmed that fast O_2 generation requires the presence of all four components: photons, $[Ru(bpy)_3]^{2+}$, persulfate, and Co_4POM. In the absence of catalyst, the O_2 yield after 15 min of illumination is ~0.2 mmol, or 12 times lower than in catalytic runs using 5 μM Co_4POM. After 10-15 minutes of illumination, the amount of O_2 reaches a plateau value, the concentration of $S_2O_8^{2-}$ decreases from its initial value of 5.0 mM to <0.2 mM (detection limit), and the concentration of $[Ru(bpy)_3]^{2+}$ decreases by <15%. Significantly, photosensitizer decomposition was markedly higher (>50%) in the absence of catalyst, indicating that it is protected from decomposition by the presence of the catalyst.

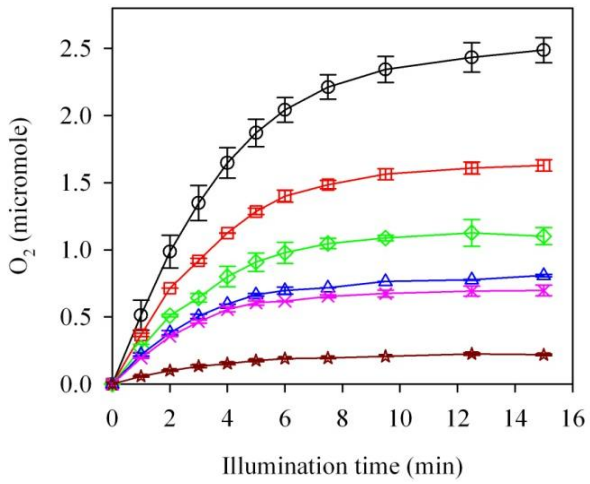

Figure 3.3. Kinetics of O_2 formation in the photocatalytic system with different concentrations of Co_4POM: 0 (brown stars), 1.5 (pink crosses), 2 (blue triangles), 3 (green diamonds), 4 (red squares), and 5 M (black circles).

In addition, after the completion of the first run, another 0.05 mL aliquot of 5 mM $Na_2S_2O_8$, was added to the reaction, the contents degassed, placed under Ar and a second run was conducted under otherwise identical conditions. O_2 evolution can be resumed with the addition of $S_2O_8^{2-}$, as shown in Figure 3.4, suggesting that the catalyst remains active, and $[Ru(bpy)_3]^{2+}$ is protected and regenerated. In the end of the second run, the final pH is 7.3 (initial pH 8.0). For the second run, TON and chemical yield decrease about ~20%. $[Ru(bpy)_3]^{2+}$ decomposes ~28%. If for each run, $[Ru(bpy)_3]^{2+}$ decreases 15% (as in 80 mM buffer), then, after the two runs, it will decompose 28% (0.15 + 0.85 × 0.15 = 0.28). We used 130 mM buffer because of the buffer capacity. With this buffer concentration, the chemical yield and quantum yield all decrease to about half that measured in 80 mM buffer.

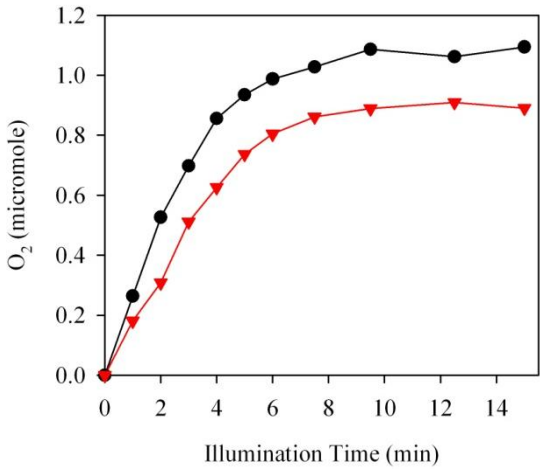

Figure 3.4. O_2 formation kinetics of the first run (black circle) and the second run (red triangle). After the completion of the first run, another 0.05 mL aliquot of 5 mM $Na_2S_2O_8$, was added to the reaction, the contents degassed, placed under Ar and a second run was conducted under otherwise identical conditions. 130 mM sodium borate buffer (initial pH 8.0) was used.

Although the stability of Co_4POM under thermal (dark) catalytic water oxidation conditions was assessed by 7 distinct and complementary techniques,[31] the catalysis conditions in the photo-driven reactions reported in this study are sufficiently different that we wished to conduct some additional catalyst stability experiments. First, careful assessment of the pre- and post-catalysis solutions (reactant concentrations and reaction conditions in Figure 3.2 caption) showed no evidence of nanoparticle formation (dynamic light scattering and Tyndall effects). Second, the kinetics of O_2 evolution using Co_4POM after one use showed identical kinetics (same curvature; see Figure 3.4), and third, the rates are the same in the first run and second run (which employed the once-used catalyst, Co_4POM) when corrected for the points below and experimental error.

These arguments and all the work assessing the stability of Co_4POM under dark catalytic water oxidation conditions provide good evidence that the catalyst is stable under these photochemical conditions up to the number of turnovers in these studies: TON = 220 per run. The kinetics (curvatures in Figures 3.3 and 3.4) and the turnover numbers were solely limited by the amount of sacrificial electron acceptor, persulfate, used.

3.2.3 Mechanism

To quantify the photocatalytic performance, we compare the average stoichiometric dioxygen chemical yields ($\Phi_{CY}= 2[O_2]_f/[Na_2S_2O_8]_0$, where $[O_2]_f$ and $[Na_2S_2O_8]_0$ are the final yield of O_2 and the initial concentration of persulfate, respectively, and the initial photon-to-O_2 generation quantum yields ($\Phi_{QY}(0) = 2[\Delta(O_2)/\Delta(h\nu)]$, where $\Delta(O_2)$ and $\Delta(h\nu)$ are the change in the total amount of O_2 produced

and the number of photons absorbed, respectively. According to eq 3.2, two photons and two $S_2O_8^{2-}$ can lead to the evolution of one O_2 in the absence of loss pathways. The $\Phi_{QY}(t)$ can also be calculated from the ratio of the rates of O_2 generation *vs* photon absorption, and is related to the slope of the plot of O_2 *vs* illumination time shown in Figure 3.3. It is clear that $\Phi_{QY}(t)$ is largest at the onset of the reaction and decreases with time, approaching zero at ~15 min. For this reason, only the initial quantum yields are compared in this work. It was shown previously that the ratio of $[O_2]$ formed to $[Na_2S_2O_8]$ consumed changes negligibly throughout the course of the catalytic runs. Only the average value for 2 $[O_2]/[Na_2S_2O_8]$ (over the course of the reaction) is measured in this study.

The values of Φ_{CY} and $\Phi_{QY}(0)$ as a function of catalyst concentration are plotted in Figure 3.3 and listed in Table 3.1.

Table 3.1. Turnover numbers (TON), chemical yields, and initial quantum yields for homogeneous visible-light-driven water oxidation catalyzed by Co_4POM .[a]

Catalyst (μM)	TON [b]	Chemical Yield [c]	Initial Quantum Yield [d]
0	N/A	0.04 ± 0.01	0.03 ± 0.01
1.5	158 ± 15	0.09 ± 0.01	0.09 ± 0.01
2	143 ± 3	0.11 ± 0.01	0.10 ± 0.01
3	149 ± 15	0.18 ± 0.02	0.14 ± 0.01
4	175 ± 6	0.28 ± 0.01	0.20 ± 0.01
5	224 ± 11	0.45 ± 0.02	0.30 ± 0.05
5 (Ru_4POM) [e]	136 ± 5	0.27 ± 0.01	0.24 ± 0.01

[a] For experimental conditions, see Figure 3.3 caption. TON and chemical yields are averaged for results at 12.5 and 15 min. [b] (O_2 yield at end of run) / (catalyst concentration) = $[O_2]_f/[\text{catalyst}]$; [c] $\Phi_{CY} = 2[O_2]_f/[Na_2S_2O_8]_0$ (the initial concentration of persulfate); [d] $\Phi_{QY}(0) = 2\,(\Delta[O_2]/\Delta(hv))_0$, (initial O_2 formation rate) / (photon flux); [e] with 5 μM Ru_4POM; reported values, excluding 0 μM, are corrected for the amount of O_2 generated in the control experiment.

In calculating these reported values, we have subtracted the maximal contribution of O_2 generated from noncatalytic pathways (control experiment without catalyst).[33] Both the chemical yield and the initial quantum yield increase with catalyst concentration.

The photocatalytic O_2 evolution in this system is believed to follow the well-established reaction mechanism presented in Figure 3.5. [24,27,28]

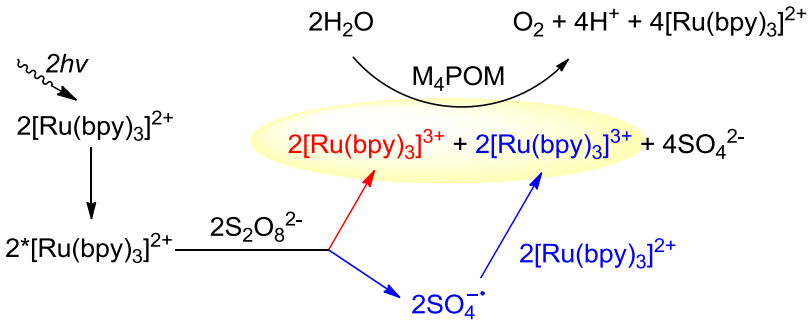

Photo excitation:	$2[Ru(bpy)_3]^{2+} + 2h\nu \rightarrow 2^*[Ru(bpy)_3]^{2+}$	(3.4)
Oxidant generation:	$2^*[Ru(bpy)_3]^{2+} + 2[S_2O_8]^{2-} \rightarrow 2[Ru(bpy)_3]^{3+} + 2SO_4^{2-} + 2SO_4^{2-}\bullet$	(3.5a)
	$2SO_4^{2-}\bullet + 2[Ru(bpy)_3]^{2+} \rightarrow 2[Ru(bpy)_3]^{3+} + 2SO_4^{2-}$	(3.5b)
Catalyst oxidation:	$4[Ru(bpy)_3]^{3+} + [M_4\text{-POM}] \rightarrow 4[Ru(bpy)_3]^{2+} + [M^+_4POM]$	(3.6)
Water oxidation:	$[M^+_4POM] + 2H_2O \rightarrow [M_4POM] + 4H^+ + O_2$	(3.7)

Figure 3.5. Principal processes of photocatalytic water oxidation by a sacrificial electron acceptor $[S_2O_8]^{2-}$ with $[Ru(bpy)_3]^{2+}$ as a photosensitizer and M_4POM (M = Ru or Co) as a water oxidation catalyst .

The reaction is initiated upon the absorption of two photons by two $[Ru(bpy)_3]^{2+}$ complexes. Due to the high extinction coefficient ($\varepsilon_{450nm} = 1.4 \times 10^4$ $M^{-1}cm^{-1}$) and high concentration of $[Ru(bpy)_3]^{2+}$ (1 mM), all the incident photons are captured by $[Ru(bpy)_3]^{2+}$ in the solution. Following photoexcitation, the excited $[Ru(bpy)_3]^{2+*}$ is quenched by $S_2O_8^{2-}$ through both bimolecular or unimolecular electron transfer

pathways.[34-36] The quenching (or electron transfer) efficiency (ϕ_q) increases with the $S_2O_8^{2-}$ concentration, and is 67% at 5.0 mM $Na_2S_2O_8$, the initial concentration used in the catalytic runs. The photo-induced electron transfer results in the generation of two $[Ru(bpy)_3]^{3+}$ and two $SO_4^{-\cdot}$. The latter radicals subsequently oxidize two additional $[Ru(bpy)_3]^{2+}$ to two $[Ru(bpy)_3]^{3+}$, with the yield of ϕ_r. Then four $[Ru(bpy)_3]^{3+}$ complexes oxidize water to make one O_2 with a yield of ϕ_c.

Based on the scheme in Figure 3.5, the chemical yield and quantum efficiency of O_2 generation can be related to the yields of individual steps (Figure 3.6):

$$\Phi_{CY} = 2\,[O_2]_f/[Na_2S_2O_8]_0 = 0.5\ \cdot(1+\phi_r)\ \cdot\phi_c \qquad (3.8)$$

$$\Phi_{QY}(t) = 2\,(\Delta[O_2]/\Delta(h\nu))_t = 0.5\ \cdot\phi_q(t)\ \cdot(1+\phi_r)\ \cdot\phi_c \qquad (3.9)$$

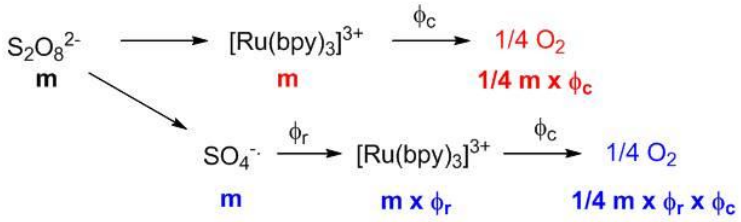

$$\Phi_{CY} = 2\times\frac{[O_2]}{[Na_2S_2O_8]} = 2\times\frac{\frac{1}{4}\cdot m\cdot\phi_c + \frac{1}{4}\cdot m\cdot\phi_r\cdot\phi_c}{m} = \frac{1}{2}\cdot(1+\phi_r)\cdot\phi_c$$

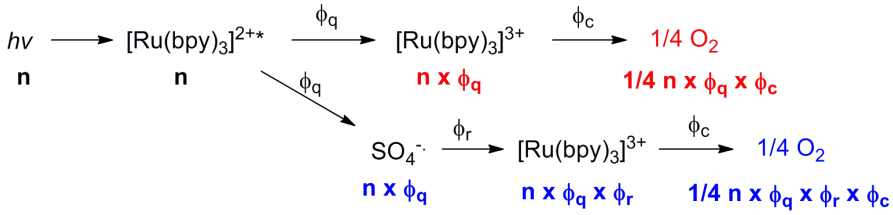

$$\Phi_{QY} = 2\times\frac{[O_2]}{h\nu} = 2\times\frac{\frac{1}{4}\cdot n\cdot\phi_q\cdot\phi_c + \frac{1}{4}\cdot n\cdot\phi_q\cdot\phi_r\cdot\phi_c}{n} = \frac{1}{2}\cdot\phi_q\cdot(1+\phi_r)\cdot\phi_c$$

Figure 3.6. Derivation of chemical yield (Φ_{CY}) and quantum yield (Φ_{QY})

Furthermore, from eqs 3.8 and 3.9, the chemical yield, quantum yield, and quenching efficiency are related by eq 3.10.

$$\Phi_{QY}(t) = \phi_q(t) \cdot \Phi_{CY} \quad (3.10)$$

This relation is confirmed to good measure by our experimental data (Table 3.1) and accounts for the observed decreasing rate (quantum yield) of O_2 formed as a function of time and the catalyst concentration. For example, using the measured initial ϕ_q and Φ_{CY} (0.67 and 0.45, respectively for 5 μM Co_4POM in Table 3.1), the initial Φ_{QY} is 0.30, which agrees well with the measured value (0.30). As the reaction proceeds, $\phi_q(t)$ and therefore $\Phi_{QY}(t)$ decreases due to the depletion of $S_2O_8^{2-}$. In measurements with different catalyst concentrations, the initial quenching efficiency ϕ_q should be identical (67%) because the same initial concentrations of $[Ru(bpy)_3]^{2+}$ and $S_2O_8^{2-}$ were used. According to eq 3.10, the reduced initial quantum yield for O_2 generation can be attributed to the decrease in the chemical yield at lower catalyst concentrations, consistent with the experimental observation shown in Figure 3.3 and Table 3.1.

Our result suggests that a key factor that limits the quantum yield is the chemical yield Φ_{CY}, which is significantly less than unity in the current systems. According to eq 2.8, Φ_{CY} is determined by both ϕ_r and ϕ_c. The ϕ_r is generally taken to be *near unity*, although several reports have indicated that it is less than unity and highly dependent on the solution environment.[37-39] In a previous study, we have determined that ϕ_c = 67% for Co_4POM at pH 8 in stoichiometric water oxidation in the dark by $[Ru(bpy)_3]^{3+}$. From the measured Φ_{CY} (0.45 at 5 μM of Co_4POM), the minimal ϕ_c (when ϕ_r = 1) can be estimated to be 0.45, consistent with the previously reported ϕ_c value.[31] Φ_{CY} (and hence ϕ_c)

increases with the catalyst concentration, implicating a competition between catalytic and noncatalytic pathways for the photogenerated $[Ru(bpy)_3]^{3+}$.

3.2.4 Ru_4POM and Co_4POM

To gain further insight on the factors limiting the quantum and chemical yields for catalytic O_2 generation, we also compared the catalytic activities of Ru_4POM and Co_4POM under identical conditions.

As seen from both Figure 3.7 and Table 3.1, the chemical yield and TON in the reactions catalyzed by Co_4POM are ~1.7 fold higher than those catalyzed by Ru_4POM, with a 1.25 higher quantum yield.

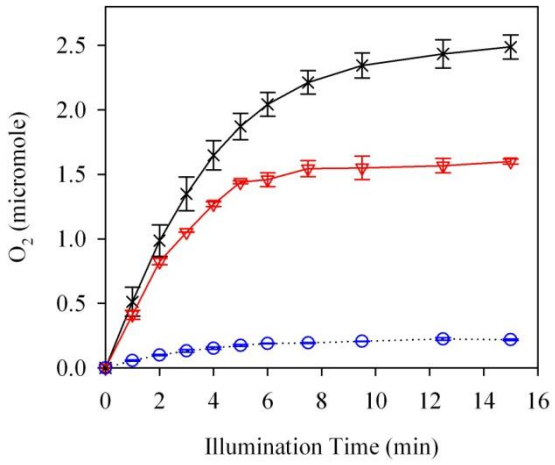

Figure 3**.7.** Kinetics of O_2 formation in the photocatalytic system using different catalysts: Ru_4POM (red triangles), Co_4POM (black crosses) and control (no catalyst, blue circles). Error bars were calculated from two independent experiments.

These three criteria demonstrate that Co_4POM, an abundant-metal-based material, catalyzes visible-light-driven water oxidation more rapidly than Ru_4POM, which contains

a precious metal, ruthenium. Furthermore, the photochemical reactions using Ru_4POM and Co_4POM were carried out under the same conditions, so ϕ_I should be the same in both systems. Therefore, a higher Φ_{CY} for Co_4POM suggests a higher ϕ_c using this catalyst. These data suggest that Co_4POM has a higher selectivity toward water oxidation than Ru_4POM which is consistent with a higher TOF for dark water oxidation by Co_4POM than by Ru_4POM.[31]

Light-driven water oxidation utilizes $[Ru(bpy)_3]^{3+}$ as an intermediate oxidant (eq 3.2). A higher ϕ_c indicates a faster conversion of $[Ru(bpy)_3]^{3+}$ to $[Ru(bpy)_3]^{2+}$ in the presence of the catalyst. The concentration of $[Ru(bpy)_3]^{3+}$ can be followed by the absorption at 670 nm (ε_{670nm} = 4.2 x 10^2 $M^{-1}cm^{-1}$) where $[Ru(bpy)_3]^{2+}$ has only a very low extinction coefficient (ε_{670nm} = 5 M^{-1} cm^{-1}). Hence, the catalytic efficiency of Ru_4POM and Co_4POM for water oxidation (ϕ_c) can also be compared from the kinetics for the disappearance of $[Ru(bpy)_3]^{3+}$ in the stoichiometric dark water oxidation system. These kinetics traces, as shown in Figure 3.8, were measured by the stopped-flow technique, in which solutions containing $[Ru(bpy)_3]^{3+}$ and the catalysts, respectively, were rapidly mixed.

It has been found that $[Ru(bpy)_3]^{3+}$ is consumed in two competing pathways: catalytic water oxidation and the self-decomposition reaction.[25] At pH 8, the $[Ru(bpy)_3]^{3+}$ half-life of ~30 s (no catalyst) is reduced to 11 s and 1.3 s on addition of Ru_4POM and Co_4POM, respectively. Here the half-life, defined as the time when the concentration decreases to one half of the initial value, is used to compare the relative decay rate of $[Ru(bpy)_3]^{3+}$ because the kinetics are complex (not single exponential). While oxidative catalysis of bpy-ligand cannot be ruled out as a pathway for the consumption of

$[Ru(bpy)_3]^{3+}$,[33] this along with the results in Figures 3.7 and 3.8, suggests that Ru_4POM and Co_4POM are both efficient WOCs, This result shows that Co_4POM is almost 10 times more efficient than Ru_4POM in catalyzing the dark reaction, eq 3.1, suggesting that Co_4POM should be also a more efficient catalyst in the photo-driven systems. Indeed, the O_2 formation kinetics show this is the case.

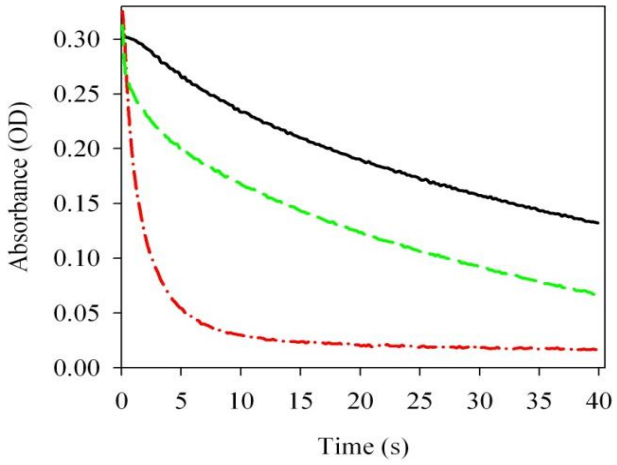

Figure 3.8. Kinetics of $[Ru(bpy)_3]^{3+}$ reduction to $[Ru(bpy)_3]^{2+}$ measured as the decrease in absorbance at 670 nm for the non-catalytic reaction (solid black line, no catalyst), 5 μM Ru_4POM (dashed green line), and 5 μM Co_4POM (dashed-dot red line). Conditions: 1 mM $[Ru(bpy)_3]^{3+}$ (initial), 80 mM sodium borate buffer, pH 8.0, 20 ^oC.

3.3 Conclusion

In summary, we have demonstrated that Co_4POM, a carbon-free, molecular WOC consisting of only earth-abundant metals, is a very efficient and stable molecular catalyst for photodriven water oxidation. Under the same conditions (pH 8), Co_4POM is more

efficient than Ru_4POM in oxidizing water which can be attributed to the higher turnover frequency for Co_4POM versus Ru_4POM.

3.4 References

(1) Barber, J. *Chem. Soc. Rev.* **2009**, *38*, 185.

(2) Lewis, N. S.; Nocera, D. G. *Proc. Nat. Acad. Sci.* **2006**, *103(43)*, 15729.

(3) Gray, H. B. *Nat. Chem.* **2009**, *1*, 7.

(4) Binstead, R. A.; Chronister, C. W.; Ni, J.; Hartshorn, C. M.; Meyer, T. J. *J. Am. Chem. Soc.* **2000**, *122*, 8464.

(5) Yagi, M.; Kaneko, M. *Chem. Rev.* **2001**, *101*, 21.

(6) Hurst, J. K. *Coord. Chem. Rev.* **2005**, *249*, 313.

(7) Zong, R.; Thummel, R. *J. Am. Chem. Soc.* **2005**, *127*, 12802.

(8) Eisenberg, R.; Gray, H. B. *Inorg. Chem.* **2008**, *47*, 1697.

(9) McDaniel, N. D.; Coughlin, F. J.; Tinker, L. L.; Bernhard, S. *J. Am. Chem. Soc.* **2008**, *130*, 210.

(10) Brimblecombe, R.; Swiegers, G. F.; Dismukes, G. C.; Spiccia, L. *Angew. Chem. Int. Ed.* **2008**, *47*, 7335.

(11) Concepcion, J. J.; Jurss, J. W.; Brennaman, M. K.; Hoertz, P. G.; Patrocinio, A. O. T.; Iha, N. Y. M.; Templeton, J. L.; Meyer, T. J. *Accts. Chem. Res.* **2009**, *42*, 1954.

(12) Hurst, J. K.; Cape, J. L.; Clark, A. E.; Das, S.; Qin, C. *Inorg. Chem.* **2008**, *47*, 1753.

(13) Betley, T. A.; Surendranath, Y.; Childress, M. V.; Alliger, G. E.; Fu, R.; Cummins, C. C.; Nocera, D. G. *Phil. Trans. R. Soc. B* **2008**, *363*, 1293.

(14) Muckerman, J. T.; Polyansky, D. E.; Wada, T.; Tanaka, K.; Fujita, E. *Inorg. Chem.* **2008**, *47*, 1787.

(15) Sala, X.; Romero, I.; ǵuez, M. R.; Escriche, L. í; Llobet, A. *Angew. Chem. Int. Ed.* **2009**, *48*, 2842.

(16) Cao, R.; Ma, H.; Geletii, Y. V.; Hardcastle, K. I.; Hill, C. L. *Inorg. Chem.* **2009**, *48*, 5596.

(17) Jiao, F.; Frei, H. *Angew. Chem. Int. Ed.* **2009**, *48*, 1841.

(18) Hull, J. F.; Balcells, D.; Blakemore, J. D.; Incarvito, C. D.; Eisenstein, O.; Brudvig, G. W.; Crabtree, R. H. *J. Am. Chem. Soc.* **2009**, *131*, 8730.

(19) Kuznetsov, A. E.; Geletii, Y. V.; Hill, C. L.; Morokuma, K.; Musaev, D. G. *J. Am. Chem. Soc.* **2009**, *131*, 6844.

(20) Duan, L.; Xu, Y.; Gorlov, M.; Tong, L.; Andersson, S.; Sun, L. *Chem. Eur. J.* **2010**, *16*, 4659.

(21) Masaoka, S.; Sakai, K. *Chem. Lett.* **2009**, *38*, 182.

(22) Geletii, Y. V.; Botar, B.; Kögerler, P.; Hillesheim, D. A.; Musaev, D. G.; Hill, C. L. *Angew. Chem. Int. Ed.* **2008**, *47*, 3896.

(23) Sartorel, A.; Carraro, M.; Scorrano, G.; Zorzi, R. D.; Geremia, S.; McDaniel, N. D.; Bernhard, S.; Bonchio, M. *J. Am. Chem. Soc* **2008**, *130*, 5006.

(24) Geletii, Y. V.; Huang, Z.; Hou, Y.; Musaev, D. G.; Lian, T.; Hill, C. L. *J. Am. Chem. Soc.* **2009**, *131*, 7522.

(25) Geletii, Y. V.; Besson, C.; Hou, Y.; Yin, Q.; Musaev, D. G.; Quinonero, D.; Cao, R.; Hardcastle, K. I.; Proust, A.; Kögerler, P.; Hill, C. L. *J. Am. Chem. Soc.* **2009**, *131*, 17360.

(26) Sartorel, A.; Miro, P.; Salvadori, E.; Romain, S.; Carraro, M.; Scorrano, G.; Valentin, M. D.; Llobet, A.; Bo, C.; Bonchio, M. *J. Am. Chem. Soc.* **2009**, *131*, 16051.

(27) Puntoriero, F.; Ganga, G. L.; Sartorel, A.; Carraro, M.; Scorrano, G.; Bonchio, M.; Campagna, S. *Chem. Commun.* **2010**, *46*, 4725.

(28) Besson, C.; Huang, Z.; Geletii, Y. V.; Lense, S.; Hardcastle, K. I.; Musaev, D. G.; Lian, T.; Proust, A.; Hill, C. L. *Chem. Commun.* **2010**, 2784.

(29) Orlandi, M.; Argazzi, R.; Sartorel, A.; Carraro, M.; Scorrano, G.; Bonchio, M.; Scandola, F. *Chem. Commun.* **2010**, *46*, 3152.

(30) Toma, F. M.; Sartorel, A.; Iurlo, M.; Carraro, M.; Parisse, P.; Maccato, C.; Rapino, S.; Gonzalez, B. R.; Amenitsch, H.; Ros, T. D.; Casalis, L.; Goldoni, A.; Marcaccio, M.; Scorrano, G.; Scoles, G.; Paolucci, F.; Prato, M.; Bonchio, M. *Nat. Chem.* **2010**, *2*, 826.

(31) Yin, Q.; Tan, J. M.; Besson, C.; Geletii, Y. V.; Musaev, D. G.; Kuznetsov, A. E.; Luo, Z.; Hardcastle, K. I.; Hill, C. L. *Science* **2010**, *328*, 342.

(32) Huang, Z. Q.; Luo, Z.; Geletii, Y. V.; Vickers, J. W.; Yin, Q. S.; Wu, D.; Hou, Y.; Ding, Y.; Song, J.; Musaev, D. G.; Hill, C. L.; Lian, T. Q. *J Am Chem Soc* **2011**, *133*, 2068.

(33) Ghosh, P. K.; Brunschwig, B. S.; Chou, M.; Creutz, C.; Sutin, N. *J. Am. Chem. Soc.* **1984**, *106*, 4772.

(34) White, H. S.; Becker, W. G.; Bard, A. J. *J. Phys. Chem.* **1984**, *88*, 1840.

(35) Kaledin, A. L.; Huang, Z.; Geletii, Y. V.; Lian, T.; Hill, C. L.; Musaev, D. G. *J. Phys. Chem. A* **2010**, *114*, 73.

(36) Kaledin, A. L.; Huang, Z.; Yin, Q.; Dunphy, E. L.; Constable, E. C.; Housecroft, C. E.; Geletii, Y. V.; Lian, T.; Hill, C. L.; Musaev, D. G. *J. Phys. Chem. A* **2010**, *114*, 6284.

(37) Horváth, A.; Bakó, Z.; Papp, S.; Keszei, C. *J. Photochem. Photobiol A: Chem.* **1990**, *52*, 271.

(38) Bolletta, F.; Juris, A.; Maestri, M.; Sandrini, D. *Inorg. Chimica Acta* **1980**, *44*, L175.

(39) Henbest, K.; Douglas, P.; Garley, M. S.; Mills, A. *J. Photochem. Photobiol A: Chem.* **1994**, *80*, 299.

Part III: Homogeneous Light-driven Water Oxidation

CHAPTER

4

Charge Transfer Dynamics in Homogeneous Systems

Partially in articles:

6. **Huang, Z.**; Geletii, Y.V.; Wu, D.; Anfuso, C. L.; Musaev, D.G.; Hill, C.L.; and Lian, T.; "*Interfacial charge transfer dynamics in TiO2-Sensitizer-Ru4POM photocatalytic systems for water oxidation*" ***Proc. SPIE,*** **2011,** *8109*, 810903

7. Kaledin, A.; **Huang, Z.**; Geletii, Y.V.; Lian, T.; Hill, C.L.; Musaev, D.G.; *"Insights into Photoinduced Electron Transfer between* $[Ru(bpy)_3]^{2+}$ *and* $[S_2O_8]^{2-}$ *in Water: Computational and Experimental Studies", **J. Phys. Chem. A***, **2010**, *114*, 73

Abstract: This chapter describes the charge transfer dynamics in the previously established homogeneous photocatalytic system driven by incident visible photons and consumption of the sacrificial electron acceptor $[S_2O_8]^{2-}$, with $[Ru(bpy)_3]^{2+}$ as a photosensitizer and $[\{Ru_4O_4(OH)_2(H_2O)_4\}(\gamma\text{-}SiW_{10}O_{36})_2]^{10-}$ (Ru_4POM) as a WOC. Our experiments based on static and ultrafast spectroscopic methods indicate that the diffusion-controlled characteristics of the charge transfer processes in solution systems are critically responsible for the relatively low overall quantum efficiency.

4.1 Introduction

The development of efficient and stable photocatalytic systems that are capable of splitting water into H_2 and O_2 by sunlight is one of the grand challenges in renewable energy research. [1-3] These photocataltic systems consist of a water oxidation catalyst (WOC), visible light photosensitizer, and H_2 evolution catalyst (or Water Reduce Catalyst, WRC). [4-21] A new family of all inorganic (carbon free) WOCs[22-32] based on transition metal substituted polyoxometalates (POM) has been synthesized, including two ones with active tetra-Ru cores, $[\{Ru_4O_4(OH)_2(H_2O)_4\}(\gamma\text{-}SiW_{10}O_{36})_2]^{10-}$ (hereafter denoted as Ru_4POM)and $[\{Ru_4O_6(OH_2)_4\}(\gamma\text{-}PW_{10}O_{36})_2]^{10-}$, and a third based on an earth abundant metals, $[Co_4(H_2O)_2(PW_9O_{34})_2]^{10-}$. As demonstrated in Chapter 3, the photocatalytic activities of these catalysts have been comprehensively evaluated in a homogeneous light-driven process using $[Ru(bpy)_3]^{2+}$ as photosensitizer and $S_2O_8^{2-}$ as a sacrificial electron acceptor, eq 4.1;

$$2\ S_2O_8^{2-} + 2\ H_2O + 2\ h\nu \rightarrow 4\ SO_4^{2-} + O_2 + 4\ H^+ \qquad (4.1)$$

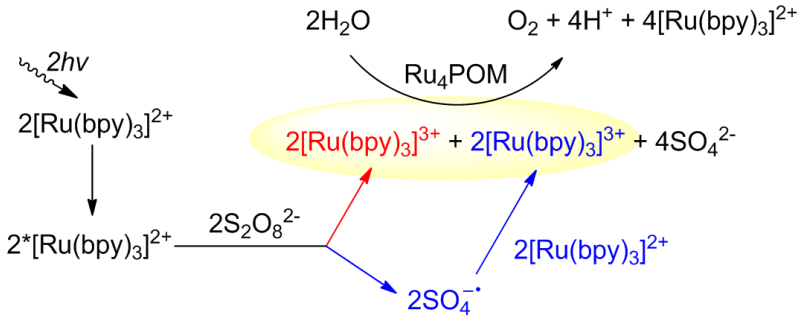

Figure 4.1. Principal processes of photocatalytic water oxidation by a sacrificial electron acceptor $[S_2O_8]^{2-}$ with $[Ru(bpy)_3]^{2+}$ as a photosensitizer and Ru_4POM as a water oxidation catalyst.

Photoinduced oxidation of $[Ru(bpy)_3]^{2+}$ to $[Ru(bpy)_3]^{3+}$ by persulfate ion has been well studied in literature and is believed to proceed via a quenching of the visible-light-accessible metal-to-ligand charge transfer (MLCT) excited state. [33,34] The products, $[Ru(bpy)_3]^{3+}$ and SO_4^- (E_o, $SO_4^{-\bullet}/SO_4^{2-}$ ~2.4 V), are both strong oxidants and the latter one quickly oxidize another $[Ru(bpy)_3]^{2+}$ to second $[Ru(bpy)_3]^{3+}$ (eq. 4.3). [35-37] The absorption of two photons and the consumption of two equivalents of $S_2O_8^{2-}$ generates 4 $[Ru(bpy)_3]^{3+}$ that sequentially oxidizes Ru_4POM by 4-electrons, which in its turn oxidizes two molecules of H_2O to O_2 thus regenerating $[Ru(bpy)_3]^{2+}$ (eq 4.4).

$$[Ru(bpy)_3]^{2+} + h\nu + S_2O_8^{2-} \rightarrow [Ru(bpy)_3]^{3+} + SO_4^{2-} + SO_4^{-\bullet} \quad (4.2)$$

$$[Ru(bpy)_3]^{2+} + SO_4^{-\bullet} \rightarrow [Ru(bpy)_3]^{3+} + SO_4^{2-} \quad (4.3)$$

$$4[Ru(bpy)_3]^{3+} + 2\,H_2O + Ru_4POM \rightarrow 4\,[Ru(bpy)_3]^{2+} + O_2 + 4H^+ + Ru_4POM \quad (4.4)$$

This reported soluble three-component homogenous solar driven water oxidation system uses Ru-polypyridyl complexes as photosensitizers.[24,27,28,38] However, the polypyridyl ligands in this sensitizer are oxidatively degraded slowly under the

photocatalytic conditions. Therefore, it is a vital to understand the problems related to the electron transfer properties and stability of Ru-based organic dyes. In order to better understand the interfacial electron transfer processes and improve the quantum yield of water oxidation in artificial photosynthetic systems in Figure 4.1, we systematically investigated the mechanism and electron transfer dynamics of the reaction through various static and time resolved fluorescence and absorption spectroscopy, as described in this chapter.

4.2 Spectroscopic methods

In addition to various static fluorescence and absorption spectroscopy for this work, the time-resolved fluorescence decay measurements and transient (fs and ns) absorption spectroscopy were employed to interrogate charge transfer dynamics in the light-driven water oxidation system.

In the time-resolved fluorescence measurements, changes in fluorescence lifetime are measured, from which electron transfer rate constants are determined. Due to the emissive MLCT excited states of the dyes in our homogeneous water oxidation system, charge transfer dynamics can be studied by following the fluorescence kinetics after optical excitation. However, other fluorescence quenching pathways, such as energy transfer, can complicate the investigation of charge transfer processes.

Transient absorption spectroscopy based on pump-probe method is another powerful tool to investigate charge transfer dynamics. Shown in Figure 4.2 is a general scheme for pump-probe experiments. A short (~150 fs in our set up) incoming pump pulse excites the sample and triggers the photo-induced event under investigation. This

pulse is generally monochromic (400 nm for our experiment, frequency doubling from the 800 nm fundamental pulse from the Ti:Sapphire laser). The second pulse -- a polychromic probe pulse with a certain spectral range, passes a delay configuration and after the delay it also hits the sample. A translational stage controlling the travelling distance of the probe pulse, thus changing the delay of the probe pulse relative to the pump pulse, is widely used for ultrafast spectroscopy with fs temporal resolution. In ns- or μs-spectrophotometer, electronic delays are used.

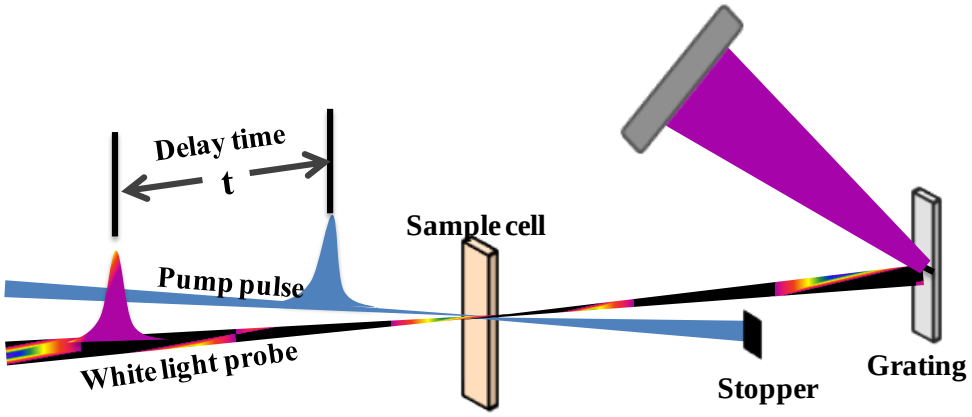

Figure 4.2. Schematic representation of pump-probe measurements.

Due to the broad-band feature of the probe pulse, this technique allows spectroscopic identification of all the species (ground and excited states, and oxidized and reduced forms) of the electron donor and acceptor present at a given time delay after optical excitation. This provides the opportunity to directly interrogate charge transfer dynamics.

4.3 Photoinduced electron transfer from $[Ru(bpy)_3]^{2+}$ to $S_2O_8^{2-}$

4.3.1 Basic theory for fluorescence quenching

Static and time-resolved fluorescence measurements can be employed to investigate the electron transfer mechanism of reaction (4.2), namely the absorption of a photon and transfer of one electron from a MLCT excited state $[Ru(bpy)_3]^{2+}*$ to $S_2O_8^{2-}$ to yield $[Ru(bpy)_3]^{2+}$, $SO_4^{-\bullet}$ and SO_4^{2-}. In literature, this process has been studied extensively using various experimental techniques. [33,34,39] Based on these extensive studies two distinct mechanisms, called "unimolecular (or static quenching)" and "bimolecular (dynamic quenching)", were proposed. The "unimolecular" mechanism results from the ground-state association of $[Ru(bpy)_3]^{2+}$ with $S_2O_8^{2-}$ to yield the $[Ru(bpy)_3]^{2+}\ldots[S_2O_8^{2-}]$ complex. While in the "bimolecular" mechanism the initial photoinduced electron transfer occurs in a collision between excited $[Ru(bpy)_3]^{2+}*$ and $S_2O_8^{2-}$. It was shown that optically bright singlet ^{1}MLCT excited state of $[Ru(bpy)_3]^{2+}*$ is extremely short lived with a lifetime of ~40 fs. It is thought to undergo an efficient intersystem crossing, via strong spin-orbit interaction, to one of the lower energy triplets.[40] These long-lived (~ 1 μs) triplet states are believed to transfer the electron to persulfate. [33]

Consider a general case of ground-state association between the fluorescent species, M (Ru photosensitizers), and quencher, L ($S_2O_8^{2-}$),

$$[M] + n[L] \xleftrightarrow{\beta_n} [ML_n] \qquad (4.5)$$

where β_n is the cumulative stability constants or equilibrium constants with n the number of associated L. The fraction (x_n) of species $[ML_n]$ is given by,

$$x_n = \frac{[ML_n]}{c_0} = \frac{\beta_n [L]^n}{\sum_i \beta_i [L]^i} \tag{4.6}$$

where c_0 is the total analytical concentration of M and β_0 is 1.

A general analysis of time-resolved fluorescence involving the ground-state associations between the photosensitizers and the quenchers allows the photoexcited complex to emit and to undergo both dynamic and static quenching reactions. Thus, the following mechanism can be proposed:

$$[*ML_n] \xrightarrow{k_r} [ML_n] + h\nu \tag{4.7}$$

$$[*ML_n] \xrightarrow{k_{nr}} [ML_n] \tag{4.8}$$

$$[*ML_n] + [L] \xrightarrow{k_q} [M^+ L^- L_{n-1}] \tag{4.9}$$

$$[*ML_n] \xrightarrow{k_n} [M^+ L^- L_{n-1}] \tag{4.10}$$

where k_r and k_{nr} are the intrinsic radiative and non-radiative decay rate constants of the [*ML_n]. k_q and k_n are dynamic and static (electron transfer) rate constants for [*ML_n]. For k_n, when n=0, $k_0 = 0$, since no quencher (L) exists in the system. We can define τ_n as:

$$\frac{1}{\tau_n} = k_r + k_{nr} + k_n \tag{4.11}$$

Here, we can assume k_r, k_{nr} and k_q are independent of the ion-pair formation effect because of the weak interaction as seen from the negligible changes in the absorption and fluorescence spectral shape of the Ru-based photosensitizer in the presence of the quencher, $[S_2O_8]^{2-}$. Hence, τ_n accounts for the intrinsic excited state relaxation and unimolecular electron transfer process. The bimolecular part is [L] concentration-dependent, and can be expressed as the product, k_q[L]. Therefore, the fluorescence

intensity (I_t), determined by the concentration of the excited emitters and its radiative rates, can be expressed by:

$$I_t = \alpha \cdot k_r \cdot c_0 \cdot e^{-k_q[L]t} \cdot \sum_n \frac{\beta_n [L]^n}{\sum_i \beta_i [L]^i} \cdot e^{-\frac{t}{\tau_n}} \tag{4.12}$$

where α is a proportional constant determined by the fluorescence detection efficiency, excitation power and extinction coefficients. Here, we assume the extinction coefficients are independent of the ion-pair formation effect. The fluorescence intensity at t = 0 is independent of [L]. Hence, we can normalize all the fluorescence decay traces for further analysis. Furthermore, the ratio of steady emission without (I_0) and with (I) quencher, the so-called Stern-Volmer equation, can be derived from integration of equation (4.12),

$$\frac{I_0}{I} = \frac{\int_0^\infty e^{-\frac{t}{\tau_0}} dt}{\int_0^\infty e^{-k_q[L]t} \cdot \sum_n \frac{\beta_n [L]^n}{\sum_i \beta_i [L]^i} \cdot e^{-\frac{t}{\tau_n}} dt} = \left\{ \sum_n \frac{\beta_n [L]^n}{\sum_i \beta_i [L]^i} \cdot \frac{\tau_n}{\tau_0} \cdot \frac{1}{1 + k_q \tau_n [L]} \right\}^{-1} \tag{4.13}$$

4.3.2 Stern-Volmer plots

In order to clarify the mechanism of the reaction (4.2) in experimental conditions for water oxidation, we have studied quenching of $[Ru(bpy)_3]^{2+*}$ in aqueous solutions by $[S_2O_8^{2-}]$ using steady-state luminescence techniques at three different buffer concentrations: a) 0.2 M pH 7.2 sodium phosphate buffer, b) 20 mM pH 7.2 sodium phosphate buffer, and c) no buffer. Buffer b was used in our study of photo-driven water oxidation reaction.

The Stern-Volmer (SV) plot, I_0/I *vs* $[S_2O_8^{2-}]$ (where I and I_0 and emission internsity of $[Ru(bpy)_3]^{2+*}$ in the presence and absence of the quencher respectively), are

shown in Figure 4.3. The SV for the solution containing high buffer concentration (buffer a) yields a linear line with a unity intercept. The SV plot significantly deviates from linearity and curves downward in solutions with 0 and 20 mM buffer.

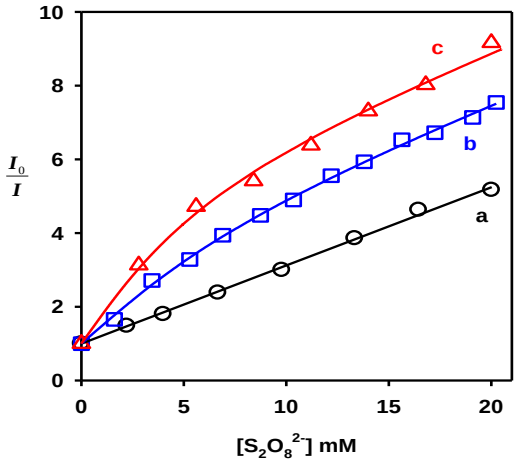

Figure 4.3. Stern-Volmer plot for solutions containing (a) 200 mM pH 7.2 phosphate buffer, (b) 20 mM pH 7.2 phosphate buffer, and (c) no buffer. All solutions contained 1 mM $[Ru(bpy)_3]^{2+}$ and were purged with Ar. Solid curves are fits according to eq (2.19) and (2.20) (see text).

The SV plot for buffer a) and c) are similar to results previously reported by Bard and co-workers for the same emitter and quencher in a different electrolyte.[33] They showed that the SV plot can be well described by a model that takes into account the formation of ground-state 1:1 ion pairs between the emitter and the quencher. According to eq 4.13, this model gives rise the following equation for emission quenching:

$$\frac{I_0}{I} = \frac{(1+K_{eq}[S_2O_8^{2-}])(1+k_q\tau_0[S_2O_8^{2-}])}{1+\frac{\tau'}{\tau_0}\frac{K_{eq}[S_2O_8^{2-}](1+k_q\tau_0[S_2O_8^{2-}])}{1+k_q'\tau'[S_2O_8^{2-}]}} \qquad (4.14)$$

where K_{eq} is the equilibrium constant of ion pair formation; τ_0 (τ') and k_q (k_q') are the unimolecular decay time and the bimolecular quenching constant of the excited emitter in free form (ion pair state), respectively. Under conditions of negligible ion-pair formation, $K_{eq}[S_2O8^{2-}]<<1$, eq 4.13 and 4.14 are simplified to:

$$\frac{I_0}{I} = 1 + k_q \tau_0 [S_2O_8^{2-}] \qquad (4.15)$$

As shown in Figure 4.3, curve a can be well fit by equation 4.15, suggesting that under high buffer concentration, the equilibrium constant is negligible and most quenchers are not in the ion-pair state. The quenching proceeds through bimolecular pathway. The slope of the linear fit gives the value of $k_q \tau_0$ of 212 M^{-1}. Using the reported $[Ru(bpy)_3]^{2+}$* lifetime, τ_0, of 0.55 *m*s,[33] we obtains a k_q of 3.9×10^8 $M^{-1}s^{-1}$. Deviation from linearity of the SV plots at low (or no) buffer concentration (curve c and b) indicates the formation of a ground-state ion pair between $[Ru(bpy)_3]^{2+}$ and $[S_2O_8^{2-}]$. Assuming that kq and kq' are similar, these SV plots can be fitted by equation 4.14, as shown in Figure 4.3. The results of the fitting are listed in Table 4.1.

Table 4.1: Results of Kinetics Fitting of the $[Ru(bpy)_3]^{2+}\ldots[S_2O_8^{2-}]$

Buffer (mM)	τ' (*n*s)	$k_q(k_q')$ ($M^{-1}s^{-1}$)	K_{eq} (M^{-1})	k_{ET} (s^{-1})	α
0	108	3.9×10^8	6.93×10^2	7.4×10^6	0.75
20	149	3.9×10^8	3.53×10^2	4.9×10^6	0.61
200	N/A	3.9×10^8	0	N/A	0

The intrinsic radiative and nonradiative rate constants of $[Ru(bpy)_3]^{2+*}\ldots[S_2O_8^{2-}]$ should be similar to the $[Ru(bpy)_3]^{2+*}$ due to the weak (a few kcal/mol) electrostatic

interaction between $[Ru(bpy)_3]^{2+}$ and $S_2O_8^{2-}$. Then, the photo induced unimolecular ET rate (k_{ET}) in eq 4.2 can be estimated as:

$$k_{ET} = \frac{1}{\tau'} - \frac{1}{\tau_0} \tag{4.16}$$

The estimated k_{ET} is ~ 7.4×10^6 s^{-1} in solutions without buffer. This result is in qualitative agreement with the computed unimolecular electron transfer rate.[39] At the buffer concentration used in our photo-driven water oxidation experiment (buffer b), the k_{ET} is ~ 4.9×10^6 s^{-1}. At 5 mM $[S_2O_8^{2-}]$, the bimolecular ET rate $k_q[S_2O_8^{2-}]$ is ~1.9×10^6 s^{-1}. Under these conditions, the unimolecular electron transfer rate is 2.5 times faster than the bimolecular pathway, suggesting that the formation of ion pair facilitates the generation of oxidant $[Ru(bpy)_3]^{3+}$. Additionally, the resulting equilibrium constant, K_{eq}, from the fittings can be used to estimate the percentage of the emitters that forms ion-pair in the ground state (α). For example, at 5.0 mM $Na_2S_2O_8$, α is 0.61 in 20 mM sodium phosphate buffer solution and 0.75 in the absence of buffer. Thus, in experimental condition (in aqueous solution and at pH 7.2 and 20 mM sodium phosphate buffer) reported in our previous paper, 61% of $[Ru(bpy)_3]^{2+*}$ quenching by $S_2O_8^{2-}$ occurs via a formation of ion-pair complex $[Ru(bpy)_3]^{2+*}\ldots[S_2O_8^{2-}]$. As shown in Figure 4.3, the ratio of I_0/I increases with decreasing buffer concentration under the same concentration of $[S_2O_8^{2-}]$, suggesting that the phosphate buffer deactivates the quenching process through inhibiting the formation of ground-state ion pair.

4.4 Electron transfer dynamics in photocatalytic systems

Here we examine the charge transfer kinetics in a homogenous photo-driven water oxidation system consisting of Ru_4POM WOC, $[Ru(bpy)_3]^{2+}$ as a sensitizer, and

persulfate as a sacrificial electron acceptor. Despite the well-known simplified mechanism, the more detailed mechanistic aspects, such as the electron transfer rates among different components, have not been extensively studied. Our preliminary studies have revealed that the efficiency of the system depends on many factors, such as the concentrations of reagents in solution, mass transport (stirring rate), light intensity, shape and volume of the reaction vessel, etc. [24,28,38]

Transient absorption studies were carried out to investigate the electron transfer kinetics in this multi-component system. As shown in Figure 4.4a, in the absence of the $[S_2O_8]^{2-}$, the transient spectra of $[Ru(bpy)_3]^{2+}$ after 400 nm excitation show a ground state bleach at 450 nm, an isosbestic point at 500 nm, and a new broad weakly-absorbing species above 500 nm due to the generation of the excited-state dye, $*[Ru(bpy)_3]^{2+}$. The earliest events associated with these excited-state evolution dynamics, i.e. the ultrafast intersystem crossing from the initial singlet excited state to the long lived triplet MLCT state have been well studied.[40] $*[Ru(bpy)_3]^{2+}$ subsequently relaxes back to its ground state through both radiative and noradiative pathways, resulting in the recovery features shown in the transient spectra (Figure 4.4a) and in the corresponding kinetic trace (Figure 4.4b). The lifetime of $*[Ru(bpy)_3]^{2+}$ was estimated to be 290 ns by a single-exponential fit to the kinetic trace (Figure 4.4b).

In the presence of a sacrificial electron acceptor, $[S_2O_8]^{2-}$, after the initial instantaneous bleach after 400 nm excitation, the bleach continued to grow until 15 μs. This kinetic feature (two-step growth) suggests the further depopulation of the $[Ru(bpy)_3]^{2+}$ due to secondary photochemical reactions in the presence of persulfate. It is believed that the photo-induced electron transfer from $*[Ru(bpy)_3]^{2+}$ to $[S_2O_8]^{2-}$

generating an oxidant, $[Ru(bpy)_3]^{3+}$ and a sulfate radical (eq 4.2). This initial photoinduced electron transfer (eq 4.2) occurs through both dynamic (diffusion) bi-molecular and static (ion-pair formation) unimolecular processes as shown in previous computational and experimental studies.[33,34,39] Our static fluorescence study shows an absorbed-photon-to-oxidant conversion yield of 0.67 for a solution containing 1 mM $[Ru(bpy)_3]^{2+}$ and 5 mM $[S_2O_8]^{2-}$ (the solution conditions of the light-driven photocatalytic solution system for O_2 evolution).

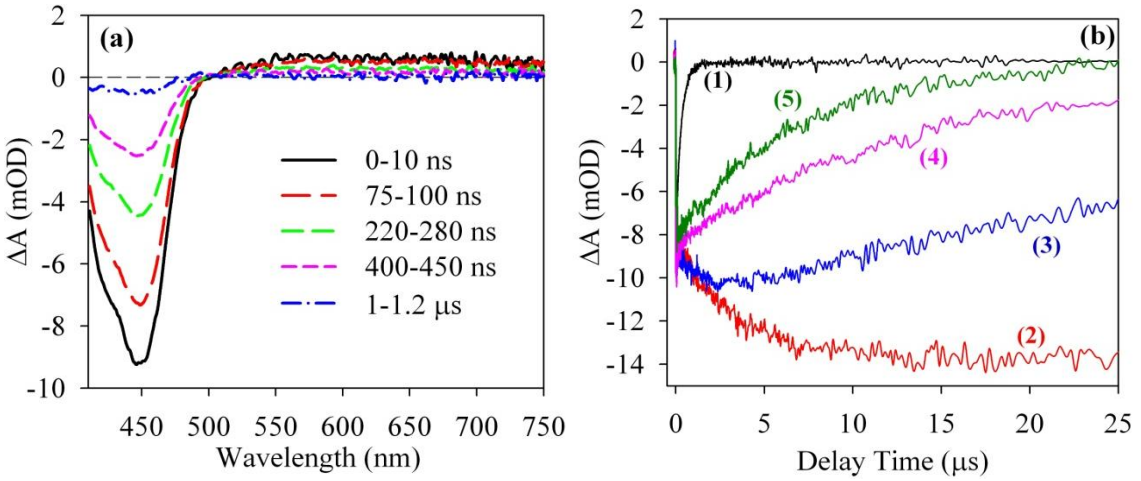

Figure 4.4. (a) Transient absorption spectra averaged over different delay times for $[Ru(bpy)_3]^{2+}$ after 400 nm excitation. (b) Transient kinetics monitored at 450 nm for (1) 50 µM $[Ru(bpy)_3]^{2+}$; (2) 50 µM $[Ru(bpy)_3]^{2+}$ with 5 mM $[S_2O_8]^{2-}$; (3-5) 50 µM $[Ru(bpy)_3]^{2+}$ with 5 mM $[S_2O_8]^{2-}$ and different concentrations of $[Ru_4POM]$: (3) 12.5 µM; (4) 35 µM; and (5) 50 µM. All samples contain 20 mM phosphate buffer (initial pH 7.2).

The reaction of photogenerated radical with $[Ru(bpy)_3]^{2+}$, as shown in eq 4.4b, is another pathway for oxidant ($[Ru(bpy)_3]^{3+}$) generation and additional ground-state

depopulation. The radical-to-oxidant reaction yield is generally taken to be *near unity*, although several reports have indicated lower yields and strong dependence on the solution environment. [35-37] Estimating from the kinetic trace in Figure 2.10b, the upper limit of the radical-to-oxidant yield in the solution under investigation (50 μM $[Ru(bpy)_3]^{2+}$ and 5 mM $[S_2O_8]^{2-}$) is ~0.8, based on the ratio of the signal sizes between the initial bleach (< 100 ns) and the final steady state bleach (after 15 μs) . Side reactions that result in $[Ru(bpy)_3]^{2+}$ decomposition also cause ground-state depopulation, which can lead to the growth seen in the kinetic trace as well. For this reason, the yield of 0.8 is believed to be an upper limit. Nevertheless, our result is consistent with the proposed mechanism shown in scheme 1 and shows that the secondary reaction of the radical occurs in the microsecond time scale under our experimental conditions.

The presence of the WOC, $[Ru_4POM]$, has a dramatic effect on the transient kinetics in this system. As shown in Figure 4.4b, the addition of 12.5 μM $[Ru_4POM]$ to the solution of 50 μM $[Ru(bpy)_3]^{2+}$ and 5 mM $[S_2O_8]^{2-}$ results in the recovery of the ground-state bleach within 5 μs. Further increase of the WOC concentration accelerates the bleach recovery. This recovery feature is due to the regeneration of $[Ru(bpy)_3]^{2+}$ ground state through WOC oxidation, during which an electron transfers from the WOC, $[Ru_4POM]$, to the oxidant, $[Ru(bpy)_3]^{3+}$, as show in eq 4.4. This electron transfer occurs on the μs time scale according to the kinetics in Figure 4.4b. This slow event can be attributed to the diffusion-controlled bimolecular process and is highly dependent on both the concentrations of each species and the solution environment (ionic strength, pH, agitation, etc). Ion-pair formation between the WOC and the oxidant due to their opposite charges may facilitate this process, but the effect is very limited. The acceleration of

bleach recovery with increasing [Ru_4POM] indicates a strong dependence of O_2 formation on the catalyst concentration, consistent with the performance in a practical photocatalytic system for O_2 evolution.

4.5 Conclusion

In summary, we performed static fluorescence measurements and nanosecond transient absorption studies of the charge separation dynamics in a homogeneous photocatalytic system based on Ru_4POM WOC, $Ru(bpy)_3$ sensitizer and $S_2O_8^{2-}$ sacrificial electron acceptor. It shows that with efficient removal of the electron, the oxidized sensitizer can oxidize the catalyst for water oxidation. Therefore, an integrated acceptor-photosensitizer-WOC composite with intact, directly-connected structure (through either electrostatic or covalent interactions) is a promising approach to accelerate the water oxidation process and hence improve the selectivity and quantum efficiency of the WOC.

4.6 References

(1) Barber, J. *Chem. Soc. Rev.* **2009**, *38*, 185.

(2) Lewis, N. S.; Nocera, D. G. *Proc. Nat. Acad. Sci.* **2006**, *103(43)*, 15729.

(3) Gray, H. B. *Nat. Chem.* **2009**, *1*, 7.

(4) Binstead, R. A.; Chronister, C. W.; Ni, J.; Hartshorn, C. M.; Meyer, T. J. *J. Am. Chem. Soc.* **2000**, *122*, 8464.

(5) Yagi, M.; Kaneko, M. *Chem. Rev.* **2001**, *101*, 21.

(6) Hurst, J. K. *Coord. Chem. Rev.* **2005**, *249*, 313.

(7) Zong, R.; Thummel, R. *J. Am. Chem. Soc.* **2005**, *127*, 12802.

(8) Eisenberg, R.; Gray, H. B. *Inorg. Chem.* **2008**, *47*, 1697.

(9) McDaniel, N. D.; Coughlin, F. J.; Tinker, L. L.; Bernhard, S. *J. Am. Chem. Soc.* **2008**, *130*, 210.

(10) Brimblecombe, R.; Swiegers, G. F.; Dismukes, G. C.; Spiccia, L. *Angew. Chem. Int. Ed.* **2008**, *47*, 7335.

(11) Concepcion, J. J.; Jurss, J. W.; Brennaman, M. K.; Hoertz, P. G.; Patrocinio, A. O. T.; Iha, N. Y. M.; Templeton, J. L.; Meyer, T. J. *Accts. Chem. Res.* **2009**, *42*, 1954.

(12) Hurst, J. K.; Cape, J. L.; Clark, A. E.; Das, S.; Qin, C. *Inorg. Chem.* **2008**, *47*, 1753.

(13) Betley, T. A.; Surendranath, Y.; Childress, M. V.; Alliger, G. E.; Fu, R.; Cummins, C. C.; Nocera, D. G. *Phil. Trans. R. Soc. B* **2008**, *363*, 1293.

(14) Muckerman, J. T.; Polyansky, D. E.; Wada, T.; Tanaka, K.; Fujita, E. *Inorg. Chem.* **2008**, *47*, 1787.

(15) Sala, X.; Romero, I.; ǵuez, M. R.; Escriche, L. í; Llobet, A. *Angew. Chem. Int. Ed.* **2009**, *48*, 2842.

(16) Cao, R.; Ma, H.; Geletii, Y. V.; Hardcastle, K. I.; Hill, C. L. *Inorg. Chem.* **2009**, *48*, 5596.

(17) Jiao, F.; Frei, H. *Angew. Chem. Int. Ed.* **2009**, *48*, 1841.

(18) Hull, J. F.; Balcells, D.; Blakemore, J. D.; Incarvito, C. D.; Eisenstein, O.; Brudvig, G. W.; Crabtree, R. H. *J. Am. Chem. Soc.* **2009**, *131*, 8730.

(19) Kuznetsov, A. E.; Geletii, Y. V.; Hill, C. L.; Morokuma, K.; Musaev, D. G. *J. Am. Chem. Soc.* **2009**, *131*, 6844.

(20) Duan, L.; Xu, Y.; Gorlov, M.; Tong, L.; Andersson, S.; Sun, L. *Chem. Eur. J.* **2010**, *16*, 4659.

(21) Masaoka, S.; Sakai, K. *Chem. Lett.* **2009**, *38*, 182.

(22) Geletii, Y. V.; Botar, B.; Kögerler, P.; Hillesheim, D. A.; Musaev, D. G.; Hill, C. L. *Angew. Chem. Int. Ed.* **2008**, *47*, 3896.

(23) Sartorel, A.; Carraro, M.; Scorrano, G.; Zorzi, R. D.; Geremia, S.; McDaniel, N. D.; Bernhard, S.; Bonchio, M. *J. Am. Chem. Soc* **2008**, *130*, 5006.

(24) Geletii, Y. V.; Huang, Z.; Hou, Y.; Musaev, D. G.; Lian, T.; Hill, C. L. *J. Am. Chem. Soc.* **2009**, *131*, 7522.

(25) Geletii, Y. V.; Besson, C.; Hou, Y.; Yin, Q.; Musaev, D. G.; Quinonero, D.; Cao, R.; Hardcastle, K. I.; Proust, A.; Kögerler, P.; Hill, C. L. *J. Am. Chem. Soc.* **2009**, *131*, 17360.

(26) Sartorel, A.; Miro, P.; Salvadori, E.; Romain, S.; Carraro, M.; Scorrano, G.; Valentin, M. D.; Llobet, A.; Bo, C.; Bonchio, M. *J. Am. Chem. Soc.* **2009**, *131*, 16051.

(27) Puntoriero, F.; Ganga, G. L.; Sartorel, A.; Carraro, M.; Scorrano, G.; Bonchio, M.; Campagna, S. *Chem. Commun.* **2010**, *46*, 4725.

(28) Besson, C.; Huang, Z.; Geletii, Y. V.; Lense, S.; Hardcastle, K. I.; Musaev, D. G.; Lian, T.; Proust, A.; Hill, C. L. *Chem. Commun.* **2010**, 2784.

(29) Orlandi, M.; Argazzi, R.; Sartorel, A.; Carraro, M.; Scorrano, G.; Bonchio, M.; Scandola, F. *Chem. Commun.* **2010**, *46*, 3152.

(30) Toma, F. M.; Sartorel, A.; Iurlo, M.; Carraro, M.; Parisse, P.; Maccato, C.; Rapino, S.; Gonzalez, B. R.; Amenitsch, H.; Ros, T. D.; Casalis, L.; Goldoni, A.; Marcaccio, M.; Scorrano, G.; Scoles, G.; Paolucci, F.; Prato, M.; Bonchio, M. *Nat. Chem.* **2010**, *2*, 826.

(31) Yin, Q.; Tan, J. M.; Besson, C.; Geletii, Y. V.; Musaev, D. G.; Kuznetsov, A. E.; Luo, Z.; Hardcastle, K. I.; Hill, C. L. *Science* **2010**, *328*, 342.

(32) Geletii, Y. V.; Yin, Q. S.; Hou, Y.; Huang, Z. Q.; Ma, H. Y.; Song, J.; Besson, C.; Luo, Z.; Cao, R.; O'Halloran, K. P.; Zhu, G. B.; Zhao, C. C.; Vickers, J. W.; Ding, Y.; Mohebbi, S.; Kuznetsov, A. E.; Musaev, D. G.; Lian, T. Q.; Hill, C. L. *Isr J Chem* **2011**, *51*, 238.

(33) White, H. S.; Becker, W. G.; Bard, A. J. *J. Phys. Chem.* **1984**, *88*, 1840.

(34) Kaledin, A. L.; Huang, Z.; Yin, Q.; Dunphy, E. L.; Constable, E. C.; Housecroft, C. E.; Geletii, Y. V.; Lian, T.; Hill, C. L.; Musaev, D. G. *J. Phys. Chem. A* **2010**, *114*, 6284.

(35) Horváth, A.; Bakó, Z.; Papp, S.; Keszei, C. *J. Photochem. Photobiol A: Chem.* **1990**, *52*, 271.

(36) Bolletta, F.; Juris, A.; Maestri, M.; Sandrini, D. *Inorg. Chimica Acta* **1980**, *44*, L175.

(37) Henbest, K.; Douglas, P.; Garley, M. S.; Mills, A. *J. Photochem. Photobiol A: Chem.* **1994**, *80*, 299.

(38) Huang, Z. Q.; Luo, Z.; Geletii, Y. V.; Vickers, J. W.; Yin, Q. S.; Wu, D.; Hou, Y.; Ding, Y.; Song, J.; Musaev, D. G.; Hill, C. L.; Lian, T. Q. *J Am Chem Soc* **2011**, *133*, 2068.

(39) Kaledin, A. L.; Huang, Z.; Geletii, Y. V.; Lian, T.; Hill, C. L.; Musaev, D. G. *J. Phys. Chem. A* **2010**, *114*, 73.

(40) Damrauer, N. H.; Cerullo, G.; Yeh, A.; Boussie, T. R.; Shank, C. V.; McCusker, J. K. *Science* **1997**, *275*, 54.

Part III: Homogeneous Light-driven Water Oxidation

CHAPTER

5

Designs for Improved Water-Oxidation

Partially in articles:

1. **Huang, Z.**; Geletii, Y.V.; Wu, D.; Anfuso, C. L.; Musaev, D.G.; Hill, C.L.; and Lian, T.; "*Interfacial charge transfer dynamics in TiO2-Sensitizer-Ru4POM photocatalytic systems for water oxidation*" ***Proc. SPIE*, 2011,** *8109*, 810903

2. Kaledin, A.; **Huang, Z.**; Yin, Q.; Dunphy, E.; Constable, E.; Housecroft, C.; Geletii, Y. V.; Lian, T.; Hill, C. L.; Musaev, D. G.; "*Insights into Photoinduced Electron Transfer Between* $[Ru(mptpy)_2]^{4+}$ *(mptpy = 4′(4-methylpyridinio)-2,2′:6′,2″-terpyridine) and* $[S_2O_8]^{2-}$*: Computational and Experimental Studies*", ***J. Phys. Chem. A*, 2010**, *114*, 6284

Abstract: Previous chapters have described our studies on a totally homogeneous (molecular) system for the visible-light driven catalytic water oxidation, using polyoxometalate molecules as water oxidation catalysts. In this chapter, other systems, including the change of photosensitizers and the introduction of more efficient electron acceptors, were tested for improved performance.

5.1 Introduction

Previous chapters have described a totally homogeneous (molecular) system for the visible-light driven catalytic water oxidation, using organic-structure-free, hence oxidatively stable molecular water oxidation catalysts (WOCs): $[\{Ru_4O_4(OH)_2(H_2O)_4\}(\gamma\text{-}SiW_{10}O_{36})_2]^{10-}$ (Ru_4POM), $[\{Ru_4O_4(OH)_2(H_2O)_4\}(\gamma\text{-}SiW_{10}O_{36})_2]^{10-}$ (Ru_4-(P)-POM) and $[Co_4(H_2O)_2(PW_9O_{34})_2]^{10-}$($Co_4$POM).[1-5] Static and time-resolved spectroscopic studies have been performed to understanding the fundamental insights of these systems, showing that the diffusion-controlled characteristics of the charge transfer processes in solution systems are critically responsible for the relatively low overall quantum efficiency.[6-8] In terms of these results, an integrated acceptor-photosensitizer-WOC composite with intact, directly-connected structure (through either electrostatic or covalent interactions) is a promising approach to accelerate the water oxidation process and hence improve the selectivity and quantum efficiency of the WOC. This chapter describes our initial attempts for the targeted improvements by introducing a new photosensitizer, $[Ru(mptpy)_2]^{4+}$, and dye-sensitized TiO_2 nanoparticles, TiO_2/Ru470.

One way to improve the performance of the homogeneous visible-light driven artificial photosynthetic system is to replace the $[Ru(bpy)_3]^{2+}$ with a better light absorber.

A ruthenium 2,2':6',2''-terpyridine (tpy) complex, $[Ru(mptpy)_2]^{4+}$ was introduced, and its photophysics and interaction with the fluorescence quencher, $[S_2O_8]^{2-}$, were studied. The quenching of the photoexcited $[Ru(mptpy)_2]^{4+}$ by $[S_2O_8]^{2-}$ primarily occurs via an unimolecular mechanism with formation of a weak ion-pair complex $\{[Ru(mptpy)_2]^{4+}...([S_2O_8]^{2-})_n\}$, where n = 1 and 2. The homogeneous systems are attempted further to be improved by the introduction of microheterogeous systems where the $Ru(bpy)_3^{2+}$ dye is replaced with the Ru-dye sensitized TiO_2 nanoparticles. The results further confirm the necessity of a well-defined integrated acceptor-photosensitizer-WOC composite (electrode).

5.2 Alternative photosensitizer: $[Ru(mptpy)_2]^{4+}$

One candidate class of dyes are ruthenium 2,2':6',2''-terpyridine (tpy) complexes, $[Ru(tpy)_2]^{4+}$, which generally: (a) have a high $Ru^{2+/3+}$ potentials (> 1.1 V vs. NHE)[9,10] as required for water oxidation, (b) have high extinction coefficients[10-12] over a broad range of the visible light spectrum, (c) exhibit an absorption spectrum that overlaps very well with the solar spectrum,[9,13] and (d) can be easily engineered to have a larger positive charge that facilitates a strong (relative to $[Ru(bpy)_3]^{2+}$) bonding both to the negatively charged reductant, i.e. persulfate, and the WOC, the Ru_4O_4-containing polyoxometalate (POM). Furthermore, becuse 4'-substituted tpy ligands in a $[Ru(mptpy)_2]^{4+}$ are linearly oriented with respect to the metal centre, they may facilitate the construction of triads in which the WOC and HEC are connected via the photosensitizer in a colinear manner. Such a configuration of triad increases the distance between the reductant and oxidant thus slowing the rate of charge recombination. In fact, previously, ruthenium tpy

complexes have been shown to be good photosensitizers in various dye sensitized TiO_2 solar cells.[14-16] In these solar cells, the photo-induced electron injection into TiO_2 is ultrafast (<100 fs), and the resulting charge separated state is long-lived (~3 μs).[10,11] For these reasons, we turned to the use of bis{4'-(4-methylpyridinio)-2,2':6,2''-terpyridine}ruthenium(II) salts, $[Ru(mptpy)_2]^{4+}$ (Figure 5.1) as a potential photosensitizer whose UV-Vis absorption spectrum is compared with $[Ru(bpy)_3]^{2+}$ in Figure 5.2.

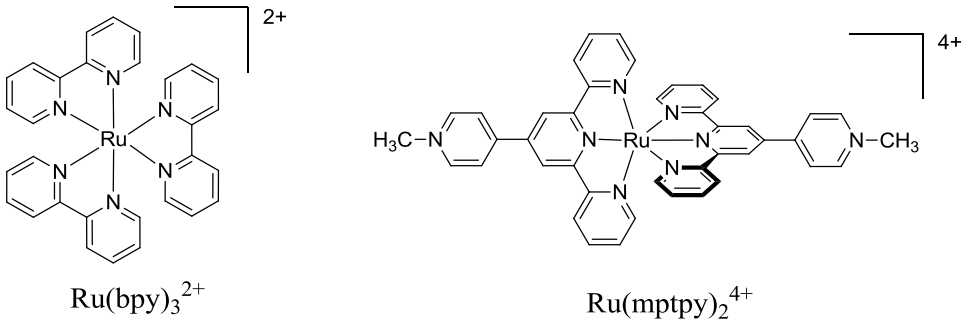

Figure 5.1. Molecular structures of $[Ru(bpy)_3]^{2+}$ and $[Ru(mptpy)_2]^{4+}$.

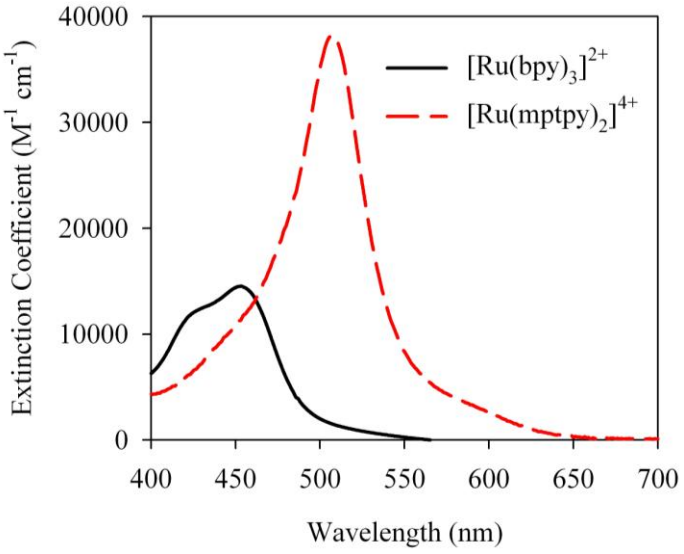

Figure 5.2. UV-Vis absorption spectra of $[Ru(bpy)_3]^{2+}$ (black) and $[Ru(mptpy)_2]^{4+}$ (red dashes)

5.2.1 Photophysics and photochemistry of $[Ru(mptpy)_2]^{4+}$

The absorption spectrum of $[Ru(mptpy)_2]^{4+}$ (Figure 5.2) shows an intense MLCT absorption band that has a peak at 507 nm with an extinction coefficient of 38,200 $M^{-1}cm^{-1}$ at this wavelength. Its emission spectrum in aqueous solution (Figure 5.3) measured by a photofluorometer after 507 nm excitation, shows a broad band at 710 nm.

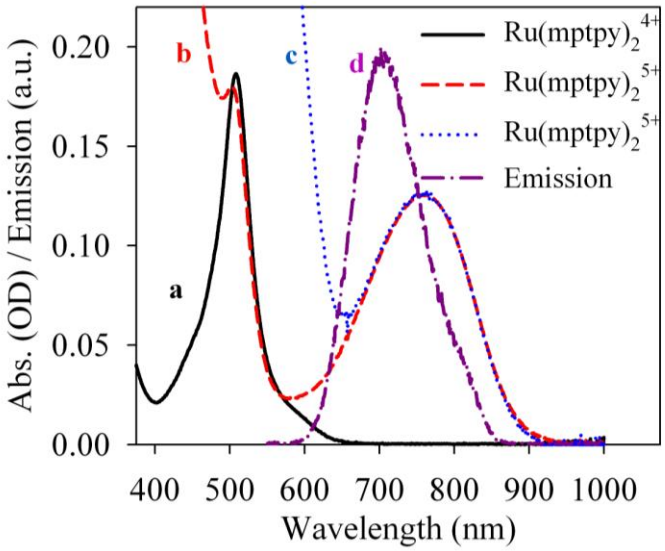

Figure 5.3. UV/Vis spectra of (a) 5 μM $[Ru(mptpy)_2]^{4+}$; (b) 150 μM $[Ru(mptpy)_2]^{5+}$ prepared by oxidizing $[Ru(mptpy)_2]^{4+}$ with excess PbO_2 powder followed by filtration; (c) a scaled spectrum of $[Ru(mptpy)_2]^{5+}$ prepared by oxidizing $[Ru(mptpy)_2]^{4+}$ with excess $[S_2O_8]^{2-}$ and exposing the solution to room light for 30 min, followed by filtration; and (d) a scaled emission spectrum of $[Ru(mptpy)_2]^{4+}$ in aqueous solution after 507 nm excitation.

The lifetimes (τ_0) of the excited state of $[Ru(mptpy)_2]^{4+}$ (i.e. $[Ru(mptpy)_2]^{4+}$*) in different solvents were obtained by fitting their fluorescence decay kinetics to first-order exponential functions. As shown in Table 5.1, the lifetime of $[Ru(mptpy)_2]^{4+}$*, τ_0, is

slightly affected by the presence of CH_3CN, varying from 174 ns in purely aqueous solution to 182 ns in solution containing 30% CH_3CN. This is similar to the solvent effect previously shown for CH_3CN on the $[Ru(bpy)_3]^{2+}$* lifetime.[17]

The transient absorption spectra of a 0.2 mM $[Ru(mptpy)_2]^{4+}$ aqueous solution, recorded after 400 nm excitation, show two features, the ground-state bleach of $[Ru(mptpy)_2]^{4+}$ at 507 nm and a new absorption band peak at ~600 nm, which are separated by a clear isosbestic point at 540 nm (Figure 5.4). The kinetics of these two features were fit to first-order exponential functions, resulting in an identical recovery/decay time constant of 170 ns. This time constant is consistent with the fluorescence lifetime of $[Ru(mptpy)_2]^{4+}$*, confirming that the absorption band seen in the transient spectra is due to the generation of $[Ru(mptpy)_2]^{4+}$* by photoexcitation. From the amplitude ratio between the ground state bleach and the excited state absorption, the extinction coefficient of the excited state is estimated to be ~9,500 $M^{-1}cm^{-2}$ at 600 nm.

The product of quenching of $[Ru(mptpy)_2]^{4+}$* by $[S_2O_8]^{2-}$ is $[Ru(mptpy)_2]^{5+}$. Authentic $[Ru(mptpy)_2]^{5+}$ was prepared by in solution by the addition of excess PbO_2 powder to a 150 μM solution of $[Ru(mptpy)_2]^{4+}$ in 0.5 M H_2SO_4. The UV/Vis spectrum of this solution (Figure 5.3) after filtration shows a new broad band centered at 763 nm assigned to $[Ru(mptpy)_2]^{5+}$. The extinction coefficient of $[Ru(mptpy)_2]^{5+}$ is estimated to be ~835 $M^{-1}cm^{-1}$ at 763 nm, or ~2% of that $[Ru(mptpy)_2]^{4+}$ at 507 nm. $[Ru(mptpy)_2]^{5+}$ is shown to be unstable by monitoring the absorbance kinetics at 763 nm of a freshly prepared $[Ru(mptpy)_2]^{5+}$ solution in 0.5 M H_2SO_4: we have found ~2%/min decomposition rate within the measurement time window (10 min).

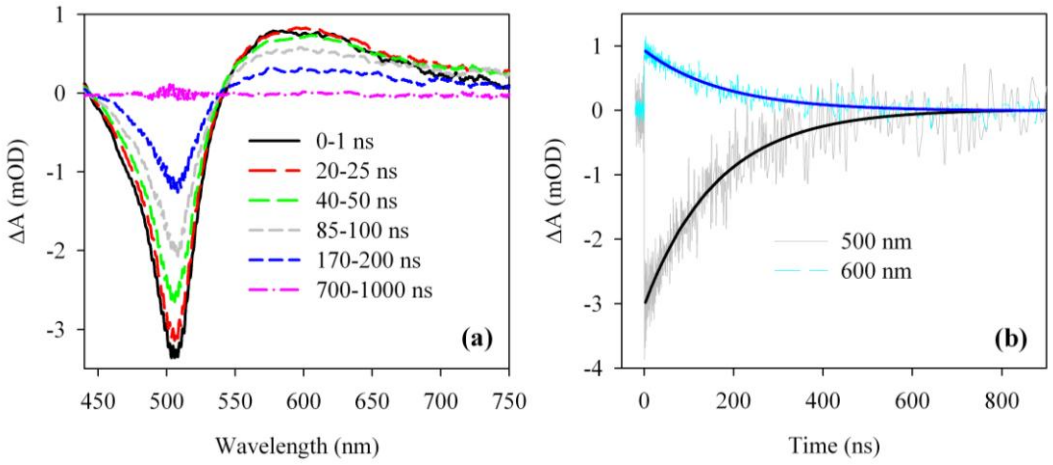

Figure 5.4. (a) Transient absorption spectra recorded after 400 nm excitation for a 0.2 mM $[Ru(mptpy)_2]^{4+}$ aqueous solution. Each transient spectrum is an average of the spectra in the indicated range of delay times. (b) Corresponding transient absorption kinetics monitored at 500 nm and 600 nm. Solid lines are first-order exponential fits.

To further confirm the photo-induced generation of $[Ru(mptpy)_2]^{5+}$ by $[S_2O_8]^{2-}$, we mixed 0.12 μM $[Ru(mptpy)_2]^{4+}$ with 33 mM $[S_2O_8]^{2-}$ and exposed the solution to room light for 30 min. The UV/Vis spectrum of the resulting solution after filtration is scaled and compared in Figure 5.3. This spectrum shows a small yet clear $[Ru(mptpy)_2]^{5+}$ absorption band after the intense $[Ru(mptpy)_2]^{4+}$ MLCT band, confirming photo-induced generation of $[Ru(mptpy)_2]^{5+}$ by $[S_2O_8]^{2-}$.

5.2.2 Time-resolved fluorescence decay measurements

Error! Bookmark not defined. The present section focuses on the first step of this overall water oxidation reaction, i.e. elucidation of the quenching mechanism of the excited state of $[Ru(mptpy)_2]^{4+}$ and electron transfer dynamics of the reaction:

$$[Ru^{II}(mptpy)_2]^{4+} + h\nu + [S_2O_8]^{2-} \rightarrow [Ru^{III}(mptpy)_2]^{5+} + SO_4^{2-} + SO_4^{-\bullet} \qquad (5.1)$$

Table 5.1. Results of Kinetics Fitting of the $\{[Ru(mptpy)_2]^{4+}\ldots([S_2O_8]^{2-})_n\}$ (n = 0, 1, 2).

CH_3CN [a]	0%	10%	20%	30%
$_0$ (ns) [b]	174	176	182	182
k_q (M^{-1} s^{-1}) [c]	$(4.1\pm0.2)\times10^7$	$(0\pm1.5)\times10^6$	$(1.4\pm0.8)\times10^7$	$(0\pm5.3)\times10^6$
$_1 = 1/k_1$ (ns)	298 ± 2	620 ± 7	803 ± 9	912 ± 7
$_2 = 1/k_2$ (ns)	149 ± 1	310 ± 4	402 ± 5	456 ± 4
K_1 (M^{-1}) [e]	$(8.9\pm0.1)\times10^3$	$(1.60\pm0.04)\times10^4$	$(1.35\pm0.04)\times10^4$	$(1.81\pm0.04)\times10^4$
K_2 (M^{-1}) [f]	180 ± 9	268 ± 17	65 ± 16	46 ± 11
G_1 (kcal/mol)[e]	-5.28 ± 0.01	-5.62 ± 0.04	-5.52 ± 0.04	-5.69 ± 0.05
G_2 (kcal/mol)[f]	-3.012 ± 0.002	-3.243 ± 0.003	-2.422 ± 0.004	-2.221 ± 0.003

[a] Volume percentage. [b] Lifetime of $[Ru(mptpy)_2]^{4+}$* in the absence of $[S_2O_8]^{2-}$. [c] bimolecular ET rate constant. [d] Unimolecular ET rate constant, k_n, for $\{[Ru(mptpy)_2]^{4+}*\ldots([S_2O_8]^{2-})_n\}$. [e] K_1 and G_1 are the equilibrium constant and binding energy, respectively, for: $[Ru(mptpy)_2]^{4+}$ + $[S_2O_8]^{2-}$ → $\{[Ru(mptpy)_2]^{4+}\ldots[S_2O_8]^{2-}\}$. [f] K_2 and G_2 are the equilibrium constant and binding energy, respectively, for: $\{[Ru(mptpy)_2]^{4+}\ldots[S_2O_8]^{2-}\}$ + $[S_2O_8]^{2-}$ → $\{[Ru(mptpy)_2]^{4+}\ldots([S_2O_8]^{2-})_2\}$

The basic theory for the fluorescence quenching mechanism has been discussed in the previous section. For $[Ru(mptpy)_2]^{4+}$, the association of two quenchers, $S_2O_8^{2-}$, is possible. Hence, the fluorescence intensity (I_t), determined by the concentration of the excited emitters and their radiative rates, can be expressed in eq. 5.2:

$$I_t = \alpha \cdot k_r \cdot \{\frac{1+K_1([S_2O_8]^{2-})\cdot e^{-\kappa_1 t} + K_1K_2([S_2O_8]^{2-})^2 \cdot e^{-\kappa_2 t}}{1+K_1([S_2O_8]^{2-}) + K_1K_2([S_2O_8]^{2-})^2}\} \cdot e^{-k_q([S_2O_8]^{2-})t} \cdot e^{-\frac{t}{\tau_0}} \quad (5.2)$$

where α is a proportional constant determined by experimental conditions, τ_0 is the intrinsic lifetime of $[Ru(mptpy)_2]^{4+}$*, and κ_n is the unimolecular electron transfer rate constant. The bracketed fraction accounts for unimolecular electron transfer effects on fluorescence decay. The three terms in the bracket describe the contribution of unimolecular electron transfer from free $[Ru(mptpy)_2]^{4+}$ (no contribution),

{[Ru(mptpy)$_2$]$^{4+}$…[S_2O_8]$^{2-}$} and {[Ru(mptpy)$_2$]$^{4+}$…([S_2O_8]$^{2-}$)$_2$}, respectively. The two additional exponential terms originate from the bimolecular quenching {k_q([S_2O_8]$^{2-}$)} and the intrinsic decay ($1/\tau_0$) processes. The fluorescence intensity at t = 0 is independent of [S_2O_8]$^{2-}$. Hence, fluorescence decay traces obtained from solutions with different concentrations of [S_2O_8]$^{2-}$ can be normalized to the same value, e.g. "1", at t = 0 for further analysis. Furthermore, the ratio of steady emission without (I_0) and with (I) quencher can be derived from integration of eq (5.2),

$$\frac{I_0}{I} = \frac{1 + K_1([S_2O_8]^{2-}) + K_1K_2([S_2O_8]^{2-})^2}{\frac{1}{1 + k_q\tau_0([S_2O_8]^{2-})} + \frac{K_1([S_2O_8]^{2-})}{1 + \tau_0\{\kappa_1 + k_q([S_2O_8]^{2-})\}} + \frac{K_1K_2([S_2O_8]^{2-})^2}{1 + \tau_0\{\kappa_2 + k_q([S_2O_8]^{2-})\}}} \quad (5.3)$$

Five of the fourteen time-resolved fluorescence decays of samples in aqueous solution with varying amounts of [S_2O_8]$^{2-}$ were selected and compared in Figure 5.5. Those kinetics traces are representative of the general trend seen for these solutions. In the presence of [S_2O_8]$^{2-}$, the fluorescence intensity is quenched. According to eq (5.2), these kinetics are governed by the same set of parameters (k_q, κ_1, κ_2, K_1 and K_2) with varying concentrations of [S_2O_8]$^{2-}$. A global-fitting technique was performed to retrieve the values of the parameters in eq 5.2. To reduce the uncertainty of the fitting, we set a constraint that the electron transfer rate in {[Ru(mptpy)$_2$]$^{4+}$…([S_2O_8]$^{2-}$)$_2$} is twice that of {[Ru(mptpy)$_2$]$^{4+}$…[S_2O_8]$^{2-}$}. This assumption is reasonable because the interaction between [Ru(mptpy)$_2$]$^{4+}$ and [S_2O_8]$^{2-}$ is weak as mentioned above. With respect to {[Ru(mptpy)$_2$]$^{4+}$…[S_2O_8]$^{2-}$}, the association of the second [S_2O_8]$^{2-}$ with {[Ru(mptpy)$_2$]$^{4+}$…([S_2O_8]$^{2-}$)$_2$} provides another unperturbed electron accepting channel. Indeed, the computational results give 199.4 ns and 108.4 ns for $1/\kappa_1$ and $1/\kappa_2$, further supporting the above assumption.[7] Under this assumption, the kinetic traces are well fit to

eq 5.2, as shown in Figure 5.5. The data for solutions containing 10-30 % CH_3CN were fitted in the same manner and the fitting parameters are summarized in Table 5.1.

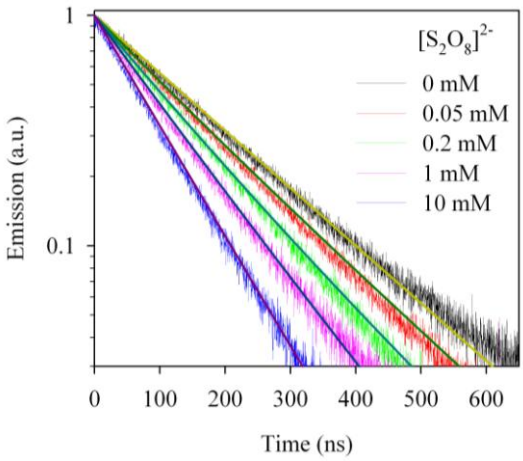

Figure 5.5. Fluorescence decay of $[Ru(mptpy)_2]^{4+}$ and $[Ru(mptpy)_2]^{4+}/[S_2O_8]^{2-}$ solutions. Samples contain the same amount (5 μM) of $[Ru(mptpy)_2]^{4+}$ but increasing amounts of $[S_2O_8]^{2-}$. Solid lines are fits to equation 5.2.

Additionally, all fluorescence intensities decay by more than 97% by the end of the measurement time window (700 ns). Integration of each kinetic trace over the spectral window of 640 – 720 nm yields a good description of the steady emission. Hence, those fourteen fluorescence decays were normalized and integrated to generate a SV plot as shown in Figure 5.6. The SV plot significantly deviates from linearity and curves downward, indicating the formation of ground-state ion pairs. Similar results were found for solutions containing 10-30 % CH_3CN, which are shown in Figure 5.6 as well. Those SV plots can be well-fitted by 5.3 using the fitting parameters obtained from the global fitting of the kinetic traces (Table 5.1). As seen from the SV plot in Figure 5.6, the quenching efficiency is smaller (<50 %) compared to that of $[Ru(bpy)_2]^{2+}$*

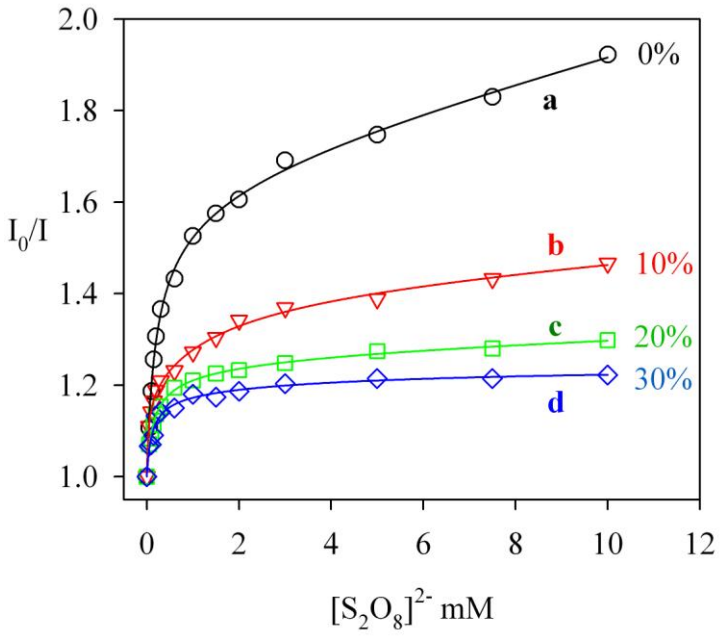

Figure 5.6. Stern-Volmer plots for solutions containing (a) 0%, (b) 10%, (c) 20% and 30% CH_3CN . All solutions contained 5 μM $[Ru(mptpy)_2]^{4+}$ and were purged with N_2. Solid curves are fits according to 5.3.

The equilibrium constants K_1 and K_2 resulting from the fittings can be used to estimate the binding energy of $\{[Ru(mptpy)_2]^{4+}\ldots([S_2O_8]^{2-})_n\}$ (n = 1, 2) according to the relationship between free energy change and equilibrium constant, $\Delta G^q = -nRT\ln K$. The estimated values are listed in Table 5.1. With such high binding energies, we expected the formation of both 1:1 and 1:2 complexes in solution. The distribution of $\{[Ru(mptpy)_2]^{4+}\ldots([S_2O_8]^{2-})_n\}$ (n = 0, 1, 2) in solution (x_n, the mole fraction) can be estimated using eq 4.6. For this specific case, eq 4.6 is reduced to eq 5.4,

$$x_n = \frac{\left(\prod_{i=0}^{n} K_i\right)\cdot\left([S_2O_8]^{2-}\right)^n}{1+K_1\left([S_2O_8]^{2-}\right)+K_1K_2\left([S_2O_8]^{2-}\right)^2} \qquad (5.4)$$

Where K_1 and K_2 are equilibrium constants for the 1:1 and 1:2 complexes (K_0 = 0). Shown in Figure 5.7, for example, is a typical simulation of the percentage of those species in aqueous solution. The percentage of free $[Ru(mptpy)_2]^{4+}$ decreases quickly with increased $[S_2O_8]^{2-}$, with ~10 % left at 0.6 mM $[S_2O_8]^{2-}$. Distribution curves for solutions with different amounts of CH_3CN show similar results due to similar values of K_1 and K_2. Hence, in our experiments, quenching processes occur mainly via the formation of the complexes $\{[Ru(mptpy)_2]^{4+}\ldots([S_2O_8]^{2-})_n\}$ (n =1, 2).

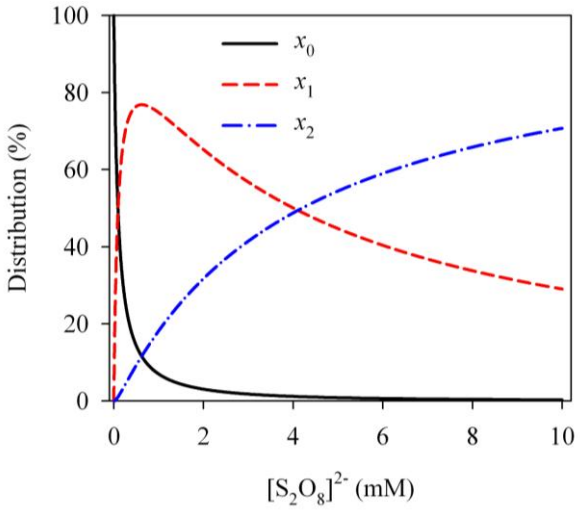

Figure 5.7. Distribution of $[Ru(mptpy)_2]^{4+}$ (x_0, black solid line), $\{[Ru(mptpy)_2]^{4+}\ldots[S_2O_8]^{2-}\}$ (x_1, red dashed line), and $\{[Ru(mptpy)_2]^{4+}\ldots([S_2O_8]^{2-})_2\}$ (x_2, blue dash-dot line) in aqueous solution.

The bimolecular rate constants decrease with increased CH_3CN, which is consistent with the reported results using $[Ru(bpy)_3]^{2+}$ and the computational data.[6,7,17]

The estimated unimolecular electron transfer lifetime in $\{[Ru(mptpy)_2]^{4+}\ldots[S_2O_8]^{2-}\}$, $1/\kappa_1$, is 298 ns in aqueous solution. The presence of CH_3CN

reduces the rate by a factor of 3 from pure aqueous solution to a solution containing 30 % CH_3CN. Furthermore, the rate of the bimolecular quenching process depends on $k_q([S_2O_8]^{2-})$. The maximum $[S_2O_8]^{2-}$ concentration used is 0.01 M, giving a $k_q([S_2O_8]^{2-})$ of 4.1×10^5 s^{-1} in aqueous solution. This value is about 12% of the κ_1 or 6 % of κ_2 in the same system. The bimolecular quenching process contributes even less to the total quenching in the presence of CH_3CN. Indeed, the contribution from the bimolecular pathway to the total fluorescence quenching is so small that its rate is not well determined in the fit, yielding rate constants with large errors as shown in Table 5.1. Under these conditions, the formation of an ion pair indeed facilitates generation of the oxidant $[Ru(mptpy)_2]^{5+}$.

5.2.3 $[Ru(mptpy)_2]^{4+}$ in solution-based water oxidation system

$[Ru(mptpy)_2]^{4+}$ was tested in the established three-component solution system as described in previous chapters. The main problem for $[Ru(mptpy)_2]^{4+}$ in these water oxidation systems is the precipitation by the addition of excess $S_2O_8^{2-}$. Precipitation can reduce the overall performance of the three-component systems. However, using $[Ru(mptpy)_2]^{4+}$ / $[S_2O_8]^{2-}$ suspension, Ru_4POM is confirmed to be photocatalytic active with a TON up to 180, as shown in Figure 5.8. This TON is similar to that from systems using the totally soluble $[Ru(bpy)_3]^{2+}$ photosensitizer. In this regard, one can expect that $[Ru(mptpy)_2]^{4+}$ can work much better after overcoming the precipitation problem. This is also consistent with our studies on the charge-transfer dynamics, showing that ion-pair formation facilitates the generation of oxidant.

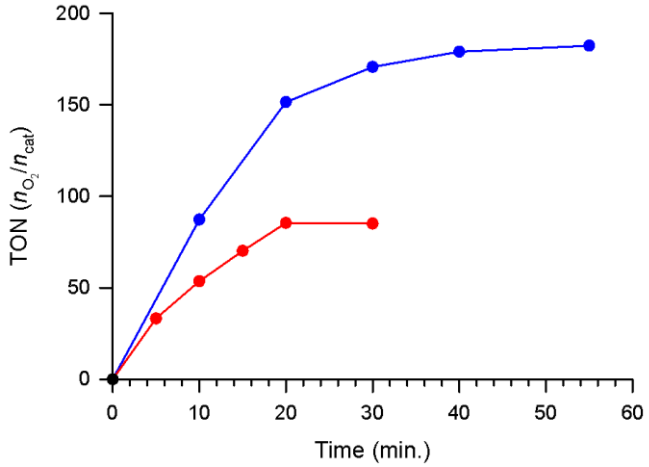

Figure 5.8. Kinetics of O_2 formation in the photocatalytic system with different concentrations of $Na_2S_2O_8$: 2.5 (red) and 5 mM (blue). 0.2 mM mM $[Ru(mptpy)_2]^{5+}$, 20 mM sodium phosphate buffer (initial pH 7.2), 2 μM Ru_4POM.

5.3 Microheterogeneous system.

Photosensitizers based on ruthenium pyridyl derivatives and other organic compounds immobilized on nanoporous semiconductor metal oxide thin films (typically TiO_2) are widely used for solar energy conversion in dye-sensitized solar cells.[18-20] In these systems, the photoinduced ultrafast electron injection from the anchoring dye to the TiO_2 nanoporous substrate[21,22] results in a *unitary* absorbed-photon-to-oxidant conversion efficiency. More importantly, the back electron transfer from the TiO_2 conduction band to the attached dye cation is much slower, resulting in a long-lived charge separation state allowing for further useful reactions. For this reason, we replaced the $[Ru(bpy)_3]^{2+}$ with a TiO_2/Ru470 nanocomposite suspension in the same solution system. However, no O_2 formation was detected.

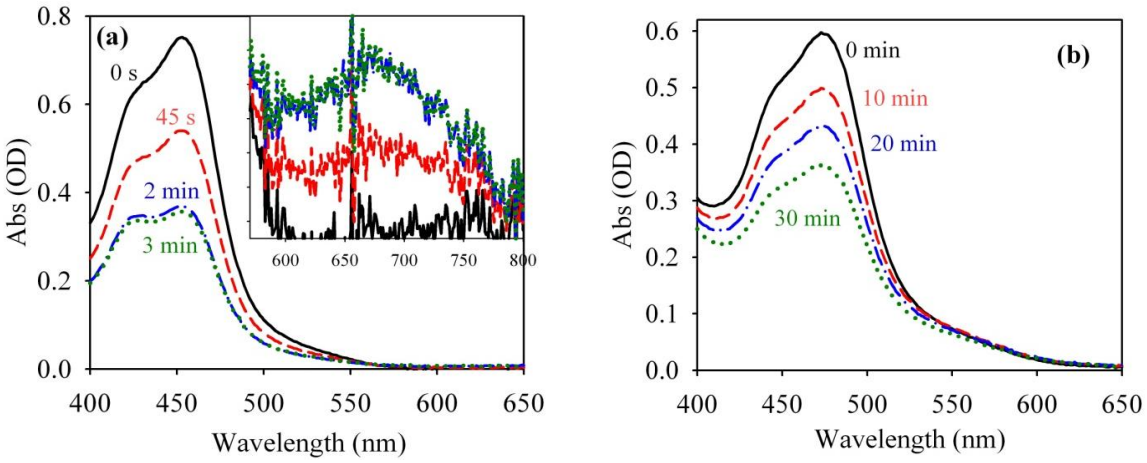

Figure 5.9. (a) UV-Vis absorption spectra of $[Ru(bpy)_3]^{2+}$ in the presence of 0.5 mM $[S_2O_8]^{2-}$ and 20 mM of pH 7.2 phosphate buffer under illumination for different lengths of time: 0 (solid), 0.75 (dashed), 2 (dash-dot), and 3 (dotted) min. Illumination: 420-520 nm, 50 mW. (b) UV-Vis absorption spectra of TiO_2/Ru470 solution (pH 1.2) in the presence of 1.3 mM $[S_2O_8]^{2-}$ under illumination for different times: 0 (solid), 10 (dashed), 20 (dash-dot), and 30 min (dotted).

To understand the negative results, we monitored the static UV-vis absorption spectra of both the $[Ru(bpy)_3]^{2+}/[S_2O_8]^{2-}$ (Figure 5.9a) and $[S_2O_8]^{2-}/TiO_2$/Ru470 nanocomposite (Figure 5.9b) solutions in the absence of the WOC after varying illumination times. The light illumination has an immediate effect on the $[Ru(bpy)_3]^{2+}/[S_2O_8]^{2-}$ system (Figure 5.9a)., converting almost all the $[Ru(bpy)_3]^{2+}$ into $[Ru(bpy)_3]^{3+}$ within 2 min. The inset in Figure 5.9a shows the accumulation of $[Ru(bpy)_3]^{3+}$, which has a small extinction coefficient at 670 nm (ε_{670} = 4.2 × 10^2 M^{-1} cm^{-1}). However, in the $[S_2O_8]^{2-}/TiO_2$/Ru470 system with similar concentrations of dye and persulfate, the light has very little effect on the UV-Vis spectra within 3 min (data not shown). A slow bleaching of the dye in $[S_2O_8]^{2-}/TiO_2$/Ru470 was observed at

increased $[S_2O_8]^{2-}$ concentrations and after longer illumination times (Figure 5.9b). An electron injected from the optically excited Ru470 into the TiO_2 colloid can be scavenged by $[S_2O_8]^{2-}$ around the TiO_2, in competition with both back recombination with the attached Ru470 cation, and electron relaxation and diffusion processes in the nanoparticles. The bleaching is likely due to the slow heterogeneous reaction between TiO_2 and $[S_2O_8]^{2-}$, which may be much slower than the back electron transfer. At neutral pH, this electron transfer is further slowed down by the repulsion between the negatively-charged TiO_2 surface (point of zero charge, 3.5[23,24]) and the negative $[S_2O_8]^{2-}$. Therefore, the use of TiO_2/Ru470 in the system has no advantages for O_2 formation. However, in principle, this drawback can be removed or at least alleviated in a heterogeneous system using a photoanode with a well-defined structure.

5.4 Conclusion

In this chapter, two other systems utilizing a potentially better photosensitizer and a better oxidant generator are tested for improved photocatalytic performance based on the established homogeneous water oxidation systems. The results indicate that a structurally well-defined photoanode consisting of the WOC and sensitizer on a TiO_2 nanocrystalline thin film should be a viable approach for photodriven water oxidation.

5.5 References

(1) Besson, C.; Huang, Z.; Geletii, Y. V.; Lense, S.; Hardcastle, K. I.; Musaev, D. G.; Lian, T.; Proust, A.; Hill, C. L. *Chem. Commun.* **2010**, 2784.

(2) Geletii, Y. V.; Huang, Z.; Hou, Y.; Musaev, D. G.; Lian, T.; Hill, C. L. *J. Am. Chem. Soc.* **2009**, *131*, 7522.

(3) Geletii, Y. V.; Yin, Q. S.; Hou, Y.; Huang, Z. Q.; Ma, H. Y.; Song, J.; Besson, C.; Luo, Z.; Cao, R.; O'Halloran, K. P.; Zhu, G. B.; Zhao, C. C.; Vickers, J. W.; Ding, Y.; Mohebbi, S.; Kuznetsov, A. E.; Musaev, D. G.; Lian, T. Q.; Hill, C. L. *Isr J Chem* **2011**, *51*, 238.

(4) Huang, Z. Q.; Luo, Z.; Geletii, Y. V.; Vickers, J. W.; Yin, Q. S.; Wu, D.; Hou, Y.; Ding, Y.; Song, J.; Musaev, D. G.; Hill, C. L.; Lian, T. Q. *J Am Chem Soc* **2011**, *133*, 2068.

(5) Puntoriero, F.; Ganga, G. L.; Sartorel, A.; Carraro, M.; Scorrano, G.; Bonchio, M.; Campagna, S. *Chem. Commun.* **2010**, *46*, 4725.

(6) Kaledin, A. L.; Huang, Z.; Geletii, Y. V.; Lian, T.; Hill, C. L.; Musaev, D. G. *J. Phys. Chem. A* **2010**, *114*, 73.

(7) Kaledin, A. L.; Huang, Z.; Yin, Q.; Dunphy, E. L.; Constable, E. C.; Housecroft, C. E.; Geletii, Y. V.; Lian, T.; Hill, C. L.; Musaev, D. G. *J. Phys. Chem. A* **2010**, *114*, 6284.

(8) Huang, Z.; Geletii, Y. V.; Wu, D.; Anfuso, C. L.; Musaev, D. G.; Hill, C. L.; Lian, T. *Proc. SPIE* **2011**, *8109*, 810903.

(9) Houamer-Rassin, C.; Chaignon, F.; She, C.; Stockwell, D.; Blart, E.; Buvat, P.; Lian, T.; Odobel, F. *J Photoch Photobio A* **2007**, *192*, 56.

(10) Maestri, M.; Armaroli, N.; Balzani, V.; Constable, E. C.; Thompson, A. M. W. C. *Inorg Chem* **1995**, *34*, 2759.

(11) Bonhote, P.; Moser, J. E.; Humphry-Baker, R.; Vlachopoulos, N.; Zakeeruddin, S. M.; Walder, L.; Gratzel, M. *J Am Chem Soc* **1999**, *121*, 1324.

(12) Constable, E. C.; Thompson, A. M. W. C. *J Chem Soc Dalton* **1994**, 1409.

(13) Beves, J. E.; Dunphy, E. L.; Constable, E. C.; Housecroft, C. E.; Kepert, C. J.; Neuburger, M.; Price, D. J.; Schaffner, S. *Dalton T* **2008**, 386.

(14) Cheung, S. T. C.; Fung, A. K. M.; Lam, M. H. W. *Chemosphere* **1998**, *36*, 2461.

(15) Pechy, P.; Rotzinger, F. P.; Nazeeruddin, M. K.; Kohle, O.; Zakeeruddin, S. M.; Humphrybaker, R.; Gratzel, M. *J Chem Soc Chem Comm* **1995**, 65.

(16) Zakeeruddin, S. M.; Nazeeruddin, M. K.; Pechy, P.; Rotzinger, F. P.; HumphryBaker, R.; Kalyanasundaram, K.; Gratzel, M.; Shklover, V.; Haibach, T. *Inorg Chem* **1997**, *36*, 5937.

(17) White, H. S.; Becker, W. G.; Bard, A. J. *J. Phys. Chem.* **1984**, *88*, 1840.

(18) Oregan, B.; Gratzel, M. *Nature* **1991**, *353*, 737.

(19) Gratzel, M. *Nature* **2001**, *414*, 338.

(20) Stockwell, D.; Yang, Y.; Huang, J.; Anfuso, C.; Huang, Z. Q.; Lian, T. Q. *J Phys Chem C* **2010**, *114*, 6560.

(21) Anderson, N. A.; Lian, T. *Coordin Chem Rev* **2004**, *248*, 1231.

(22) Anderson, N. A.; Lian, T. Q. *Annu Rev Phys Chem* **2005**, *56*, 491.

(23) Parks, G. A.; Bruyn, P. L. D. *J Phys Chem-Us* **1962**, *66*, 967.

(24) Pechenyuk, S. I. *Russ Chem B* **1999**, *48*, 1017.

Part IV: Photophysics of Polyoxometalates

CHAPTER

6

Photophysics of Polyoxometalate-based Chromophores

Unpublished results

Abstract: Understanding the photophysics of polyoxometalates (POMs) is necessary for clarifying the charge transfer dynamics in both homogeneous multiple-component systems and heterogeneous dyadic or triadic nanocomposite electrodes. More importantly, it is crucial to realize another approach to construct oxidatively stable photodriven water oxidation catalytic systems: all inorganic semiconductor metal oxide-metal-water oxidation catalyst (SMO-M-WOC) triads. This part (this and the next chapters) describes our efforts to understand the fundamental photophysics of the polyoxometalates. This chapter summarizes our investigation into several coloured polyoxometalates, including Ru_4POM WOC, a giant $\{Mo_{72}V_{30}\}$ keplerate and $[Co^{II}_2(H_2O)W_{11}O_{39}]^{8-}$.

6.1 Introduction

Robust chromophores in covalent connection with water oxidation catalysts (WOCs) serving as photocatalytic charge-separation centers to drive the multi-electron thermodynamic limiting steps in artificial photosynthesis systems (water splitting and CO_2 reduction) are highly desired. [1-14] In developing robust all-inorganic photocatalytic units for water oxidation and CO_2 reduction, hetero-bimetallic chromophores anchored on mesoporous silica substrates (MCM-41) have been reported recently.[1-13] Some of these all-inorganic colored complexes have been shown to exhibit photocatalytic activities under visible light illumination.[1,11,14-17] These heterobinuclear chromophores (M1-O-M2 structure, where M1=Ti(IV) or Zr(IV); M2=Ce(III), Cr(III), Co(II), Sn(II), Cu(I)) feature enhanced visible absorbtivity originating from a broad metal-to-metal

charge transfer (MMCT) absorption. The lifetime of the MMCT electronic excited state in Ti(IV)-O-Mn(II) has been reported to be ~2 μs.[10]

In addition, it was reported recently that Ce(III) directly supported on a TiO_2 substrate forms strong charge transfer complexes with absorption bands extending to 620 nm due to the Ce(III)-O-Ti(IV) MMCT transition.[18] This band in Ce-TiO_2 nanoparticles is further shifted to the red compared to those in zeolite pores, presumably because of the presence of lower energy Ti(IV) states in TiO_2 than in isolated Ti(IV).[18] TiO_2-supported Fe(III),[11,19] Cr[12] and Cu[17] MMCT structures with enhanced absorption extending to ~600 nm have been also reported. It is worthy to note that similar charge transfer complexes, TiO_2/Fe(II)$(CN)_6$ and TiO_2/catechol, with molecular adsorbates have been studied since the 1980s, showing that the charge separated states are long lived with lifetimes extending out to ms. [20-24]

All these results suggest the possibility of constructing all-inorganic light-harvesting charge transfer triads by interfacing our molecular POM-based WOCs with the reported MMCT chromophore. This is similar to the reported structure TiOCr–IrO_2/MCM-41 by Frei et. al.[6,13]

More recently, MMCT complexes between the Ce(III) and Keggin POMs with absorption bands extending to 550 nm were also reported. [9] Our all-inorganic WOCs are composed of multiple d-electron metal oxide clusters such as Ru_4O_4 (in Ru_4POM) and Co_4O_4 (in Co_4POM), multiply ligated and stabilized by polyoxometalate ligands.[25-29] The POM-based WOCs can be chromophores. For example, the extinction coefficient of Ru_4POM at pH 7 at 450 nm is ~12,000 M^{-1} cm^{-1}. [30] The wide spectral range and the high extinction coefficient of Ru_4POM are comparable to those of many ruthenium

polybipyridyl photosensitzers.[31,32] This also suggests the possibility of constructing photoactive dyads composed of nanoporous SMO and POM-based molecular WOC/chromophores.

In addition to the highly absorbing attributes of many transition-metal substituted POM molecules, their electronic excited state lifetime is another crucial factor for making a useful photocatalytic unit when anchored on SMO substrates. Long-lived charge separation states are always expected to match the slow multiple-electron water oxidation kinetics. Understanding the photophysics of polyoxometalates (POMs) is also necessary for clarifying the charge transfer dynamics in both homogeneous multiple-component systems and heterogeneous dyadic or triadic nanocomposite electrodes.

Although the redox chemistry of polyoxometalates has been extensively studied, their photophysics are barely investigated.[33,34] This chapter briefly summarizes our investigation into several coloured polyoxometalates, including the Ru_4POM WOCs,[35-37] a giant $\{Mo_{72}V_{30}\}$ keplerate,[38] and a $[Co^{II}_2(H_2O)W_{11}O_{39}]^{8-}$.[39]

6.2 Results and Discussion

6.2.1 Ru_4POM

Our initial attention focuses on Ru_4POM and Ru_4-(P)-POM (for crystal structures see Figure 3.1, in Chapter 3), two carbon-free molecules that have been demonstrated to be efficient WOCs and extensively studied by many electrochemical and computational techniques. [27,35,36,40-42] However, their photophysics have not been investigated extensively yet.

Shown in Figure 6.1 is a UV-Vis spectrum of Ru_4POM in a 0.1 M HCl aqueous solution. It is important to note that the optical absorption properties of Ru_4POM highly depend on pH and oxidation states.[36,37]

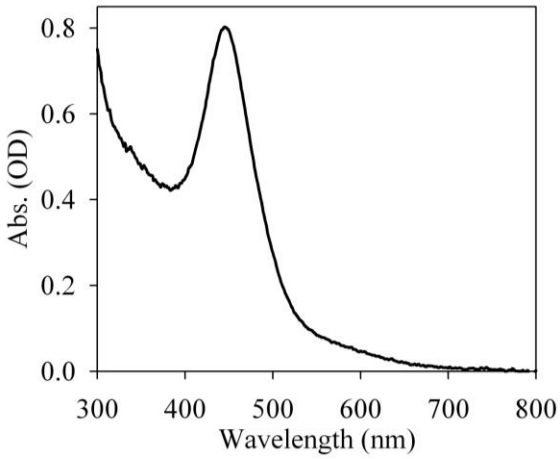

Figure 6.1 UV-Vis spectra of Ru_4POM in 0.1 M HCl aqueous solution.

The excited state dynamics were investigated by femtosecond visible pump-probe spectroscopy. The transient visible absorption spectra of Ru_4POM in 0.1 M HCl after 400 nm excitation (Figure 6.2a) show a new broad absorbing species with maximum at ~530 nm. This might indicate a Ru metal-to-polyoxometalate charge transfer (MPCT) process (which will be more clearly seen in the next chapter), where the absorption feature can be attributed to the W(V) d-d transitions and W(V)-W(VI) intervalence charge transfer (IVCT) transitions in the reduced anionic ligand.[43-48] The kinetics of the formation and decay of this photo-induced absorption feature can be monitored at 530 nm. As shown in Figure 6.2b, the formation time can be considered as instantaneous within the time resolution of this measurement (~150 fs). However, this excited state is short lived, decaying with a lifetime of ~2 ps.

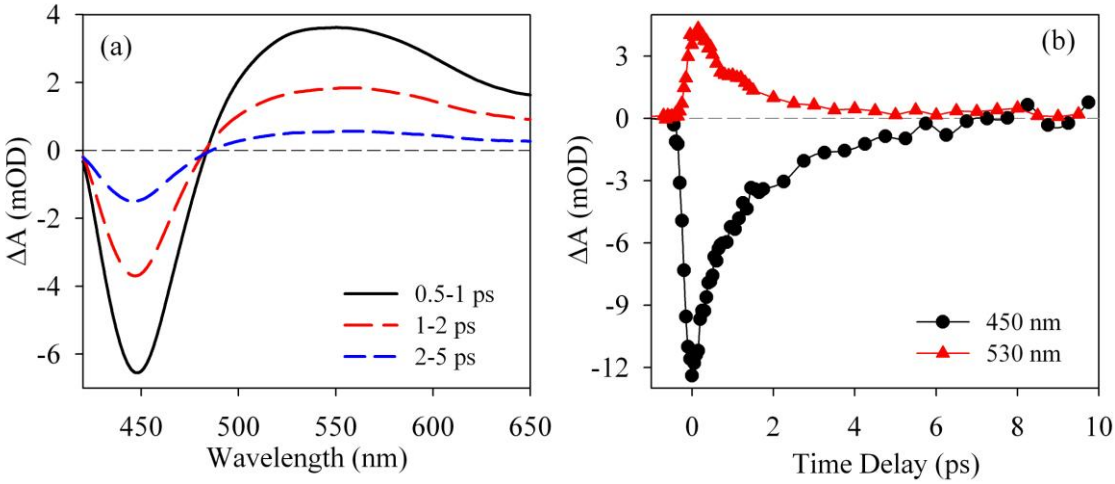

Figure 6.2 Transient absorption studies of Ru_4POM in 0.1 M HCl. (a) Average spectra at different time windows; and (b) kinetics probed at 450 (black dots) and 530 nm (red triangles) after 400 nm excitation.

In order to lengthen the lifetime of the excited states, we loaded this chromophore onto nanoporous substrates (TiO_2 and ZrO_2) in 0.1 M HCl. However, the transient spectra and kinetics are unaffected. In addition, the transient results strongly depend on the pH (or protonation states of the WOCs). In neutral pH, there are no detectable transient signals after 400 nm excitation either in solution or on nanoporous substrates. Under all circumstances, the Ru_4-(P)-POM shows similar spectral dynamics after photoexcitation.

We have screened a wide range of known, colored transition metal-substituted POMs with reasonable extinction coefficients in the visible range for sunlight harvesting. Our results show that almost all candidates have extremely-short excited state lifetimes (< 2 ps). However, there are two exceptions that will be presented in the next two sections.

6.2.2 $\{Mo_{72}V_{30}\}$ keplerate

$(Na_8K_{16}(VO)(H2O)_5[K_{10}\{(Mo)Mo_5O_{21}(H_2O)_3(SO_4)\}_{12}(VO)_{30}\ (H_2O)_{20}]\bullet 150H_2O$ is a giant $\{Mo_{72}V_{30}\}$ keplerate polyoxometalate complex of several nanometers in diameter. Unlike other common "nanoclusters", this nanosized metal oxide cluster is an actual molecule. Therefore, its molecular properties can be more easily altered and determined far more rigorously and precisely.

Figure 6.3 shows the UV-Vis spectrum of this giant POM molecule. This nanosized molecule has an enormous extinction coefficient in the visible region, of around 71,000 $M^{-1}cm^{-1}$ at 510 nm, making it a plausible light sensitizer despite its huge molecular weight.[38]

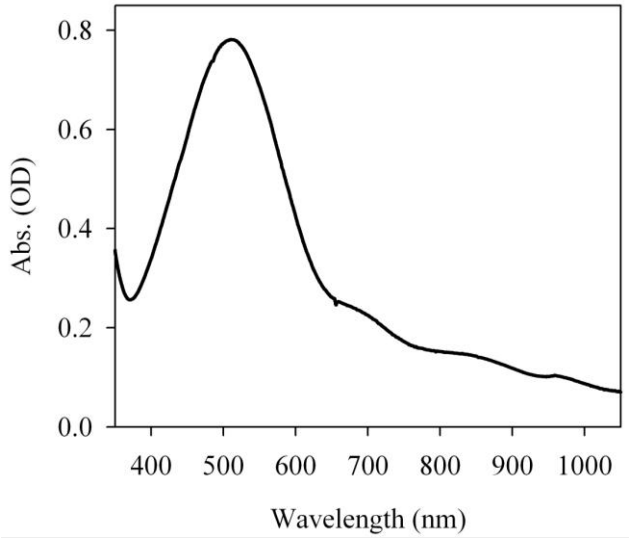

Figure 6.3 UV-Vis spectrum of the $\{Mo_{72}V_{30}\}$ keplerate in aqueous solution.

Transient absorption spectra of the $\{Mo_{72}V_{30}\}$ keplerate in aqueous solution after 400 nm excitation show two clear spectral features: a ground state bleach at 510 nm and an absorbing species at 650 nm (Figure 6.4a). These instantaneously formed excited-state

features have a lifetime of ~10 ps, as shown in Figure 6.4b. In addition, the immobilization of this molecule onto a nanoporous TiO_2 substrate has no effect on the transient results. Although this lifetime is markedly longer than those of Ru_4-based WOCs and those of many other POM chromophores we have studied, this $\{Mo_{72}V_{30}\}$ keplerate still requires ultrafast charge extraction (< 10 ps) to the semiconductor-metal-oxide electrode substrate to create long-lived charge-separation states for further solar fuel production. Therefore, the introduction of intramolecular charge trapping centers in all these POM chromophores is necessary for lengthening the excited state lifetimes.

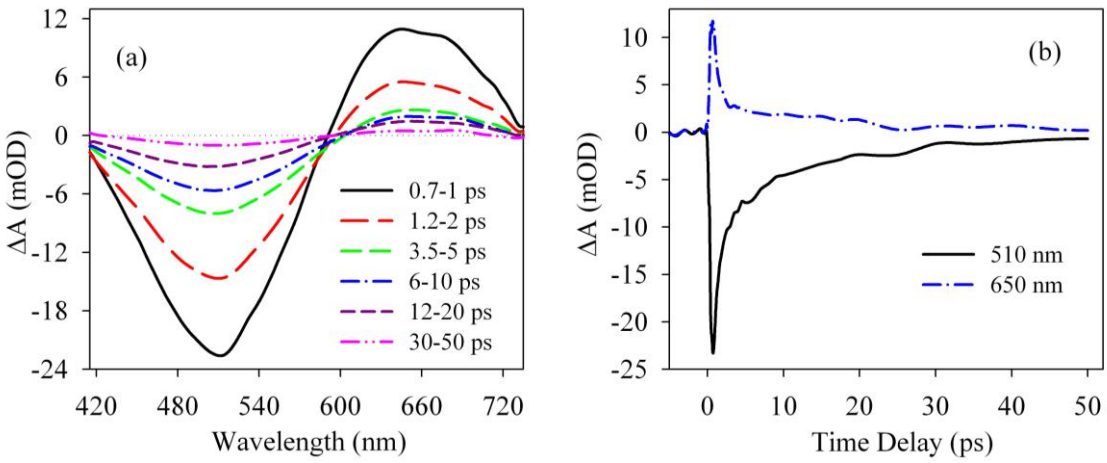

Figure 6.4 Transient absorption studies of the $\{Mo_{72}V_{30}\}$ keplerate in aqueous solution. (a) Average spectra at different time windows; and (b) kinetics probed at 510 (black line) and 650 nm (blue dot-dashed line) after 400 nm excitation.

6.2.3 $[Co^{II}_2(H_2O)W_{11}O_{39}]^{8-}$

The other POM molecule we have studied that has a relatively long-lived excited state is the dicobalt Keggin anion (with one central Co) $[Co^{II}_2(H_2O)W_{11}O_{39}]^{8-}$ which has a Co(II)Co(II) oxidation state (and hence this molecule is denoted as Co(II)Co(II)). It was

originally published in 1956.[39] This polyoxoanion has a clear absorption feature in the visible region with an extinction coefficient of around 1000 $M^{-1}cm^{-1}$ at 400 nm, as shown in Figure 6.5. Its one-electron-oxidized counterpart, $[Co^{II}Co^{III}(H_2O)W_{11}O_{39}]^{7-}$ (denoted as Co(II)Co(III)), has distinct visible absorption features, exhibiting more intense absorbance below 500 nm and another absorption band after 700 nm. This is probably indicative of the different natures of the possible MPCT transition in Co(II)Co(II) and the inter-valence-charge transfer in Co(II)Co(III) molecules.

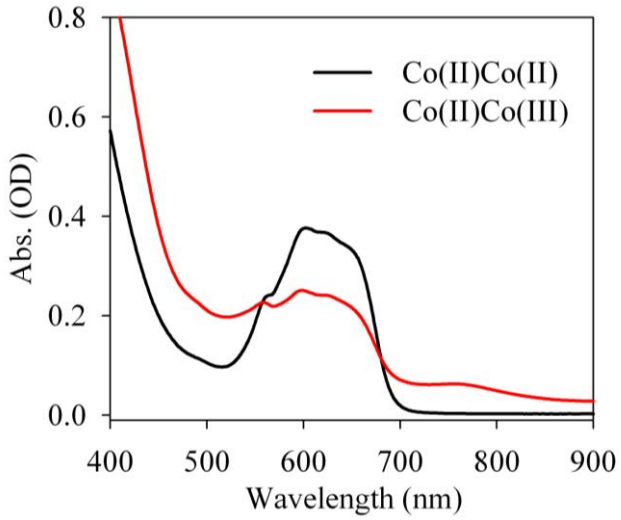

Figure 6.5 UV-Vis spectra of the $[Co^{II}_2(H_2O)W_{11}O_{39}]^{8-}$ (Co(II)Co(II), black) and $[Co^{II}Co^{III}(H_2O)W_{11}O_{39}]^{7-}$ (Co(II)Co(III), red) in aqueous solution.

For the Co(II)Co(II) molecule, photoexcitation at 400 nm results in an intense broad absorption band centered at 475 nm and another absorbing feature above 675 nm, in addition to the ground state bleach at 620 nm, as shown in Figure 6.6a. These two new absorbing bands in the excited state transient absorption spectra show similar features to the ground state absorption features of its one-electron-oxidized counterpart,

Co(II)Co(III). This suggests a photo-induced electron injection into the polytungstate ligand, and hence, a MPCT transition, resulting in a Co(II)Co(III) inter-valence-charge transfer (IVCT) chromophoric unit. Most significantly, the excited-state lifetime of this species is over 100 ps (Figure 6.6c), which is by far the longest we have seen in any POM chromophore so far.

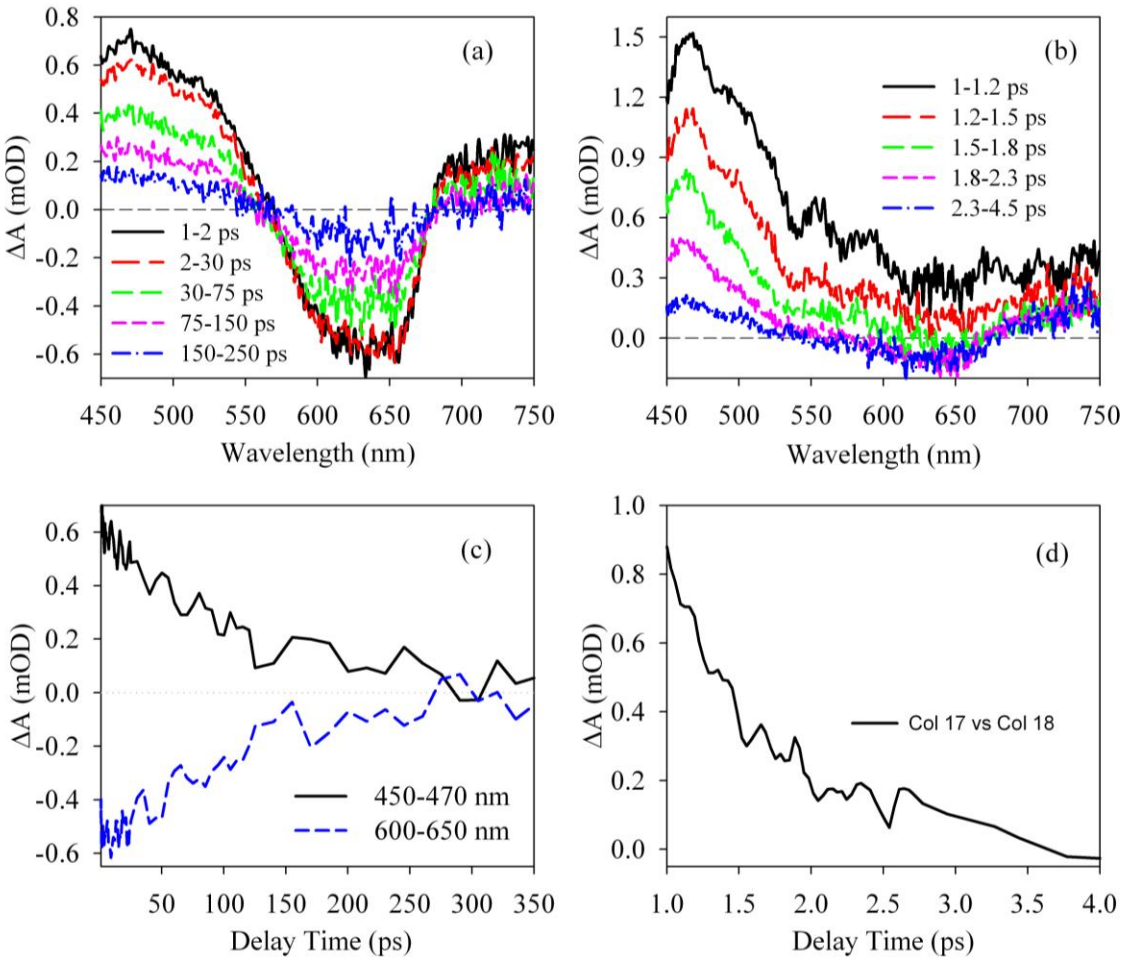

Figure 6.6 Transient spectra of (a) Co(II)Co(II) and (b) Co(II)Co(III) in aqueous solution averaged over different time windows after 400 nm excitation. Transient kinetics of (c) Co(II)Co(II) (1-350 ps) and (d) Co(II)Co(III) (1-4 ps) in aqueous solution averaged over different spectral windows after 400 nm excitation.

To further confirm the distinct nature of the possible MPCT and IVCT transitions, the transient dynamics of the excited states in the Co(II)Co(III) molecule were also studied and are shown in Figure 6.6b. The transient spectra of Co(II)Co(III) molecule after optical excitation are clearly very different from those of the Co(II)Co(II) molecule with an extremely short-lived lifetime (Figure 6.6d).

6.3 Conclusion

In conclusion, this short chapter briefly summarizes our efforts in seeking long-lived polyoxometalate molecular chromophores for constructing all-inorganic photocatalytic units towards efficient solar fuel production. In addition, understanding the fundamental photophysics of polyoxometalate molecules is also crucial to clarifying the intermolecular or interfacial charge transfer dynamics in both homogeneous and heterogeneous multiple-component systems using polyoxometalate WOCs. Our investigations show that most POM chromophores are short-lived, requiring better molecular designs for ultrafast charge trapping or extraction. Furthermore, the nature of the charge transfer transition needs to be studied in more depth, which will be shown in the next chapter.

6.4 References

(1) Lin, W.; Frei, H. *J. Phys. Chem. B* **2005**, *109*, 4929.

(2) Nakamura, R.; Frei, H. *J. Am. Chem. Soc.* **2006**, *128*, 10668.

(3) Han, H.; Frei, H. *Microporous Mesoporous Mater.* **2007**, *103*, 265.

(4) Nakamura, R.; Okamoto, A.; Osawa, H.; Irie, H.; Hashimoto, K. *J. Am. Chem. Soc.* **2007**, *129*, 9596.

(5) Han, H.; Frei, H. *J. Phys. Chem.* **2008**, *112*, 8391.

(6) Han, H.; Frei, H. *J. Phys. Chem.* **2008**, *112*, 16156.

(7) Wu, X.; Weare, W. W.; Frei, H. *Dalton Trans.* **2009**, 10114.

(8) Somorjai, G. A.; Frei, H.; Park, J. Y. *J. Am. Chem. Soc.* **2009**, *131*, 16589.

(9) Takashima, T.; Nakamura, R.; Hashimoto, K. *J. Phys. Chem. C* **2009**, *113*, 17247.

(10) Cuk, T.; Weare, W. W.; Frei, H. *J. Phys. Chem. C* **2010**, *114*, 9167.

(11) Yu, H.; Irie, H.; Shimodaira, Y.; Hosogi, Y.; Kuroda, Y.; Miyauchi, M.; Hashimoto, K. *J. Phys. Chem. C* **2010**, *114*, 16481.

(12) Irie, H.; Shibanuma, T.; Kamiya, K.; Miura, S.; Yokoyama, T.; Hashimoto, K. *Appl. Catal. B* **2010**, *96*, 142.

(13) Sivasankar, N.; Weare, W. W.; Frei, H. *J. Am. Chem. Soc.* **2011**, *133*, 12976.

(14) Lin, J.; Zhang, C. C. *Phys Chem Chem Phys* **2011**, *13*, 3896.

(15) Nakamura, R.; Frei, H. *Journal of the American Chemical Society* **2006**, *128*, 10668.

(16) Han, H.; Frei, H. *J. Phys. Chem. C* **2008**, *112*, 16156.

(17) Irie, H.; Kamiya, K.; Shibanuma, T.; Miura, S.; Tryk, D. A.; Yokoyama, T.; Hashimoto, K. *J Phys Chem C* **2009**, *113*, 10761.

(18) Nakamura, R.; Okamoto, A.; Osawa, H.; Irie, H.; Hashimoto, K. *Journal of the American Chemical Society* **2007**, *129*, 9596.

(19) Dimitrijevic, N. M.; Libera, J. A.; Elam, J. W.; Sather, N. F.; Rajh, T. *Chem Mater* **2010**, *22*, 409.

(20) Lu, H.; Prieskorn, J. N.; Hupp, J. T. *J Am Chem Soc* **1993**, *115*, 4927.

(21) Vrachnou, E.; Vlachopoulos, N.; Graetzel, M. *J. Chem. Soc., Chem. Commun.* **1987**, 868.

(22) Ghosh, H. N.; Asbury, J. B.; Weng, Y.; Lian, T. *Journal of Physical Chemistry B* **1998**, *102*, 10208.

(23) Weng, Y.-X.; Wang, Y.-Q.; Asbury, J. B.; Ghosh, H. N.; Lian, T. *Journal of Physical Chemistry B* **2000**, *104*, 93.

(24) Wang, Y.; Hang, K.; Anderson, N. A.; Lian, T. *Journal of Physical Chemistry B* **2003**, *107*, 9434.

(25) Besson, C.; Huang, Z.; Geletii, Y. V.; Lense, S.; Hardcastle, K. I.; Musaev, D. G.; Lian, T.; Proust, A.; Hill, C. L. *Chem. Commun.* **2010**, 2784.

(26) Geletii, Y. V.; Huang, Z.; Hou, Y.; Musaev, D. G.; Lian, T.; Hill, C. L. *J. Am. Chem. Soc.* **2009**, *131*, 7522.

(27) Geletii, Y. V.; Yin, Q. S.; Hou, Y.; Huang, Z. Q.; Ma, H. Y.; Song, J.; Besson, C.; Luo, Z.; Cao, R.; O'Halloran, K. P.; Zhu, G. B.; Zhao, C. C.; Vickers, J. W.; Ding, Y.; Mohebbi, S.; Kuznetsov, A. E.; Musaev, D. G.; Lian, T. Q.; Hill, C. L. *Isr J Chem* **2011**, *51*, 238.

(28) Huang, Z. Q.; Luo, Z.; Geletii, Y. V.; Vickers, J. W.; Yin, Q. S.; Wu, D.; Hou, Y.; Ding, Y.; Song, J.; Musaev, D. G.; Hill, C. L.; Lian, T. Q. *J Am Chem Soc* **2011**, *133*, 2068.

(29) Puntoriero, F.; Ganga, G. L.; Sartorel, A.; Carraro, M.; Scorrano, G.; Bonchio, M.; Campagna, S. *Chem. Commun.* **2010**, *46*, 4725.

(30) Geletii, Y. V.; Besson, C.; Hou, Y.; Yin, Q.; Musaev, D. G.; Quinonero, D.; Cao, R.; Hardcastle, K. I.; Proust, A.; Kögerler, P.; Hill, C. L. *J. Am. Chem. Soc.* **2009**, *131*, 17360.

(31) Kalyanasundaram, K. *Coord. Chem. Rev.* **1982**, *46*, 159.

(32) Kalyanasundaram, K.; Grätzel, M. *Coord. Chem. Rev.* **1998**, *77*, 347.

(33) Duncan, D. C.; Netzel, T. L.; Hill, C. L. *Inorg Chem* **1995**, *34*, 4640.

(34) Fox, M. A.; Duncan, D. C. *J Phys Chem A* **1998**, *102*, 4559.

(35) Besson, C.; Huang, Z. Q.; Geletii, Y. V.; Lense, S.; Hardcastle, K. I.; Musaev, D. G.; Lian, T. Q.; Proust, A.; Hill, C. L. *Chem Commun* **2010**, *46*, 2784.

(36) Geletii, Y. V.; Besson, C.; Hou, Y.; Yin, Q. S.; Musaev, D. G.; Quinonero, D.; Cao, R.; Hardcastle, K. I.; Proust, A.; Kogerler, P.; Hill, C. L. *J Am Chem Soc* **2009**, *131*, 17360.

(37) Geletii, Y. V.; Koegerler, P.; Hillesheim, D. A.; Musaev, D. G.; Hill, C. L.; Botar, B. *Angew Chem Int Edit* **2008**, *47*, 3896.

(38) Botar, B.; Kogerler, P.; Hill, C. L. *Chem Commun* **2005**, 3138.

(39) Baker, L. C. W.; Mccutcheon, T. P. *J Am Chem Soc* **1956**, *78*, 4503.

(40) Geletii, Y. V.; Huang, Z. Q.; Hou, Y.; Musaev, D. G.; Lian, T. Q.; Hill, C. L. *J Am Chem Soc* **2009**, *131*, 7522.

(41) Kuznetsov, A. E.; Geletii, Y. V.; Hill, C. L.; Morokuma, K.; Musaev, D. G. *J Am Chem Soc* **2009**, *131*, 6844.

(42) Quinonero, D.; Kaledin, A. L.; Kuznetsov, A. E.; Geletii, Y. V.; Besson, C.; Hill, C. L.; Musaev, D. G. *J Phys Chem A* **2010**, *114*, 535.

(43) Sanchez, C.; Livage, J.; Launay, J. P.; Fournier, M.; Jeannin, Y. *J. Am. Chem. Soc.* **1982**, *104*, 3194.

(44) Sanchez, C.; Livage, J.; Launay, J. P.; Fournier, M. *J. Am. Chem. Soc.* **1983**, *105*, 6817.

(45) Buckley, R. I.; Clark, R. J. H. *Coord. Chem. Rev.* **1985**, *65*, 167.

(46) Kozik, M.; Hammer, C. F.; Baker, L. C. W. *J. Am. Chem. Soc.* **1986**, *108*, 7627.

(47) Chiang, M.-H.; Soderholm, L.; Antonio, M. R. *Eur. J. Inorg. Chem.* **2003**, *2003*, 2929.

(48) Gao, G.; Xu, L.; Wang, W.; An, W.; Qiu, Y. *J. Mat. Chem.* **2004**, *14*, 2024.

Part IV: Photophysics of Polyoxometalates

CHAPTER

7

Characterization of a Metal-to-Polyoxometalate Charge Transfer Molecular Chromophore

Partially in articles:

(‡Equal contribution) ‡Zhao, C.; ‡**Huang, Z.**; Rodríguez-Córdoba, W.; Kambara, C. S.; Musaev, D. G.; O'Halloran, K.; Hardcastle, K. I.; Lian, T.; Hill, C. L.; "*Synthesis and Characterization of a Metal-to-POM Charge Transfer Molecular Chromophore Based on Rhenium Polyoxometalate*", ***J. Amer. Chem. Soc.* 2011, Submitted**.

Abstract: $[P_4W_{35}O_{124}\{Re(CO)_3\}_2]^{16-}$ (**1**), a Wells-Dawson $[\alpha_2\text{-}P_2W_{17}O_{61}]^{10-}$ polyoxometalate (POM) supported $[Re(CO)_3]^+$ complex, containing covalent W^{VI}–O–Re^I bonds has been characterized by several methods. This complex shows a high visible absorptivity (ε_{500nm} = 4000 $M^{-1}\cdot cm^{-1}$ in water) due to the formation of a Re^I-to-POM charge transfer (MPCT) band. The complex is investigated by computational modeling and transient absorption measurements in the visible and the mid-IR regions. The optical excitation of the MPCT transition results in an instantaneous (<50 fs) electron transfer from the Re^I center to the POM ligand.

7.1 Introduction

Recently, chromophores containing heterobinuclear groups linked by an oxo bridge (M–O–M'; M = Zr^{IV}, Ti^{IV}; M' = Cu^I, Ce^{III}, Sn^{II}, etc.) and supported on mesoporous substrates have been shown to be promising in conjunction with photocatalytic solar fuel production.[1-13] These heterogeneous heterobinuclear units possess enhanced visible absorptivity and all-inorganic structures for oxidative stability. Their visible absorption properties originate from the photo-induced formation of long-lived metal-to-metal charge transfer (MMCT) excited states that can be effectively coupled with multi-electron-transfer catalysts. In spite of the reported successes from these heterobinuclear chromophores, molecular/homogeneous counterparts are sought because their geometrical and electronic structures as well as their chemical properties (e.g. interfacing with catalysts) can be more extensively altered and all their properties can be studied and optimized more readily than for heterogeneous analogues.[14-18] Inspired by the heterogeneous bimetallic assemblies on mesoporous silica and the well-known

metal-to-(organic) ligand charge transfer (MLCT) complex, (bpy)$Re^{I}(CO)_3Cl$ (bpy = 2,2'–bipyridyl),[19-21] we have been seeking a new general type of charge transfer chromophore in which a polyoxometalate (POM) unit as a whole (delocalized orbitals involving many tungsten atoms) replaces the single metal center or bpy as the electron acceptor. POMs would be logical candidates for such an application because they are oxidatively, hydrolytically (over varying pH ranges) and thermally stable, can accommodate multiple metals with varying potentials, but they haven't yet been systematically explored as tunable electron-accepting chromophores.[22,23] This chapter describe our recent report[24] about a new complex comprising the $[Re(CO)_3]^+$ unit supported on a POM, the defect Wells-Dawson-type $[\alpha_2\text{-}P_2W_{17}O_{61}]^{10-}$, that exhibits an intense Re-to-POM charge transfer transition. This is an example of a potentially general transition that we will refer to as metal-to-POM charge transfer (MPCT). Unlike the well-documented MMCT heterobimetallic chromophores,[1-13] this study involves multi-metal and delocalized orbitals in the acceptor (POM) unit. This complex, $[P_4W_{35}O_{124}\{Re(CO)_3\}_2]^{16-}$ (**1**), has been characterized by computational and multiple time-resolved spectroscopic studies.

7.2 Results and Discussion

Synthesis and the related characterizations (Crystallography, ^{31}P NMR, thermogravidity analysis, elemental analysis, etc), and computational details can be found in our recent report.[24] This section only focused on the spectroscopic studies. Other details are only presented when necessary, such as Figure 7.1 (crystal structure) and 7.2 (the calculated HOMO and LUMO).

7.2.1 Static spectroscopy

The X-ray structure of **1** is shown in Figure 7.1.

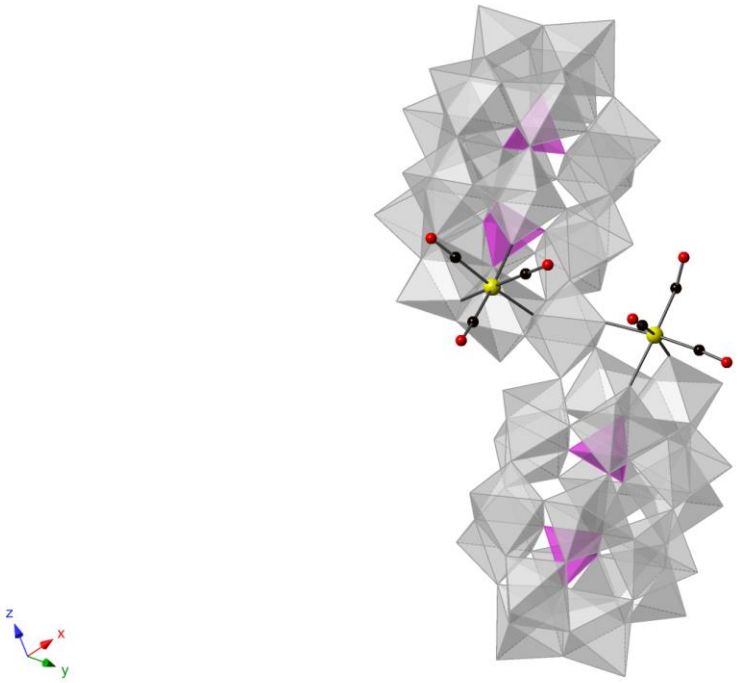

Figure 7.1. (a) X-ray structure of $[P_4W_{35}O_{124}\{Re(CO)_3\}_2]^{16-}$ (**1**) in combined polyhedral and ball-and-stick notation. Re: yellow; O: red; C: black; WO_6 octahedra: gray; PO_4 tetrahedra: purple.[24]

Each half of this dimerized structrue has C_s symmetry, and shows two symmetric and one anti-symmetric IR-active C-O stretching modes at 1869, 1890, and 2006 cm^{-1} (Figure 7.2).[25,26] These bond lengths and CO stretching frequencies are consistent with those observed in other Re(I) carbonyl complexes.[19-21,27,28]

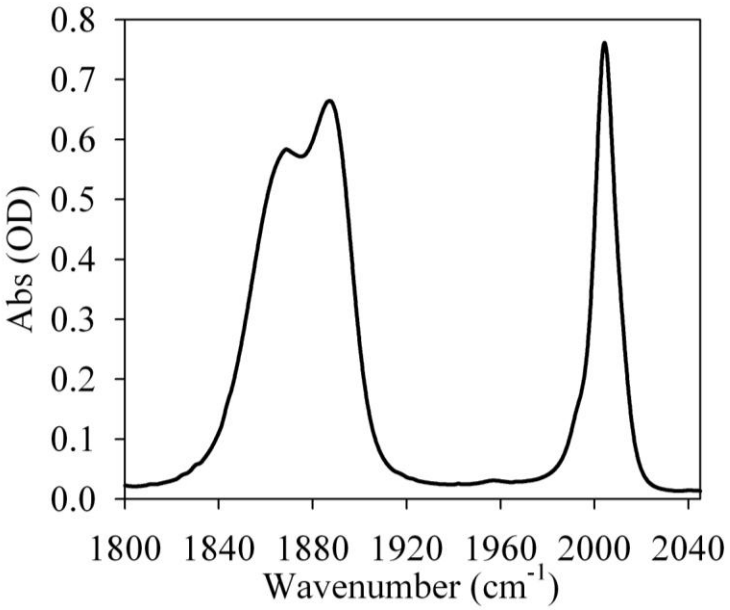

Figure 7.2. FTIR spectra of **1** in CH_2Cl_2 showing the C-O stretching modes.

In contrast to its colorless components, $K_{10}[\alpha_2\text{-}P_2W_{17}O_{61}]\cdot 20H_2O$ and $Re(CO)_3(CH_3CN)_3(BF_4)$, solid **1** is dark red. The UV-vis spectrum of **1** in CH_2Cl_2 (Figure 7.3a) and in H_2O (Figure 7.3b) shows intense broad absorption (up to 700 nm) covering the entire UV and visible regions. The synthetic precursor, $[\alpha_2\text{-}P_2W_{17}O_{61}]^{10-}$, has O*2p* → W*5d* transitions that absorb only below 300 nm and the ligand-to-metal-charge-transfer band in the $[Re(CO)_3(CH_3CN)_3]^+$ precursor absorbs only below 380 nm (Figure 7.3b). In addition, **1** has unexpectedly high visible absorptivity (ε_{400nm} ~ 6,200 and 4,500 $M^{-1}\cdot cm^{-1}$ in water and CH_2Cl_2, respectively). Importantly, the wide spectral range and the high extinction coefficients of **1** are comparable to those of many ruthenium polybipyridyl photosensitzers,[29,30] but **1** is free of the oxidatively and hydrolytically unstable polypyridyl ligands.

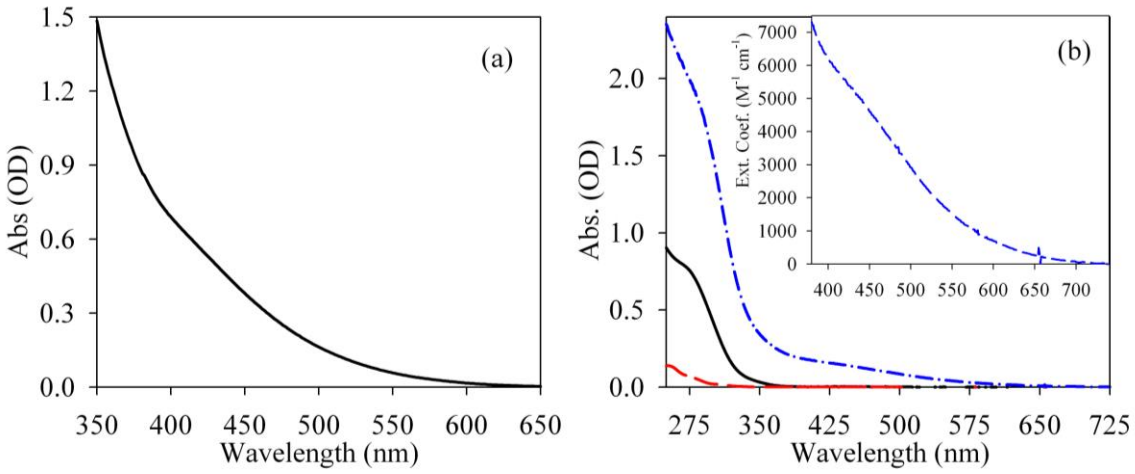

Figure 7.3.(a) UV-Vis spectra of **1** in CH_2Cl_2; (b) UV-Vis absorption spectra of $K_{10}[\alpha_2$-$P_2W_{17}O_{61}]\cdot 20H_2O$ (black line), $Re(CO)_3(CH_3CN)_3(BF_4)$ (red dashed) and **1** (blue dash-dot) in H_2O. The inset shows the extinction coefficients of **1** in H_2O.

7.2.2 Computation[24]

We have investigated the origin of high visible absorptivity of **1** by computational modeling.[24] As shown in Figure 7.4, the HOMO and LUMO of **M1** (which is a computational model of **1)** are very clearly the $Re(CO)_3$- and POM-based orbitals, respectively. The lowest excited state of **M1** is a triplet at 56.3 kcal/mol (or 2.45 ev, or 506 nm) higher in energy than the ground singlet state. In this triplet state, almost one unpaired spin is located on the W and O atoms of POM ligand indicating a transfer of the electron density from the $Re(CO)_3$-based HOMO to the POM-based LUMO. Another unpaired spin (~1.02e) is located on the $–O_b$-$Re(CO)_3$ fragment, where O_b is the bridging oxygen atom between the $Re(CO)_3$ unit and the POM. Thus, the visible absorption of **1**, shown in Figure 7.3a, can be attributed to the Re-to-POM ligand charge transfer transition. Similar to previously reported MMCT chromophores, the charge transfer

interaction is enhanced by the formation of W-O-Re covalent bonds and occurs mostly among the metal centers. However, the electron in the charge transfer excited state in **1** is delocalized among many W and O centers, a characteristic that resembles the MLCT states in Re and Ru bipyridyl complexes.

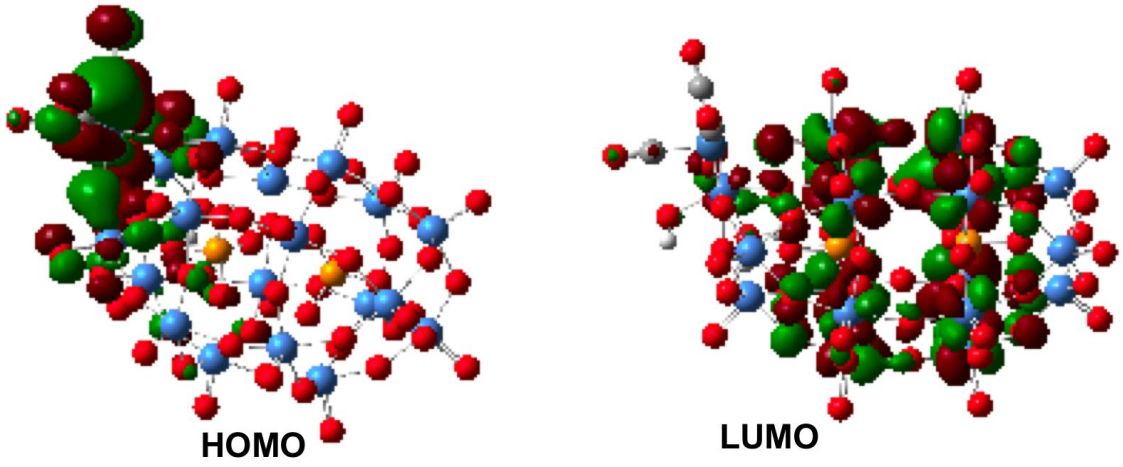

Figure 7.4. The calculated HOMO and LUMO of the model complex $[\{P_2W_{18}O_{63}[Re(CO)_3]\}(H_2O)(OH)]^{8-}$, **M1**. (See our recent report for the computational modeling). [24]

7.2.3 Femtosecond pump-probe spectroscopy

The charge transfer dynamics were investigated by femtosecond visible pump-probe spectroscopy. The transient visible absorption spectra (Figure 7.5) of **1** show a new broad absorbing species with maximum at ~640 nm. This absorption feature can be attributed to the W(V) d-d transitions and W(V)-W(VI) intervalence charge transfer (IVCT) transitions in the reduced Wells-Dawson anionic ligand, generally known as "heteropoly blues". [31-36] In addition, for a Wells-Dawson POM anion, the polar and

equatorial sites have different electron affinities and the reduction preferentially occurs in the equatorial sites.[32-34,37,38] This is also the case for **1**, in which the electron density in the LUMO is distributed among the 12 equatorial WO_6 octahedrons, as shown in Figure 7.4.

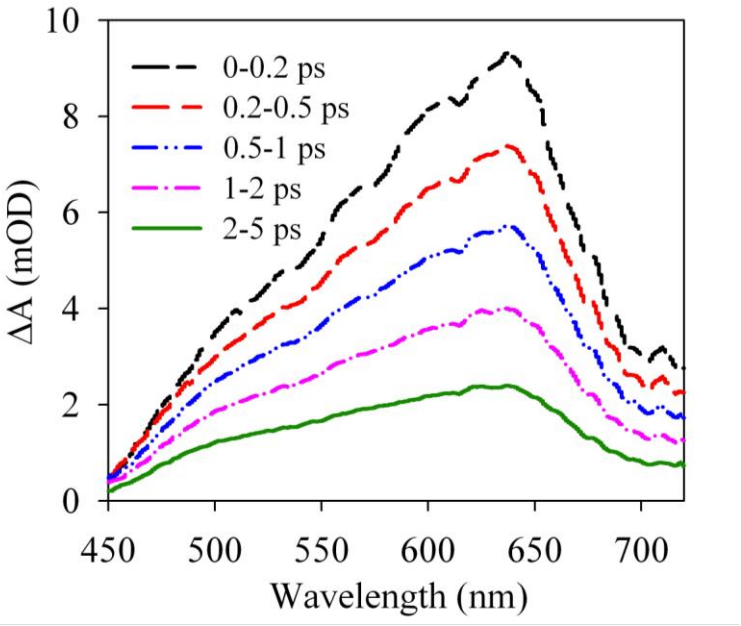

Figure 7.5. Average transient visible absorption spectra of **1** in CH_2Cl_2 at indicated delay time windows after 400 nm excitation.

The kinetics of the formation and decay of this photo-induced absorption feature can be monitored at 640 nm. As shown in Figure 7.6 and Table 7.1, the best fit yields a formation time of ~35 ± 15 fs, which can be considered as instantaneous within the time resolution of this measurement (~150 fs), consistent with the nature of the metal-to-POM charge transfer transition. However, this CT excited state is short lived, decaying with an average lifetime of 1.4 ps.

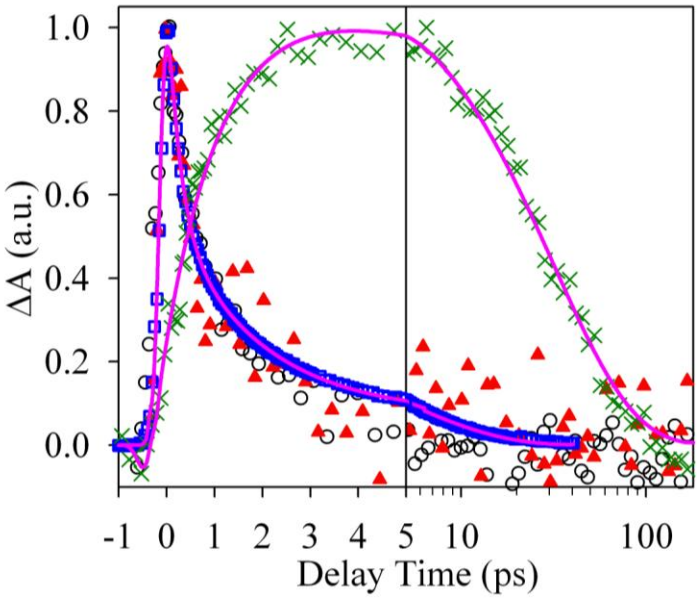

Figure 7.6. Transient kinetics of **1** in CH_2Cl_2 at 640 nm (blue squares), 1927 cm^{-1} (red triangles), 1982 cm^{-1} (green crosses) and 2020 cm^{-1} (circles) after 400 nm excitation. Also shown are fits (pink lines) to the kinetics at 640 nm and 1982 cm^{-1} by multiple exponential functions. The delay time is in linear scale in the left panel (-1 to 5 ps) and in logarithmic scale in the right panel (5 – 200 ps).

Table 7.1 Fitting parameters for kinetic traces after 400 nm excitation. The kinetic traces were modeled as multi-exponential decays analytically convoluted with the instrument response function. τ_{ave} is the amplitude weighted average time constant, $\Sigma(a_i \times \tau_i) / \Sigma a_i$.

	Rise time, fs	τ_1, ps (a_1, %)	τ_2, ps (a_2, %)	τ_3, ps (a_3, %)	τ_{ave}, ps
640 nm	35 ± 15	0.25 ± 0.07 (60)	1.4 ± 0.2 (29)	7.3 ± 0.5 (11)	1.4 ± 0.2
2020 cm^{-1}	35 ± 15	0.24 ± 0.05 (50)	1.6 ± 0.2 (50)	--	0.92 ± 0.13
1982 cm^{-1}	1200 ± 180	32 ± 0.3 (100)	--	--	32 ± 0.3

In addition to the formation of the reduced POM ligands discussed above, the MPCT excited state of **1** should also generate oxidized Re(II) centers. The latter can be most unambiguously probed by monitoring the CO stretching bands, the frequencies of which are sensitive to the charge density on the Re center because of the Re-to-CO dπ-π* back bonding.[39] For this reason, the dynamics of CO stretching modes of **1** were investigated using femtosecond visible pump and IR probe spectroscopy. Following 400 nm excitation, bleaches of the CO stretching bands in the ground electronic state (~1860, 1890 and ~2000 cm^{-1}) and two new absorption bands at~1925 and 2020 cm^{-1}, blue-shifted from the ground state positions, were formed instantaneously, as shown in Figure 7.7. This is consistent with the formation of the MPCT excited state, in which the electron density at the Re center is reduced, shifting the CO stretching to higher frequencies.[39] Because of the spectral overlaps, only one broad feature at ~1925 cm^{-1} (instead of two peaks) is observed. The transient kinetics of excited state CO stretching bands are compared in Figure 7.6, which show the same decay kinetics as the transient visible feature assigned to the reduced POM ligand. This agreement further confirms the assignment of the Re-to-POM CT transition in **1**.

The decay of the MPCT excited state leads to the formation of two positive absorption bands at ~1850, and 1980 cm^{-1}, red-shifted from the ground state bleaches, as shown in Figure 7.7. This can also be clearly seen in Figure 7.6, which shows that the formation kinetics of these features agrees well with the decay of the MPCT excited state bands (in the visible and mid-IR). We attribute these features to the formation of "hot" ground state molecules, in which the energy of the excitation is converted into the vibrational energy of the complex in the ground electronic state. The broadened and red-

shifted CO bands undergo a continuous blue shift and narrowing with a time constant of 32 ps (Table 7.1), consistent with a vibrational cooling process of related molecules.[40-45] The red-shifted CO stretching bands can result from the vibration excitation of the CO stretching modes as well as anharmonically coupled low frequency modes.

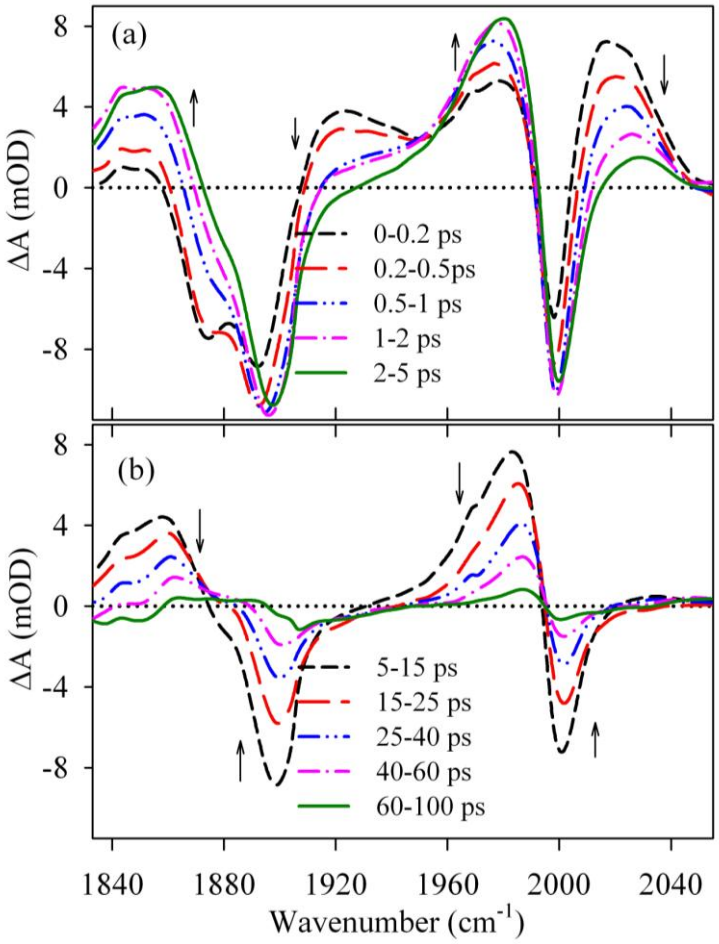

Figure 7.7. Average transient mid-IR (a, 0~5 ps; b, 5~100 ps) absorption spectra of **1** in CH_2Cl_2 at indicated delay time windows after 400 nm excitation. Arrows indicate the directions of amplitude changes.

To further clarify the nature of the hot ground state, we conducted transient IR pump/IR probe experiments where only the CO stretching mode at the electronic ground

state is excited. In this case (Figure 7.8), a red-shifted CO band assignable to the 1-2 transition is also observed and it decays with a similar time constant. However, this feature does not undergo continuous blue shift and narrowing. This comparison suggests that the hot ground state (shown in Figure 7.7) contains both the excitation of the CO stretching mode (to v=1 state) and anharmonically coupled low frequency modes.

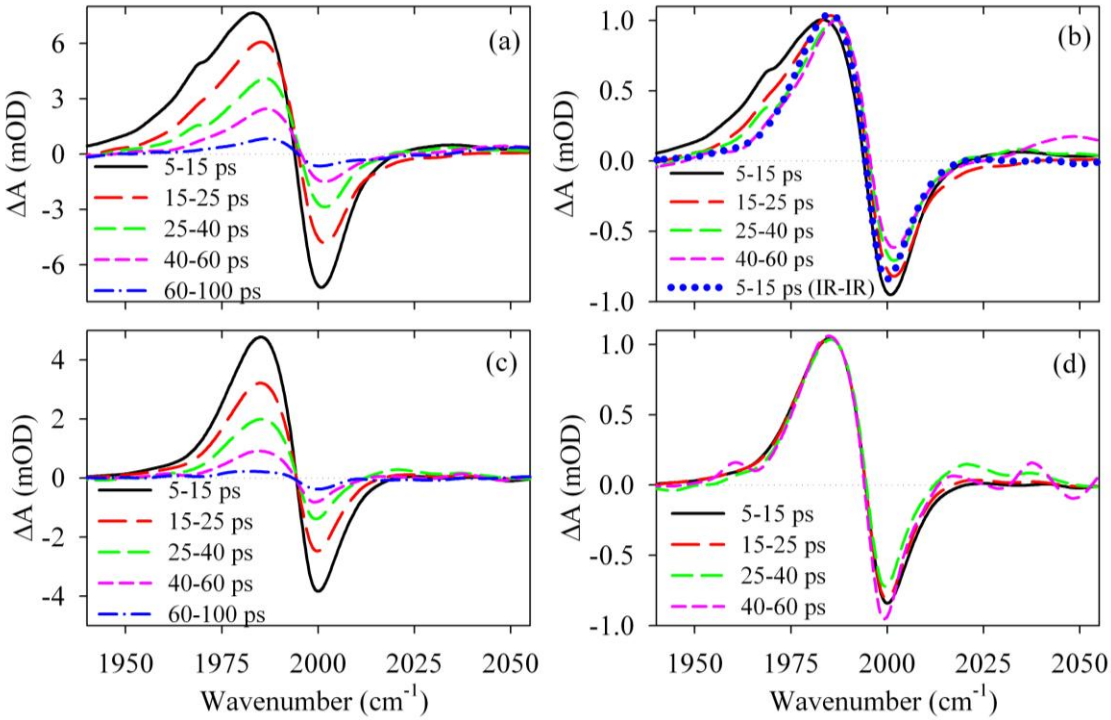

Figure 7.8. Average transient IR spectra at indicated delay time windows after 400 nm (a and b) and 2000 cm^{-1} (c and d) excitation. (b) and (d) are the normalized spectra of (a) and (c), respectively. In (b), the normalized spectrum from panel (d) (at 5~15 ps after 2000 cm^{-1} excitation) is also shown for comparison.

In addition, transient kinetics of the "hot" ground excited state and the 1-2 transition after 400 nm and 2000 cm^{-1} excitation, respectively, are compared in Figure

7.9. The initial component in the kinetics resulted from IR (2000 cm^{-1}) excitation can be attributed to a fast energy transfer among the CO stretching modes. Clearly, these kinetics show the same decay after ~ 5 ps.

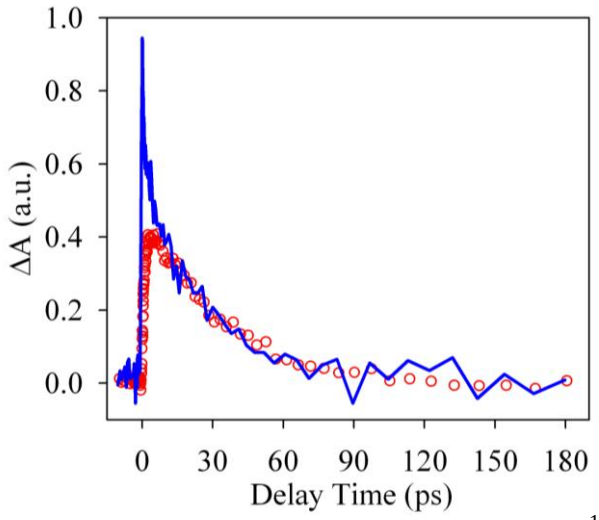

Figure 7.9. Comparison of transient kinetics monitored at 1982 cm^{-1} after 400 nm (red circles) and 2000 cm^{-1} (blue line) excitation.

7.3 Conclusion

In conclusion, we have characterized a molecular metal-to-polyoxometalate CT (MPCT) chromophore. Comprehensive computational and spectroscopic studies show that the high visible absorption in this complex can be attributed to a MPCT transition involving charge transfer from the Re(I) center to the POM. The orbitals and transition addressed in this study are distinct from those in the well-documented heterobimetallic systems because the acceptor orbitals are delocalized and multi-metal. In constrast, the heterobimetallic systems exhibit fairly localized orbitals that reside primarily on a single acceptor metal.[1-13]

7.4 References

(1) Lin, W.; Frei, H. *J. Phys. Chem. B* **2005**, *109*, 4929.

(2) Nakamura, R.; Frei, H. *J. Am. Chem. Soc.* **2006**, *128*, 10668.

(3) Han, H.; Frei, H. *Microporous Mesoporous Mater.* **2007**, *103*, 265.

(4) Nakamura, R.; Okamoto, A.; Osawa, H.; Irie, H.; Hashimoto, K. *J. Am. Chem. Soc.* **2007**, *129*, 9596.

(5) Han, H.; Frei, H. *J. Phys. Chem.* **2008**, *112*, 8391.

(6) Han, H.; Frei, H. *J. Phys. Chem.* **2008**, *112*, 16156.

(7) Wu, X.; Weare, W. W.; Frei, H. *Dalton Trans.* **2009**, 10114.

(8) Somorjai, G. A.; Frei, H.; Park, J. Y. *J. Am. Chem. Soc.* **2009**, *131*, 16589.

(9) Takashima, T.; Nakamura, R.; Hashimoto, K. *J. Phys. Chem. C* **2009**, *113*, 17247.

(10) Cuk, T.; Weare, W. W.; Frei, H. *J. Phys. Chem. C* **2010**, *114*, 9167.

(11) Yu, H.; Irie, H.; Shimodaira, Y.; Hosogi, Y.; Kuroda, Y.; Miyauchi, M.; Hashimoto, K. *J. Phys. Chem. C* **2010**, *114*, 16481.

(12) Irie, H.; Shibanuma, T.; Kamiya, K.; Miura, S.; Yokoyama, T.; Hashimoto, K. *Appl. Catal. B* **2010**, *96*, 142.

(13) Sivasankar, N.; Weare, W. W.; Frei, H. *J. Am. Chem. Soc.* **2011**, *133*, 12976.

(14) Hou, Y.; Abrams, B. L.; Vesborg, P. C. K.; Björketun, M. E.; Herbst, K.; Bech, L.; Setti, A. M.; Damsgaard, C. D.; Pedersen, T.; Hansen, O.; Rossmeisl, J.; Dahl, S.; Nørskov, J. K.; Chorkendorff, I. *Nature Mater.* **2011**, *10*, 434.

(15) Duan, L. L.; Tong, L. P.; Xu, Y. H.; Sun, L. C. *Energy & Env. Sci.* **2011**, *4*, 3296.

(16) Yin, Q.; Tan, J. M.; Besson, C.; Geletii, Y. V.; Musaev, D. G.; Kuznetsov, A. E.; Luo, Z.; Hardcastle, K. I.; Hill, C. L. *Science* **2010**, *328*, 342.

(17) Sala, X.; Romero, I.; íguez, M. R.; Escriche, L. í; Llobet, A. *Angew. Chem. Int. Ed.* **2009**, *48*, 2842.

(18) Wang, M.; Sun, L. *ChemSusChem* **2010**, *3*, 551.

(19) Kalyanasundaram, K. *J. Chem. Soc., Faraday Trans. 2* **1986**, *82*, 2401.

(20) Worl, L. A.; Duesing, R.; Chen, P.; Ciana, L. D.; Meyer, T. J. *J. Chem. Soc., Dalton Trans.* **1991**, 849.

(21) Ziessel, R.; Juris, A.; Venturi, M. *Inorg. Chem.* **1998**, *37*, 5061.

(22) Hill, C. L. *Chem. Rev.* **1998**, *98*, 1.

(23) Borrás-Almenar, J. J.; Coronado, E.; Müller, A.; Pope, M. T. *Polyoxometalate Molecular Science. Proceedings of the NATO Advanced Study Institute, Tenerife, Spain from 25 August to 4 September 2001*; Kluwer Academic Publishers: Dordrecht, 2003; Vol. 98.

(24) Zhao, C.; Huang, Z.; Rodríguez-Córdoba, W.; Kambara, C. S.; Musaev, D. G.; O'Halloran, K.; Hardcastle, K. I.; Lian, T.; Hill, C. L. *J. Am. Chem. Soc.* **2011**, *Submitted*.

(25) Gamelin, D. R.; George, M. W.; Glyn, P.; Grevels, F.-W.; Johnson, F. P. A.; Klotzbuecher, W.; Morrison, S. L.; Russell, G.; Schaffner, K.; Turner, J. J. *Inorg. Chem.* **1994**, *33*, 3246.

(26) Asbury, J. B.; Wang, Y.; Lian, T. *Bull. Chem. Soc. Japan* **2002**, *75*, 973.

(27) Nagata, T.; Pohl, B. M.; Weiner, H.; Finke, R. G. *Inorg. Chem.* **1997**, *36*, 1366.

(28) Wrighton, M.; Morse, D. L. *J. Am. Chem. Soc.* **1974**, *96*, 998.

(29) Kalyanasundaram, K. *Coord. Chem. Rev.* **1982**, *46*, 159.

(30) Kalyanasundaram, K.; Grätzel, M. *Coord. Chem. Rev.* **1998**, *77*, 347.

(31) Sanchez, C.; Livage, J.; Launay, J. P.; Fournier, M.; Jeannin, Y. *J. Am. Chem. Soc.* **1982**, *104*, 3194.

(32) Sanchez, C.; Livage, J.; Launay, J. P.; Fournier, M. *J. Am. Chem. Soc.* **1983**, *105*, 6817.

(33) Buckley, R. I.; Clark, R. J. H. *Coord. Chem. Rev.* **1985**, *65*, 167.

(34) Kozik, M.; Hammer, C. F.; Baker, L. C. W. *J. Am. Chem. Soc.* **1986**, *108*, 7627.

(35) Chiang, M.-H.; Soderholm, L.; Antonio, M. R. *Eur. J. Inorg. Chem.* **2003**, *2003*, 2929.

(36) Gao, G.; Xu, L.; Wang, W.; An, W.; Qiu, Y. *J. Mat. Chem.* **2004**, *14*, 2024.

(37) Prados, R. A.; Pope, M. T. *Inorg. Chem.* **1976**, *15*, 2547.

(38) Keita, B.; Jean, Y.; Levy, B.; Nadjo, L.; Contant, R. *New J. Chem.* **2002**, *26*, 1314.

(39) Wang, Y.; Asbury, J. B.; Lian, T. *J. Phys. Chem. A* **2000**, 4291.

(40) Lian, T.; Bromberg, S. E.; Asplund, M. C.; Yang, H.; Harris, C. B. *J. Phys. Chem.* **1996**, *100*, 11994.

(41) Doorn, S. K.; Dyer, R. B.; Stoutland, P. O.; Woodruff, W. H. *J. Am. Chem. Soc.* **1993**, *115*, 6398.

(42) Li, G.; Parimal, K.; Vyas, S.; Hadad, C. M.; Flood, A. H.; Glusac, K. D. *J. Am. Chem. Soc.* **2009**, *131*, 11656.

(43) Gabrielsson, A.; Hartl, F.; Zhang, H.; Smith, J. R. L.; Towrie, M.; Antonín Vlček, J.; Perutz, R. N. *J. Am. Chem. Soc.* **2006**, *128*, 4253.

(44) Wang, C.; Mohney, B. K.; Williams, R. D.; Petrov, V.; Hupp, J. T.; Walker, G. C. *J. Am. Chem. Soc.* **1998**, *120*, 5848.

(45) Dougherty, T. P.; Heilweil, E. J. *Chem. Phys. Lett.* **1994**, *227*, 19.

Part V: Heterogeneous systems: composite triadic photoanodes

C H A P T E R

8

Interfacial Charge Transfer in a TiO_2-Ru470-Ru_4POM Triad

Partially in articles:

Huang, Z.; Geletii, Y.V.; Wu, D.; Anfuso, C. L.; Musaev, D.G.; Hill, C.L.; Lian, T.; "*Interfacial charge transfer dynamics in TiO_2-Sensitizer-Ru_4POM photocatalytic systems for water oxidation*" ***Proc. SPIE*, 2011,** *8109,* 810903

Abstract: Efficient solar-driven catalytic water oxidation is one of the main challenges in solar-to-fuel conversion. In this chapter, we investigate three approaches for constructing electron acceptor –sensitizer – catalysts systems for photocatalytic water oxidation and detail our current understanding of the relevant fundamental processes involved. We demonstrated that an all-inorganic molecular water oxidation catalyst (WOC), $[\{Ru_4O_4(OH)_2(H_2O)_4\}(\gamma\text{-}SiW_{10}O_{36})_2]^{10-}$ (or Ru_4POM), catalyzed a homogenous O_2 evolution system with 27% quantum efficiency in homogeneous solution in the presence of sensitizer $[Ru(bpy)_3]^{2+}$ and sacrificial electron donor.[1] This suggests the feasibility of a heterogeneous photoelectrochemical system in which the photoanode integrates all three components: electron acceptor, photosensitizer, and WOC. We prepare a photocatalytic electrode based on Ru_4POM and a dye-sensitized nanoporous TiO_2 film for efficient light-harvesting and charge separation. Ultrafast spectroscopic studies of this triadic nanocomposite indicate efficient charge separation from the excited sensitizer to TiO_2 and efficient regeneration of the ground state of the dye. The latter can be attributed to Ru_4POM oxidation by the photogenerated dye cation and has a yield of > 80% within 1 ns.

8.1 Introduction

As shown in the previous chapters, in recent years, a series of transition metal substituted polyoxometalates (POMs) have been demonstrated to be efficient molecular WOCs in homogeneous light-driven water oxidation systems[1-5] and electrocatalysis.[6] These POM WOCs appear as ideal candidates for constructing composite photoanodes for water oxidation. To guide this effort, we have carried out transient absorption studies

of charge separation and recombination kinetics in photocatalytic water oxidation systems using POM WOCs.

In Chapter 4, we described the charge transfer dynamics in an established homogeneous photocatalytic system[1] driven by incident visible photons and consumption of the sacrificial electron acceptor $[S_2O_8]^{2-}$, with $[Ru(bpy)_3]^{2+}$ as a photosensitizer and $[\{Ru_4O_4(OH)_2(H_2O)_4\}(\gamma\text{-}SiW_{10}O_{36})_2]^{10-}$ (Ru_4POM) as a WOC. Our experiments based on static[1,7] and ultrafast spectroscopic methods indicate that the diffusion-controlled characteristics of the charge transfer processes in solution systems are critically responsible for the relatively low overall quantum efficiency. In this regard, a heterogeneous photoelectrochemical system is highly desired in which the photoanode integrates together the three components: electron acceptor, photosensitizer, and WOC.

As shown in this chapter, this conclusion is supported by transient absorption spectroscopic studies on a TiO_2/Ru470/Ru_4POM photoanode, where Ru470 is a ruthenium bipyridyl dye sensitizer that has an intense metal-to-ligand-charge-transfer (MLCT) band at ~470 nm. In this model electrode, the optical excitation of Ru470 leads to ultrafast electron injection from the excited Ru470 to the TiO_2 nanoparticles, which can be monitored by transient visible/IR absorption spectroscopy.[8,9] The resulting charge-separated state is relatively long lived, up to the ms time scale. In the presence of WOCs, the Ru470 cation anchored onto the TiO_2 film can efficiently oxidize Ru_4POM-WOC, resulting in the regeneration of the ground-state of Ru470 and oxidized WOC. This WOC oxidation process is ultrafast, leading to > 80% of Ru470 regeneration within 1 ns, which is promising for efficient water oxidation using this type of photoanode.

8.2 Results and discussion

We prepared a photoelectrode by co-depositing Ru470 and Ru_4POM on the surface of a nanoporous TiO_2 thin film. UV-vis spectra of the as-prepared electrode and its components are shown in Figure 8.1.

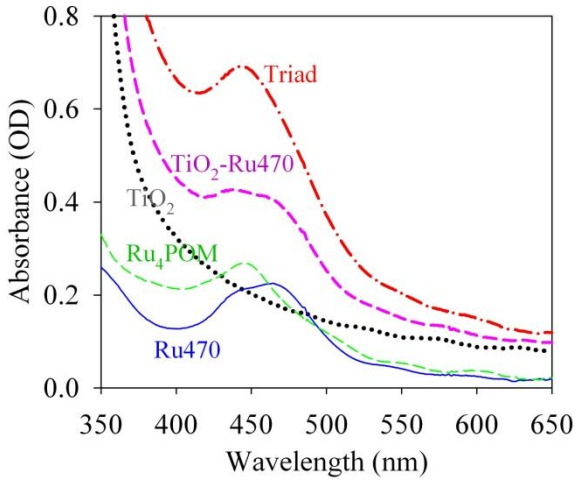

Figure 8.1. UV-Vis absorption spectra of TiO_2 (thick dotted), TiO_2/Ru470 (thick dashed), and the as-prepared electrode (thick-dotted-dashed). Also shown are absorption spectra of Ru_4POM (thin dashed) and Ru470 (thin solid) on TiO_2 after subtraction of TiO_2 absorption.

This film was prepared using acidic Ru_4POM solution (pH 1). At pH 1, Ru_4POM has a characteristic absorption feature at 445 nm (Figure 8.1).[10,11] Therefore, immersing the Ru470 sensitized TiO_2 film into the Ru_4POM acidic solution results in the appearance of the optical absorption features of the Ru_4POM in the electrode UV-Vis spectrum. The overlap of spectral features between Ru_4POM and Ru470 results in a difficulty for selective photoexcitation of Ru470. Although at pH >4, the extinction coefficient of the

Ru_4POM is greatly reduced due to the deprotonation of the Ru_4POM,[10,11] it is not able to attach to TiO_2 surface. Additionally, the Ru470 tends to leach from the TiO_2 surface and the Ru_4POM can feasibly remove the Ru470 from the substrate surface. Therefore, we prepared this electrode using acidic Ru_4POM. In addition, due to the competitive binding between Ru470 and Ru_4POM on the TiO_2 surface, the estimation of the ratio between these two components is difficult, and several possible structures are shown in Figure 8.2. Although there is an overlap in the ground state absorption spectra of Ru470 and Ru_4POM (Figure 8.1), these structures can be distinguished through ultrafast spectroscopy due to differences in their transient kinetics after 400 nm excitation.

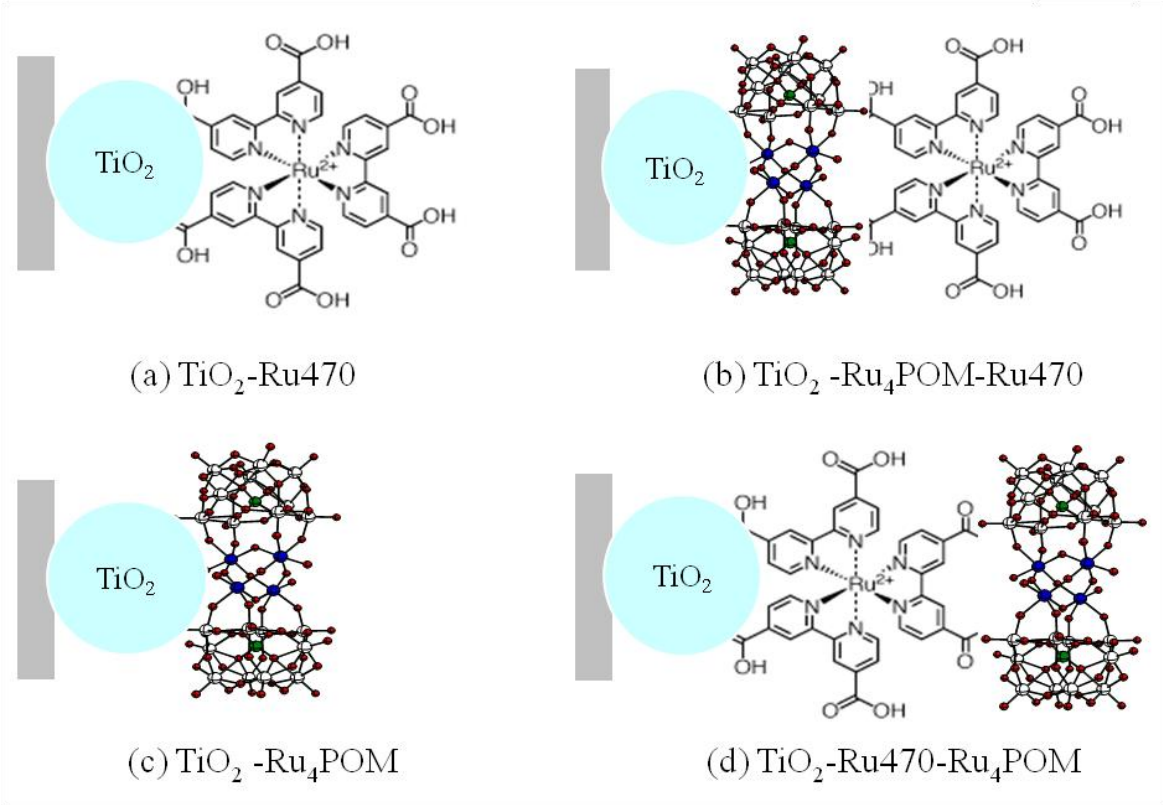

Figure 8.2. Possible structures (a-d) on the as-prepared electrode. The desired structure is shown in (d)

The TiO_2/Ru470 dyad shown in Figure 8.2a has been well studied, as shown in Figure 8.3.[8,9] Ultrafast biphasic electron injection from both the high energy singlet and lower energy triplet MLCT excited states of Ru470 into the TiO_2 conduction band is followed by a much slower back electron transfer to the Ru470 cation, resulting in a charge-separated state with a lifetime up to milliseconds.

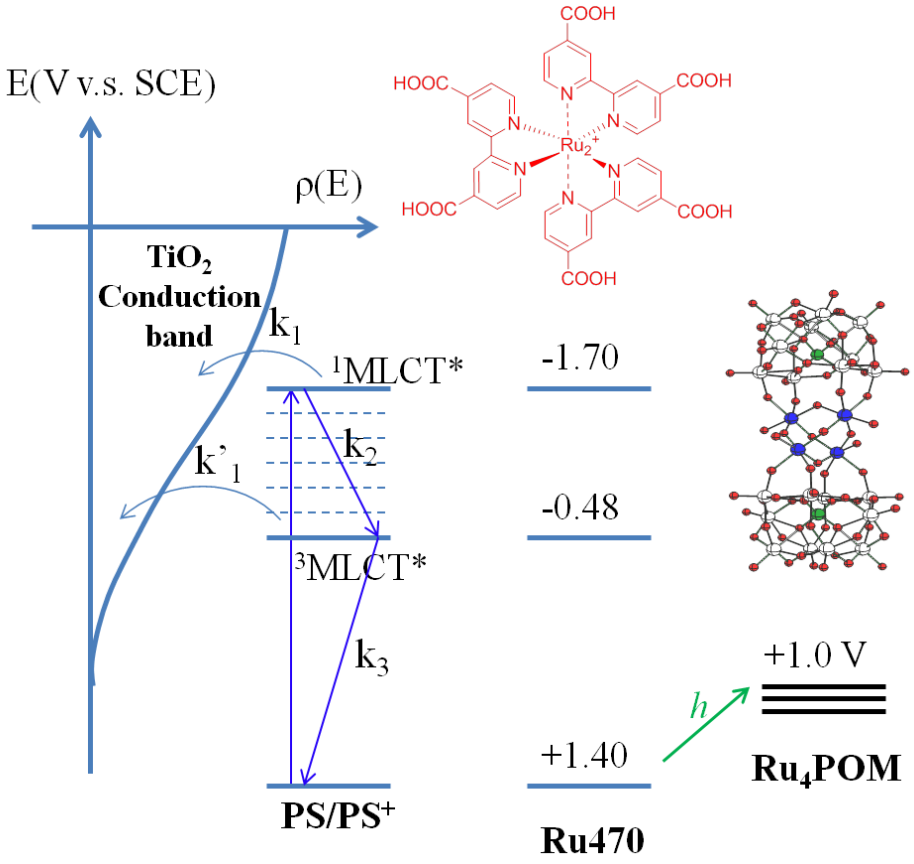

Figure 8.3. Schematic illustration of the photo-induced two-state injection model on the dye-sensitized nanoporous TiO_2 systems. The redox potentials for the ground and excited states (nonrelaxed and relaxed) of several dyes are shown to the right. Energies for the ^{1}MLCT* state are calculated assuming excitation at 400 nm (3.1 eV); shown as well is the Ru_4POM oxidation potential.

Transient visible pump/IR probe spectroscopy was used to investigate the interfacial electron transfer dynamics in this TiO_2/Ru470 dyad. The electron injection is confirmed by the intense absorption in the mid-IR after optical excitation. Figure 8.4b shows the kinetics of this mid-IR absorption after 400 nm excitation. This mid-IR signal results from free carrier absorption, intrasubband transitions and trap absorption.[12] Therefore, this strong absorbance resulting from the injected electron in the TiO_2 conduction band proves an unambiguous probe demonstrating the arrival of injected electrons to the semiconductor conduction band.[13-36] However, relaxation of the electron over time through conduction band states can result in a decrease in the absorption signal due to cross-section decay, complicating the analysis of the observed signal with either relaxation or adsorbate recombination.[29,37,38]

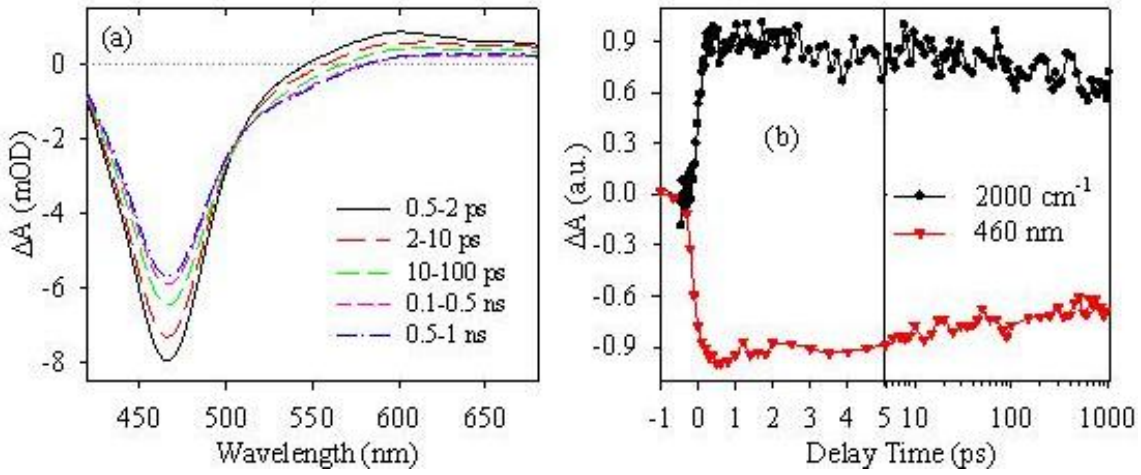

Figure 8.4. (a) Average transient spectra of TiO_2-Ru470 films at indicated time windows after 400 nm excitation. (b) Transient kinetics monitored at 460 nm (red triangles) and 2000 cm^{-1} (black dots) after 400 nm excitation.

We also carried out transient visible spectroscopy studies to investigate this interfacial charge transfer process in this TiO_2/Ru470 dyad. Displayed in Figure 8.4a are transient visible absorption spectra, showing ground state bleach and broad absorption features. The transient spectra of TiO_2/Ru470 evolve with time, particularly in the initial several ps. After 100 ps, the transient spectra are unchanged. This is due to the slow component of the electron injection, leading to the gradual conversion of ^{3}MLCT excited states to the oxidized states. The slight bleach recovery and spectral evolution of the MLCT band can be attributed to the spectral overlap of the ground bleach and oxidized state absorption. [39] In addition, the charge separation state with electrons in the TiO_2 and holes (positive charges) on the Ru470 creates a transient electric field. This photo-generated electric field can modulate both the absorption characteristics of ground, excited and oxidized states, altering the transient absorption spectra. This is the well-known transient Stark effect in dye-sensitized systems.[40-43] The bleach recovery is also clearly seen in the transient kinetics of this MLCT band monitored at 460 nm, as shown in Figure 8.4b.

The photoexcitation of Ru_4POM on TiO_2 prepared from an acidic solution (Figure 8.2c) after 400 nm excitation results in a ground state bleach at 445 nm and the formation of a new species with intense absorption at $\lambda > 500$ nm, as shown in Figure 6.2 in Chapter 6. As mentioned in Chapter 6, however, these spectral features are very short-lived and the transient signal completely disappears within 20 ps. The short-lived spectral characteristics of the Ru_4POM/TiO_2 also imply that the transient kinetics for the TiO_2/Ru_4POM/Ru470 system (Figure 8.2b) should only contain features from either the excited Ru470 by direct optical excitation or the Ru470 cation after electron transfer from

the Ru470 excited states to the TiO_2 conduction band. Both of these two species are long-lived: the MLCT excited state of Ru470 has a lifetime up to several hundred nanoseconds[39], and the charge-separated state (reduced TiO_2/oxidized Ru470) has a lifetime up to milliseconds.

Finally, in the targeted triadic configuration in Figure 8.2d, the ground state of Ru470 is believed to regenerate via Ru_4POM oxidation by the photo-generated Ru470 cations, This is believed to be due to the similar structure and energetics of Ru470 and $[Ru(bpy)_3]^{2+}$, and because the $[Ru(bpy)_3]^{3+}$ in the solution system is capable of oxidizing water to O_2 catalyzed by Ru_4POM. Figure 8.5a shows the transient spectra of the as prepared TiO_2/Ru470/Ru_4POM electrode averaged over different delay times. The transient spectral characteristics at 1-1.2 ps after 400 nm excitation has a bleach that overlaps well with the ground state absorption of the as-prepared electrode (inverted for better comparison). In addition, it has a broad, intense new absorption species above 500 nm quite similar to that of Ru_4POM/TiO_2 (Figure 6.2). These spectral features (bleach and absorption) result from the direct excitation of both Ru_4POM and Ru470 on TiO_2. As the bleach signal recovers, it gradually blue shifts over time until it matches the ground state absorption spectrum of the TiO_2/Ru470 dyad after 15 ps. Meanwhile, the absorption band above 500 nm is completely quenched after 15 ps. These spectral dynamics imply that some of the Ru_4POM molecules are directly attached to the TiO_2 substrate. The photoexcitation of these molecules only affects the transient spectra and kinetics before 15 ps due to the short-lived photo-excited Ru_4POM species. 15 ps after optical excitation, the bleach continues to recover, with more than 80% of the bleach recovering within 1 ns

(with respect to the spectrum at 20 ps). This is very different from that of the long-lived charge-separated states in the TiO_2/Ru470 dyad (Figure 8.4).

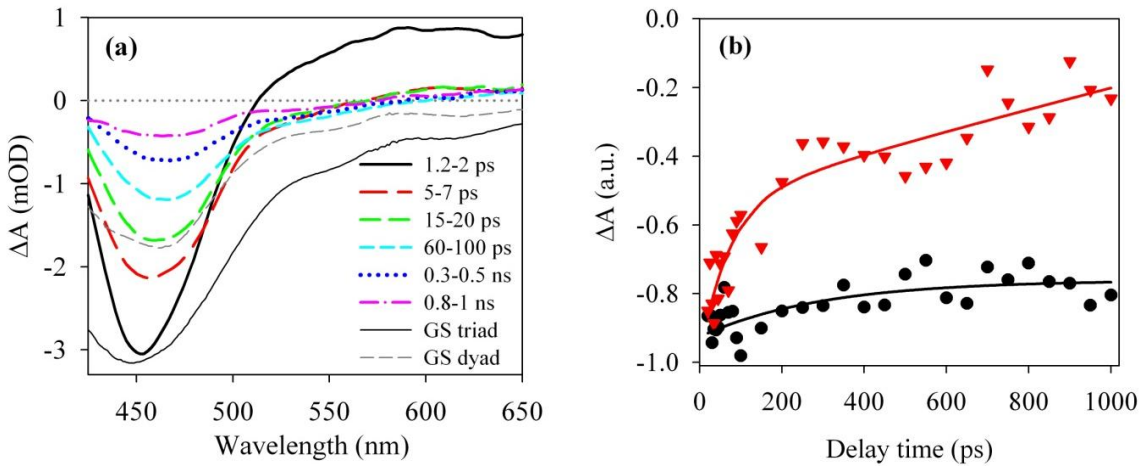

Figure 8.5. (a) Transient visible spectra of the triad averaged over indicated delay times after 400 nm excitation. Also shown are ground state absorption spectra (inverted for better comparison) of the triad (solid thin line) and the TiO_2/Ru470 dyad (dashed thin line). (b) Transient kinetics of the Ru470 ground state bleach of the electrode (red triangles) and the TiO_2/Ru470 dyad (black circles). Kinetics are normalized after 20 ps to exclude the effect of Ru_4POM directly attached to the TiO_2 substrate. Solid lines are exponential fits to the data.

To exclude the effect of Ru_4POM directly attached to the TiO_2 substrate (Figure 8.2c) on the transient kinetics, we compared the Ru470 ground state bleach recovery in the dyad (Figure 8.2a) with those of the as-prepared electrode after 20 ps. As it can be seen in Figure 8.5b, the ground state of Ru470 is substantially (>80%) regenerated within 1 ns in the presence of Ru_4POM.

These results indicate that the excited states of photosensitizers (e.g. Ru470) resulting from optical excitation are efficiently quenched by ultrafast electron transfer to TiO_2, leading to the generation of long lived charge-separated states consisting of oxidized dyes and reduced TiO_2. Subsequently, electron transfer from Ru_4POM to the oxidized dyes proceeds on the ns time scale, which competes with the back electron transfer process from the TiO_2 conduction band to the anchored dye cation. These electron-relay processes eventually result in further spatial charge separation with the electron located in the TiO_2 and with the hole localized on Ru_4POM. This charge separated state should have a longer lifetime than that of the TiO_2/Ru470 dyad (millisecond) and should thus be long enough for the slow step of water oxidation. The details of these charge recombination dynamics are under investigation in our laboratories.

8.3 Conclusion

In this work, our femtosecond studies on a model triad electrode reveal that the photoinduced excited states of the sensitizer are efficiently quenched by ultrafast electron transfer to TiO_2, while the resulting sensitizer cation can oxidize the WOC. The generation of the first oxidized state of [Ru_4POM] occurs within 1 ns, significantly faster than the lifetime of cation, suggesting the feasibility of such triadic photoanode for efficient water oxidation.

8.4 References

(1) Geletii, Y. V.; Huang, Z. Q.; Hou, Y.; Musaev, D. G.; Lian, T. Q.; Hill, C. L. *J Am Chem Soc* **2009**, *131*, 7522.

(2) Besson, C.; Huang, Z. Q.; Geletii, Y. V.; Lense, S.; Hardcastle, K. I.; Musaev, D. G.; Lian, T. Q.; Proust, A.; Hill, C. L. *Chem Commun* **2010**, *46*, 2784.

(3) Geletii, Y. V.; Yin, Q. S.; Hou, Y.; Huang, Z. Q.; Ma, H. Y.; Song, J.; Besson, C.; Luo, Z.; Cao, R.; O'Halloran, K. P.; Zhu, G. B.; Zhao, C. C.; Vickers, J. W.; Ding, Y.; Mohebbi, S.; Kuznetsov, A. E.; Musaev, D. G.; Lian, T. Q.; Hill, C. L. *Isr J Chem* **2011**, *51*, 238.

(4) Huang, Z. Q.; Luo, Z.; Geletii, Y. V.; Vickers, J. W.; Yin, Q. S.; Wu, D.; Hou, Y.; Ding, Y.; Song, J.; Musaev, D. G.; Hill, C. L.; Lian, T. Q. *J Am Chem Soc* **2011**, *133*, 2068.

(5) Puntoriero, F.; La Ganga, G.; Sartorel, A.; Carraro, M.; Scorrano, G.; Bonchio, M.; Campagna, S. *Chem Commun* **2010**, *46*, 4725.

(6) Toma, F. M.; Sartorel, A.; Iurlo, M.; Carraro, M.; Parisse, P.; Maccato, C.; Rapino, S.; Gonzalez, B. R.; Amenitsch, H.; Da Ros, T.; Casalis, L.; Goldoni, A.; Marcaccio, M.; Scorrano, G.; Scoles, G.; Paolucci, F.; Prato, M.; Bonchio, M. *Nat Chem* **2010**, *2*, 826.

(7) Kaledin, A. L.; Huang, Z. Q.; Geletii, Y. V.; Lian, T. Q.; Hill, C. L.; Musaev, D. G. *J Phys Chem A* **2010**, *114*, 73.

(8) Anderson, N. A.; Lian, T. Q. *Annu Rev Phys Chem* **2005**, *56*, 491.

(9) Anderson, N. A.; Lian, T. *Coordin Chem Rev* **2004**, *248*, 1231.

(10) Geletii, Y. V.; Botar, B.; Koegerler, P.; Hillesheim, D. A.; Musaev, D. G.; Hill, C. L. *Angew Chem Int Edit* **2008**, *47*, 3896.

(11) Geletii, Y. V.; Besson, C.; Hou, Y.; Yin, Q. S.; Musaev, D. G.; Quinonero, D.; Cao, R.; Hardcastle, K. I.; Proust, A.; Kogerler, P.; Hill, C. L. *J Am Chem Soc* **2009**, *131*, 17360.

(12) Pankove, J. I. *Optical Processes in Semiconductors*; Dover: New York, 1975.

(13) Anderson, N. A.; Lian, T. *Coord. Chem. Rev.* **2004**, *248*, 1231.

(14) Ai, X.; Anderson, N. A.; Asbury, J. B.; Hao, E.; Lian, T. *Proceedings of SPIE-The International Society for Optical Engineering* **2003**, *5223*, 147.

(15) Anderson, N. A.; Ai, X.; Lian, T. *J. Phys, Chem. B* **2003**, *107*, 14414.

(16) Anderson, N. A.; Ai, X.; Chen, D.; Mohler, D. L.; Lian, T. *Journal of Physical Chemistry B* **2003**, *107*, 14231.

(17) Asbury, J. B.; Anderson, N. A.; Hao, E.; Lian, T. *J. Phys. Chem. B* **2003**, *107*, 7376.

(18) Ai, X.; Guo, J.; Anderson, N. A.; Lian, T. *Journal of Physical Chemistry B* **2004**, *108*, 12795.

(19) Hao, E.; Anderson, N. A.; Asbury, J. B.; Lian, T. *J. Phys. Chem. B* **2002**, *106*, 10191.

(20) Asbury, J. B.; Hao, E.; Wang, Y.; Ghosh, H. N.; Lian, T. *J. Phys. Chem. B* **2001**, *105*, 4545.

(21) Asbury, J. B.; Wang, Y. Q.; Hao, E. C.; Ghosh, H. N.; Lian, T. *Res. Chem. Interm.* **2001**, *27*, 393.

(22) Anderson, N. A.; Hao, E.; Ai, X.; Hastings, G.; Lian, T. *Chem. Phys. Lett.* **2001**, *347*, 304.

(23) Wang, Y.; Asbury, J. B.; Lian, T. *J. Phys. Chem. A* **2000**, *104*, 4291.

(24) Ghosh, H. N.; Asbury, J. B.; Lian, T. *PINSA-A: Proc. Indian Natl. Sci. Acad., Part A* **2000**, *66*, 177.

(25) Asbury, J. B.; Hao, E.; Wang, Y.; Lian, T. *J. Phys. Chem. B* **2000**, *104*, 11957.

(26) Asbury, J. B.; Ellingson, R. J.; Ghosh, H. N.; Ferrere, S.; Nozik, A. J.; Lian, T. *J. Phys. Chem. B* **1999**, *103*, 3110.

(27) Asbury, J. B.; Wang, Y.; Lian, T. *J. Phys. Chem. B* **1999**, *103*, 6643.

(28) Ghosh, H. N.; Asbury, J. B.; Lian, T. *J. Phys. Chem. B* **1998**, *102*, 6482.

(29) Ghosh, H. N.; Asbury, J. B.; Weng, Y.; Lian, T. *J. Phys. Chem. B* **1998**, *102*, 10208.

(30) Ellingson, R. J.; Asbury, J. B.; Ferrere, S.; Ghosh, H. N.; Sprague, J. R.; Lian, T.; Nozik, A. J. *J. Phys. Chem. B* **1998**, *102*, 6455.

(31) Heimer, T. A.; Heilweil, E. J.; Bignozzi, C. A.; Meyer, G. J. *J. Phys. Chem. A* **2000**, *104*, 4256.

(32) Heimer, T. A.; Heilweil, E. J. *J. Phys. Chem. B* **1997**, *101*, 10990.

(33) Ai, X.; Anderson, N. A.; Guo, J.; Lian, T. *Journal of Physical Chemistry B* **2005**, *109*, 7088.

(34) Guo, J.; She, C.; Lian, T. *Journal of Physical Chemistry B* **2005**, *109*, 7095.

(35) Guo, J.; Stockwell, D.; Ai, X.; She, C.; Anderson, N. A.; Lian, T. *Journal of Physical Chemistry B* **2006**, *110*, 5238.

(36) She, C.; Anderson, N. A.; Guo, J.; Liu, F.; Goh, W.-H.; Chen, D.-T.; Mohler, D. L.; Tian, Z.-Q.; Hupp, J. T.; Lian, T. *Journal of Physical Chemistry B* **2005**, *109*, 19345.

(37) Weng, Y.-X.; Wang, Y.-Q.; Asbury, J. B.; Ghosh, H. N.; Lian, T. *J. Phys. Chem. B* **2000**, *104*, 93.

(38) Huang, J.; Stockwell, D.; Boulesbaa, A.; Guo, J.; Lian, T. *J. Phys. Chem. C* **2008**, *112*, 5203.

(39) Kalyanasundaram, K. *Coordin Chem Rev* **1982**, *46*, 159.

(40) Ardo, S.; Sun, Y. L.; Castellano, F. N.; Meyer, G. J. *Journal of Physical Chemistry B* **2010**, *114*, 14596.

(41) Ardo, S.; Sun, Y.; Staniszewski, A.; Castellano, F. N.; Meyer, G. J. *J Am Chem Soc* **2010**, *132*, 6696.

(42) Pastore, M.; De Angelis, F. *J Phys Chem Lett* **2011**, *2*, 1261.

(43) Boxer, S. G. *Journal of Physical Chemistry B* **2009**, *113*, 2972.

Part V: Heterogeneous systems: composite triadic photoanodes

C H A P T E R

9

Interfacial Charge Transfer in Well-defined TiO_2-Sensitizer-Ru_4POM Triads

Unpublished results

Abstract: This chapter continues to show our efforts to build efficient three-component dye-sensitized-photoelectrochemical (PEC) electrodes and to understand their interfacial charge transfer dynamics. Two other Ru-polypyridal dyes with phosphonate binding groups are used for constructing these TiO_2-sensitizer-WOC triads. These two dyes allow us to make well-defined triadic structures for spectroscopic studies and offer greater hydrolytic stability for PEC work. Ultrafast spectroscopic studies of these triadic nanocomposites indicate efficient charge separation from the excited sensitizer to TiO_2 and efficient regeneration of the ground states of the dyes. The latter can be attributed to Ru_4POM oxidation by the photogenerated dye cations and has yields of > 60% within 1 ns. In addition, the PEC tests on these electrodes show markedly enhanced photocurrent by the presence of Ru_4POM WOCs.

9.1 Introduction

Providing renewable pollution-free energy sources, especially solar fuels, is one of the most important scientific challenges of the 21st century, and in this context, the direct, efficient, sustained sunlight-driven splitting of water into H_2 and O_2 remains one of the most desirable targets. [1-8] As stated in Chapter 1, the central motivation of this work is to develop solar-driven water oxidation and splitting systems that are lower-cost, more stable and more efficient than existing systems. One of the general goals is to prepare and characterize hydrolytically and oxidatively stable triadic nanoassemblies. These nanocomposite triads compose three units: a semiconductor metal oxide (generally TiO_2) as electron acceptor, a photosensitizer (a Ru-polypiridyl complex), and an all-inorganic robust polyoxometalate (POM) water oxidation catalyst (WOC).

The performance of these photoanodes can be evaluated when connected to an external circuit where the photoinjected electrons are removed to a counter electrode for proton reduction. To achieve high solar energy conversion efficiency in a practical device, optimizations are needed in three areas: (1) the photosensitizer should optimally have absorption characteristics which cover a substantial region of the solar irradiance spectrum and generate a long-lived excited state; (2) the electron acceptor should facilitate the formation of the charge-separated state and the oxidation of the catalyst; and (3) the water oxidation catalyst should be fast and selective. Additionally, both the individual components and the nano-assembly or PEC cell as a whole must be hydrolytically and oxidatively stable.

We have shown a promising proof-of-principle case, the TiO_2/Ru470/Ru_4POM photoanode.[9] However, that particular electrode structure is not hydrolytically stable and is not well-defined. Consequently, both the PEC studies and spectroscopic investigation are difficult.

To overcome the unstable surface attachment of Ru470 on TiO_2 nanoparticles, RuP2 and RuC2 were introduced, which can perform the dual role of sensitizing titania and immobilizing our water oxidation catalysts on the metal oxide surface. These two dyes are modified $Ru(bpy)_3^{2+}$ as shown in Figure 9.1. The phosphonate binding groups employed in these dyes offer greater hydrolytic stability than carboxylates, which we found early on to be incompatible with aqueous conditions (Chapter 8).

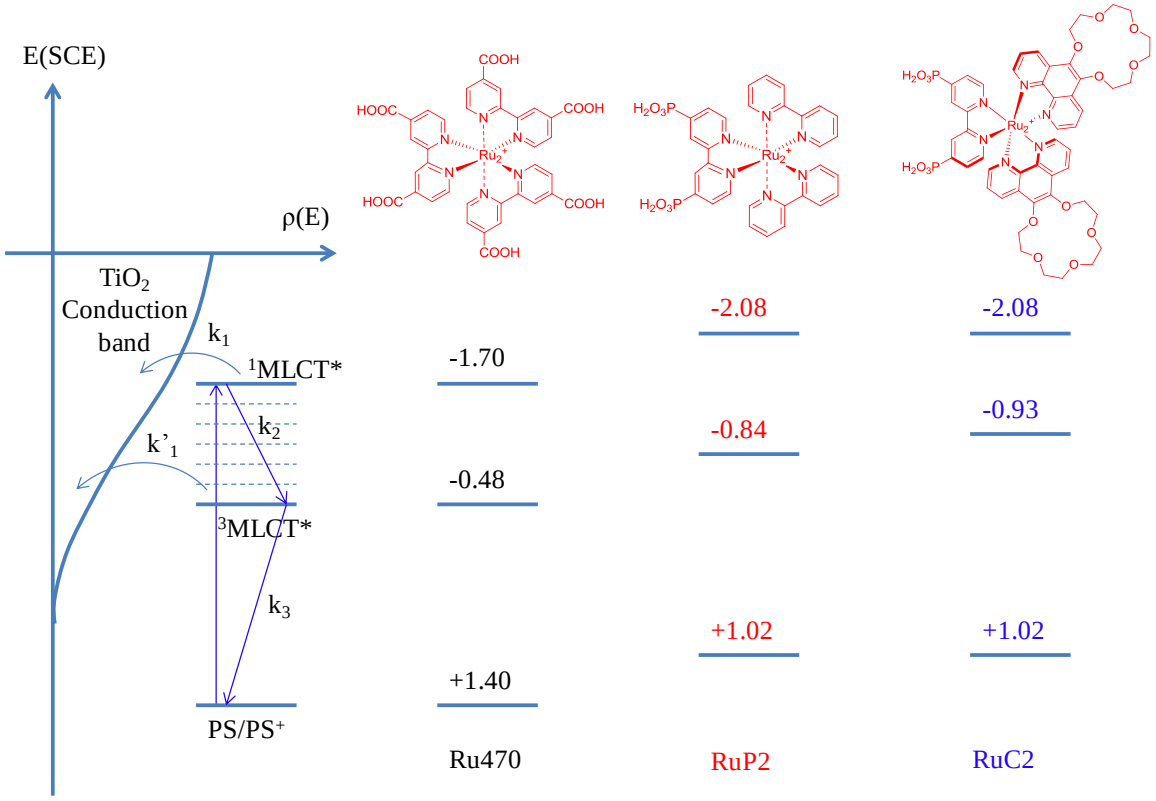

Figure 9.1. Structures of Ru470, RuP2, and RuC2, and the schematic illustration of the two-state injection model. Electron injection (k'_1) from the unthermalized excited state competes with intramolecular relaxation (k_2), whereas the relaxed excited state injects with a rate constant k_1. Competition between k_1 and k_2 leads to biphasic injection kinetics. The redox potentials for the ground and excited states (nonrelaxed and relaxed) of several dyes are shown to the right.[10] Energies for the ^{1}MLCT* state are calculated assuming excitation at 400 nm (3.1 eV)

9.2 Results and Discussion

9.2.1 TiO_2-RuP2-Ru_4POM

RuP2 has been proven to be promising in several dye-sensitized photoelectrochemical cells for water splitting or CO_2 reduction using nanoporous TiO_2

substrates. [11-15] In addition, the positive charge of the Ru^{2+} center is capable of picking up the highly negative Ru_4POM from the solution, forming a stable and well-defined TiO_2/RuP2/Ru_4POM (Figure 9.2) triadic structure.[16]

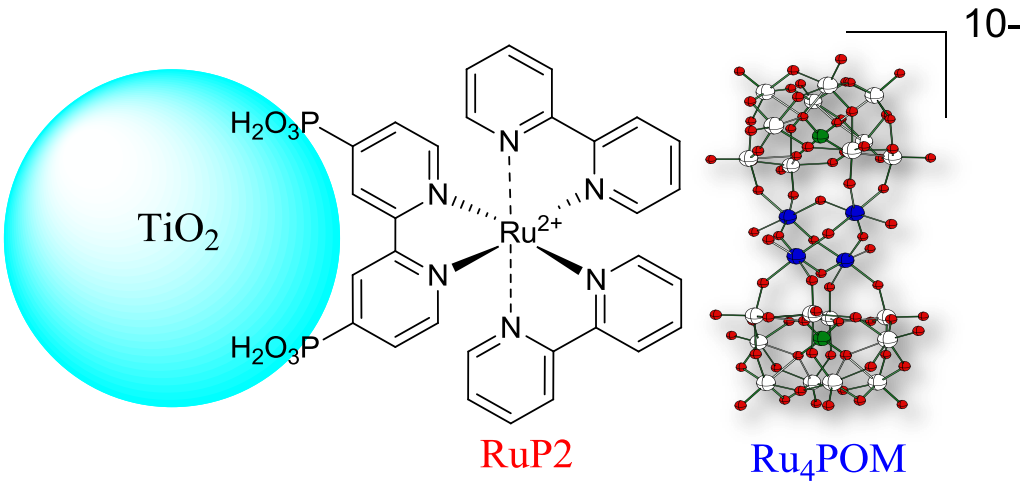

Figure 9.2. Schematic representation of the TiO_2/RuP2/Ru_4POM triadic construct.

The Bonchio group has reported some preliminary kinetic results for this composite on the μs time scale, where an accelerated RuP2 ground state bleach recovery was observed in the presence of Ru_4POM.[16] However, these kinetic features can also be due to either the increased back electron transfer rate or the interaction solely between the excited RuP2 dye and the attached Ru_4POM. More elaborated works are required to clarify the interfacial charge transfer dynamics in this triadic photoanode, especially on the earlier time scales (ns, ps and even fs), which is the focus of this section.

The triadic TiO_2/RuP2/Ru_4POM nanocomposites have been successfully synthesized, as indicated by the visible color change of the films and their static absorption spectra (Figure 9.3).

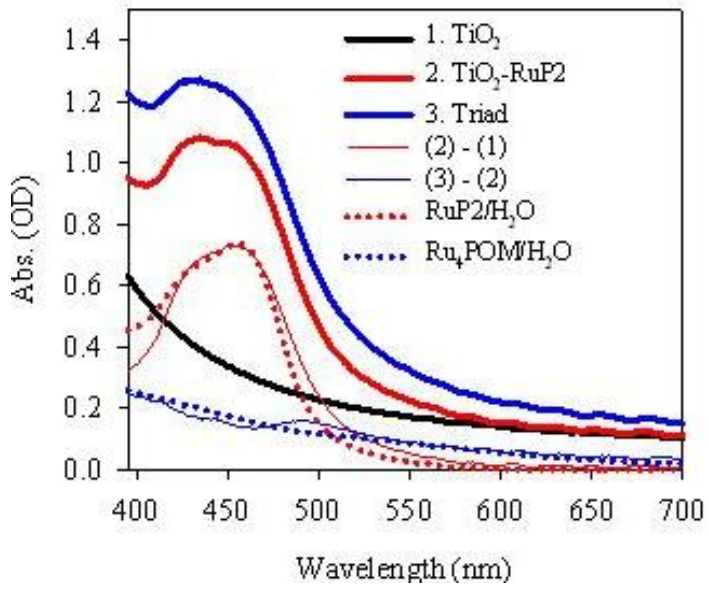

Figure 9.3. UV-Vis absorption spectra of TiO_2 (thick black line), TiO_2/RuP2 (thick red line), and the triad (thick blue line). Also shown are absorption spectra of Ru_4POM (red thin blue line) and RuP2 (thin red line) on TiO_2 after subtraction of TiO_2 absorption and Ru_4POM (blue dotted line) and RuP2 (red dotted line) in H_2O.

The charge transfer dynamics were investigated by femtosecond visible pump-IR probe spectroscopy. Shown in Figure 9.4 are absorption dynamics of injected electrons in TiO_2 following 400 nm excitation of the adsorbed RuP2. Upon injection of an electron to the TiO_2 conduction band, a broad positive absorption in the mid-IR region is observed. This mid-IR signal results from free carrier absorption, intrasubband transitions and trap absorption.[17] The interfacial electron injection dynamics probed at 2000 cm^{-1} are shown in Figure 9.4. Photoinduced electron injection dynamics in this system are biphasic, consisting of a distinct <100 fs ultrafast component and one or more slower components on picosecond and longer timescales. This biphasic electron injection process is presented

in Figure 9.1, where, in contrast, the bare TiO_2 film as a control shows only small signal because of the weak absorption at 400 nm (bandgap E_g = 3.0~3.2 eV for TiO_2).

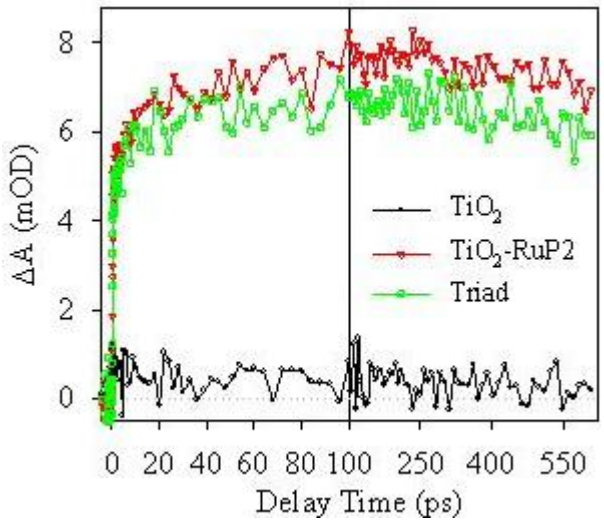

Figure 9.4. Transient IR absorption kinetics after 400 nm excitation for films of bare TiO_2 (black dots), TiO_2-RuP2 (red triangles), and the triad (green squares).

Optical excitation of RuP2 at 400 nm excites the molecule to its ^{1}MLCT* state, high (~1.2 eV) above the ^{3}MLCT state (Figure 9.1). This unthermalized ^{1}MLCT* state is also energetically much higher (~1.5 eV) than the TiO_2 conduction band edge with sufficient driving force for electron injection to TiO_2. RuP2 in its ^{1}MLCT* excited state can also undergo ultrafast (<100 fs) electronic relaxation (k_2) within the excited state manifold to the ^{3}MLCT. Injection from nonequilibrated excited states (k'_1) competes with the intramolecular relaxation (k_2). At the thermoequilibrated ^{3}MLCT excited state, electron injection to TiO_2 occurs with a much slower rate constant (k_1). The slower k_1 (compared to k'_1) results from the lower density of states in TiO_2 at that energy level

(reduced electronic coupling strength) and the reduced driving forces according to the Marcus electron transfer theory. [18-20]

Significantly, the presence of Ru_4POM does not alter the electron injection kinetics, confirming the photo-induced electron transfer from RuP2 excited states to TiO_2 instead of to the Ru_4POM.

The charge transfer dynamics were further investigated by transient visible spectroscopy. The transient absorption spectra of the dyad are shown in Figure 9.5a. Optical excitation results in the instantaneous formation of a bleach due to the depopulation of the RuP2 ground state. Similar to results for TiO_2/Ru470 (Chapter 8), the transient spectra of TiO_2/RuP2 evolve with time, particularly in the first 100 ps. After 100 ps, the transient spectra are unchanged. The spectral evolution can be due to the Stark effect, [21-24] as discussed in Chapter 8, and to the slow component of the electron injection that leads to the gradual conversion of ^{3}MLCT excited states to the oxidized states. Indeed, the electron injection dynamics in Figure 9.4 shows a slow component with a time constant of several tens of ps. The slight bleach recovery of the MLCT band is probably due to the overlap of ground state and oxidized state absorption spectra. [25] The transient stark effects can also result in the complication to the spectra and kinetics. The bleach recovery can clearly be seen in the transient kinetics monitored at 470 nm, as shown in Figure 9.6b.

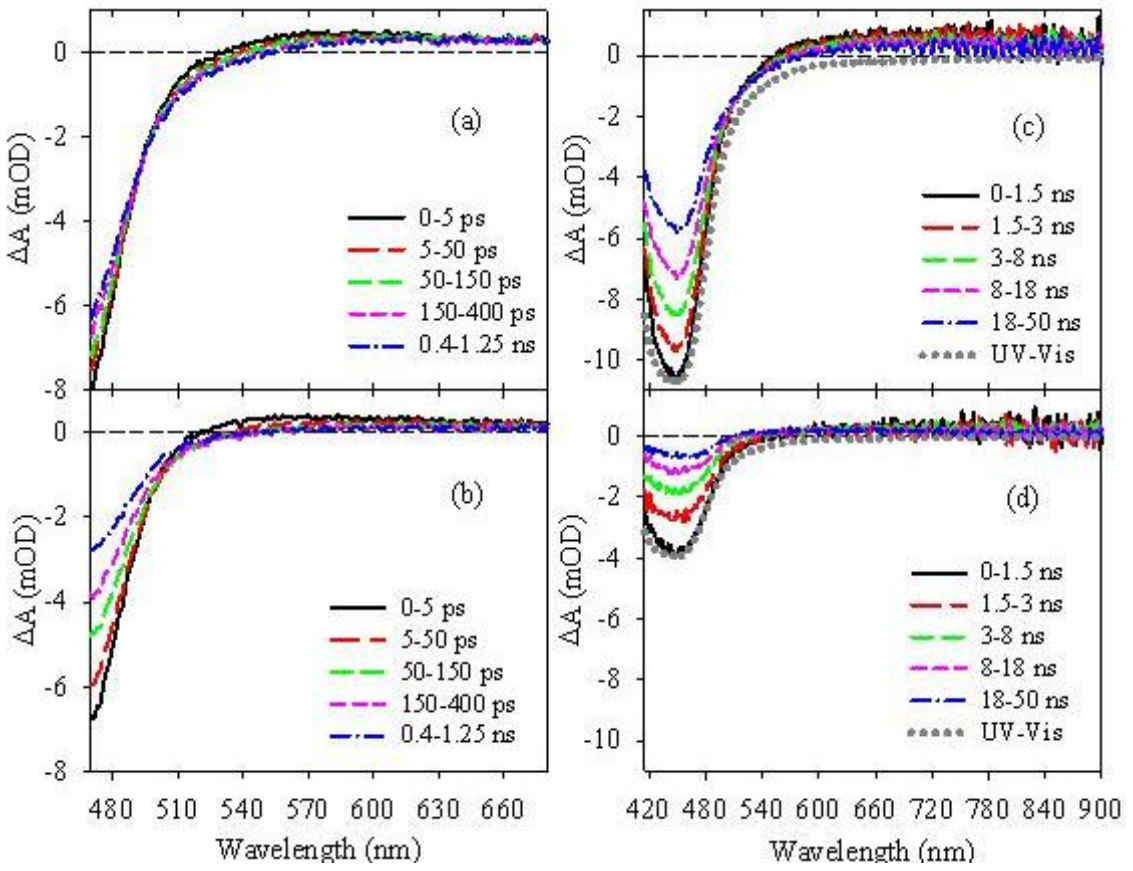

Figure 9.5. Average transient spectra of TiO_2/RuP2 (a and c) and the triad (b and d) for different time scales: (a and b, 0-1.25 ns) and (c and d, 0-50 ns) after 400 nm excitation. Shown in c and d are the static UV-Vis spectra (inverted for better comparison) of RuP2 on TiO_2 as well.

In the presence of Ru_4POM, the transient spectra of the triad at different delay times after 5 ps consistently show two only species, the ground state bleach and the absorption due to the formation of oxidized RuP2.[26,27] This indicates an increased electron injection rate from excited RuP2 to the TiO_2 conduction band. This can be due to the change of protonation states (surface pH) after picking the Ru_4POM from the solution pH 3.2. As shown in the previous report, decreased pH can accelerate the electron

injection on dye-sensitized TiO_2 nanoporous films.[28] In addition, the presence of the high negative charge (10^-) can be another driving force for electrons (negative charge) to move preferentially to the TiO_2 nanoparticles. Significantly, with the presence of Ru_4POM, the regeneration of the ground states of RuP2 are accelerated, which is shown from the spectral comparison between the dyad (Figure 9.5c) and the triad (Figure 9.5d) on the ns time scale. The transient kinetics of the RuP2 ground state recovery are also compared, as shown in Figure 9.6. Clearly, in the presence of Ru_4POM, the ground state of RuP2 is substantially (~70%) regenerated within 1 ns.

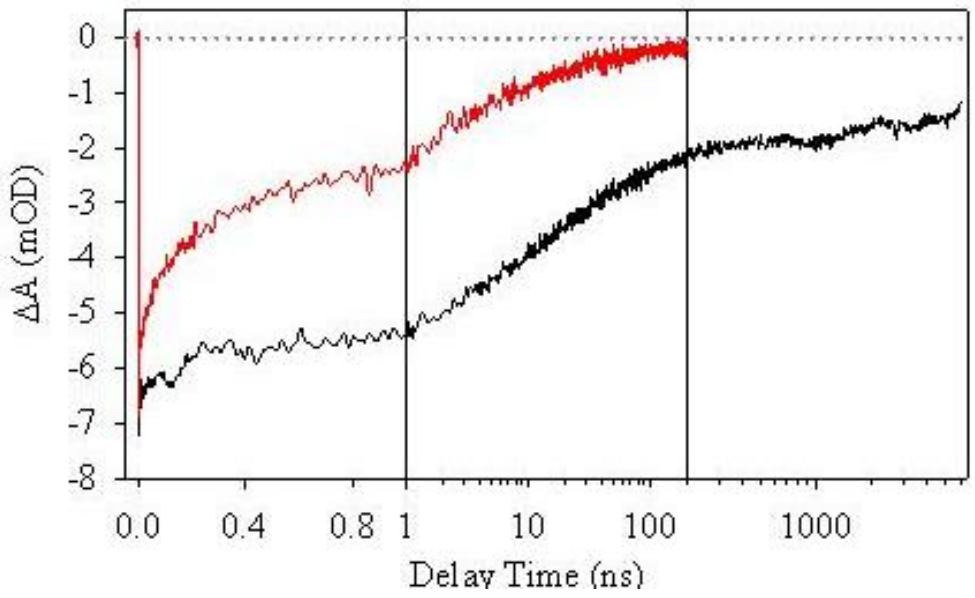

Figure 9.6. Transient kinetics of TiO_2/P2 (black) and the triad (red) monitored at 475 nm after 400 nm excitation. The decay time is in linear scale in the left panel (~0.1-1 ns) and in logarithmic scale in the middle (1-200 ns) and right (200-6000 ns) panels.

The ultrafast recovery of the ground state bleach may either be due to efficient electron transfer from the attached WOCs or increased back electron transfer from TiO_2

to the oxidized dyes. This ambiguity has been clarified by transient IR absorption spectroscopy, as shown in Figure 9.4, since the presence of the Ru_4POM does not affect the electron dynamics in the TiO_2 conduction band. Therefore, the ground state bleach recovery in the transient visible study is due to the oxidation of Ru_4POM, resulting in the long-lived charge-separated states required for efficient water oxidation at the photoanodes.

9.2.2 TiO_2-RuC2-Ru_4POM

Initial studies with the commercial sensitizer Ru470 and Ru_4POM suggested that the desired electron transfer occurs from the POM to the oxidized dye. However, the hydrolytic stability of the TiO_2-carboxylate linkage proved inadequate for aqueous photoelectrochemical (PEC) studies. For this reason, we have moved to the phosphonate substituted systems RuP2 and RuC2 (Figure 9.1), as dyes of this type have successfully been used in aqueous systems. RuC2 has been designed to strengthen interactions with the catalyst by including crown ether groups which can be metallated by alkali or alkaline earth metals, thus increasing the positive charge and introducing the possibility of weak coordinative interactions with the terminal oxo-groups of the POM. In addition, the RuC2 dye has an absorbtivity (19,000 M^{-1} cm^{-1}) that is 80% higher than that of RuP2 (12,000 M^{-1} cm^{-1}) at 455 nm.

In preparing the RuC2 triad (Figure 9.7) for the transient spectroscopic and PEC studies, we found that RuC2 is adsorbed just as efficiently on TiO_2 as RuP2, and that the RuC2-sensitized film can also rapidly take up enough POM to make an effective triad (sufficient loading is achieved within minutes), as shown in Figure 9.8. It is expected that

the electrode can be further optimized by varying the amount of charge introduced by the metal cation (e.g. changing Na^+ for Ca^{2+}). Our transient spectroscopy studies also reveal that transient kinetics resulting from these RuC2-based dyads and triads are similar to those for the RuP2-based ones, as shown in Figure 9.8b. The oxidized RuC2 can efficiently take an electron from the attached Ru_4POM, consequently forming a long-lived charge-separation state that is promising for solar fuel production. All these positive attributes listed above make RuC2 a more promising photosensitizer that RuP2 and Ru470 in this triadic photoanode for water splitting.

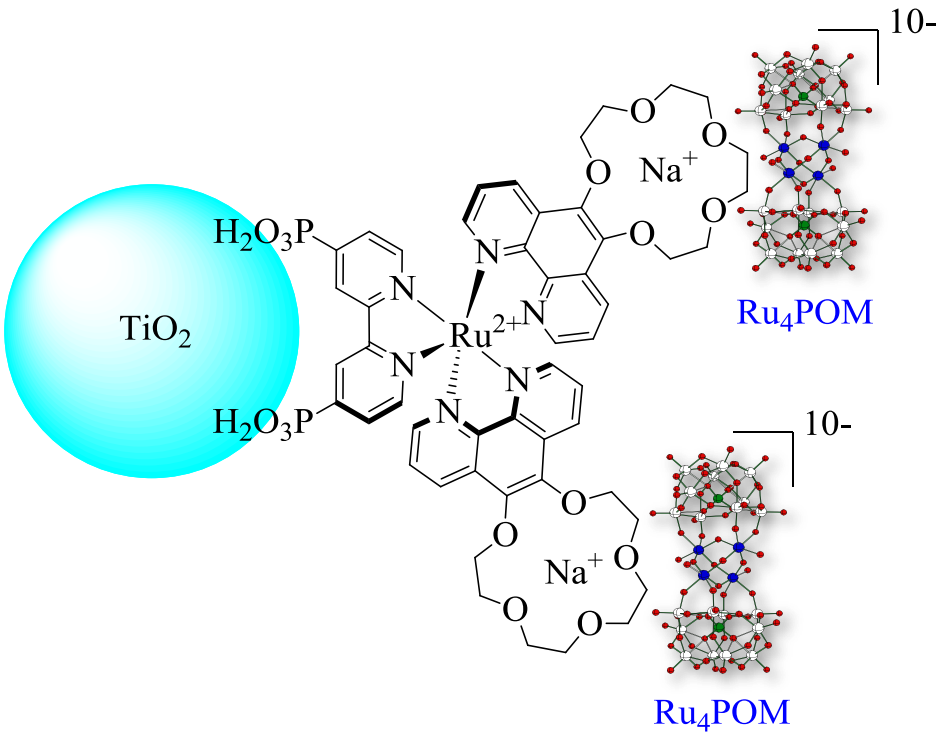

Figure 9.7. Schematic representation of the TiO_2/RuC2/Ru_4POM triadic construct. The Na^+ can be replaced by other cation of various positive charges.

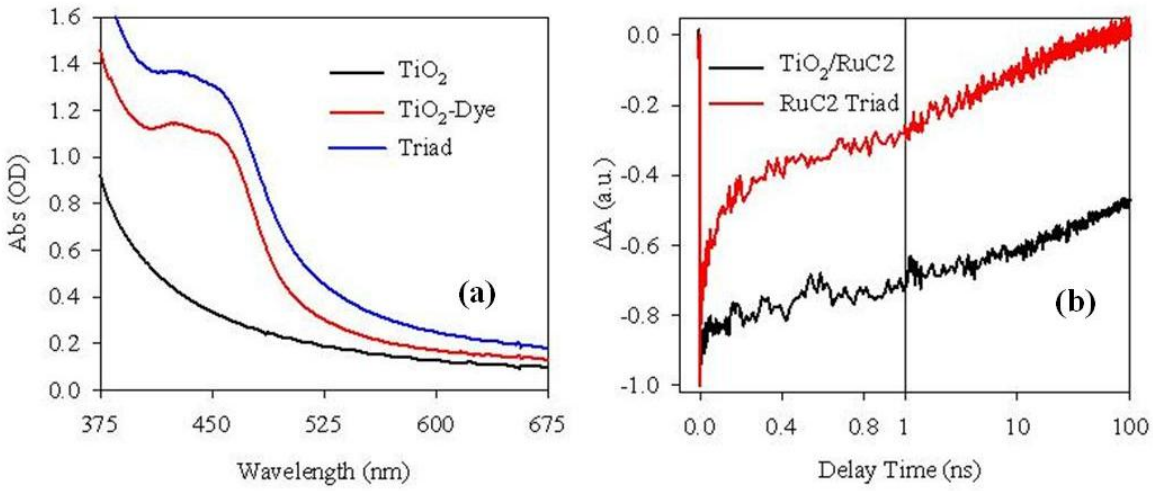

Figure 9.8. (a) UV-Vis absorption spectra of TiO_2 (black line), TiO_2/RuC2 (red line), and the RuC2 triad (blue line). (b) Transient kinetics of TiO_2/RuC2 (black) and the RuC2 triad (red) at 475 nm after 400 nm excitation. The decay time is in linear scale in the left panel (~0.1-1 ns) and in logarithmic scale in the right panel (1-100 ns).

9.3 Photoelectrochemical performance

These strongly associated SMO-sensitizer-WOC triads using zwitterionic Ru-polypyridal dyes were designed not only for spectroscopic studies but, more importantly, to serve as efficient photoanodes in practical photoelectrochemical (PEC) water-splitting cells. The hydrolytic and oxidative stability of these triadic components are essential for optimal PEC performance.

In the water oxidation triads, the electrons of the photogenerated charge transfer excited states of the sensitizer are transferred to the SMO substrate, while the holes of these states sequentially oxidize the attached WOC. The performance of such triads can be evaluated by connecting them to an external circuit, such that the photoinjected electrons are immediately removed from the anode to reduce H_2O to H_2 at the cathode.

The latter can be equipped with a water (or CO_2) reduction catalyst. The developed triadic photoanodes were tested in a home-made three-electrode cell under visible light illumination. A schematic illustration of our PEC set up is shown in Figure 9.9.

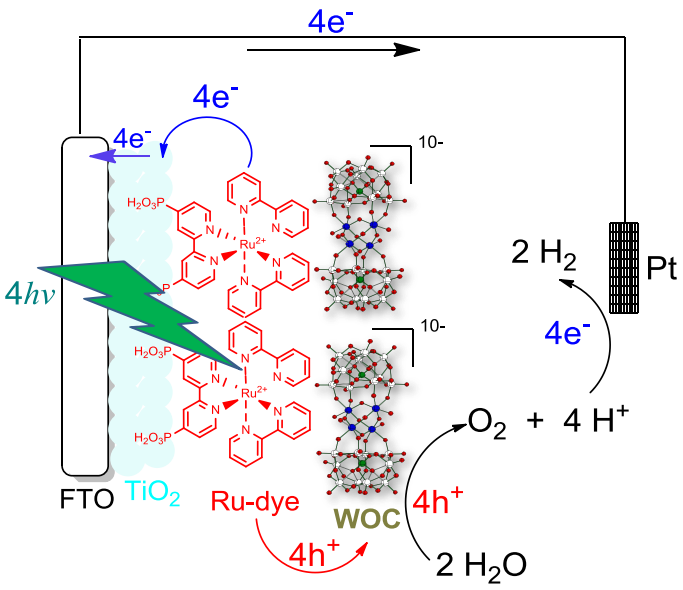

Figure 9.9. Schematic representation of a water splitting system using RuP2 supported on a nanoporous TiO_2 substrate as photosensitizer, and the attached Ru_4POM as WOC. Counter electrode: Pt; Reference electrode: Ag/AgCl (3M NaCl); Light source: Xenon lamp (filtered to 450–470 nm).

Preliminary photoelectochemical studies on TiO_2/RuP2/Ru_4POM and TiO_2/RuC2-/Ru_4POM triad electrodes show enhanced currents upon irradiation (Figure 9.10). However, a certain level of hydrolysis is hampering these studies. Further investigation of buffers, surface protection and other conditions to minimize this problem are necessary. Qualitatively, these studies have shown that triad electrodes are more stable than simple TiO_2-dye electrodes, and that RuC2 based triads are more stable than RuP2 based triads.

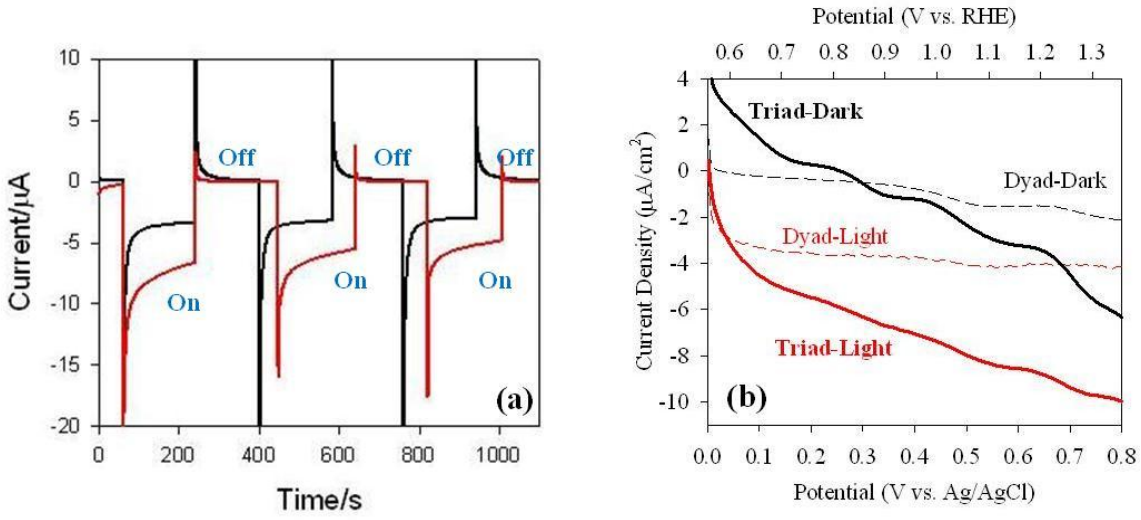

Figure 9.10. Performance tests of the RuP2-based dyadic and triadic photoanode. (a) I-t profile under illumination with dark intervals. (b) Cyclic voltammetry of the electrodes under illumination and in the dark. Electrolyte: 3~5mM Na_2SiF_6-$NaHCO_3$ (pH=5.8); Illumination: 450-470 nm; Reference: Ag/AgCl, 3 M NaCl; Counter electrode: Pt.

It is worthy to note that wiggle CV features in Figure 9.10b are probably indicative of the different oxidation states in Ru_4POM.[29,30] In this regard, combination of the PEC setup with the transient spectroscopic techniques, as shown in Figure 9.11, can provide a new approach to study the sequential 4-electron transfer dynamics in these systems as long as particular external biases are used for pre-oxidization of the WOC to certain oxidation states.

In addition, for this specific charge transfer studies, aqueous systems are not necessarily involved. To reduce the complexity of the system and also to improve the stability of the linkage, an innocent organic environment with appropriate ionic electrolytes would be a more promising approach.

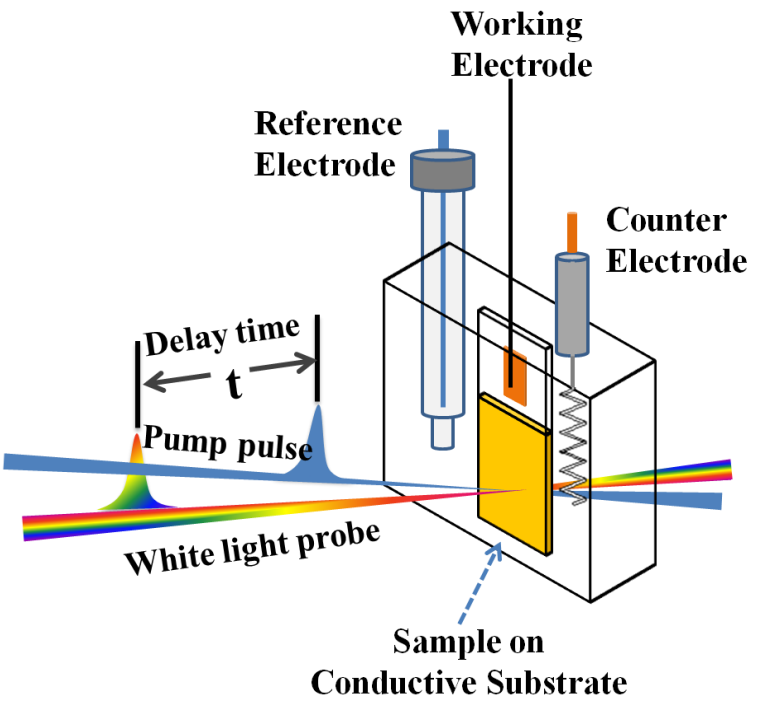

Figure 9.11. Schematic representation of the EC-TAS technique, combining both the electrochemistry and transient absorption spectroscopy.

9.4 Conclusion

TiO_2-Ru dye-Ru_4POM triads have been assembled using RuP2 and RuC2. All systems show ultrafast electron transfer as indicated by substantial bleach recovery in < 1 ns. For the RuP2 system, transient IR measurements confirm that the overall direction of electron transfer is from Ru_4POM to TiO_2. Preliminary photoelectochemical studies on TiO_2/RuP2/Ru_4POM and TiO_2/RuC2/Ru_4POM triads/electrodes show enhanced currents upon irradiation.

9.5 References

(1) Chow, J.; Kopp, R. J.; Portney, P. R. *Science* **2003**, *302*, 1528.

(2) Lewis, N. S.; Nocera, D. G. *Proc. Nat. Acad. Sci.* **2006**, *103(43)*, 15729.

(3) Balzani, V.; Credi, A.; Venturi, M. *ChemSusChem* **2008**, *1*, 26.

(4) Kanan, M. W.; Nocera, D. G. *Science* **2008**, *321*, 1072.

(5) Flamigni, L.; Collin, J.-P.; Sauvage, J.-P. *Acc. Chem. Res.* **2008**, *41*, 857.

(6) Magnuson, A.; Anderlund, M.; Johansson, O.; Lindblad, P.; Lomoth, R.; Polivka, T.; Ott, S.; Stensjö, K.; Styring, S.; Sundström, V.; Hammarström, L. *Accts. Chem. Res.* **2009**, *42*, 1899.

(7) Gust, D.; Moore, T. A.; Moore, A. L. *Accts. Chem. Res.* **2009**, *42*, 1890.

(8) Dau, H.; Zaharieva, I. *Accts. Chem. Res.* **2009**, *42*, 1861.

(9) Huang, Z.; Geletii, Y. V.; Wu, D.; Anfuso, C. L.; Musaev, D. G.; Hill, C. L.; Lian, T. *Proc. SPIE* **2011**, *8109*, 810903.

(10) Anderson, N. A.; Lian, T. *Coord. Chem. Rev.* **2004**, *248*, 1231.

(11) Youngblood, W. J.; Lee, S.-H. A.; Kobayashi, Y.; Hernandez-Pagan, E. A.; Hoertz, P. G.; Moore, T. A.; Moore, A. L.; Gust, D.; Mallouk, T. E. *J. Am. Chem. Soc.* **2009**, *131*, 926.

(12) Youngblood, W. J.; Lee, S.-H. A.; Maeda, K.; Mallouk, T. E. *Accts. Chem. Res.* **2009**, *42*, 1966.

(13) Spiccia, L.; Brimblecombe, R.; Koo, A.; Dismukes, G. C.; Swiegers, G. F. *J Am Chem Soc* **2010**, *132*, 2892.

(14) Spiccia, L.; Brimblecombe, R.; Koo, A.; Dismukes, G. C.; Swiegers, G. F. *ChemSusChem* **2010**, *3*, 1146.

(15) Xu, Y. H.; Duan, L. L.; Tong, L. P.; Akermark, B.; Sun, L. C. *Chem Commun* **2010**, *46*, 6506.

(16) Orlandi, M.; Argazzi, R.; Sartorel, A.; Carraro, M.; Scorrano, G.; Bonchio, M.; Scandola, F. *Chem Commun* **2010**, *46*, 3152.

(17) Pankove, J. I. *Optical Processes in Semiconductors*; Dover: New York, 1975.

(18) Marcus, R. A. *Annu Rev Phys Chem* **1964**, *15*, 155.

(19) Marcus, R. A. *Angew Chem Int Edit* **1993**, *32*, 1111.

(20) Marcus, R. A.; Sutin, N. *Biochim Biophys Acta* **1985**, *811*, 265.

(21) Ardo, S.; Sun, Y. L.; Castellano, F. N.; Meyer, G. J. *Journal of Physical Chemistry B* **2010**, *114*, 14596.

(22) Ardo, S.; Sun, Y.; Staniszewski, A.; Castellano, F. N.; Meyer, G. J. *J Am Chem Soc* **2010**, *132*, 6696.

(23) Pastore, M.; De Angelis, F. *J Phys Chem Lett* **2011**, *2*, 1261.

(24) Boxer, S. G. *Journal of Physical Chemistry B* **2009**, *113*, 2972.

(25) Kalyanasundaram, K. *Coordin Chem Rev* **1982**, *46*, 159.

(26) Song, W. J.; Brennaman, M. K.; Concepcion, J. J.; Jurss, J. W.; Hoertz, P. C.; Luo, H. L.; Chen, C. C.; Hanson, K.; Meyer, T. J. *J Phys Chem C* **2011**, *115*, 7081.

(27) Brennaman, M. K.; Patrocinio, A. O. T.; Song, W. J.; Jurss, J. W.; Concepcion, J. J.; Hoertz, P. G.; Traub, M. C.; Iha, N. Y. M.; Meyer, T. J. *ChemSusChem* **2011**, *4*, 216.

(28) She, C. X.; Anderson, N. A.; Guo, J. C.; Liu, F.; Goh, W. H.; Chen, D. T.; Mohler, D. L.; Tian, Z. Q.; Hupp, J. T.; Lian, T. Q. *Journal of Physical Chemistry B* **2005**, *109*, 19345.

(29) Geletii, Y. V.; Besson, C.; Hou, Y.; Yin, Q. S.; Musaev, D. G.; Quinonero, D.; Cao, R.; Hardcastle, K. I.; Proust, A.; Kogerler, P.; Hill, C. L. *J Am Chem Soc* **2009**, *131*, 17360.

(30) Geletii, Y. V.; Botar, B.; Koegerler, P.; Hillesheim, D. A.; Musaev, D. G.; Hill, C. L. *Angewandte Chemie-International Edition* **2008**, *47*, 3896.

Part VI: Heterogeneous systems: composite dyadic photoanodes

CHAPTER

10

Heterogeneous systems: composite dyadic photoanodes

Unpublished results

Abstract: This short chapter describes our extensive efforts to prepare and characterize low band gap oxide-WOC dyads for photocatalytic water oxidation using our molecular, tunable, and carbon-free POM-based WOCs. The low band gap oxide semiconductor used here is hematite (α-Fe_2O_3). It functions as the light harvesting component, overcoming the potential instability problem of organic containing sensitizers such as $Ru(bpy)_3^{2+}$ and derivatives.

10.1 Introduction

Many of the existing solar driven water oxidation systems use Ru-polypyridyl complexes as photosensitizers because of their large extinction coefficients in the visible region and long lived metal-to-ligand charge transfer excited states. [1-10] However, the polypyridyl ligand (and its derivatives) in these sensitizers are very likely to succumb to degradation long before the targeted number of turnovers is achieved in light-driven water splitting devices. This is true in part because water oxidation and splitting will involve production of hydroxyl radicals and other reactive oxygen species that will ultimately destroy all organic ligands and facilitate their conversion to the thermodynamically most stable products, CO_2 and H_2O.

In order to improve the oxidative and hydrolytic stability of the light-driven water splitting devices, it's of great potential importance to use inorganic light absorbers. One approach is to use nanocrystalline thin films as photoanodes. Numerous metal-oxide materials have been used directly as photocatalysts for water oxidation.[11,12] Since the pioneer work performed in 1972 by Fujishima and Honda,[13] enormous numbers of electrode materials have been explored.[12,14,15] However, band gaps of materials that can

effectively split water, such as TiO_2 are too large for practical solar energy conversion.[16,17] Doping TiO_2 to increase its absorption in the visible region or use of low band gap semiconductor materials has led to only limited success.[18-22] Alternatively, iron oxide (α-Fe_2O_3, hematite) has a band gap of 2.1 eV,[23] allowing for the absorption of ~40% of the incident sunlight energy.[24] In addition to its abundance and environmental compatibility, α-Fe_2O_3 is photoelectrochemically stable in various neutral and alkaline aqueous electrolytes.[25,26]

In addition, the photocatalytic efficiency can be improved by increasing the lifetime of the electron-hole pairs and the rate of the water oxidation reaction. This can be achieved by depositing efficient catalysts on the metal-oxide surface.[21,27-30] A few metal oxides or phosphates (RuO_2, Co_3O_4, Co-phosphate, IrO_2, etc) have been demonstrated to enhance the performance of the metal oxide electrode. For example, the deposition of Co oxide catalysts on α-Fe_2O_3 films was reported to enhance water oxidation photocurrents and shift their onsets to lower bias in photoelectrochemical cells.[27,28] These results suggest that oxide-catalyst heterostructures can indeed improve the efficiency of water oxidation. Unfortunately, the structure and performance of the oxide-catalyst heterostructures are not amenable to extensive optimization and molecular level investigations because the structures of these catalysts are largely unknown. Furthermore, even though the presence of IrO_2 yields the most efficient α-Fe_2O_3 photanode with a ~40% incident photon to current efficiency (IPCE) at 400 nm,[31] the total solar energy conversion efficiency remains ~2%, far lower than the maximum theoretical limit (13%) for a hematite photoanode.[32] Therefore, further improvement of the electrode

performance requires the incorporation of more efficient catalysts, such as molecular catalysts.

Recently WOCs based on polyoxometalate (POM) stabilized multi-d-electron-metal oxide clusters have been reported.[33-39] These carbon-free complexes combine the stability advantages of heterogeneous metal oxide catalysts with the several advantages of homogeneous catalysts (ease of experimental and computational investigation, some ability to control the geometrical and electronic structures around and at the active site, etc). While the tetra-cobalt POM, $[Co_4(H_2O)_2(PW_9O_{34})_2]^{10-}$ (henceforth "Co_4POM") is as fast as any WOC to date,[36] nearly all POM WOC evaluations to date have been conducted in solution (dark and light-driven reactions with different oxidants under a range of conditions). The behavior of these molecular catalysts when immobilized on anodes and photoanodes is important for several applications of WOCs. Combining our soluble, carbon-free WOCs with the colored/narrow-bandgap inorganic photoanode, hematite, can potentially lead to significantly more efficient and stable photocatalytic water oxidation systems. These systems can also have well-defined structures allowing for extensive optimization and molecular level investigations.

This chapter describes our efforts to construct well-defined, robust, and efficient all-inorganic hematite/WOC dyad photoanodes. Co_4POM has been proven to be stable in homogenous chemical or photochemical water oxidation systems, but its photoelectrochemical (PEC) stability on the semiconductor metal oxide anode remains a problem.[40] Although this issue has not been completely addressed, we have been working on the stability improvement. This short chapter reports the successful immobilization of Co_4POM on hematite, as shown in Figure 10.1. This involves a new type of POM

immobilization on surfaces based on the use of hydrophobic POM counterions that facilitates not only POM surface attachment but also to a certain degree protects the POM from concentrated aqueous hydroxide media. In the presence of the hydrophobic POM counterions, instead of general complete decomposition to Co oxide, the X-ray photoelectron spectroscopic (XPS) results indicate that the Co_4POM undergoes some structural transformation.

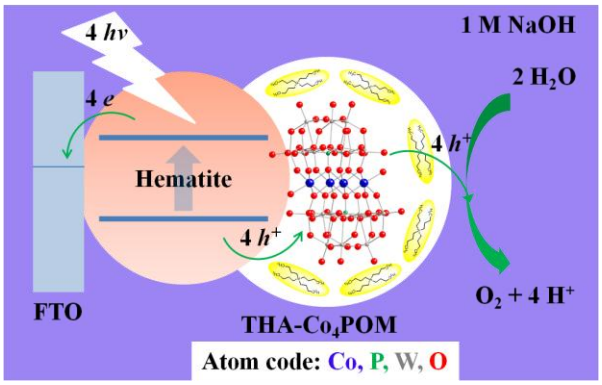

Figure 10.1. Surface structure and water oxidation at the hematite/THA-Co_4POM photoanode.

10.2 Results and discussion

WOC immobilization involves drop casting a toluene solution of the highly hydrophobic tetra-*n*-heptylammonium ($[CH_3(CH_2)_6]_4N^+$ or "THA") salt of Co_4POM on a hematite electrode surface followed by treatment with 1 M aqueous NaOH (details in the Chapter 2). These photoanodes were evaluated in 1 M NaOH electrolyte using a three-electrode photoelectrochemical cell with a saturated Ag/AgCl electrode and a Pt wire as the reference and counter electrodes, respectively.

The current density under illumination (320-720 nm, 100 mW/cm^2) increases two-fold (Figure 10.2) relative to the hematite electrode alone (no surface WOC coating).

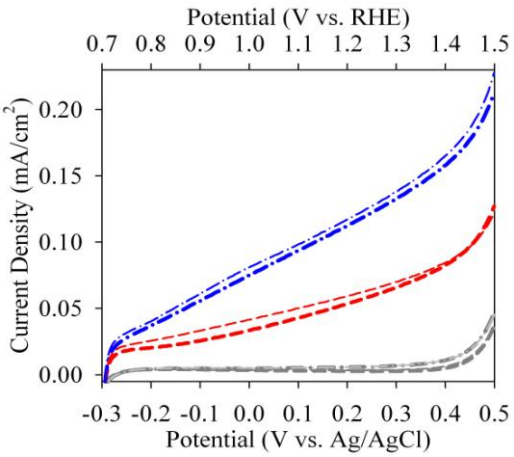

Figure 10.2. *I-V* characteristics under illumination of hematite (thick red dashes) and hematite/THA-Co_4POM after NaOH treatment (thick blue dash-dots), after washing with toluene (thin red dashes) and re-use of the film, i.e. re-applying the Co_4POM WOC (thin blue dash-dots). Grey lines are dark *I-V* plots for hematite (thick dashes) and hematite/THA-Co_4POM (thick dash-dots). Electrolyte: 1 M NaOH; scanning rate: 50 mV/s; illumination: 320-720 nm, 100 mW/cm^2.

Several experiments were conducted to clarify the significance of the results in Figure 10.2. First, this three-component photoanode was washed with toluene which has two immediate effects: it removes the hydrophobic Co_4POM from the photoanode based on spectroscopic measurements, and it reduces the photocurrent to that of bare hematite film (Figures 10.2). Second, this film after washing with toluene was re-usable (i.e. after re-application of the Co_4POM WOC, Figure 10.2). The current-voltage curves are identical after 10 scans and six minutes (Figure 10.3). Third, control experiments show

that hematite with a monolayer of $Co(NO_3)_2$, prepared by the well-known procedure,[41] results in similar degree of photocurrent enhancement as the Co_4POM-modified surface but exhibits markedly different *I-V* characteristics (Figure 10.4).

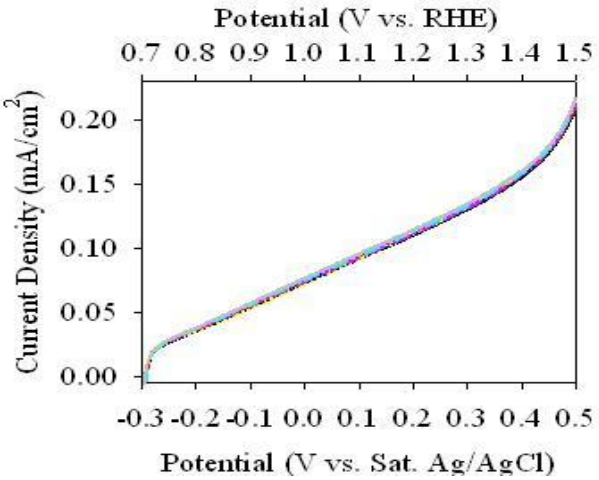

Figure 10.3. Ten *I-V* scans of the hematite/THACo_4POM electrode used for Figure 10.2.

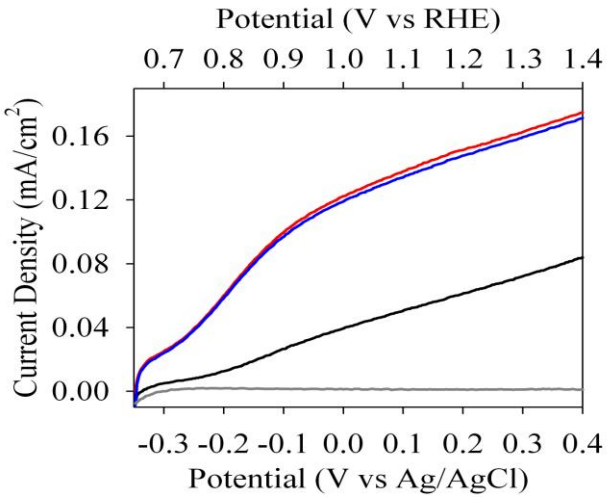

Figure 10.4. *I-V* characteristics under illumination of hematite (black), and hematite/$Co(NO_3)_2$ before (red) and after (blue) extensive toluene washing. The grey line indicates the dark current from the hematite film.

Several experiments address the stability of this new class of photoanodes. First, the many characteristic vibrational bands of the THA and Co_4POM[36,42,43] units are unchanged before and after use under PEC (photo-induced catalytic water oxidation) conditions (Figure 10.5). Second, the photoelectrochemical performance of the standard $Co(NO_3)_2$ coated hematite electorde,[41] is unaffected by extensive washing with toluene. Third, the degree of protection of the WOC complex from the concentrated hydroxide depends on the ratio of THA to Co_4POM. In strongly basic aqueous solutions of Co_4POM (e.g. $Na_{10}[Co_4(H_2O)_2(PW_9O_{34})_2]$ with no THA present) where water oxidation is thermodynamically more facile ($2H_2O \rightarrow 4H^+ + O_2, E_0$=1.23–0.059×pH V), this POM decomposes immediately. In the presence of 24 equivalents of THA per equivalent of Co_4POM, there is, remarkably, no detectable decomposition of the Co_4POM to Co oxide after extensive use (e.g. > 10 *I-V* scans). With insufficient protective THA counterions (THA:Co_4POM 7.4:1) present, there is slow decomposition of the Co_4POM to Co oxide and different *I-V* characteristics are exhibited (Figure 10.6).

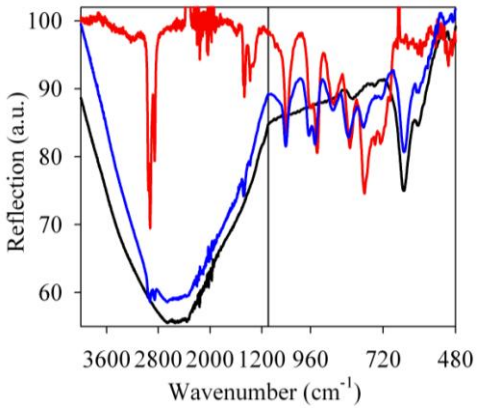

Figure 10.5. Attenuated total reflection infrared spectra of hematite/THA-Co_4POM electrode after photoelectrochemical use (blue), hematite (black) and THACo_4POM (red).

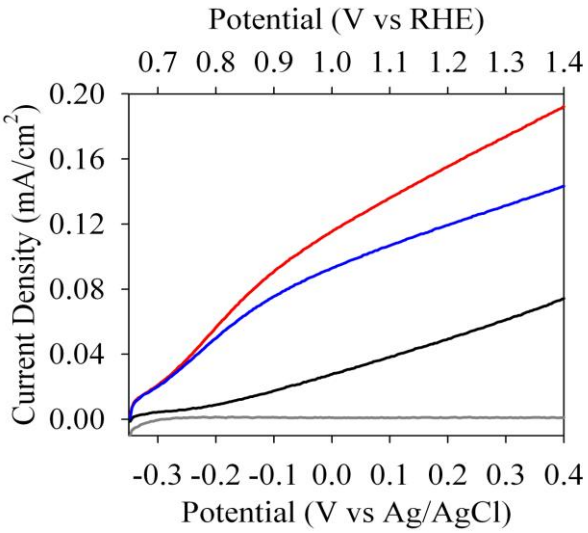

Figure 10.6. *I-V* characteristics under illumination of hematite (black), and hematite/THACo_4POM ($THA_{7.6}H_{2.4}[Co_4(H_2O)_2(PW_9O_{34})_2]$) before (red) and after (blue) toluene treatment. The grey line indicates the dark current of the hematite films.

In addition, SEM photomicrographs show no Co oxide presence on the films after use as photoelectrodes in 1M NaOH.

However, the XPS shows that the ratio of Co, P and W in the hematite-THACo_4POM electrodes is altered by use as a photoelectrode. This suggests that (1) it may be possible that some portion of Co_4POM in the sample remained intact, resulting in the appearance of the characteristic IR signals of Co_4POM; and (2) structural transformation occurs during the PEC experiments and the new species is an active WOC.

10.3 Conclusion

In conclusion, we show in this chapter a new type of POM immobilization on surfaces based on the use of hydrophobic POM counterions that facilitates not only POM surface attachment but also to a certain degree protects the POM from concentrated

aqueous hydroxide media. In the presence of the hydrophobic POM counterions, instead of general complete decomposition to Co oxide, the X-ray photoelectron spectroscopic (XPS) results indicate that the Co_4POM undergoes some structural transformation.

10.4 References

(1) Youngblood, W. J.; Lee, S.-H. A.; Kobayashi, Y.; Hernandez-Pagan, E. A.; Hoertz, P. G.; Moore, T. A.; Moore, A. L.; Gust, D.; Mallouk, T. E. *J. Am. Chem. Soc.* **2009**, *131*, 926.

(2) Youngblood, W. J.; Lee, S.-H. A.; Maeda, K.; Mallouk, T. E. *Accts. Chem. Res.* **2009**, *42*, 1966.

(3) Spiccia, L.; Brimblecombe, R.; Koo, A.; Dismukes, G. C.; Swiegers, G. F. *J Am Chem Soc* **2010**, *132*, 2892.

(4) Spiccia, L.; Brimblecombe, R.; Koo, A.; Dismukes, G. C.; Swiegers, G. F. *Chemsuschem* **2010**, *3*, 1146.

(5) Xu, Y. H.; Duan, L. L.; Tong, L. P.; Akermark, B.; Sun, L. C. *Chem Commun* **2010**, *46*, 6506.

(6) Reisner, E.; Powell, D. J.; Cavazza, C.; Fontecilla-Camps, J. C.; Armstrong, F. A. *J Am Chem Soc* **2009**, *131*, 18457.

(7) Woolerton, T. W.; Sheard, S.; Reisner, E.; Pierce, E.; Ragsdale, S. W.; Armstrong, F. A. *J Am Chem Soc* **2010**, *132*, 2132.

(8) Song, W. J.; Glasson, C. R. K.; Luo, H. L.; Hanson, K.; Brennaman, M. K.; Concepcion, J. J.; Meyer, T. J. *J Phys Chem Lett* **2011**, *2*, 1808.

(9) Song, W. J.; Brennaman, M. K.; Concepcion, J. J.; Jurss, J. W.; Hoertz, P. C.; Luo, H. L.; Chen, C. C.; Hanson, K.; Meyer, T. J. *J Phys Chem C* **2011**, *115*, 7081.

(10) Song, W. J.; Chen, Z. F.; Brennaman, M. K.; Concepcion, J. J.; Patrocinio, A. O. T.; Iha, N. Y. M.; Meyer, T. J. *Pure Appl Chem* **2011**, *83*, 749.

(11) Lewis, N. S.; Nocera, D. G. *P Natl Acad Sci USA* **2006**, *103*, 15729.

(12) Walter, M. G.; Warren, E. L.; McKone, J. R.; Boettcher, S. W.; Mi, Q. X.; Santori, E. A.; Lewis, N. S. *Chem Rev* **2010**, *110*, 6446.

(13) Fujishima, A.; Honda, K. *Nature* **1972**, *238*, 37.

(14) Kalyanasundaram, K. *Sol Cells* **1985**, *15*, 93.

(15) Kudo, A.; Miseki, Y. *Chem Soc Rev* **2009**, *38*, 253.

(16) Fujishima, A.; Honda, K. *Nature* **1972**, *238*, 37.

(17) Linsebigler, A. L.; Lu, G. Q.; Yates, J. T. *Chem Rev* **1995**, *95*, 735.

(18) Zhigang, Z.; Jinhua, Y.; Sayama, K.; Arakawa, H. *Nature* **2001**, *414*, 625.

(19) Maeda, K.; Takata, T.; Hara, M.; Saito, N.; Inoue, Y.; Kobayashi, H.; Domen, K. *J Am Chem Soc* **2005**, *127*, 8286.

(20) Maeda, K.; Teramura, K.; Lu, D.; Takata, T.; Saito, N.; Inoue, Y.; Domen, K. *Nature* **2006**, *440*, 295.

(21) Maeda, K.; Domen, K. *The Journal of Physical Chemistry C* **2007**, *111*, 7851.

(22) Liu, G.; Yang, H. G.; Wang, X.; Cheng, L.; Pan, J.; Lu, G. Q.; Cheng, H.-M. *J Am Chem Soc* **2009**, *131*, 12868.

(23) Lindgren, T. V., L.; Wang, H.; Lindquist, S.-E. *Chemical Physics of Nanostructured Semiconductors* **2003**, 83.

(24) Sun, J. W.; Zhong, D. K.; Gamelin, D. R. *Energ Environ Sci* **2010**, *3*, 1252.

(25) Dareedwards, M. P.; Goodenough, J. B.; Hamnett, A.; Trevellick, P. R. *J Chem Soc Farad T 1* **1983**, *79*, 2027.

(26) Zhong, D. K.; Gamelin, D. R. *J Am Chem Soc* **2010**, *132*, 4202.

(27) Zhong, D. K.; Sun, J.; Inumaru, H.; Gamelin, D. R. *J Am Chem Soc* **2009**, *131*, 6086.

(28) Kay, A.; Cesar, I.; GrÃ¤tzel, M. *J Am Chem Soc* **2006**, *128*, 15714.

(29) Cesar, I.; Kay, A.; Gonzalez Martinez, J. A.; GrÃ¤tzel, M. *J Am Chem Soc* **2006**, *128*, 4582.

(30) Cesar, I.; Sivula, K.; Kay, A.; Zboril, R.; GraÌˆtzel, M. *The Journal of Physical Chemistry C* **2009**, *113*, 772.

(31) Tilley, S. D.; Cornuz, M.; Sivula, K.; Gratzel, M. *Angew Chem Int Edit* **2010**, *49*, 6405.

(32) Murphy, A. B.; Barnes, P. R. F.; Randeniya, L. K.; Plumb, I. C.; Grey, I. E.; Horne, M. D.; Glasscock, J. A. *Int J Hydrogen Energ* **2006**, *31*, 1999.

(33) Geletii, Y. V.; Botar, B.; Kögerler, P.; Hillesheim, D. A.; Musaev, D. G.; Hill, C. L. *Angew. Chem. Int. Ed.* **2008**, *47*, 3896.

(34) Cao, R.; Ma, H.; Geletii, Y. V.; Hardcastle, K. I.; Hill, C. L. *Inorg. Chem.* **2009**, *48*, 5596.

(35) Geletii, Y. V.; Huang, Z.; Hou, Y.; Musaev, D. G.; Lian, T.; Hill, C. L. *J. Am. Chem. Soc.* **2009**, *131*, 7522.

(36) Yin, Q.; Tan, J. M.; Besson, C.; Geletii, Y. V.; Musaev, D. G.; Kuznetsov, A. E.; Luo, Z.; Hardcastle, K. I.; Hill, C. L. *Science* **2010**, *328*, 342.

(37) Huang, Z.; Luo, Z.; Geletii, Y. V.; Vickers, J.; Yin, Q.; Wu, D.; Hou, Y.; Ding, Y.; Song, J.; Musaev, D. G.; Hill, C. L.; Lian, T. *J. Am. Chem. Soc.* **2011**, *133*, 2068.

(38) Sartorel, A.; Carraro, M.; Scorrano, G.; Zorzi, R. D.; Geremia, S.; McDaniel, N. D.; Bernhard, S.; Bonchio, M. *J. Am. Chem. Soc* **2008**, *130*, 5006.

(39) Besson, C.; Huang, Z.; Geletii, Y. V.; Lense, S.; Hardcastle, K. I.; Musaev, D. G.; Lian, T.; Proust, A.; Hill, C. L. *Chem. Commun.* **2010**, 2784.

(40) Stracke, J. J.; Finke, R. G. *J. Am. Chem. Soc* **2011**, *133*, 14872.

(41) Kay, A.; Cesar, I.; Grätzel, M. *J. Am. Chem. Soc.* **2006**, *128*, 15714.

(42) Rocchiccioli-Deltcheff, C.; Thouvenot, R.; Franck, R. *Spectrochimica Acta* **1976**, *32A*, 587.

(43) Rocchiccioli-Deltcheff, C.; Fournier, M.; Franck, R.; Thouvenot, R. *Inorg. Chem.* **1983**, *22*, 207.

Part VI: Heterogeneous systems: composite dyadic photoanodes

CHAPTER

11

Photophysics of Hematite Photoanodes

Unpublished work

Abstract: This chapter reports our transient studies on hematite electrodes on the fs-to-μs time scale, showing for the first time the clear transient spectra after optical excitation. This chapter also summarizes our efforts to collect direct evidence for the transient spectral assignments.

11.1 Introduction

Photoelectrochemical water splitting ($H_2O + h\nu \rightarrow H_2 + ½ O_2$) is a promising approach to convert solar flux into chemical energy stored in the form of hydrogen for energy and environmental sustainability.[1,2] Since the pioneer work performed in 1972 by Fujishima and Honda,[3] enormous numbers of electrode materials have been explored[1,4-8]. One of the most attractive is iron oxide (α-Fe_2O_3, hematite).[9-11] This oxide has a band gap of 2.1 eV,[12] allowing for the absorption of ~40% of the incident sunlight energy.[11] In addition to its abundance and environmental compatibility, α-Fe_2O_3 is photoelectrochemically stable in various neutral and alkaline aqueous electrolytes.[13,14] However, these advantages are balanced against other less desirable intrinsic properties, such as insufficient reduction potential of the conduction band electron, high resistence,[15] short hole-diffusion length[16], short-lived excitons[17], and slow surface O_2 evolution kinetics.[14,18-21] Many effective approaches have been employed to overcome these less-desired properties, including tandem cell configuration [22-24], surface water oxidation catalysts (WOCs),[14,18-21], impurity doping[18,25,26] and nano-scale morphology engineering.[27-31] However, the current highest solar energy conversion efficiency remains ~2% using a hematite/IrO_2 WOC photoanode, far lower than the maximum theoretical limit (13%) for a hematite photoanode.[32]

To further improve the solar conversion efficiency, a thorough understanding of the interfacial charge transfer dynamics and their dependence on the applied bias and attached surface WOCs in these hematite-based systems is crucial. Indeed, even the photophysics of this photoanode material is highly interesting. However, this is an area that remains highly unexplored, in contrast to the wide-bandgap mesoporous TiO_2. [33-46]

Optical excitation of the semiconductor generates electrons and holes. The holes can oxidize water molecules or recombine with the electron. The competition between these pathways determines the photocatalytic efficiency. To date, the transient spectral assignment and the kinetics of the photo-generated carriers in hematite from ultrafast studies are still not clear. In 1984, Nozik et. al. showed that dumping electrons by radiolysis into iron oxide resulted in absorption enhancement above 500 nm.[47] Therefore, it was generally believed that the conduction band electrons have a broad absorption feature. This study was the basis of almost all reports[48-54] before 2011 about hematite charge carrier dynamics on the fs- and ps- time scale.[17] All these early transient studies focused on fs-to-ns timescales and often employed high excitation conditions, showing extremely short-lived spectral features (< 100 ps). These findings had been typically used to account for the notoriously low incident-photon-to-current-conversion efficiency (IPCE) before the new benchmark from a new dendritic-nanostructured hematite photoanode.[18]

However, more recent studies (with a better signal-to-noise ratio for kinetic studies) by Durrant and co-workers[55-57] showed that the recombination rate is excitation power (or electron-hole concentration) dependent and the process obeys a power law. Under their excitation power (~0.2 mJ/cm^2), their transient absorption (TA) spectra of

nanoporous hematite films measured in an argon atmosphere are characterized by a long-lived (μs-to-ms) absorption peak at 580 nm and a tail that extends to the near IR. They also show that, in the presence of WOCs or under positive biases, the lifetime is lengthened, while the addition of a hole acceptor (methanol) reduced it dramatically. Therefore, they assigned the absorption band at 580 nm to trapped holes in hematite. However, due to the limitation of their set up, high-resolution spectra are impossible to achieve, and thus a definitive spectral assignment is questionable. Despite that, these new studies put the spectral assignment (hole, electron, trapped hole, trapped electron, surface species, etc.) of transient species in hematite under debate. Therefore, more clear transient spectra are necessary for confirming the transient spectral assignment in order to elucidate the interfacial charge transfer dynamics and their dependence on the applied bias and attached surface WOCs.

This chapter reports our transient study on the hematite electrode on the fs-to-μs time scale, showing for the first time clear transient spectra. This chapter also summarizes our efforts to collect direct evidence for the transient spectral assignments.

11.2 Results and discussion

11.2.1 Electronic spectra of hematite

Hematite has a corundum structure, where the arrangement of the cations and anions produces distorted $Fe(O)_6$ octahedra with the d^5 high spin Fe^{3+} center.[58] Interestingly, the high-spin d^5 configuration arranges in a way with spins coupled ferromagnetically in the (001) basal planes and anti-ferromagnetically along the [001] direction, leading to anisotropy in charge transport.[59,60]

The distorted octahedral structural features and the magnetic coupling between the adjacent Fe^{3+} octahedral centers make it so that the forbidden *d-d* transitions in a perfect, isolated high-spin d^5 octahedron are allowed. It is generally believed that two types of *d-d* electronic transitions exist in hematite: high-spin d^5 transitions and the pair excitations resulting from the simultaneous excitation of two neighboring Fe^{3+} cations that are magnetically coupled.[61-63] Shown in Figure 11.1 is a UV-Vis spectrum of a hematite film. This film was synthesized using electrochemical deposition methods and consists of hematite nanoparticles with diameters between 50 and 80 nm.[31,64] The static absorption spectrum can be well fit to a multiple-Gaussian function. The resolved transitions are consistent with literature simulation values as shown in Table 11.1.[63]

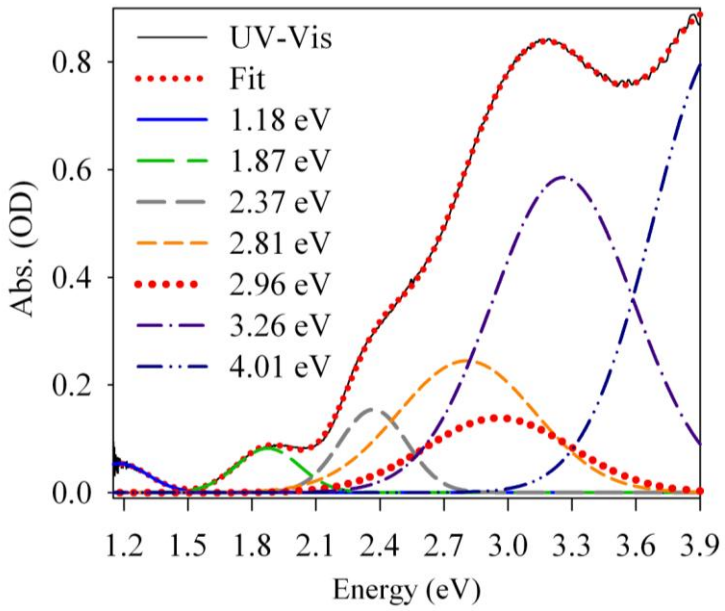

Figure 11.1. UV-Vis spectrum (black) of a hematite film. Synthesis details can be found elsewhere.[31,64] The UV-Vis spectrum is fit to a multiple-Gaussian function. The fitting result (red dots) shows a good agreement with the UV-Vis spectrum. Each Gaussian component is shown and indicated by the position of its center.

Table 11.1. *d-d* transitions in hematite.

[a] Transition	$^6A_1 \rightarrow {}^4T_1$	$^6A_1 \rightarrow {}^4T_2$	$2(^6A_1) \rightarrow 2(^4T_2)$	$^6A_1 \rightarrow {}^4E, {}^4A_1$	$^6A_1 \rightarrow {}^4T_2$	$^6A_1 \rightarrow {}^4E$	$^6A_1 \rightarrow {}^4T_1$
Literature (nm)	884	649	529	444	404	380	319
Fit (nm)	1050	661	523	441	419	381	309

[a] These transitions can be seen more easily in a Tanabe-Sugano diagram for high-spin Fe^{3+} (d^5) in octahedral coordination.[63]

In addition to the *d-d* transitions originating from the ligand field induced d-orbital splitting (a typical example of the Stark effect), there are two types of band-to-band transitions: the ligand to metal charge-transfer (LMCT) transition and the inter-valence charge-transfer (IVCT) transition.

In general, the valence band of a 3*d*-transition metal oxide consists mainly of the O2*p* band, while the conduction band is formed primarily by the 4s band of the transition metal anion. A partially filled 3*d* band, located between the 4s and O2*p* bands, can also be an important contribution to the valence band. The LMCT transition for hematite occurs at >3.5 eV, while the bandgap of hematite measured in photoelectrochemistry is ~2.2 eV. Therefore, the generally known bandgap transition in hematite is not due to the direct intense LMCT transition. In fact, in addition to the LMCT transition, there is another model to account for the band-to-band transition. It has been shown that the activation energy for the "intrinsic" conduction to create a Fe^{2+}/Fe^{4+} pair is ~2 eV. [65] Therefore, the ~2 eV bandgap originates from the charge transfer between neighboring Fe^{3+} ions. The two band-to-band transition models are well presented in a drawing by Matsumoto,[66] as shown in Figure 11.2.

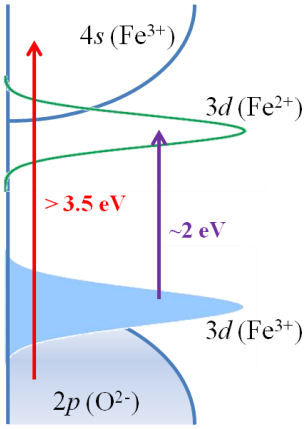

Figure 11.2. Band structure of iron oxide (**redrawn from reference**[66]).

11.2.2 Femtosecond visible measurements

Shown in Figure 11.3 are fs-transient spectra after 400 nm excitation. The main features associated with these spectra are bleach bands below 460 and at 525 nm, clear absorption bands at 470, 500 and 570 nm, and a featureless broad absorption above 570 nm. Furthermore, a clear isosbestic point at 555 nm exists in the normalized spectra (Figure 11.3b). Spectral evolution occurs initially until it reaches a stable spectral shape after about 100 ps, which can be clearly seen in the normalized spectra (Figure 11.3b). However, the isosbestic point exists at all delay times in the normalized spectra. Therefore, this can be contributed to a long-lived species that exists in all the transient spectra. Before 100 ps, therefore, different components appear and evolve with distinct kinetics. Due to these spectral characteristics, these long-lived components can be removed from the transient spectra after some simple spectral manipulations.

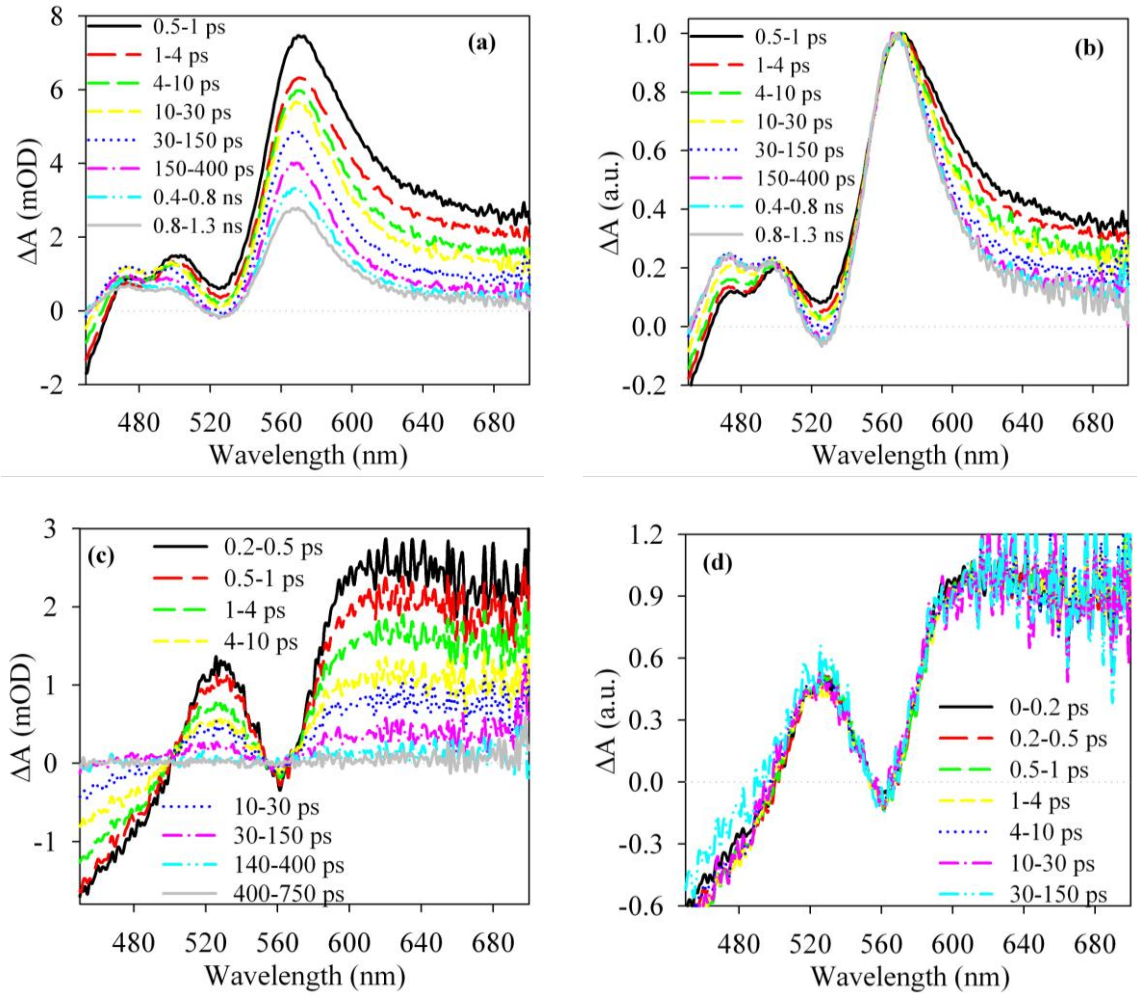

Figure 11.3. (a) Average transient visible spectra of hematite after 400 nm excitation (170 nJ/pulse); (b) Normalized spectra in (a); (c) The resulting average spectra after the spectral subtraction described in the text; (d) Normalized spectra in (c).

To remove these long-lived features, the spectra from 750 – 1300 ps were averaged and scaled to have the same amplitude at the isosbestic point (555 nm) at all delay times. This scaled spectrum was then subtracted from the original spectra for each delay time; the resulting spectra are shown in Figure 11.3c. These spectra have clear bleach (< 450 and 560 nm) and absorption (525 and > 600 nm) bands, which are short-

lived and disappear after about 100 ps. Several isosbestic points (at 500, 555 and 565 nm) exist and suggest that all the spectral features follow the same kinetics. This is confirmed to be the case by the corresponding normalized spectra compared in Figure 11.3d. The normalized spectra are only plotted at early times, as these spectra disappear after 150 ps. The featureless and short-lived band above 600 nm agrees with most of the early literature results, which state that the photogenerated charge carriers are extremely short lived and > 80% recovers within 10 ps. [17,48-54] In these early reports, these results are assigned to the transient signal of the electrons in the conduction band based on the radiolysis study in 1984 as mentioned above. [47] This short-lived signal is also confirmed by a recent study[67] that probed the transient absorption signal at 800 nm where the long-lived components have very little absorption contribution. This short-lived species is generally believed to be assigned to the ultrafast carrier-trapping process in colloidal metal oxide nanoparticles.[38,39,68,69] However, there is no direct experimental evidence for this assignment.

To better understand the origins of the transient features, we conducted the same measurements on films synthesized from other approaches. Shown in Figure 11.4a are UV-Vis spectra of three flat, crystalline hematite films of different thicknesses grown by an atomic layer deposition technique.[70] Compared to the UV-Vis spectrum of the nanoparticle film (Figure 11.1), the spectral features are consistent, while the long tail above 600 nm is probably due to scattering.

The transient spectra of the film with medium thickness are displayed in Figure 11.4b and 11.4c. Results for the other two films are not shown due to their similarities. All the features in the transient spectra of the nanoparticle film are also present in Figure

11.4b and 11.4c. Similarly, as shown in Figure 11.4d, these transient spectra primarily consist of two components with different kinetics.

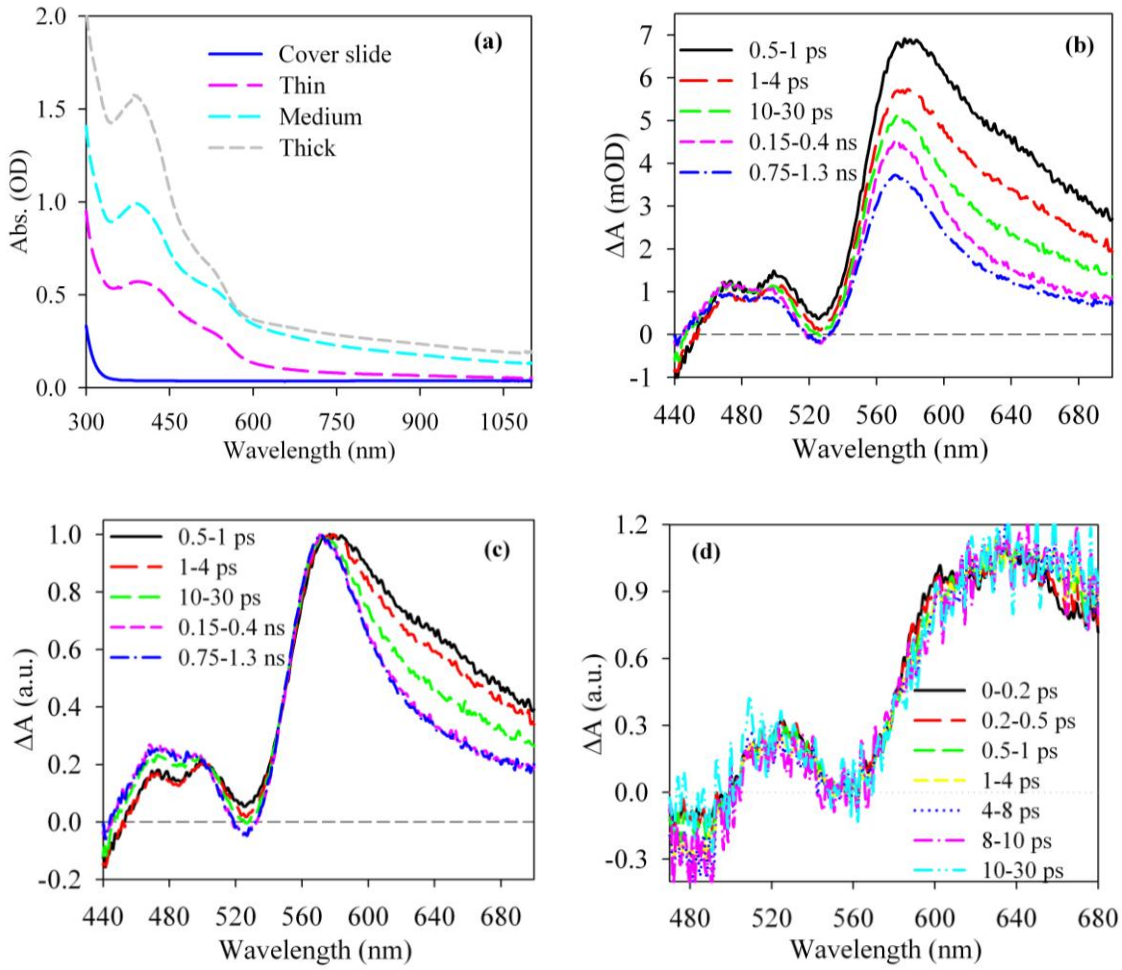

Figure 11.4. (a) UV-Vis spectra of films synthesized by atomic layer deposition techniques. Synthetic method can be found elsewhere.[71] (b) Average transient visible spectra of the medium hematite film after 400 nm excitation (170 nJ/pulse); (c) Normalized spectra in (b); (d) The resulting normalized average spectra after the spectral subtraction described in the text.

The transient kinetics of the resulting species after the spectral subtraction are shown in Figure 11.5. The normalized kinetic traces do not depend on the samples and thus probably originate from some intrinsic properties of hematite solid yet to be known. These kinetics reveal the resulting signals after spectral subtraction are short-lived, with a lifetime of about 10 ps.

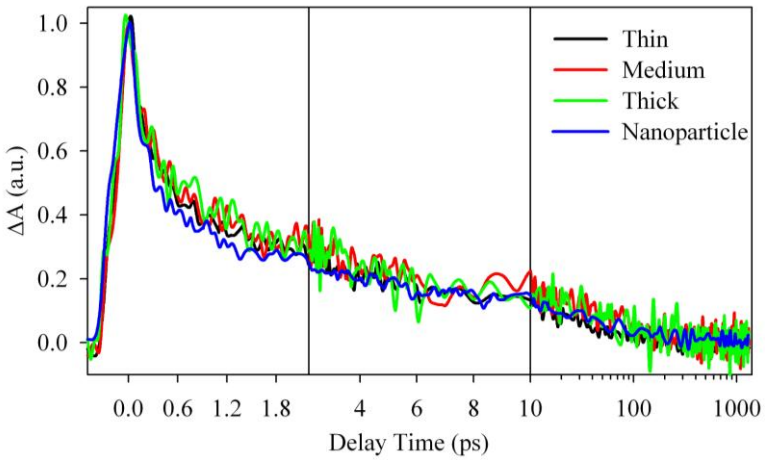

Figure 11.5. Transient kinetics of the resulting spectra after spectral subtraction as discussed in the text. These kinetics are monitored at 625 nm. The x-axis of the right panel is plotted in a logarithmic scale.

We have also performed transient studies on a hematite colloid solution. Shown in Figure 11.6a is the UV-Vis spectrum of the hematite colloid in aqueous solution at neutral pH. The main absorption features of solid films (Figure 11.1 and Figure 11.4a) can still be recognized here. The transient spectra (Figure 11.6b) of the colloidal solution also show characteristic bands similar to that in the solid films. This suggests that transitions associated with these excited-state spectral features are intrinsic to the hematite materials. However, the normalized spectra (Figure 11.6c) are identical at all

delay times, excluding a spectral evolution process as seen for the solid films. In addition, the excited state is short-lived as shown in Figure 11.6d, and decays > 85% in 100 ps. This is very different from the kinetics of the solid films monitored at the isosbestic point (~555 nm) of the normalized spectra, which extends into the microsecond time scale and will be discussed later.

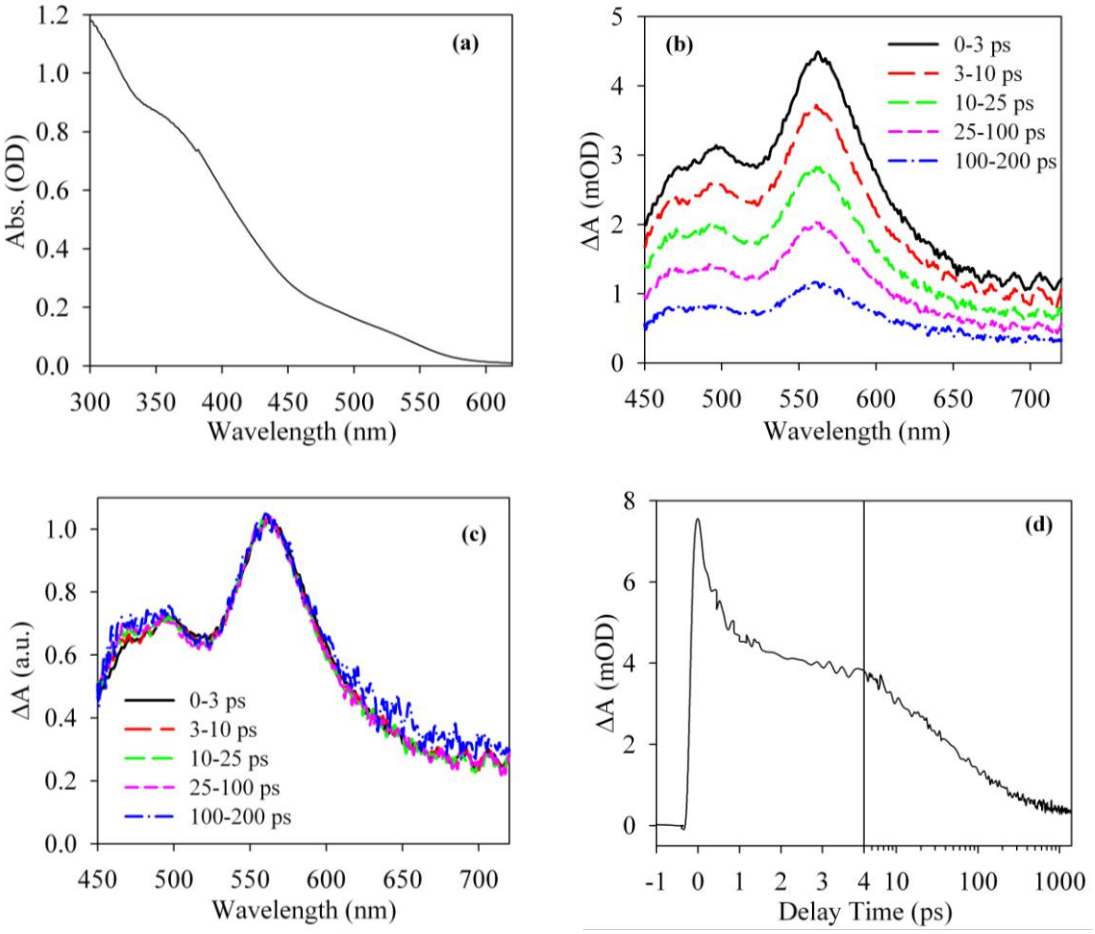

Figure 11.6. (a) UV-Vis spectra of a colloidal hematite aqueous solution synthesized by hydrolysis methods. Synthetic details can be found elsewhere.[72] (b) Average transient visible spectra after 400 nm excitation; (c) Normalized spectra in (b); (d) Transient kinetics monitored at 560 nm. The x-axis of the right panel in (d) is in a logarithmic scale.

The transient dynamics of the photoinduced charge carriers in hematite were first reported in 1998 by Zhang et. al.,[17] where only the kinetic traces at several wavelengths above 650 nm were shown. Based on these kinetic analyses, the authors concluded that the charge carriers are extremely short-lived. Indeed, as shown in Figure 11.4, there is an ultrafast decaying feature, which decays > 80% within 10 ps, as shown in Figure 11.5a. However, the kinetics of the transient species are wavelength-dependent, as reported later.[48,50,51,69] This can also clearly be seen in the normalized spectra of the solid films in Figure 11.3b and 11.4c. This property indicates that the transient spectra originate from more than one species. Therefore, a clear transient spectrum is necessary in order to clarify the transient dynamics and to identify the transient species after photoexcitation.

Transient spectra in the first several ps have been reported. Nadtochenko et. al. presented the first transient spectra of hematite, showing only an extremely short-lived featureless broad absorption band above 400 nm up to the near-IR.[49] However, these spectra are questionable due to the low signal-to-noise quality. The second report on the transient spectra of hematite (5 nm in toluene) was by Zou et.al, where they showed a broad absorption band (500 – 700 nm) that peaks at ~530 nm.[53] Spectral analysis was again hampered by the data quality. The third (and also the last) report on this time scale was published very recently by Zhang et. al.[69], where, however, only a single transient spectrum at 0.5 ps above 550 nm was shown. This spectrum seems to be a broad absorption band with a peak at ~570 nm, similar to the early time spectra of the solid films here (Figure 11.3b and Figure 11.4c). In any case, all these spectral components are shown to be extremely short-lived, with > 80% decay within 10 ps. This is difficult to

connect with the recently reported high IPCE (> 40%) using hematite photoanodes.[9,18,22,30]

On the μs-to-ms time scale, Durrant el. al have shown high-quality transient kinetics of hematite films at different wavelengths.[55,56,73] However, the transient spectra they have obtained are not good enough for clear spectral assignment. The low-resolution spectra that results from connecting the signals at merely several wavelengths only show a single absorption band that peaks at ~580 nm.

As mentioned above, the assignment of the transient spectral features is under debate. The radiolysis experiments by Nozik show that adding electrons to hematite results in a broad absorption feature above 500 nm,[47] while accumulated PEC evidence shows that the signal at ~580 nm is due to the trapped holes after photoexcitation. Therefore, the first clear transient absorption spectra with many fine spectral structures revealed here is crucial to solving these inconsistencies and to bridging the gap between studies on the fs-to-ns and μs-to-ms time scales. In this regard, the assignment of the spectral features is essential.

11.2.3 Nanosecond visible measurements

Shown in Figure 11.7a are average ns transient spectra of a solid hematite film at indicated delay times. Given that our probe pulse has a width of ~0.5 ns, spectra before 0.5 ns time delay after the optical excitation are missing. As shown previously, however, in the fs results (Figure 11.3), the spectral evolution only occurs in the first 100 ps. Therefore, we can expect that all the spectra at different delay-time windows should only

differ in amplitude. This is the case as shown in Figure 11.6b where all the normalized spectra from 0 to 6 μs are the same.

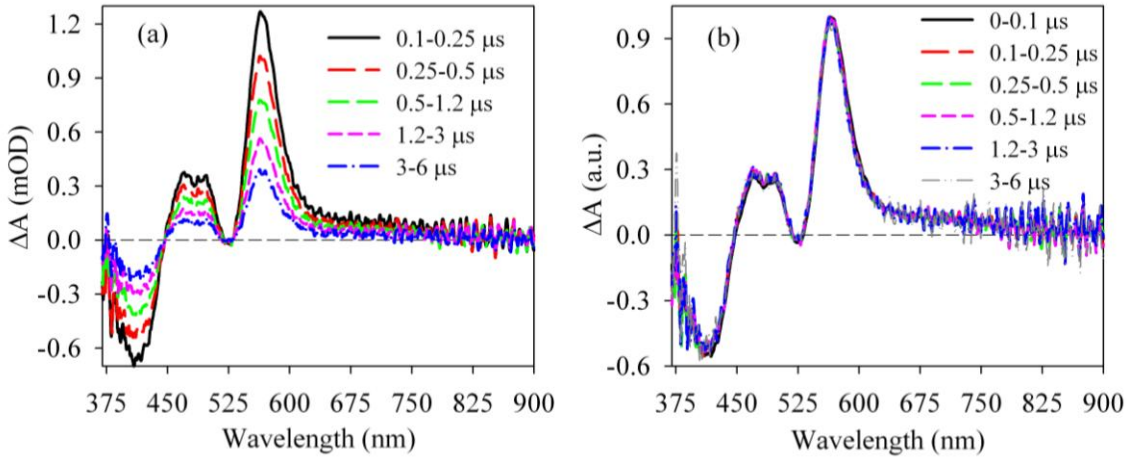

Figure 11.7. Average transient visible spectra of hematite after 400 nm excitation. (a) Original spectra from 0.1 – 6 μs; (b) Normalized spectra.

The transient kinetics of the solid films monitored at 555 nm (the isosbestic point of the normalized transient spectra) are compared in Figure 11.8a. Within the first 3 ps, the kinetics decay about 50%. Following this ultrafast component, the signals decay with only slight changes in amplitude within 100 ps. After that, the spectra gradually decay into the microsecond and even longer time scales. The corresponding long-lived spectral feature is probably the one that was identified in Durrant's works. [55,56,73]

In addition, these kinetics are sample-dependent. The most obvious differences occur after 100 ps. Hence, the kinetics are compared in Figure 11.8b, where the kinetic traces are normalized to the signal at 100 ps. Although the origins of this dependence are under investigation, Figure 11.8b shows a clear trend that the decay rates of the excited state increase with decreasing film thickness.

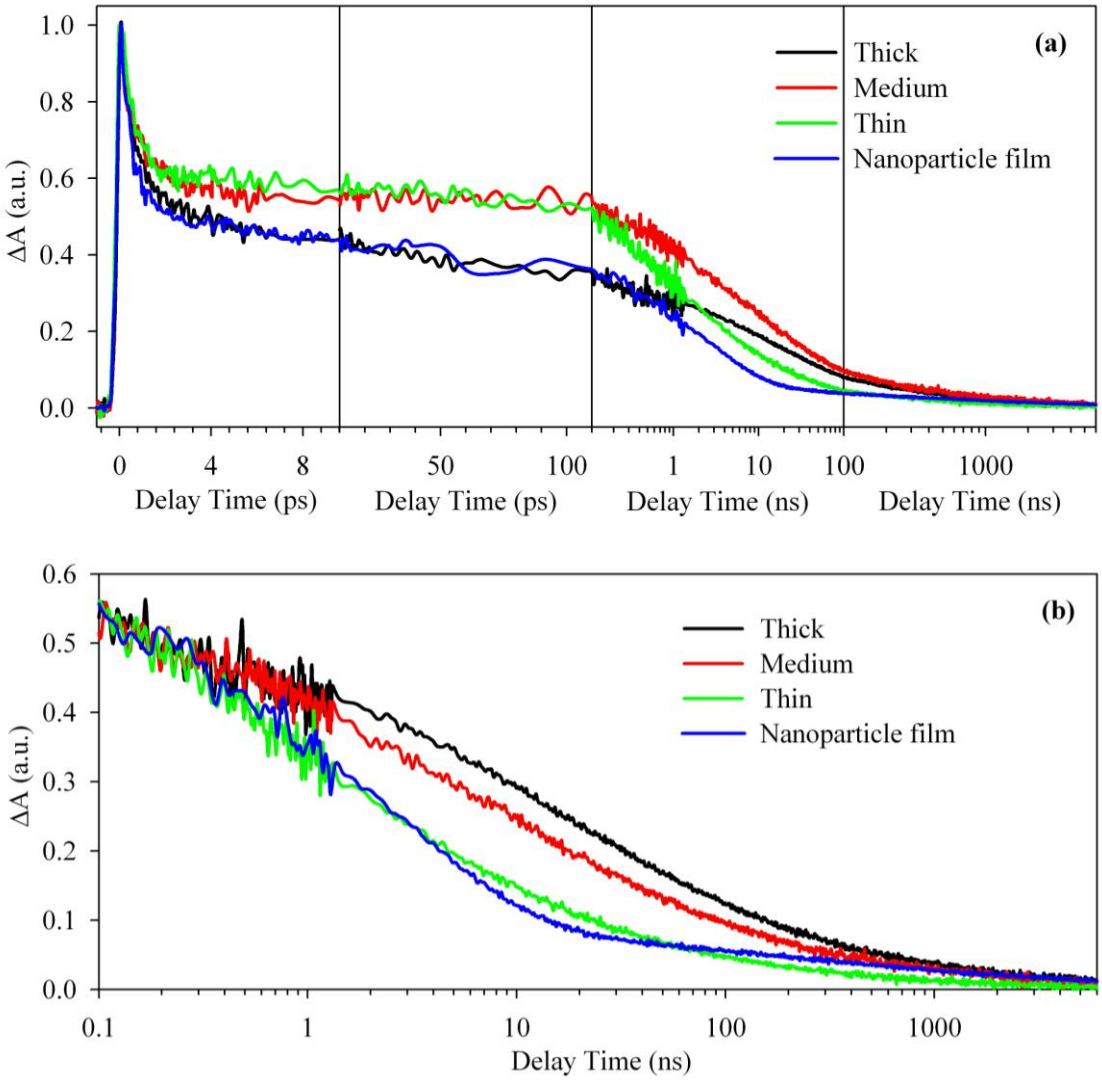

Figure 11.8. Transient kinetics of solid hematite films after 400 nm excitation. These kinetics are monitored at 555 nm (the isosbestic point of the normalized fs spectra). (a) Normalized at $t = 0$; (b) Normalized at 100 ps.

11.2.4 Transient spectra assignment: Stark effect

After 100 ps, the transient spectra are well-defined and have wavelength-independent kinetic properties. Therefore, we focus here on the spectral analysis and assignment for a transient spectrum averaged over 1 to 1000 ns, as shown in Figure 11.9.

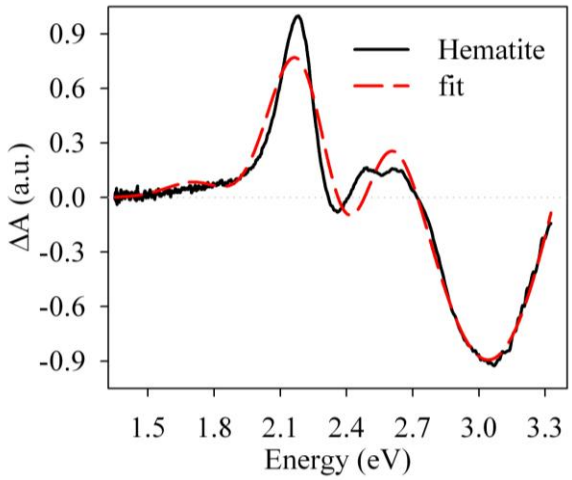

Figure 11.9. A transient spectrum of the hematite film averaged over 1 to 1000 ns (black solid). The red dashed spectrum is a fit to a linear combination of various first- and second-derivative Gaussian components of the static UV-Vis spectrum.

This transient absorption spectrum (TAS) that is seen in Figure 11.9 can result from three effects. First, the depopulation of the ground state causes the bleach feature. Second, the initially generated charge carriers could create an electric field that causes spectral splitting and shifts. This is the so-called Stark effect and has been preliminarily discussed in Chapter 8. And, third, the further excitation of the initially generated photo carriers (electrons or holes or both) by the probe light may cause absorption features in the spectrum.

We first noted that the three main absorption bands in the ground state absorption (GSA) spectrum, 411 (3.01), 520 (2.38), and 653 (1.90) nm (eV), have their corresponding bleach features in the TAS, as indicated in Figure 11.10. In addition, the overall features (peak and valley) of the transient spectrum possess attributes typical of first or second derivatives of Gaussian bands. This implies that the transient electric field

produced by the photo-generated charge carriers might have an electric effect on the other transitions, which frequently occurs in quantum confinement materials.[74-80]

The explicit consequence of the applied electric field is well known as the Stark effect. For a system possessing randomly oriented dipoles, if an external electric field is applied across this system in one direction, those dipoles aligned with the field are red-shifted in energy, while those aligned against the field are blue-shifted, leading to a broadening of the absorption feature. This effect can be mapped out mathematically.[81]

First, the magnitude and direction of the electric field-induced spectral shift depends on the dot product, $-\boldsymbol{E}_{\text{ext}}\cdot\Delta\boldsymbol{\mu}$, where $\boldsymbol{E}_{\text{ext}}$ and $\Delta\boldsymbol{\mu}$ are the applied external field and the difference between the chromophore's permanent dipole moments in the excited and ground states, respectively. Second, an additional contribution exists that originates from the electric-field induced dipoles and is given by $-\Delta\boldsymbol{\alpha}\cdot|\boldsymbol{E}_{\text{ext}}|^2$, where $\Delta\boldsymbol{\alpha}$ is the difference between the chromophore's polarizability in the excited and ground states. Therefore, the total shift in the transition frequency ($\Delta\nu$) will be:

$$\Delta\nu = -\frac{1}{h}\cdot\left(E_{ext}\cdot\Delta\mu + \left|E_{ext}\right|^2\cdot\Delta\alpha\right) \tag{11.1}$$

where h is the Planck constant. The effect on the overall absorption spectrum, $\varepsilon(\nu, \boldsymbol{E})$, can be shown by writing out a Taylor expansion in both the Stark shift and the spectral spacing between interacting states:

$$\begin{aligned}\varepsilon(\nu,E) &= \varepsilon(\nu,0) + \frac{\partial\varepsilon(\nu,0)}{\partial\nu}\Delta\nu + \frac{1}{2}\frac{\partial^2\varepsilon(\nu,0)}{\partial\nu^2}|\Delta\nu|^2 + \ldots \\ &= \varepsilon(\nu,0) - \frac{1}{h}\frac{\partial\varepsilon(\nu,0)}{\partial\nu}\left(E_{ext}\cdot\Delta\mu + |E_{ext}|^2\,\Delta\alpha\right) \\ &\quad + \frac{1}{2h^2}\frac{\partial^2\varepsilon(\nu,0)}{\partial\nu^2}\left(E_{ext}\cdot\Delta\mu + |E_{ext}|^2\,\Delta\alpha\right)^2 + \ldots\end{aligned} \tag{11.2}$$

If the system is isotropic, terms that depend on any odd power of $|\boldsymbol{E}_{\text{ext}}|$ average to zero, while those that depend on even powers of $|\Delta\boldsymbol{E}_{\text{ext}}|$ remain, and thus, eq 11.2 is transformed into,

$$\Delta\varepsilon(\nu) = -\frac{\partial\varepsilon(\nu,0)}{\partial\nu}\frac{\Delta\alpha\,|\,E_{ext}\,|^2}{h} + \frac{1}{2}\frac{\partial^2\varepsilon(\nu,0)}{\partial\nu^2}\frac{|\,\Delta\mu\,|^2|\,E_{ext}\,|^2}{3h^2}\ldots \qquad (11.3)$$

Equation 11.3 shows the total effect of the external field on the absorption spectrum. In this ideal, isotropic system that is under the effect of an unidirectional external electric field, the change in polarizability of the molecule upon excitation results in a spectral shape similar to the first derivative of the ground state spectrum, while the change in permanent dipole leads to a second-derivative like feature.

The discussion here is based on a highly-simplified model system. In a real system, the resulting spectrum due to the Stark effect depends on many factors, such as molecular orientations, directions of electric field, $\Delta\alpha$, $\Delta\mu$, line shapes, higher orders of polarizability…etc.[77,79] Without knowing the details of the physical origins for the hematite TAS, attempting to fit it according to the Stark effect scheme can be very complicated. As a result, the fitting results cannot be expected to be a simple superposition of the 1st and 2nd derivative of the Gaussian components in the GSA spectrum. However, a fit by this simple superposition method generates a spectrum that is quite consistent with the experimental results as shown in Figure 11.8. The contributions from different Gaussian components are summarized in Table 11.2. These percentage contributions shown in Table 11.2 have little meaning since they also include the pre-exponential coefficients in the Gaussian terms. However, Table 11.2 presents fairly-good error bars and also indicates that some of the components do not contribute to the

transient Stark spectra. Therefore, the photo-induced Stark-effect can account for most of the transient spectral features.

Table 11.2. Contributions of different Gaussian components (indicated by its center) to the fitting result.

[a]Band (eV)	1.18	1.87	2.37	2.81	2.96	3.26	4.01
[b]1st	0%	(7.0±0.9)%	(33±2)%	(2.8±1.7)%	0%	0%	(38±12)%
[c]2st	0%	(0.4±0.1)%	(5.5±0.1)%	(1.4±0.9)%	(6.4±0.8)%	(5.5±1.3)%	0%

(a) Center of the ground state transition; (b) and (c) are relative contributions from the first and second derivatives the ground state components, respectively.

11.2.5 Transient spectra assignment: dye-sensitized approaches

Electron donors, hole scavengers and electrochemical methods have been widely employed to assign TAS of charge carriers (electron or hole) in the well-studied TiO_2 nanoporous films.[40,82,83] In particular, the dye sensitization approach provides straightforward assignment of the spectral features if photo-induced electron injection can occur.

Many dye molecules have been tested, yet there is no detectable attachment of the dyes on the electrode surface based on our static absorption measurement. It has been reported that the sulfate group can serve as a linker for the attachment of molecules onto the hematite surface.[84,85] Orange II, an azo dye with sulfate linkers has been used as a probe of the surface area of the hematite.[18,64] However, even with this dye, we did not observe detectable absorption signal after the surface coating. The main reason is that the

film we used for transient spectroscopic studies are not thick enough (~220 nm, estimated based on reference [31,64]) to have sufficient surface area for adequate dye attachment.

In addition, we have clear evidence that optical excitation of the RhB molecule results in electron injection from the excited RhB* to the attached γ-Fe_2O_3. This experiment was designed for understanding the transient spectra of electrons in the conduction band of hematite, given the similarity between hematite (α-Fe_2O_3) and γ-Fe_2O_3. However, the injected electrons after 525 nm excitation are not detectable spectroscopically due to their low extinction coefficient. Despite this, we can estimate the extinction coefficient (~700 M^{-1} cm^{-1}) of the γ-Fe_2O_3 colloids after 400 nm excitation by comparing with the transient RhB signal.

11.2.6 Transient spectra assignment: photoelectrochemical approaches

We have also performed transient studies in the context of a photoelectrochemical cell, which was originally designed for understanding the interfacial charge transfer dynamics during water oxidation reactions (Figure 11.10). However, the transient results up to 6 μs (noise level ~0.5 mOD) are not affected in the presence of catalysts and under bias.

11.3 Concluding remarks

This chapter reports the first clear transient absorption spectra of hematite samples synthesized by different approaches. Given all of the above experimental details and the Stark effect analysis, it is possible that the transient spectral features might be due to the Stark effect caused by the charge carriers in the bulk, although all literatures have

assigned their observed signals to either electrons or holes. The absorption cross sections of the charge carriers could be very small, as that in the γ-Fe_2O_3, and thus, do not show up in the transient spectrum. In addition, the thickness-dependent kinetics could indicate the diffusion process of the carriers in the bulk to the surface.

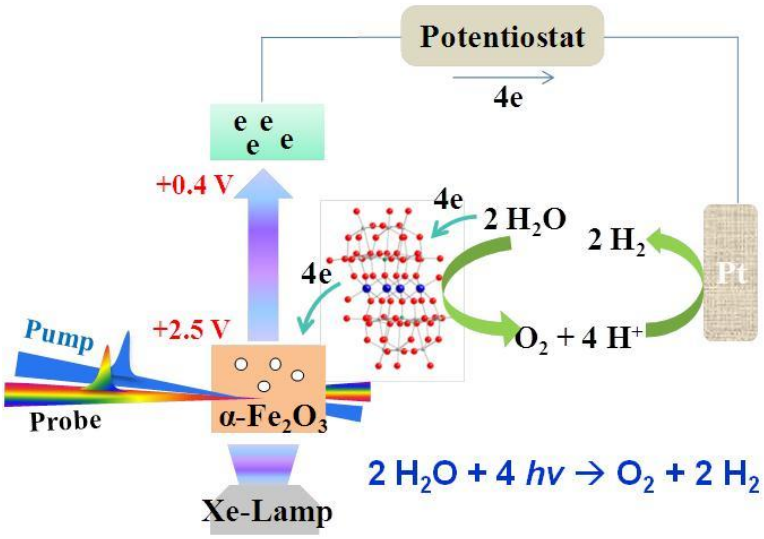

Figure 11.10. Schematic presentation of transient spectroscopic studies in the context of a photoelectrochemical cell.

11.4 References

(1) Walter, M. G.; Warren, E. L.; McKone, J. R.; Boettcher, S. W.; Mi, Q. X.; Santori, E. A.; Lewis, N. S. *Chem Rev* **2010**, *110*, 6446.

(2) Lewis, N. S.; Nocera, D. G. *P Natl Acad Sci USA* **2006**, *103*, 15729.

(3) Fujishima, A.; Honda, K. *Nature* **1972**, *238*, 37.

(4) Kalyanasundaram, K. *Sol Cells* **1985**, *15*, 93.

(5) Kudo, A.; Miseki, Y. *Chem Soc Rev* **2009**, *38*, 253.

(6) Maeda, K.; Domen, K. *J Phys Chem Lett* **2010**, *1*, 2655.

(7) Osterloh, F. E. *Chem Mater* **2008**, *20*, 35.

(8) Bard, A. J.; Fox, M. A. *Accounts Chem Res* **1995**, *28*, 141.

(9) Tilley, S. D.; Cornuz, M.; Sivula, K.; Gratzel, M. *Angew Chem Int Edit* **2010**, *49*, 6405.

(10) Sivula, K.; Le Formal, F.; Gratzel, M. *Chemsuschem* **2011**, *4*, 432.

(11) Sun, J. W.; Zhong, D. K.; Gamelin, D. R. *Energ Environ Sci* **2010**, *3*, 1252.

(12) Lindgren, T. V., L.; Wang, H.; Lindquist, S.-E. *Chemical Physics of Nanostructured Semiconductors* **2003**, 83.

(13) Dareedwards, M. P.; Goodenough, J. B.; Hamnett, A.; Trevellick, P. R. *J Chem Soc Farad T 1* **1983**, *79*, 2027.

(14) Zhong, D. K.; Gamelin, D. R. *J Am Chem Soc* **2010**, *132*, 4202.

(15) Bosman, A. J.; Vandaal, H. J. *Adv Phys* **1970**, *19*, 1.

(16) Kennedy, J. H.; Frese, K. W. *J Electrochem Soc* **1977**, *124*, C130.

(17) Cherepy, N. J.; Liston, D. B.; Lovejoy, J. A.; Deng, H. M.; Zhang, J. Z. *J Phys Chem B* **1998**, *102*, 770.

(18) Kay, A.; Cesar, I.; Gratzel, M. *J Am Chem Soc* **2006**, *128*, 15714.

(19) Kleiman-Shwarsctein, A.; Hu, Y. S.; Stucky, G. D.; McFarland, E. W. *Electrochem Commun* **2009**, *11*, 1150.

(20) Majumder, S. A.; Khan, S. U. M. *Int J Hydrogen Energ* **1994**, *19*, 881.

(21) Zhong, D. K.; Sun, J. W.; Inumaru, H.; Gamelin, D. R. *J Am Chem Soc* **2009**, *131*, 6086.

(22) Brillet, J.; Cornuz, M.; Le Formal, F.; Yum, J. H.; Gratzel, M.; Sivula, K. *J Mater Res* **2010**, *25*, 17.

(23) Aroutiounian, V. M.; Arakelyan, V. M.; Shahnazaryan, G. E.; Stepanyan, G. M.; Turner, J. A.; Khaselev, O. *Int J Hydrogen Energ* **2002**, *27*, 33.

(24) Nozik, A. J. *Appl Phys Lett* **1977**, *30*, 567.

(25) Kleiman-Shwarsctein, A.; Hu, Y. S.; Forman, A. J.; Stucky, G. D.; McFarland, E. W. *J Phys Chem C* **2008**, *112*, 15900.

(26) Kleiman-Shwarsctein, A.; Huda, M. N.; Walsh, A.; Yan, Y. F.; Stucky, G. D.; Hu, Y. S.; Al-Jassim, M. M.; McFarland, E. W. *Chem Mater* **2010**, *22*, 510.

(27) LaTempa, T. J.; Feng, X. J.; Paulose, M.; Grimes, C. A. *J Phys Chem C* **2009**, *113*, 16293.

(28) Cesar, I.; Sivula, K.; Kay, A.; Zboril, R.; Graetzel, M. *J Phys Chem C* **2009**, *113*, 772.

(29) Mao, A.; Han, G. Y.; Park, J. H. *J Mater Chem* **2010**, *20*, 2247.

(30) Brillet, J.; Gratzel, M.; Sivula, K. *Nano Lett* **2010**, *10*, 4155.

(31) Spray, R. L. M., J. K.; Choi, Y.-S. *J. Phys. Chem. C* **2011**, *115*, 3497.

(32) Murphy, A. B.; Barnes, P. R. F.; Randeniya, L. K.; Plumb, I. C.; Grey, I. E.; Horne, M. D.; Glasscock, J. A. *Int J Hydrogen Energ* **2006**, *31*, 1999.

(33) Cowan, A. J.; Tang, J. W.; Leng, W. H.; Durrant, J. R.; Klug, D. R. *J Phys Chem C* **2010**, *114*, 4208.

(34) Tang, J. W.; Durrant, J. R.; Klug, D. R. *J Am Chem Soc* **2008**, *130*, 13885.

(35) Serpone, N.; Lawless, D.; Khairutdinov, R.; Pelizzetti, E. *Journal Of Physical Chemistry* **1995**, *99*, 16655.

(36) Leytner, S.; Hupp, J. T. *Chemical Physics Letters* **2000**, *330*, 231.

(37) Bahnemann, D. W.; Hilgendorff, M.; Memming, R. *The Journal of Physical Chemistry B* **1997**, *101*, 4265.

(38) Zhang, J. *J Phys Chem B* **2000**, *104*, 7239.

(39) Zhang, J. Z. *Acc. Chem. Res.* **1997**, *30*, 423.

(40) Tang, J.; Durrant, J. R.; Klug, D. R. *J Am Chem Soc* **2008**, *130*, 13885.

(41) Cowan, A. J.; Tang, J.; Leng, W.; Durrant, J. R.; Klug, D. R. *The Journal of Physical Chemistry C* **2010**, *ASAP*.

(42) Furube, A.; Murai, M.; Watanabe, S.; Hara, K.; Katoh, R.; Tachiya, M. *J. Photochem. Photobio. A-Chem.* **2006**, *182*, 273.

(43) Tamaki, Y.; Furube, A.; Murai, M.; Hara, K.; Katoh, R.; Tachiya, M. *J Am Chem Soc* **2006**, *128*, 416.

(44) Tamaki, Y.; Furube, A.; Murai, M.; Hara, K.; Katoh, R.; Tachiya, M. *Phys. Chem. Chem. Phys.* **2007**, *9*, 1453

(45) Tamaki, Y.; Hara, K.; Katoh, R.; Tachiya, M.; Furube, A. *The Journal of Physical Chemistry C* **2009**, *113*, 11741.

(46) Yoshihara, T.; Katoh, R.; Furube, A.; Tamaki, Y.; Murai, M.; Hara, K.; Murata, S.; Arakawa, H.; Tachiya, M. *J Phys Chem B* **2004**, *108*, 3817.

(47) Dimitrijevic, N. M.; Savic, D.; Micic, O. I.; Nozik, A. J. *Journal Of Physical Chemistry* **1984**, *88*, 4278.

(48) Xiong, G.; Joly, A. G.; Holtom, G. P.; Wang, C. M.; McCready, D. E.; Beck, K. M.; Hess, W. P. *J Phys Chem B* **2006**, *110*, 16937.

(49) Nadtochenko, V. A.; Denisov, N. N.; Gak, V. Y.; Gostev, F. E.; Titov, A. A.; Sarkisov, O. M.; Nikandrov, V. V. *Russ Chem B+* **2002**, *51*, 457.

(50) Joly, A. G.; Xiong, G.; Wang, C. M.; McCready, D. E.; Beck, K. M.; Hess, W. P. *Appl Phys Lett* **2007**, *90*.

(51) Joly, A. G.; Williams, J. R.; Chambers, S. A.; Xiong, G.; Hess, W. P.; Laman, D. M. *J Appl Phys* **2006**, *99*.

(52) He, Y. P.; Miao, Y. M.; Li, C. R.; Wang, S. Q.; Cao, L.; Xie, S. S.; Yang, G. Z.; Zou, B. S.; Burda, C. *Phys Rev B* **2005**, *71*.

(53) Fu, L. M.; Wu, Z. Y.; Ai, X. C.; Zhang, J. P.; Nie, Y. X.; Xie, S. S.; Yang, G. Z.; Zou, B. S. *J Chem Phys* **2004**, *120*, 3406.

(54) Fan, H. M.; You, G. J.; Li, Y.; Zheng, Z.; Tan, H. R.; Shen, Z. X.; Tang, S. H.; Feng, Y. P. *J Phys Chem C* **2009**, *113*, 9928.

(55) Cowan, A. J.; Barnett, C. J.; Pendlebury, S. R.; Barroso, M.; Sivula, K.; Gratzel, M.; Durrant, J. R.; Klug, D. R. *J Am Chem Soc* **2011**, *133*, 10134.

(56) Pendlebury, S. R.; Barroso, M.; Cowan, A. J.; Sivula, K.; Tang, J. W.; Gratzel, M.; Klug, D.; Durrant, J. R. *Chem Commun* **2011**, *47*, 716.

(57) Tang, J. W.; Cowan, A. J.; Durrant, J. R.; Klug, D. R. *J Phys Chem C* **2011**, *115*, 3143.

(58) Cornell, R. M.; Schwertmann, U. *The Iron Oxide*; Wiley-VCH, 2003.

(59) Nakau, T. *J Phys Soc Jpn* **1960**, *15*, 727.

(60) Benjelloun, D.; Bonnet, J. P.; Doumerc, J. P.; Launay, J. C.; Onillon, M.; Hagenmuller, P. *Mater Chem Phys* **1984**, *10*, 503.

(61) Sherman, D. M.; Waite, T. D. *Am Mineral* **1985**, *70*, 1262.

(62) Sherman, D. M. *Phys Chem Miner* **1996**, *23*, 214.

(63) Sherman, D. M. *Phys Chem Miner* **1985**, *12*, 161.

(64) Spray, R. L.; Choi, K. S. *Chem Mater* **2009**, *21*, 3701.

(65) Goodenough, J. B. *Abstr Pap Am Chem S* **1992**, *203*, 614.

(66) Matsumoto, Y. *J Solid State Chem* **1996**, *126*, 227.

(67) Korobchevskaya, K.; George, C.; Diaspro, A.; Manna, L.; Cingolani, R.; Comin, A. *Appl Phys Lett* **2011**, *99*.

(68) Ling, Y. C.; Wang, G. M.; Wheeler, D. A.; Zhang, J. Z.; Li, Y. *Nano Lett* **2011**, *11*, 2119.

(69) Kronawitter, C. X.; Vayssieres, L.; Shen, S.; Guo, L.; Wheeler, D. A.; Zhang, J. Z.; Antoun, B. R.; S., M. S. *Energ Environ Sci* **2011**, *4*, 3889.

(70) George, S. M. *Chem Rev* **2010**, *110*, 111.

(71) Lin, Y. J.; Zhou, S.; Sheehan, S. W.; Wang, D. W. *J Am Chem Soc* **2011**, *133*, 2398.

(72) He, Y. T.; Wan, J. M.; Tokunaga, T. *J Nanopart Res* **2008**, *10*, 321.

(73) Barroso, M.; Cowan, A. J.; Pendlebury, S. R.; Gratzel, M.; Klug, D. R.; Durrant, J. R. *J. Am. Chem. Soc* **2011**, *133*, 14868.

(74) Hilinski, E. F.; Lucas, P. A.; Wang, Y. *J Chem Phys* **1988**, *89*, 3435.

(75) Norris, D. J.; Sacra, A.; Murray, C. B.; Bawendi, M. G. *Phys Rev Lett* **1994**, *72*, 2612.

(76) Seibold, K.; Navangul, H.; Labhart, H. *Chemical Physics Letters* **1969**, *3*, 275.

(77) Boxer, S. G.; Goldstein, R. A.; Lockhart, D. J.; Middendorf, T. R.; Takiff, L. *Journal Of Physical Chemistry* **1989**, *93*, 8280.

(78) Lockhart, D. J.; Boxer, S. G. *P Natl Acad Sci USA* **1988**, *85*, 107.

(79) Lockhart, D. J.; Boxer, S. G. *Biochemistry-Us* **1987**, *26*, 664.

(80) Zhu, H. M.; Song, N. H.; Lian, T. Q. *J Am Chem Soc* **2011**, *133*, 8762.

(81) Parson, W. W. *Modern Optical Spectroscopy: With Exercises and Examples from Biophysics and Biochemistry*; Springer, 2007.

(82) Leng, W. H.; Barnes, P. R. F.; Juozapavicius, M.; O'Regan, B. C.; Durrant, J. R. *J Phys Chem Lett* **2010**, *1*, 967.

(83) Meekins, B. H.; Kamat, P. V. *Acs Nano* **2009**, *3*, 3437.

(84) Bandara, J.; Mielczarski, J. A.; Kiwi, J. *Langmuir* **1999**, *15*, 7670.

(85) Bandara, J.; Mielczarski, J. A.; Kiwi, J. *Langmuir* **1999**, *15*, 7680.